NOAA Project
Report

Development of two tsunami inundation maps and continuation of the meteotsunami characterization for the GOM

Final Report to the
National Tsunami Hazard Mitigation Program (NTHMP)
in Completion of Project Awards
NA20NWS4670066

Authors

Juan J Horrillo	Texas A&M University at Galveston
Wei Cheng	
Alwin Jose	
Yuchen Shang	

Collaborators:

Brad Baker	Santa Rosa County Emergency Management Director

Under the guidance of
NTHMP Mapping and Modeling Subcommittee

National Tsunami Hazard Mitigation Program

National Oceanic and Atmospheric Administration

Ocean Engineering
Texas A&M University at Galveston
Galveston, Texas, 77553

November 2021

Contents

List of Figures

List of Tables

1 Executive Summary

Potential tsunami sources for the GOM are local submarine landslides, which have been examined in the past by the Atlantic and Gulf of Mexico Tsunami Hazard Assessment Group [ten Brink et al., 2009b]. In their findings, they stated that submarine landslides in the GOM are considered a potential tsunami hazard. However, the probability of such an event (tsunamis generated by large landslides) is low. The probability of occurrence is related to ancient (geological) massive landslides which were probably active prior to 7,000 years ago when large quantities of sediments were emptied into the Gulf of Mexico. Nowadays, sediment continues to empty into the Gulf of Mexico mainly from the Mississippi River. This sediment supply contributes to the slope steepening and the increase of fluid pore pressure in sediments, which may lead to further landslide activities and hence, the reason for this study in determining the potential tsunami hazard and its effects in the Gulf of Mexico.

For the triggering mechanism (tsunami generation) we use five geological sources, i.e., the Eastbreaks, Mississippi Canyon, West Florida landslides, and two Yucatán landslides introduced in [Horrillo et al., 2018]. A probabilistic approach was implemented in our previous study, see [Horrillo et al., 2015], to fill gaps along the continental shelf between the geological landslide sources by adding synthetic landslide sources (four in total) to cover the entire northern part of the GOM. Our probabilistic approach confirmed a recurrence period of major landslide events of around 8000 years, consistent with findings by [Geist et al., 2013].

These geological and probabilistic tsunami sources (nine in total) are used as the maximum credible events that could happen in the region according to the local bathymetry, seafloor slope, and sediment information. These credible events are then used to determine the inundation impact on selected communities along the GOM. The extent and magnitude of the tsunami inundation in those selected locations are achieved by using a combination of 3D and 2D coupled-numerical models. For instance, the 3D model, TSUNAMI3D, is used for tsunami generation to determine the initial dynamic wave or initial source and results are passed as an input to the 2D non-hydrostatic model, NEOWAVE, to determine the tsunami wave propagation and the detailed runup and inundation extent in each of the communities. Tsunami flooding inland-extent, maximum inundation water depth, momentum flux and direction, current velocity and vorticity can then be determined within the inundation-prone areas of the selected communities. Also, tsunami inundation and hurricane category flooding can be compared to access tsunami hazard in unmapped locations.

This project focused on the implementation of recent developments in the tsunami science recommended by the National Tsunami Hazard Mitigation Program - Modeling Mapping Subcommittee - Strategic Plan (NTHMP-MMS-SP) into our current Gulf of Mexico (GOM) tsunami mitigation products. Four main developments for tsunami mitigation have been created under this project for communities in the GOM that will provide guidance to state emergency managers for tsunami hazard mitigation and warning purposes.

The first is the development of tsunami inundation maps in Don Pedro Island-Boca Grande-Captiva Island, FL and Marco Island, FL. Maximum tsunami inundation extent, water height, and momentum flux magnitude and direction are determined from each landslide sources, as well as the maximum of maximum inundation maps from all nine landslide

sources. The two new tsunami inundation map products add to the existing 16 mapped locations, which provide so far good coverage of the most populous coastal areas along the GOM.

The second is a continuing study of the comparison between existing SLOSH hurricane flooding data and our tsunami inundation result, in order to provide temporal-low-order estimate for tsunami hazard areas (community) where inundation studies have not yet been assigned/executed or where little bathymetric and elevation data exists. The adopted approach to define a quick estimate of tsunami vulnerability areas in the GOM has been taken from the existing hurricane storm surge flooding results along coastal areas, in which storm flooding map products are based on hurricane category. The existing storm surge flooding maps cover almost the entire GOM coastal regions and thus they are very well known among GOM regional emergency managers and other parties.

The third is to produce the velocity and vorticity magnitude maps for all the landslide scenarios, for Don Pedro Island-Boca Grande-Captiva Island, FL and Marco Island, FL. Based on these maritime maps, location of strong currents and their damaging levels are identified. The tsunami hazard maritime products such as tsunami current magnitude, vorticity, safe/hazard zones would be central for future developments of maritime hazard maps, maritime emergency response and as well as infrastructure planning. We hope that the results herein may assist the maritime communities, port managers and other NTHMP's interested parties.

The fourth task is a continuation of the study to obtain an understanding of meteotsunami through the characterization of physical parameters in northwestern GOM as a continuation from northeastern GOM studies [Cheng et al., 2021, Horrillo et al., 2020]. The generation and propagation/amplification patterns of meteotsunami waves in northwestern GOM are studied using maximum anomaly tracking, and coastal communities vulnerable to meteotsunami inundation are identified through a suite of idealized numerical experiments covering the entire western GOM, with parameters from different incident wave direction, forward speed and trajectory position.

Although the recurrence of destructive tsunami events have been verified to be quite low in the GOM, our work has confirmed that submarine landslide events with similar characteristics to those used here, have indeed the potential to cause severe damage to GOM coastal communities. Therefore, this work is intended to provide guidance to local emergency managers to help managing urban growth, evacuation planning, and public education with final objective to mitigate potential tsunami hazards in the GOM.

2 Introduction

2.1 Background

The U.S. Tsunami Warning System has included Gulf of Mexico (GOM) coasts since 2005 in order to enable local emergency management to act in response to tsunami warnings. To plan for the warning response, emergency managers must understand what specific areas within their jurisdictions are threatened by tsunamis. Coastal hazard areas susceptible to

tsunami inundation can be determined by historical events, by modeling potential tsunami events (worst-case scenarios), or by using a probabilistic approach to determine the rate of recurrence or likelihood of exceeding a certain threshold. As the GOM coastal regions have no significant recent historical tsunami records, numerical modeling and probabilistic methodologies for source identification must be used to determine coastal hazard zones.

Potential tsunami sources for the GOM are local submarine landslides [ten Brink et al., 2009b]; sources outside the GOM are considered a very low threat and may not significantly impact GOM coastal communities or infrastructure [Knight, 2006]. Although a massive tsunamigenic underwater landslide in the GOM is considered a potential hazard, the frequency of such events (though not well-constrained) is probably quite low based on historical evidence [Dunbar and Weaver, 2008] and available data on ages of failures which suggest they were probably active prior to 7,000 years ago when large quantities of sediments were emptied into the GOM [ten Brink et al., 2009b]. However, sediments continue to empty into the GOM, mainly from the Mississippi River, contributing to slope steepening and the increase of fluid pore pressure in sediments which may lead to unstable slopes that can be subsequently triggered to failure by seismic loading [Masson et al., 2006, ten Brink et al., 2009a, Dugan and Stigall, 2010, Harbitz et al., 2014]. In addition, the unique geometry of the GOM basin makes even unlikely tsunami events potentially hazardous to the entire Gulf Coast. Waves tend to refract along continental slopes; thus, given the curved geomorphology of the GOM shelf and the concave shape of the coastline, any outgoing tsunami wave could potentially affect the opposite coast in addition to the coast close to the landslide source.

Five large-scale geological submarine landslides with tsunamigenic potential have been identified within the GOM [ten Brink et al., 2009b, Chaytor et al., 2016], representing possible worst-case tsunami scenarios affecting GOM coasts in the past. In order to generate a more complete picture of landslide tsunami potential in the GOM, a probabilistic approach has been implemented to develop four additional synthetic landslide sources which fill gaps along the continental shelf between the geological landslide sources [Pampell-Manis et al., 2016]. These probabilistic tsunami sources are considered to be the maximum credible events that could happen in a particular region of the GOM according to the local bathymetry, seafloor slope, sediment information, and seismic loading. The probabilistic maximum credible events together with the geological sources form a suite of tsunami sources that have been used within coupled 3D and 2D numerical models to model tsunami generation and propagation throughout the GOM and to develop high-resolution inundation maps for the inundation-prone areas of two new communities along the Gulf Coast: Don Pedro Island-Boca Grande-Captiva Island, FL and Marco Island, FL. These inundation studies showed that tsunamis triggered by massive submarine landslides have the potential to cause widespread and significant inundation of coastal cities. All of the 18 communities from both previous and current work and nine landslide sources are shown in Fig. 1.

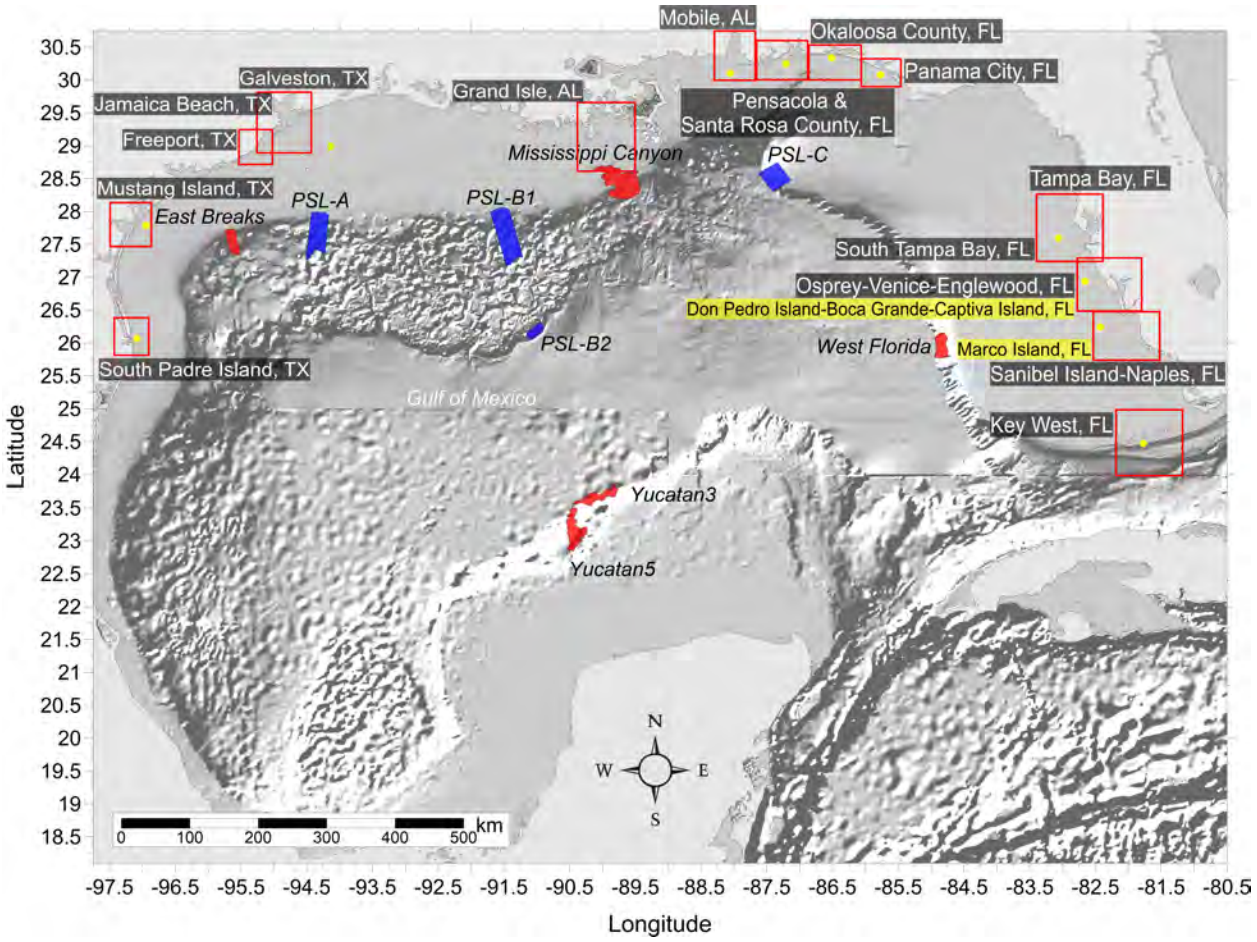

Figure 1: Selected communities or geography regions along the US GOM coastline where tsunami maps have been developed. Red rectangles denote 3 arcsecond (∼90m) domains of coastal communities where tsunami inundation has been modeled (highlighted Don Pedro Island-Boca Grande-Captiva Island, FL and Marco Island, FL are developed in the current project); red hatched areas are geological landslide sources; blue hatched areas are Probabilistic Submarine Landslide (PSL) sources; yellow dots are locations of numerical wave gauges. The zero-meter elevation contour is drawn to show the GOM coastline.

While high-resolution tsunami inundation studies have been completed for these 18 communities and are planned for additional locations, vulnerability assessments are still essential for coastal locations where inundation studies have not yet been performed or planned, or where there is a lack of high-resolution bathymetric and/or elevation data. Therefore, we aim to extend the results of the completed mapping studies in order to provide estimates of tsunami inundation zones for hazard mitigation efforts in unmapped locations. Inundation maps with even low resolution are useful to emergency managers to create first-order evacuation maps, and some methods currently exist to provide low-resolution estimates of hazard zones for regions which do not currently have or warrant high-resolution maps. For example, guidance given by the National Tsunami Hazard Mitigation Program (NTHMP) Mapping and Modeling Subcommittee in "Guidelines and Best Practices to Establish Areas of Tsunami Inundation for Non-modeled or Low-hazard Regions" (available from `https://nws.weather.gov/nthmp/documents/3nonmodeledregionguidelines.pdf`) recommends that coastal areas and areas along ocean-connected waterways that are below 10 m (33 ft) elevation are at risk for most tsunamis, and rare and large tsunamis may inundate above this elevation. However, in low-lying coastal regions such as along the Gulf Coast, the 10 m (33 ft) elevation contour is too far inland to be reasonably applicable for estimating potential tsunami inundation zones. The guidance additionally suggests that low-lying areas are prone to inundation within 3 km (1.9 mi) inland for locally-generated tsunamis and within 2 km (1.3 mi) inland for distant sources. While these distances may be reasonable for some regions of the Gulf Coast, prevalent bathymetric and topographic features such as barrier islands/peninsulas complicate the method of delineating inundation-prone areas based on distance from the shoreline. As a result, the purpose of the current work is to improve the methodology which compares modeled tsunami inundation to modeled/predicted hurricane storm surge. Specifically, we aim to identify the hurricane category which produces modeled maximum storm surge that best approximates the maximum tsunami inundation in the two new locations modeled in this project. Even though many physical aspects of storm surge inundation are completely different from those of tsunamis (time scale, triggering mechanism, inundation process, etc.), good agreement or clear trends between tsunami and storm surge flooding on a regional scale can be used to provide first-order estimates of potential tsunami inundation in communities where detailed inundation maps have not yet been developed or are not possible due to unavailability of high-resolution bathymetry/elevation data. Additionally, since tsunamis are not well-understood as a threat along the Gulf Coast, while hurricane hazards are well-known, this method of predicting tsunami inundation from storm surge provides a way for GOM emergency managers to better prepare for potential tsunami events based on more understandable and accessible information. This hurricane-tsunami comparison was first carried out in Horrillo et al. [2016] (award number NA14NWS4670049) where five previously mapped locations were studied, namely South Padre Island, TX, Galveston, TX, Mobile, AL, Panama City, FL, and Tampa, FL; then as a regular procedure for all the newly mapped locations during the following mapping projects.

Recent tsunamis have shown that the maritime community requires additional information and guidance about tsunami hazards and post-tsunami recovery [Wilson et al., 2012, 2013]. To accomplish mapping and modeling activities to meet NTHMP's planning/response purposes for the maritime community and port emergency management and other customer

requirements, it is necessary to continue the process to include maritime products in our current inundation map development. These activities will include tsunami hazard maritime products generated by GOM's tsunami sources (submarine landslides) that may impact specifically ship channels, bay inlets, harbors, marinas, and oil infrastructures (e.g., designated lightering and oil tanker waiting zones), which has already been applied in other tsunami risk regions, e.g., California, Oregon and Washington. It is worth noting that Galveston was the first city where we implemented the maritime products [Horrillo et al., 2016]. South Padre Island, TX, Mobile, AL, Panama City, FL, and Tampa, FL, Pensacola, FL, Key West, FL, Okaloosa County, FL, Santa Rosa County, FL and Mustang Island, TX, were implemented in project NA15NWS4670031 and NA16NWS4670039 [Horrillo et al., 2017], and then as a regular procedure for all the newly mapped locations during the following mapping projects.

An additional task is a study where we conducted numerical experiments to investigate the generation and propagation of meteotsunami waves and assessed hazards on a broad scale in the northwestern Gulf of Mexico (GOM), as a continuation from northeastern GOM studies [Cheng et al., 2021, Horrillo et al., 2020]. Also in this study we attempt an MT characterization for Clearwater,FL along the west coast of Florida to get maximum MT wave amplitude (η_{max_MT}) expected for a given pressure disturbance condition using MT Rose Plots. This characterization can be used to generate Emergency Response Playbooks (ERP) for various places that can be used by emergency planners and interested parties to add the MT component to the storm surge. Last, to provide a broader and faster way to predict the hazards on a broad scale, an optimal artificial neural network (ANN) was trained using data from a large number of MT simulations in the northeastern GOM.

2.2 Regional and Historical Context

Don Pedro Island-Boca Grande-Captiva Island, FL

The Don Pedro Island-Boca Grande (Gasparilla Island)-Captiva Island area in southwest Florida was selected for this project to fill in between the Osprey-Venice-Englewood, FL and Sanibel Island, FL mapping areas investigated in Horrillo et al. [2019]. In this study, the finest grid (1/3 arcsecond) also includes Rotonda West on the mainland. Don Pedro Island, Rotonda West, and northern part of the Gasparilla Island all belong to Charlotte County, while southern Gasparilla Island and Captiva Island belong to Lee County in Florida. Cayo Costa sits in between Boca Grande and Captiva Island, but its northern portion (Cayo Costa State Park) is not included in this study because there are no residents. These islands form a chain of barrier islands separated by a few inlets. Don Pedro Island can only be accessed from the mainland by boat, while Boca Grande is accessible via Boca Grande Causeway. North Captiva Island can not be reached via bridge too, but Captiva Island is connected to mainland through Sanibel Island via Sanibel Captiva Rd, Periwinkle Way and eventually Sanibel Causeway. The population of Boca Grande was reported to be 1,705 in 2012, and Captiva was 583 according to the 2010 census.

Marco Island, FL

The Marco Island 1/3 arcsecond computational domain encompasses the entire Marco Island, as well as the Fred Key, Helen Key, Tripod Key and Kice Island southeast of the Marco Island. This area is located south of Naples, which was mapped in Horrillo et al. [2019]. The maps from this mapping project, together with those from Horrillo et al. [2019], provide a complete tsunami inundation mapping coverage for populated southwestern Florida coast.

Marco Island is a barrier island in the Collier County, Florida, known for its beach and boating resorts. The population was 16,413 according to the 2010 census. The island can only be accessed from the mainland via the Collier Blvd and San Marco Rd.

Recent Hurricane History

Florida is frequented by hurricanes due to its unique location and long coastlines. Our study location in southwestern Florida is no exception. This area has been visited by many major hurricanes, and recent ones are briefly summarized as follows.

Hurricane Irma became category 4 when it landed on Marco Island in 2017, down from category 5 when it first hit Cuba, which greatly reduced the damage. Nonetheless, Irma still remains as one of the costliest storms in the history of Florida. Wind from Hurricane Irma damaged many homes and uprooted and knocked over trees, and caused power outage to Collier County, Lee County, Charlotte County, and Sarasota County. Four miles of beach area in southern Gasparilla Island and southern eight miles of beach in North Captiva Island were critically eroded threatening development. Some parts of the Marco Island saw 1–2 feet of water.

The last major hurricane that hit Florida before Irma was Hurricane Wilma which made landfall in Collier County, FL on October 24, 2005. Mandatory evacuations were ordered for Collier County residents southwest of US 41. The peak of storm surge occurred in the Naples area, and the Naples Airport was damaged significantly. Charlotte and Manatee only suffered minor damage from Wilma.

Hurricane Charley, a category 4 hurricane, made landfall in southwest Florida (Cayo Costa, north of Captiva Island) in mid-August, 2004, and caused ten deaths and severe damage to buildings and crops, making it the second costliest hurricane at the time. Southwestern Florida, including Sarasota and Charlotte County, has seen the most severe damage. Charley's relatively small size produced only 2 m of storm surge (comparing to its intensity), nonetheless, it breached North Captiva Island and opened up a 450 m wide inlet. The hurricane left many house damaged on Gasparilla Island, North Captiva Island and Captiva Island. The most severe damage occurred in Boca Grande, where power lines were snapped and house were destroyed/damaged.

Other major hurricanes that have made landfall in Florida but did not make much impact in southwestern Florida include Hurricane Ivan in 2004, Hurricane Dennis in 2005.

2.3 Summary

Although the probability of a large-scale tsunami event in the GOM is low, this and previous studies have indicated that tsunami events with characteristics similar to those detailed

in Horrillo et al. [2015] have the potential to cause severe flooding and damage to GOM coastal communities that is similar to or even greater than that seen from major hurricanes, particularly in open beach and barrier island regions. Tsunami hazard maritime products such as tsunami current magnitude, vorticity, safe/hazard zones would be central for future developments of maritime hazard maps, maritime emergency response as well as infrastructure planning. The results of this work are intended to provide guidance to local emergency managers to help with managing urban growth, evacuation planning, and public education with the vision to mitigate potential GOM tsunami hazards.

This report is organized as follows. Section 3 briefly describes all 9 landslide sources used for tsunami modeling (3.1) and the numerical models used for simulations (3.2). Section 4 covers the inundation and momentum flux maps for Don Pedro Island-Boca Grande-Captiva Island, FL and Marco Island, FL. The comparison between tsunami inundation and hurricane storm surge inundation (tsunami inundation in terms of hurricane category) is given in Section 5 for the two new Gulf Coast communities. Current velocity and vorticity maps are described in Section 6 for the two new communities. Section 7 presents numerical results for a meteotsunami parameter study of northwestern GOM/Texas-Louisiana coast, with identification of coastal communities vulnerable to meteotsunami inundation. Concluding remarks on general trends seen among the communities and practical applications for other regions are given in Section 10.

3 Tsunami Inundation Modeling

3.1 Landslide Tsunami Sources

Nine large-scale landslide configurations were created assuming an unstable (gravity-driven) sediment deposit condition. Five of these landslide configurations are geological events identified by ten Brink et al. [2009b]: the Eastbreaks, Mississippi Canyon, and West Florida submarine landslides; and Chaytor et al. [2016]: the Yucatán #3 and Yucatán #5 landslides, which are shown as red hatched regions in Fig. 1. The Yucatán Shelf/Campeche Escarpment was the last remaining area of the GOM that had not been evaluated for landslide tsunami hazards, until high-resolution mapping data collected in 2013 [Paull et al., 2014] shows that the Yucatán Shelf/Campeche Escarpment margin has been subjected to intense modifications by Cenozoic mass wasting processes. Although no known tsunami events have been linked to these Yucatán sources, numerical modeling result shows that they are capable of generating tsunamis that could propagate throughout the GOM Basin [Chaytor et al., 2016]. The other four were obtained using a probabilistic methodology based on work by Maretzki et al. [2007] and Grilli et al. [2009] and extended for the GOM by Pampell-Manis et al. [2016]. The probabilistic landslide configurations were determined based on distributions of previous GOM submarine landslide dimensions through a Monte Carlo Simulation (MCS) approach. The MCS methodology incorporates a statistical correlation method for capturing trends seen in observational data for landslide size parameters while still allowing for randomness in the generated landslide dimensions. Slope stability analyses are performed for the MCS-generated trial landslide configurations using landslide and sediment properties and regional seismic loading (Peak Horizontal ground Acceleration, PHA) to determine landslide configurations which fail and produce a tsunami. The probability of each tsunamigenic failure is calculated based on the joint probability of the earthquake PHA and the probability that the trial landslide fails and produces a tsunami wave above a certain threshold. Those failures which produce the largest tsunami amplitude and have the highest probability of occurrence are deemed the most extreme probabilistic events, and the dimensions of these events are averaged to determine maximum credible probabilistic sources. The four maximum credible Probabilistic Submarine Landslides (PSLs) used as tsunami sources for this study are termed PSL-A, PSL-B1, PSL-B2, and PSL-C and are shown as blue hatched regions in Fig. 1. For a more complete discussion of GOM submarine landslide sources, the reader can consult Horrillo et al. [2015, 2018], Pampell-Manis et al. [2016].

Table 1: Submarine Landslide general information.

Submarine Landslide	Location (Lon, Lat)	Age/Recurrence (Years)	Area (km^2)	Volume (km^3)	Excavation Depth (m)	Modeled Volume (km^3)
East Breaks	-95.68, 27.70	$\sim 10000 - 25000$	~ 519.52	~ 21.95	~ 160	26.7
Mississippi	-90.00, 28.60	$\sim 7500 - 11000$	~ 3687.26	~ 425.54	~ 300	425
West Florida	-84.75, 25.95	> 10000	~ 647.57	~ 16.2	~ 150	18.4
Yucatán #3	-90.07, 23.00	–	~ 578	~ 38	~ 278	39.3
Yucatán #5	-89.80, 23.54	–	~ 1094	~ 70.2	~ 385	69.5
PSL-A	-94.30, 27.98	$\sim 7700 - 7800$	~ 1686	~ 57	~ 67	58
PSL-B1	-91.56, 28.05	$\sim 5400 - 5500$	~ 3118	~ 69	~ 44	57.3
PSL-B2	-91.01, 26.17	$\sim 4700 - 4800$	~ 282	~ 45	~ 323	68
PSL-C	-87.20, 28.62	$\sim 550 - 650$	~ 1529	~ 315	~ 404	357

3.2 Numerical Models

For the nine landslide tsunami sources considered here, tsunami wave development and subsequent propagation and inundation of coastal communities was modeled using coupled 3D and 2D numerical models [Horrillo et al., 2015]. The tsunami generation phase was modeled using the 3D model TSUNAMI3D [Horrillo, 2006, Horrillo et al., 2013], which solves the finite difference approximation of the full Navier-Stokes equations and the incompressibility (continuity) equation. Water and landslide material are represented as Newtonian fluids with different densities, and the landslide-water and water-air interfaces are tracked using the Volume of Fluid (VOF) method of Hirt and Nichols [1981], which is simplified to account for the large horizontal/vertical aspect ratio of the tsunami wave and the selected computational cell size required to construct an efficient 3D grid. The pressure term is split into hydrostatic and non-hydrostatic components. Although TSUNAMI3D has the capability of variable grids, the nesting capability necessary for modeling detailed inundation of coastal regions is too computationally intensive within the fully 3D model; thus, detailed inundation modeling is achieved by coupling the 3D model to a 2D model. Once the tsunami wave generated by the 3D model is fully developed, the wave is passed as an initial condition to the 2D model for modeling wave propagation and coastal inundation. The generated wave is considered fully developed when the total wave energy (potential plus kinetic) reaches a maximum and before the wave leaves the computational domain, as discussed in López-Venegas et al. [2015]. The 2D model used here is NEOWAVE [Yamazaki et al., 2008], a depth-integrated and non-hydrostatic model built on the nonlinear shallow water equations which includes a momentum-conserved advection scheme to model wave breaking and two-way nested grids for modeling higher-resolution wave runup and inundation. Propagation and inundation are calculated via a series of nested grids of increasing resolution, from 15 arcsecond (450 m) resolution for a domain encompassing the entire northern GOM (Fig. 1), to finer resolutions of 3 arcseconds (90 m, from NOAA NCEI Coastal Relief Models), 1 arcsecond (30 m), and 1/3 arcsecond (10 m, from NOAA NCEI Tsunami Inundation Digital Elevation Models [DEMs]) to model detailed inundation of the most populated/ inundation-prone areas of each coastal community. The 3 arcsecond (90 m) subdomains encompassing each coastal community studied here are shown by red rectangles in Fig. 1.

4 Tsunami Maps

Tsunami inundation depth and extent has been modeled for two selected coastal communities: Don Pedro Island-Boca Grande-Captiva Island, FL and Marco Island, FL. Inundation (flooding) is determined by subtracting land elevation from water elevation, and elevations used are in reference to the Mean High Water (MHW) tidal datum. For this study, the tsunami inundation depth/extent modeled for each community is the maximum-of-maximums (MOM) inundation, which is calculated as the maximum inundation depth from an ensemble of inundation depths produced by each of the nine tsunami sources considered. That is, once inundation in a community has been modeled for each of the nine sources, the overall maximum inundation depth in each computational grid cell is taken as the MOM tsunami inundation in that cell. This approach gives a worst-case scenario of estimated tsunami inundation for each coastal community.

In this section, the numerical results (inundation and momentum flux maps) for each landslide source are presented for Don Pedro Island-Boca Grande-Captiva Island, FL and Marco Island, FL. The MOM inundation map from all sources and the maximum inundation map by source are also shown. A summary table of each location's numerical gauge (at an approximate water depth of 20 m) shows maximum wave amplitude and arrival time after each landslide failure.

It is worth noting, however, that for both communities, the MOM tsunami inundation is produced solely by the Mississippi Canyon submarine landslide failure. That geological failure is the largest in both area and volume of material removed, and therefore produces the highest amplitude wave of all sources simulated.

4.1 Don Pedro Island-Boca Grande-Captiva Island, FL

Table 2: Maximum tsunami wave amplitude and corresponding arrival time after landslide failure at Don Pedro Island-Boca Grande-Captiva Island, FL numerical wave gauge: 26°56'19.22"N, 82°39'34.28"W (Fig. 1), approximate water depth 18 m.

Tsunami Source	Maximum Wave Amplitude (m)	Arrival Time After Landslide Failure (hr)
East Breaks	0.37	4.0
PSL-A	0.58	3.7
PSL-B1	0.64	3.0
PSL-B2	1.50	3.1
Mississippi Canyon	4.27	2.6
PSL-C	1.16	2.6
West Florida	1.14	2.2
Yucatan #3	0.52	3.1
Yucatán #5	0.26	3.1

Don Pedro Island-Boca Grande-Captiva Island, FL
East Breaks submarine landslide
Maximum Momentum Flux

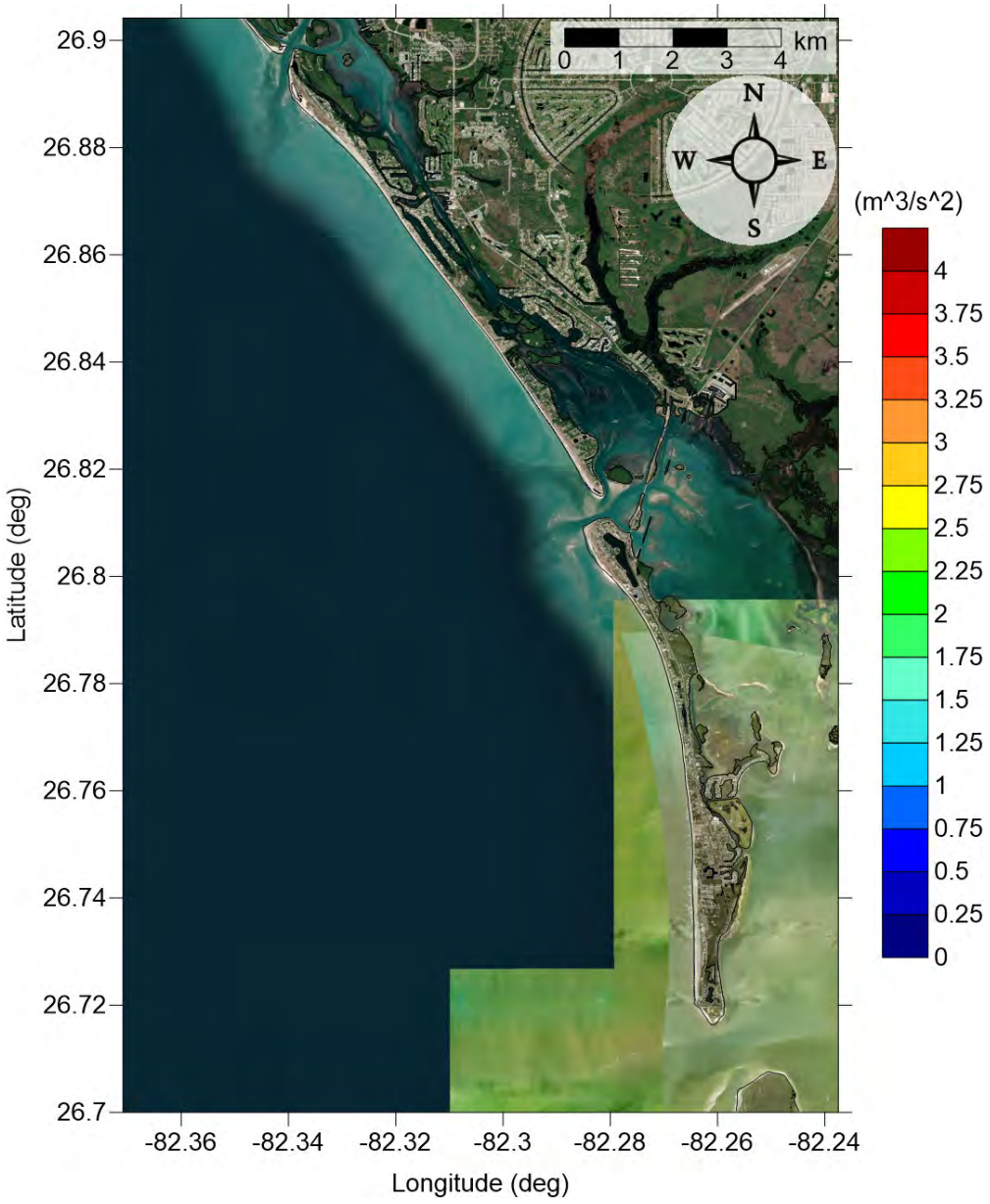

Figure 2: Maximum momentum flux (m^3/s^2) caused by the East Breaks submarine landslide in Don Pedro Island-Boca Grande, FL. Arrows represent direction of maximum momentum flux. Contour drawn is the zero-meter contour for land elevation.

Don Pedro Island-Boca Grande-Captiva Island, FL
East Breaks submarine landslide
Maximum Momentum Flux

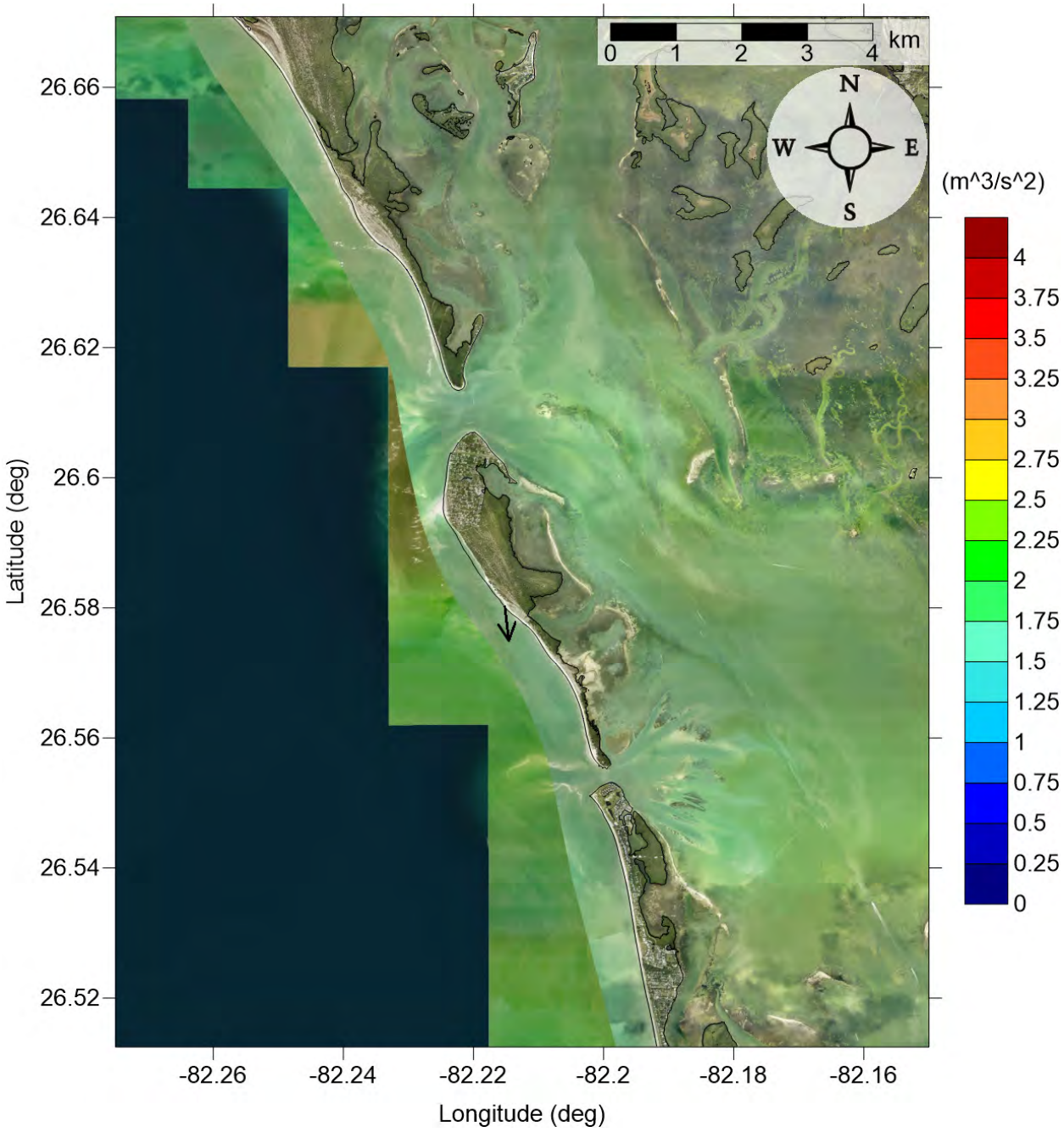

Figure 3: Maximum momentum flux (m^3/s^2) caused by the East Breaks submarine landslide in Captiva Island, FL. Arrows represent direction of maximum momentum flux. Contour drawn is the zero-meter contour for land elevation.

Don Pedro Island-Boca Grande-Captiva Island, FL
East Breaks submarine landslide
Maximum Inundation Depth

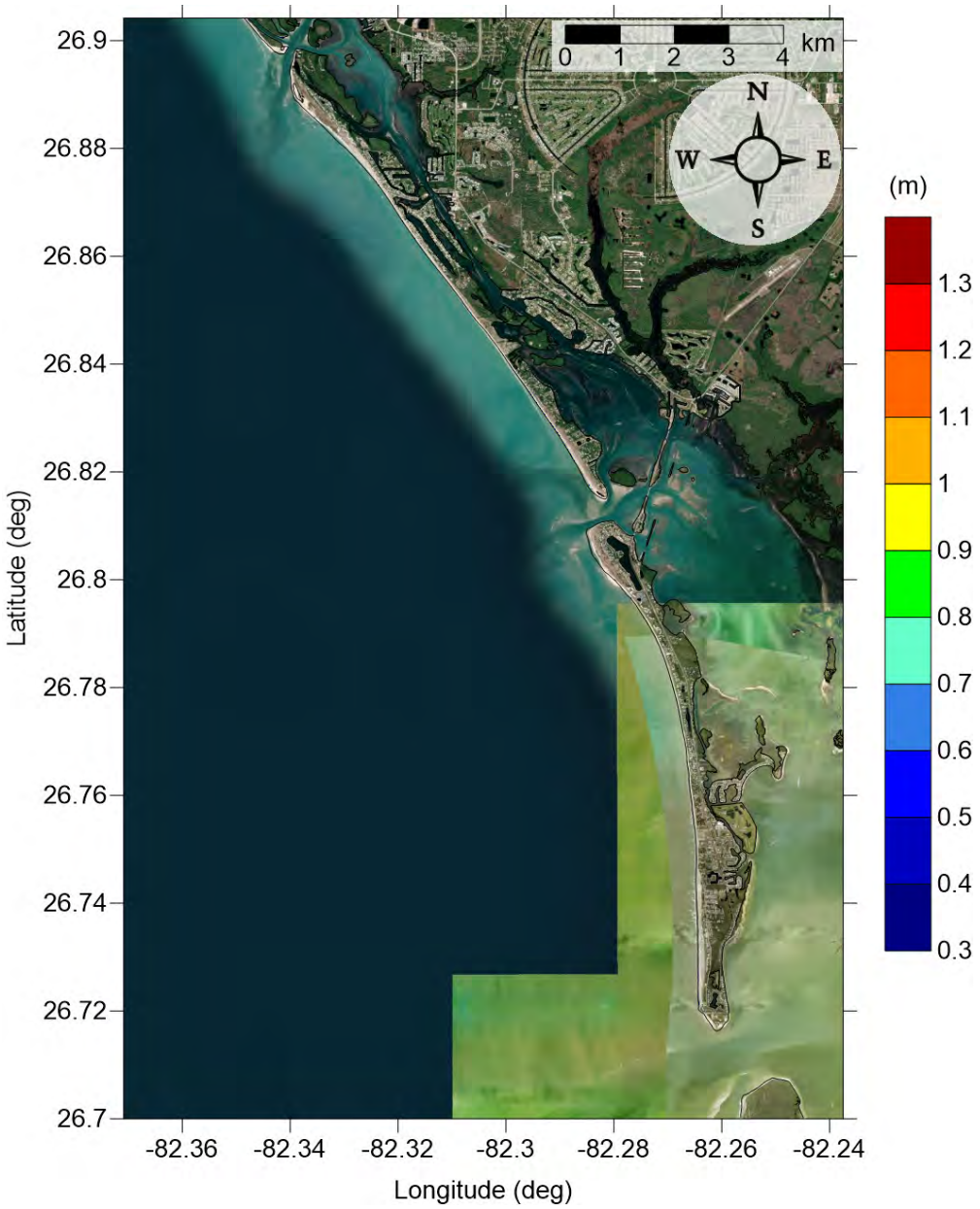

Figure 4: Maximum inundation depth (m) caused by the East Breaks submarine landslide in Don Pedro Island-Boca Grande, FL. Contour drawn is the zero-meter contour for land elevation.

Don Pedro Island-Boca Grande-Captiva Island, FL
East Breaks submarine landslide
Maximum Inundation Depth

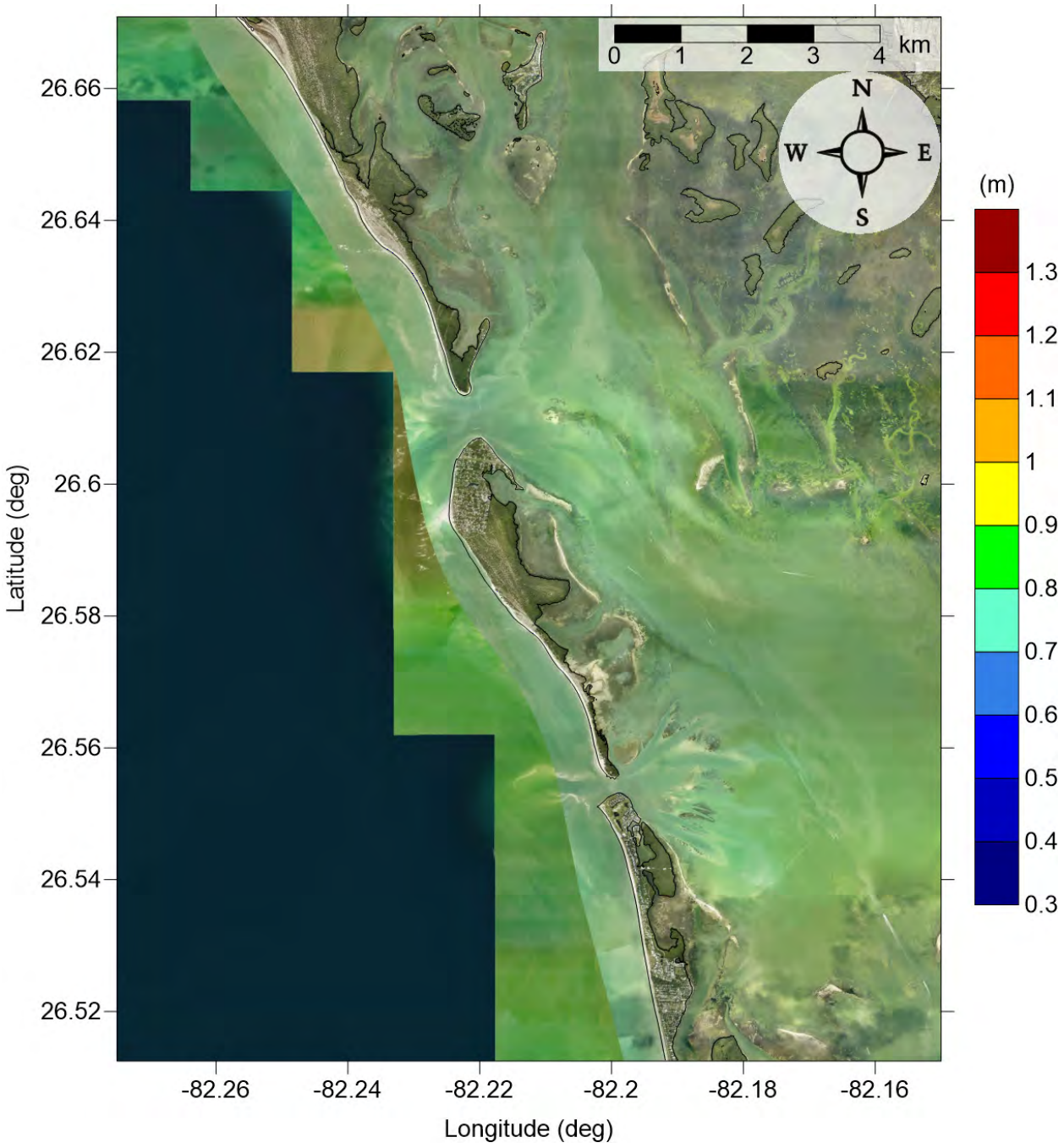

Figure 5: Maximum inundation depth (m) caused by the East Breaks submarine landslide in Captiva Island, FL. Contour drawn is the zero-meter contour for land elevation.

Don Pedro Island-Boca Grande-Captiva Island, FL
Probabilistic Submarine Landslide A
Maximum Momentum Flux

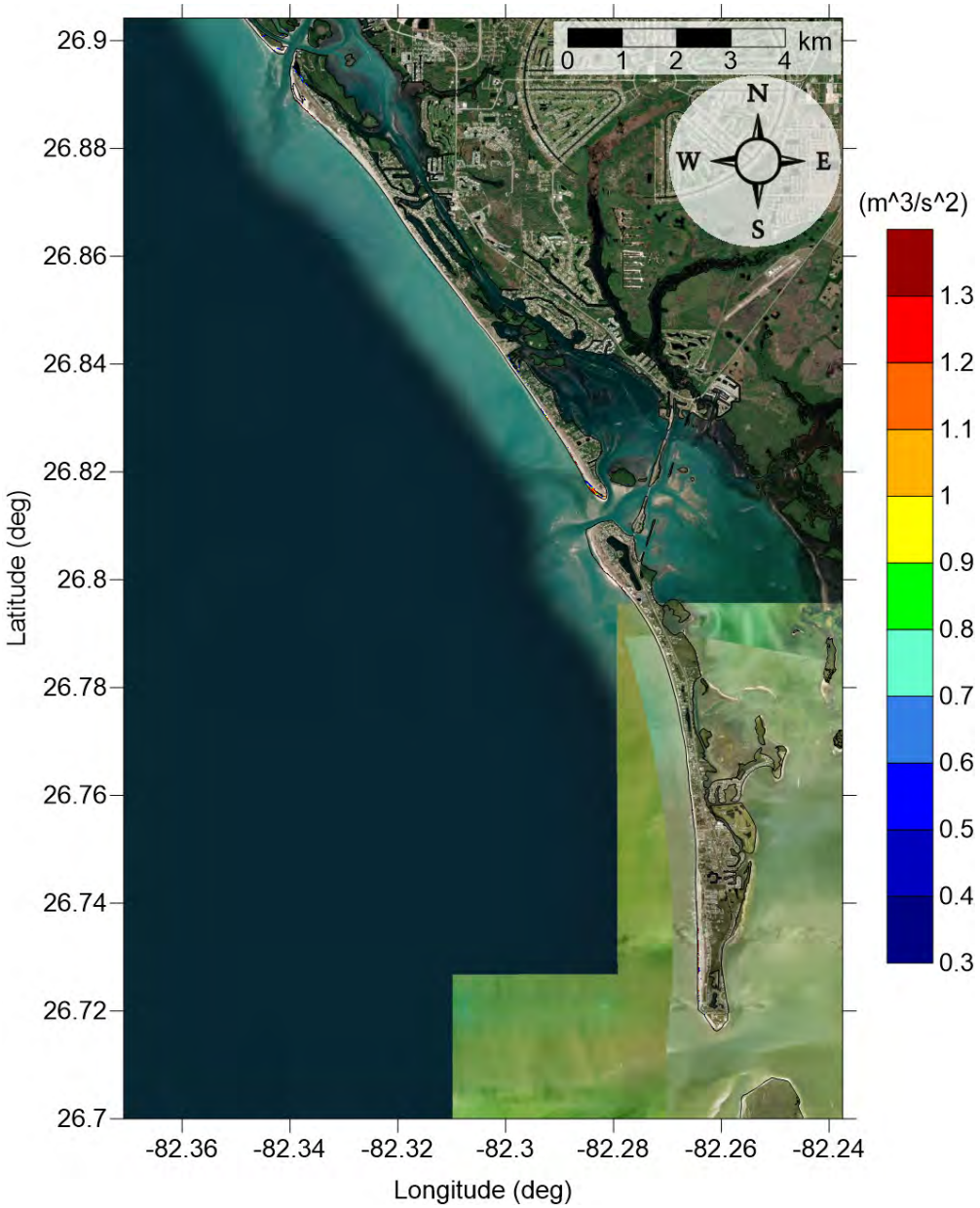

Figure 6: Maximum momentum flux (m^3/s^2) caused by the Probabilistic Submarine Landslide A in Don Pedro Island-Boca Grande, FL. Arrows represent direction of maximum momentum flux. Contour drawn is the zero-meter contour for land elevation.

Don Pedro Island-Boca Grande-Captiva Island, FL
Probabilistic Submarine Landslide A
Maximum Momentum Flux

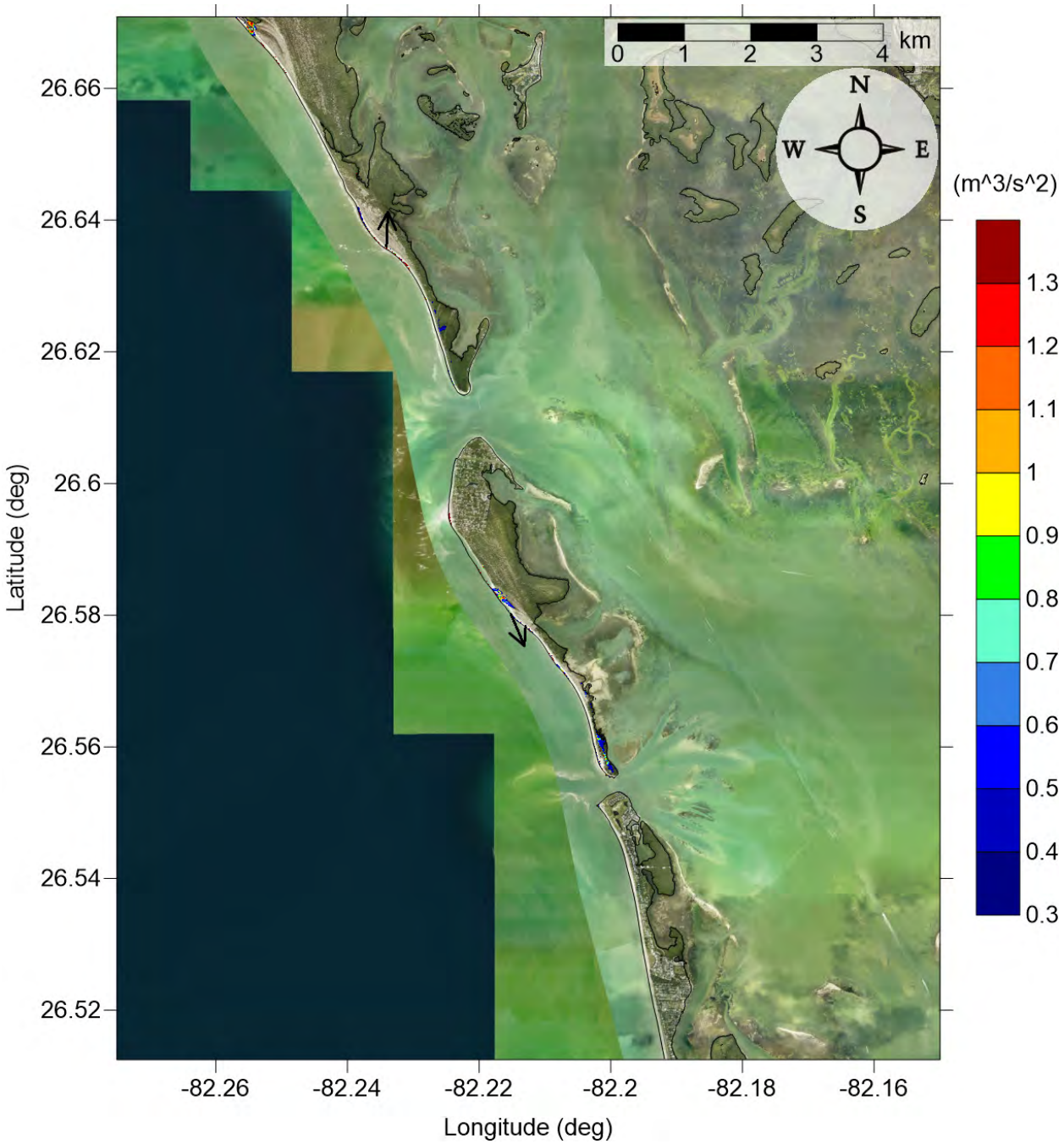

Figure 7: Maximum momentum flux (m^3/s^2) caused by the Probabilistic Submarine Landslide A in Captiva Island, FL. Arrows represent direction of maximum momentum flux. Contour drawn is the zero-meter contour for land elevation.

Don Pedro Island-Boca Grande-Captiva Island, FL
Probabilistic Submarine Landslide A
Maximum Inundation Depth

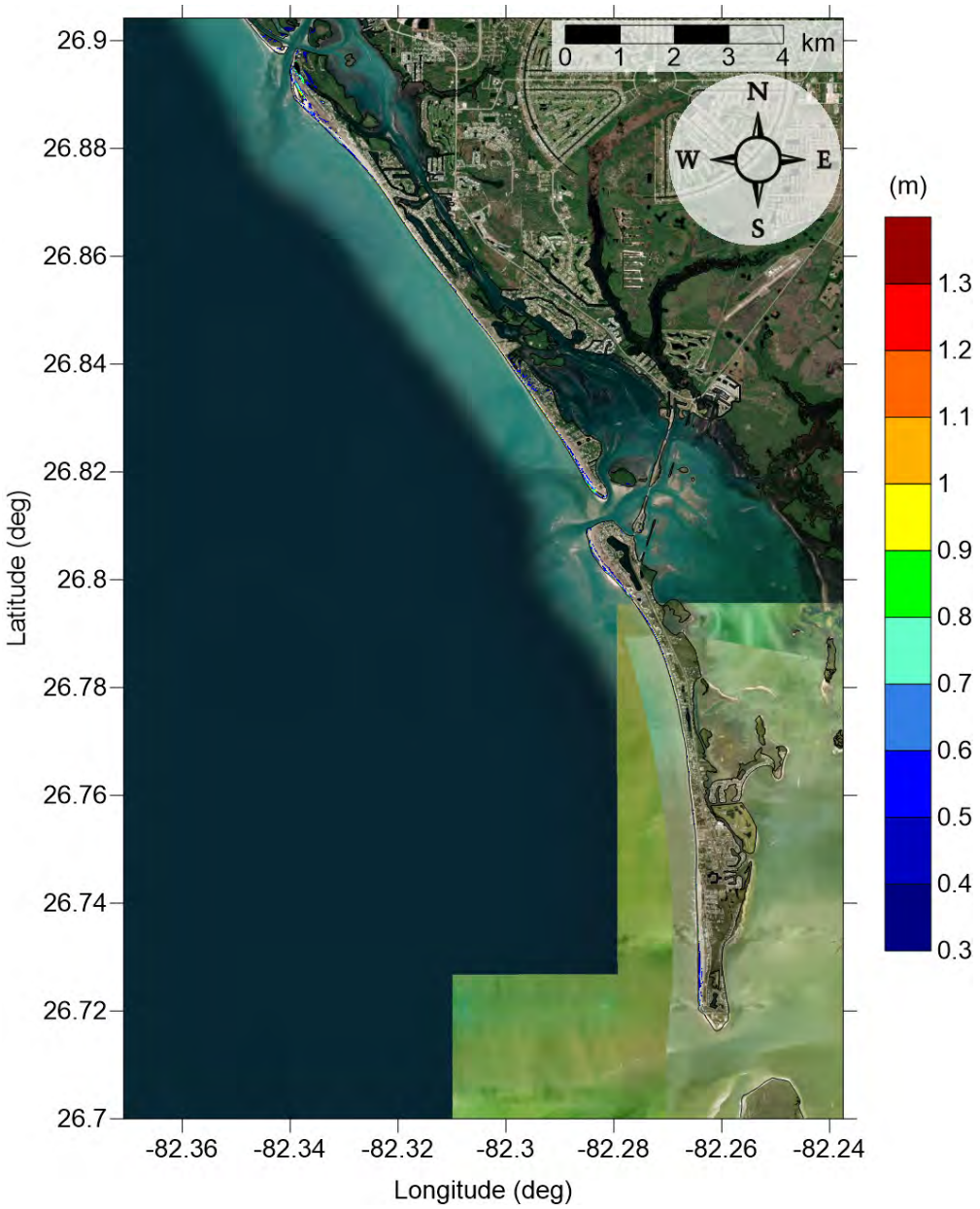

Figure 8: Maximum inundation depth (m) caused by the Probabilistic Submarine Landslide A in Don Pedro Island-Boca Grande, FL. Contour drawn is the zero-meter contour for land elevation.

Don Pedro Island-Boca Grande-Captiva Island, FL
Probabilistic Submarine Landslide A
Maximum Inundation Depth

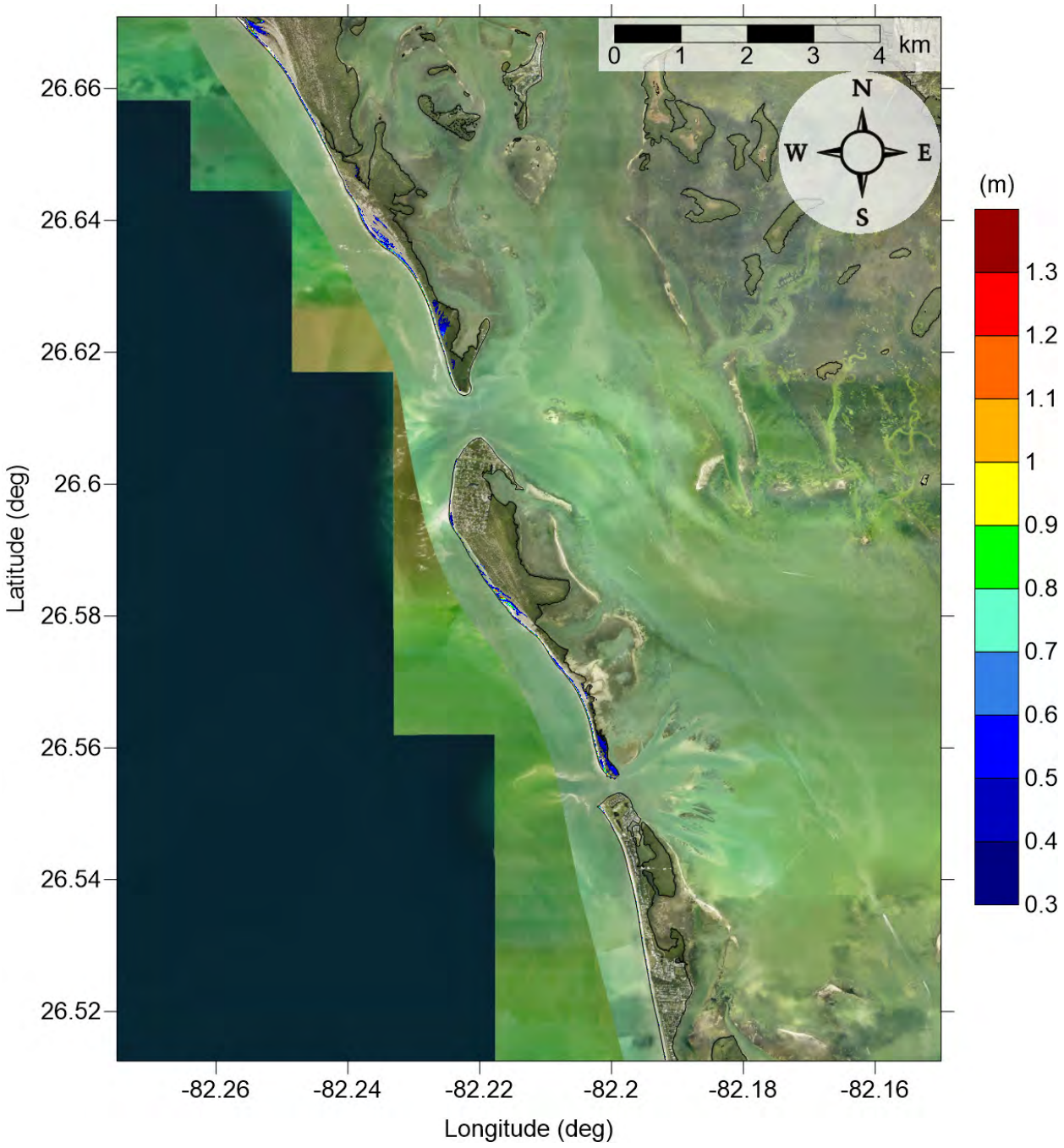

Figure 9: Maximum inundation depth (m) caused by the Probabilistic Submarine Landslide A in Captiva Island, FL. Contour drawn is the zero-meter contour for land elevation.

Don Pedro Island-Boca Grande-Captiva Island, FL
Probabilistic Submarine Landslide B1
Maximum Momentum Flux

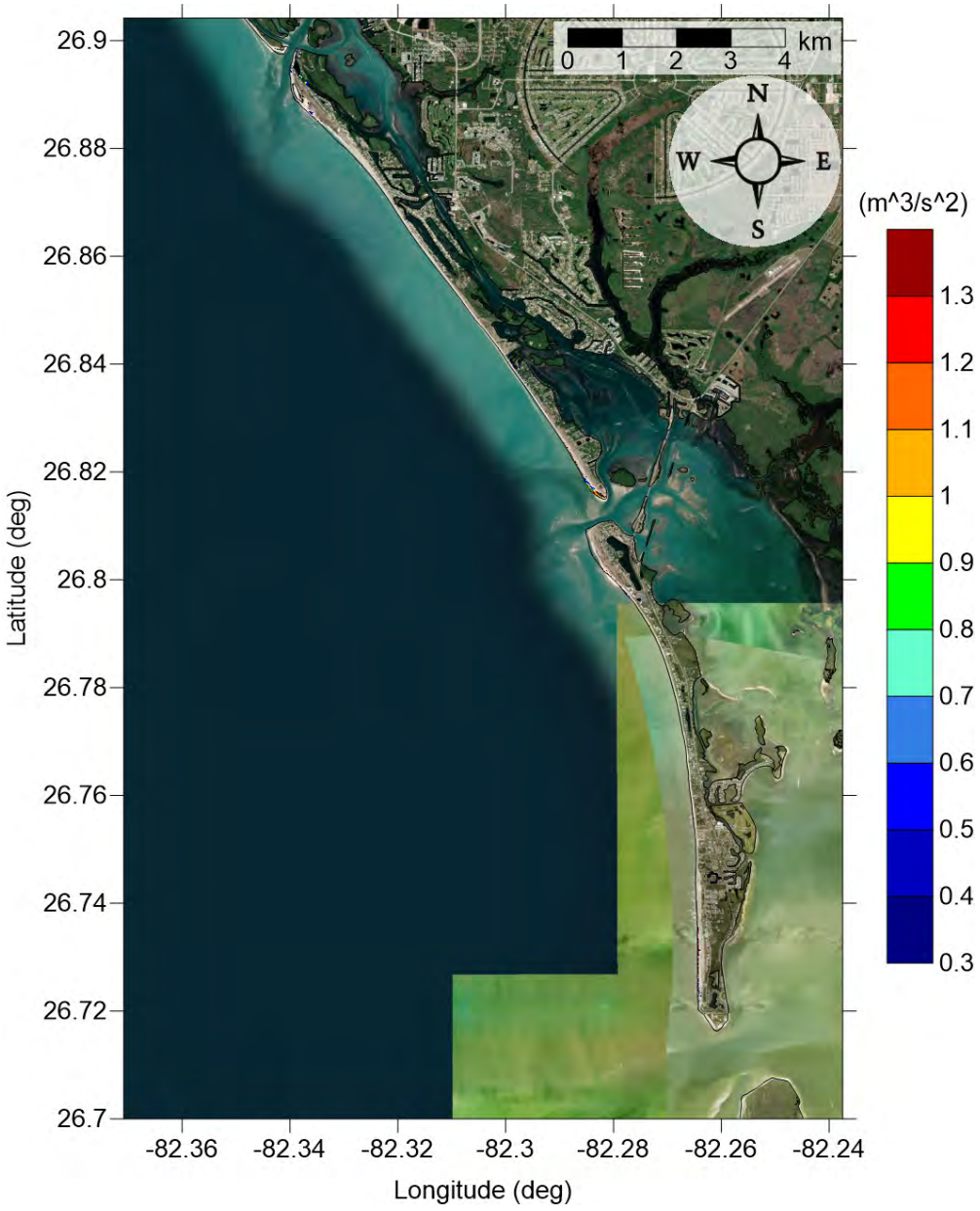

Figure 10: Maximum momentum flux (m^3/s^2) caused by the Probabilistic Submarine Landslide B1 in Don Pedro Island-Boca Grande, FL. Arrows represent direction of maximum momentum flux. Contour drawn is the zero-meter contour for land elevation.

Don Pedro Island-Boca Grande-Captiva Island, FL
Probabilistic Submarine Landslide B1
Maximum Momentum Flux

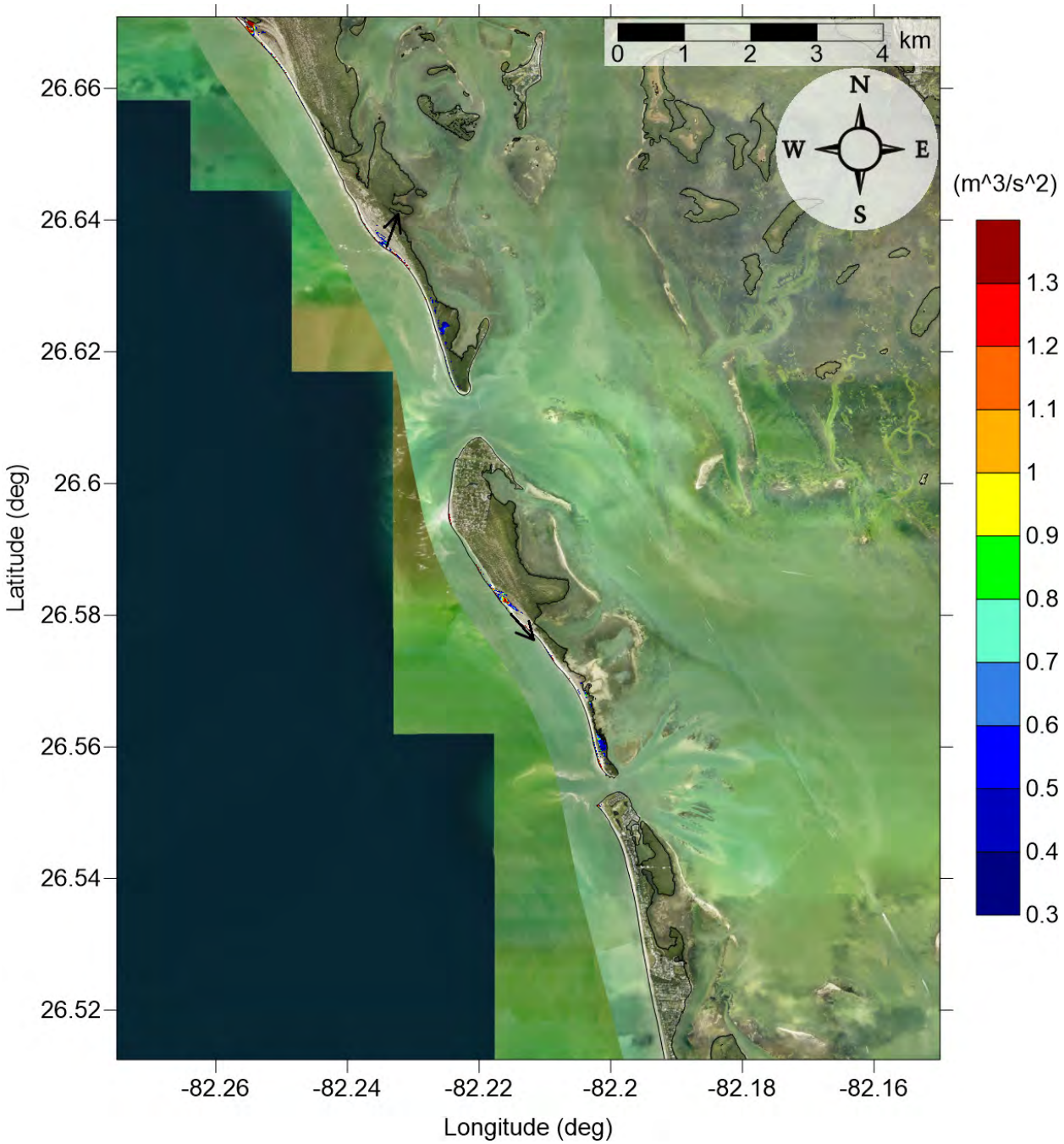

Figure 11: Maximum momentum flux (m^3/s^2) caused by the Probabilistic Submarine Landslide B1 in Captiva Island, FL. Arrows represent direction of maximum momentum flux. Contour drawn is the zero-meter contour for land elevation.

Don Pedro Island-Boca Grande-Captiva Island, FL
Probabilistic Submarine Landslide B1
Maximum Inundation Depth

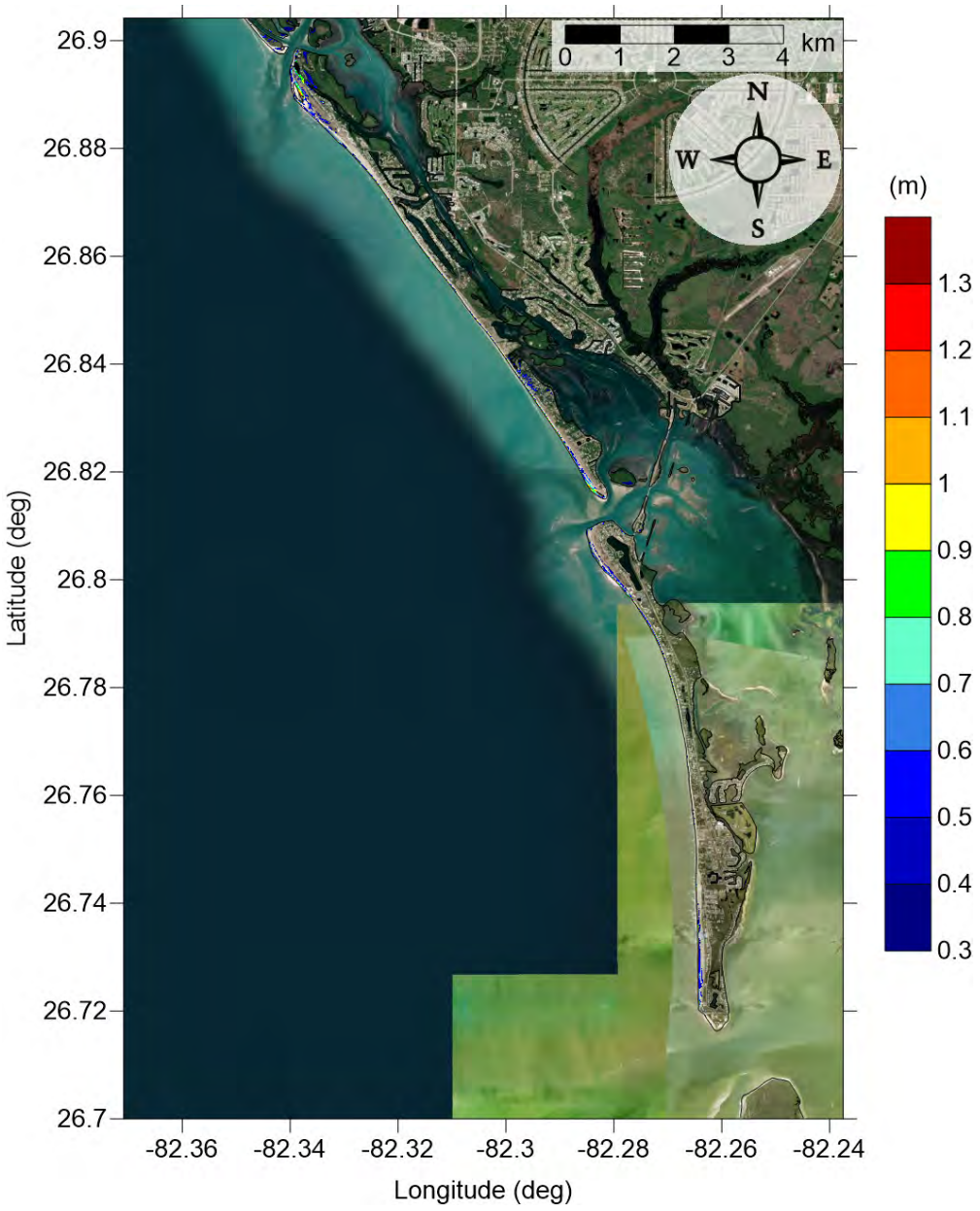

Figure 12: Maximum inundation depth (m) caused by the Probabilistic Submarine Landslide B1 in Don Pedro Island-Boca Grande, FL. Contour drawn is the zero-meter contour for land elevation.

Don Pedro Island-Boca Grande-Captiva Island, FL
Probabilistic Submarine Landslide B1
Maximum Inundation Depth

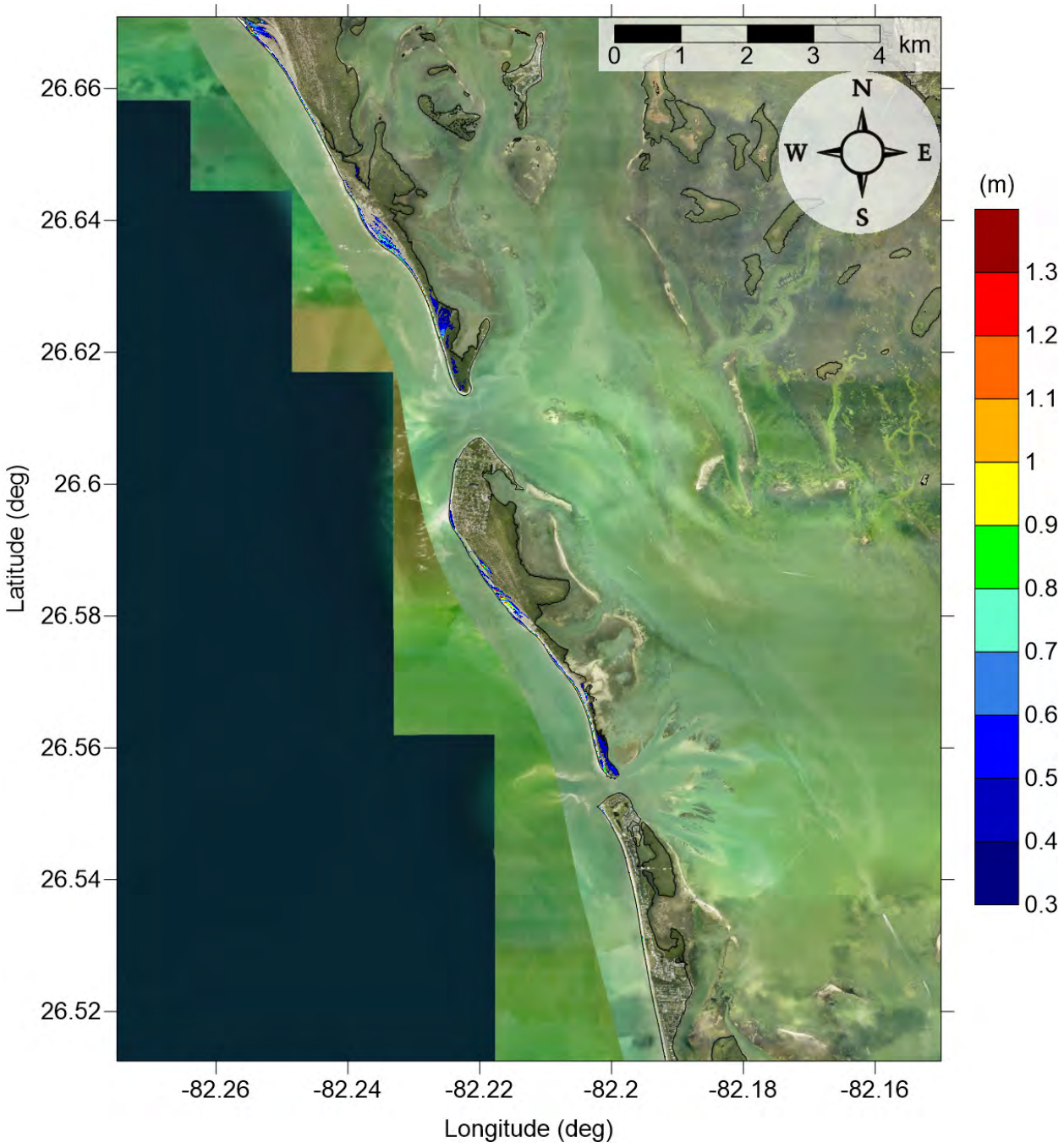

Figure 13: Maximum inundation depth (m) caused by the Probabilistic Submarine Landslide B1 in Captiva Island, FL. Contour drawn is the zero-meter contour for land elevation.

Don Pedro Island-Boca Grande-Captiva Island, FL
Probabilistic Submarine Landslide B2
Maximum Momentum Flux

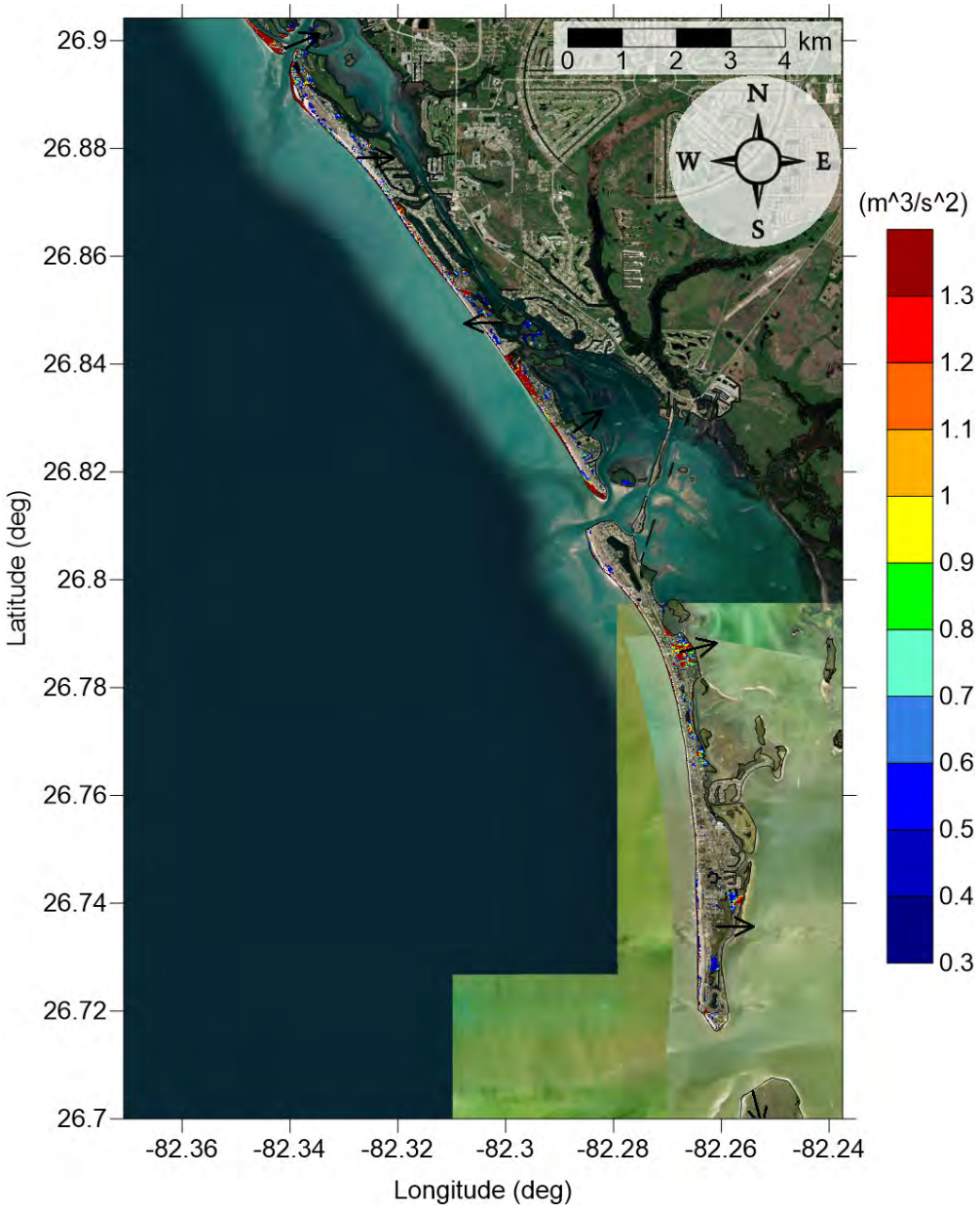

Figure 14: Maximum momentum flux (m^3/s^2) caused by the Probabilistic Submarine Landslide B2 in Don Pedro Island-Boca Grande, FL. Arrows represent direction of maximum momentum flux. Contour drawn is the zero-meter contour for land elevation.

Don Pedro Island-Boca Grande-Captiva Island, FL
Probabilistic Submarine Landslide B2
Maximum Momentum Flux

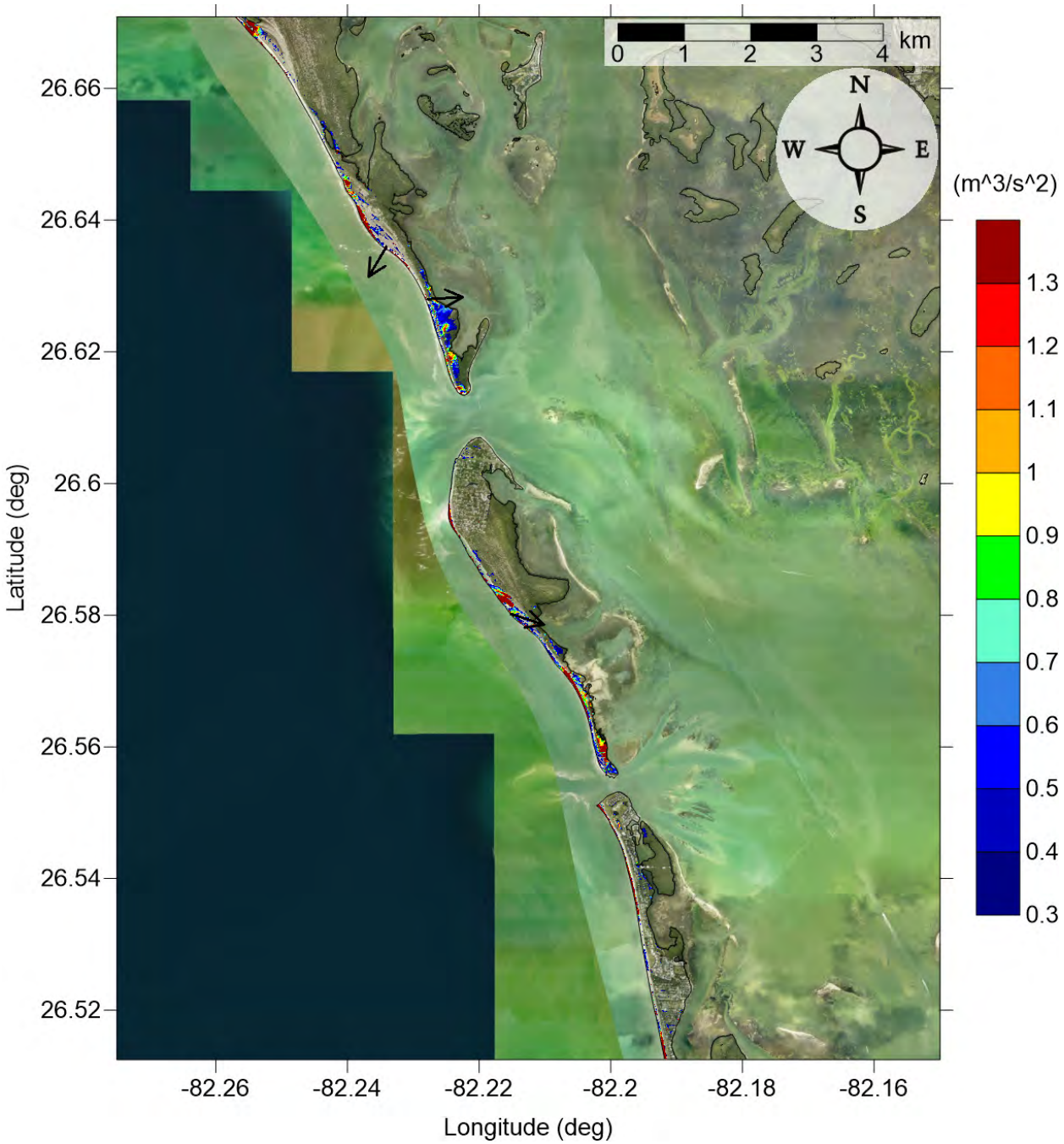

Figure 15: Maximum momentum flux (m^3/s^2) caused by the Probabilistic Submarine Landslide B2 in Captiva Island, FL. Arrows represent direction of maximum momentum flux. Contour drawn is the zero-meter contour for land elevation.

Don Pedro Island-Boca Grande-Captiva Island, FL
Probabilistic Submarine Landslide B2
Maximum Inundation Depth

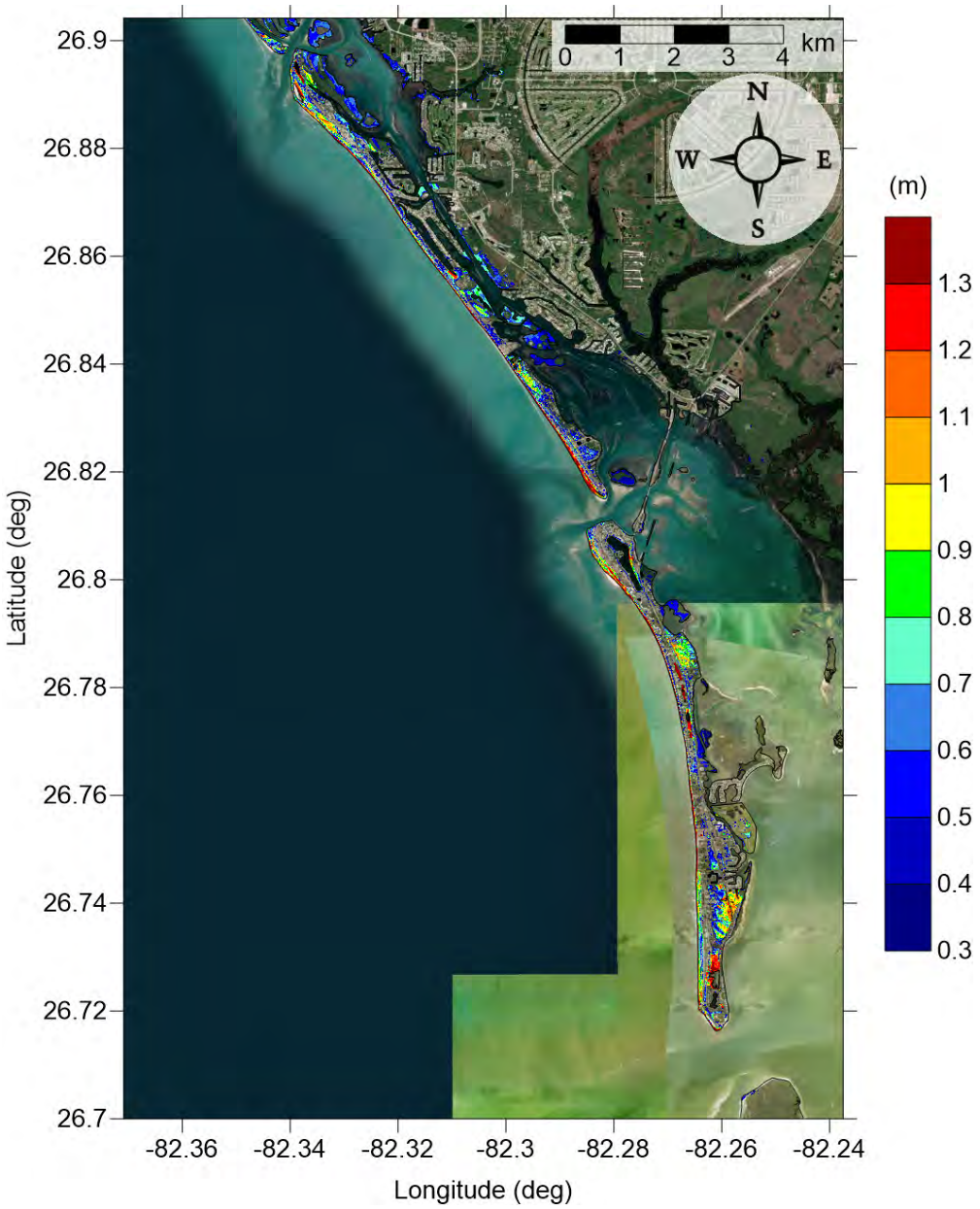

Figure 16: Maximum inundation depth (m) caused by the Probabilistic Submarine Landslide B2 in Don Pedro Island-Boca Grande, FL. Contour drawn is the zero-meter contour for land elevation.

Don Pedro Island-Boca Grande-Captiva Island, FL
Probabilistic Submarine Landslide B2
Maximum Inundation Depth

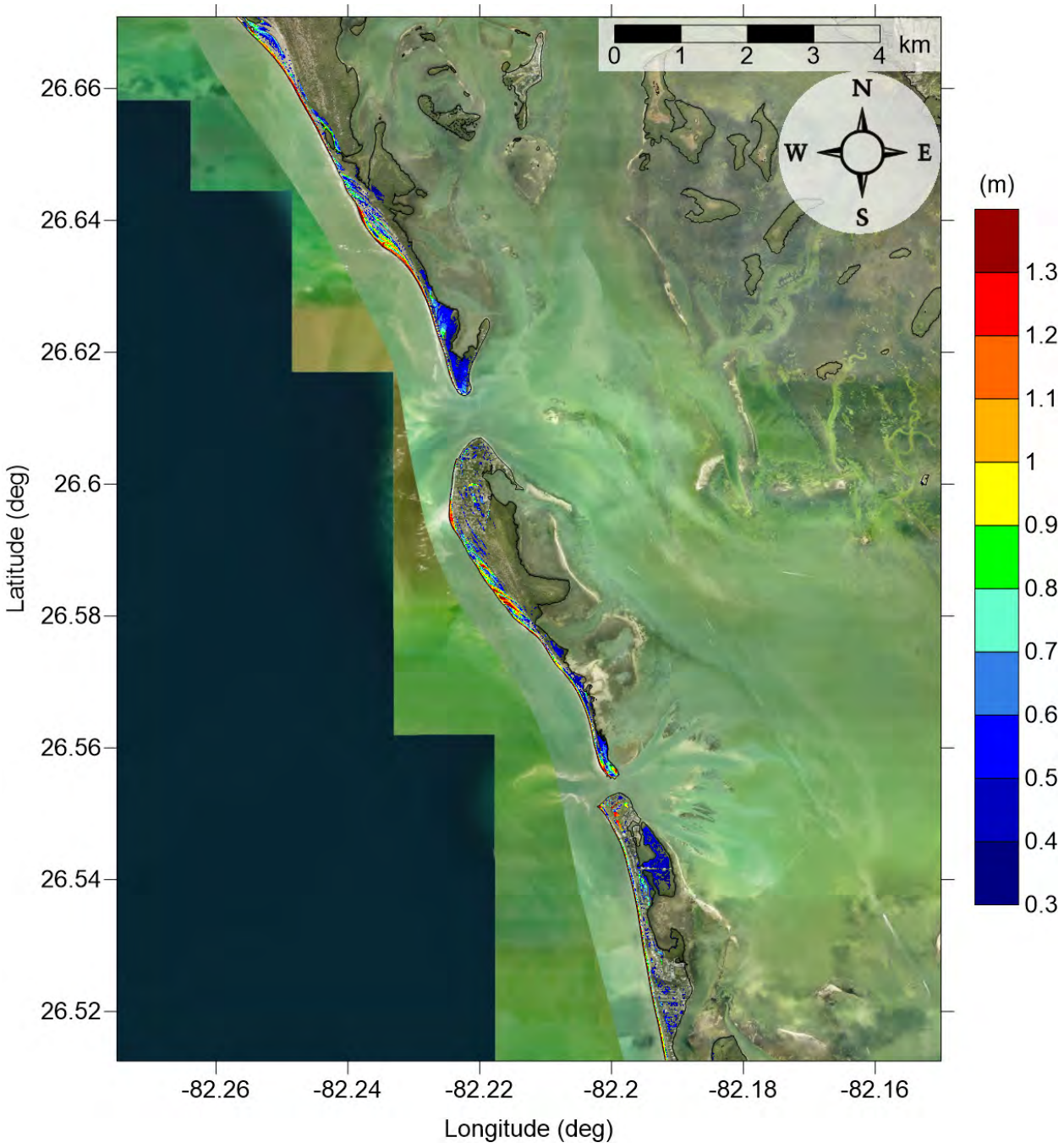

Figure 17: Maximum inundation depth (m) caused by the Probabilistic Submarine Landslide B2 in Captiva Island, FL. Contour drawn is the zero-meter contour for land elevation.

Don Pedro Island-Boca Grande-Captiva Island, FL
Mississippi Canyon submarine landslide
Maximum Momentum Flux

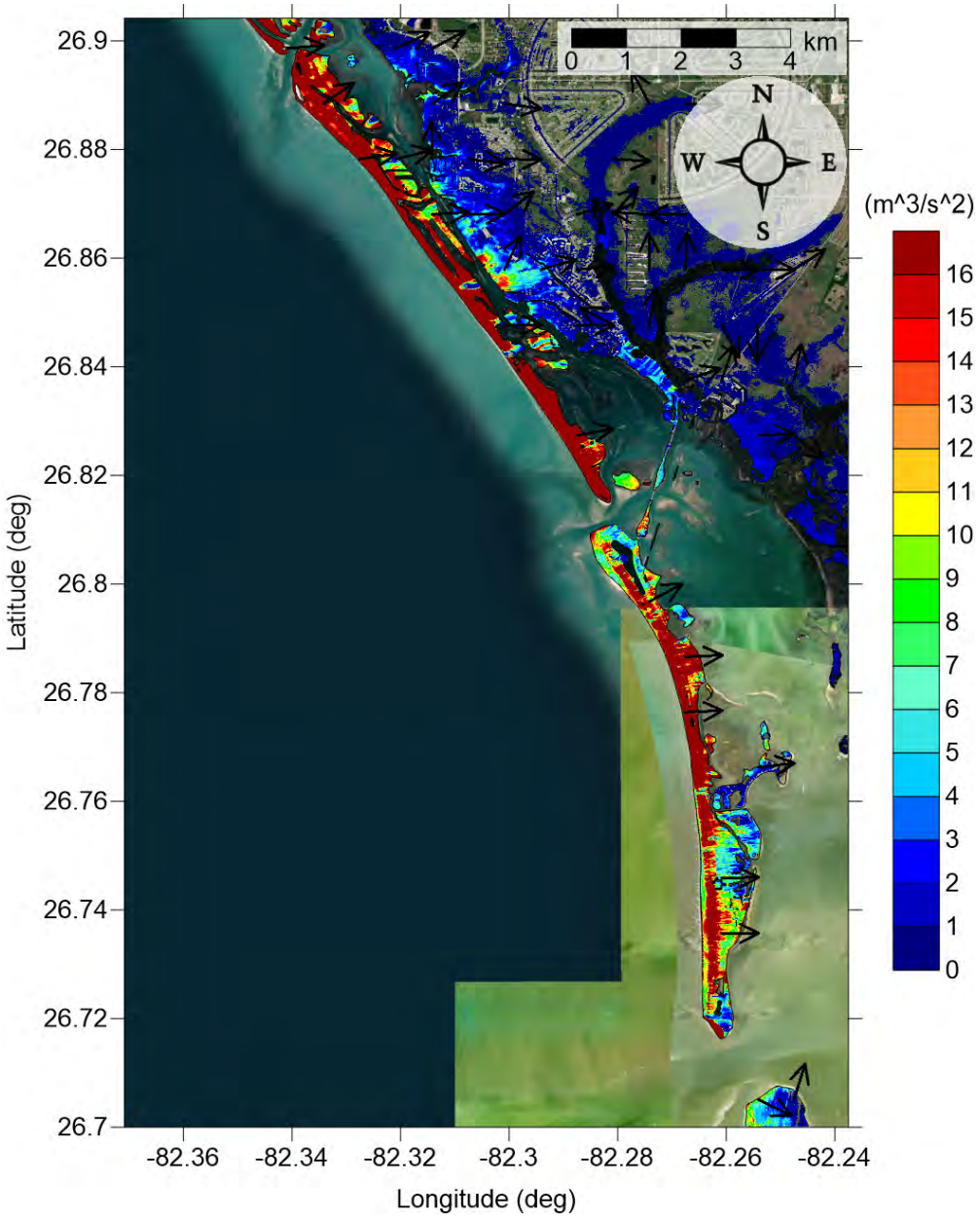

Figure 18: Maximum momentum flux (m^3/s^2) caused by the Mississippi Canyon submarine landslide in Don Pedro Island-Boca Grande, FL. Arrows represent direction of maximum momentum flux. Contour drawn is the zero-meter contour for land elevation.

Don Pedro Island-Boca Grande-Captiva Island, FL
Mississippi Canyon submarine landslide
Maximum Momentum Flux

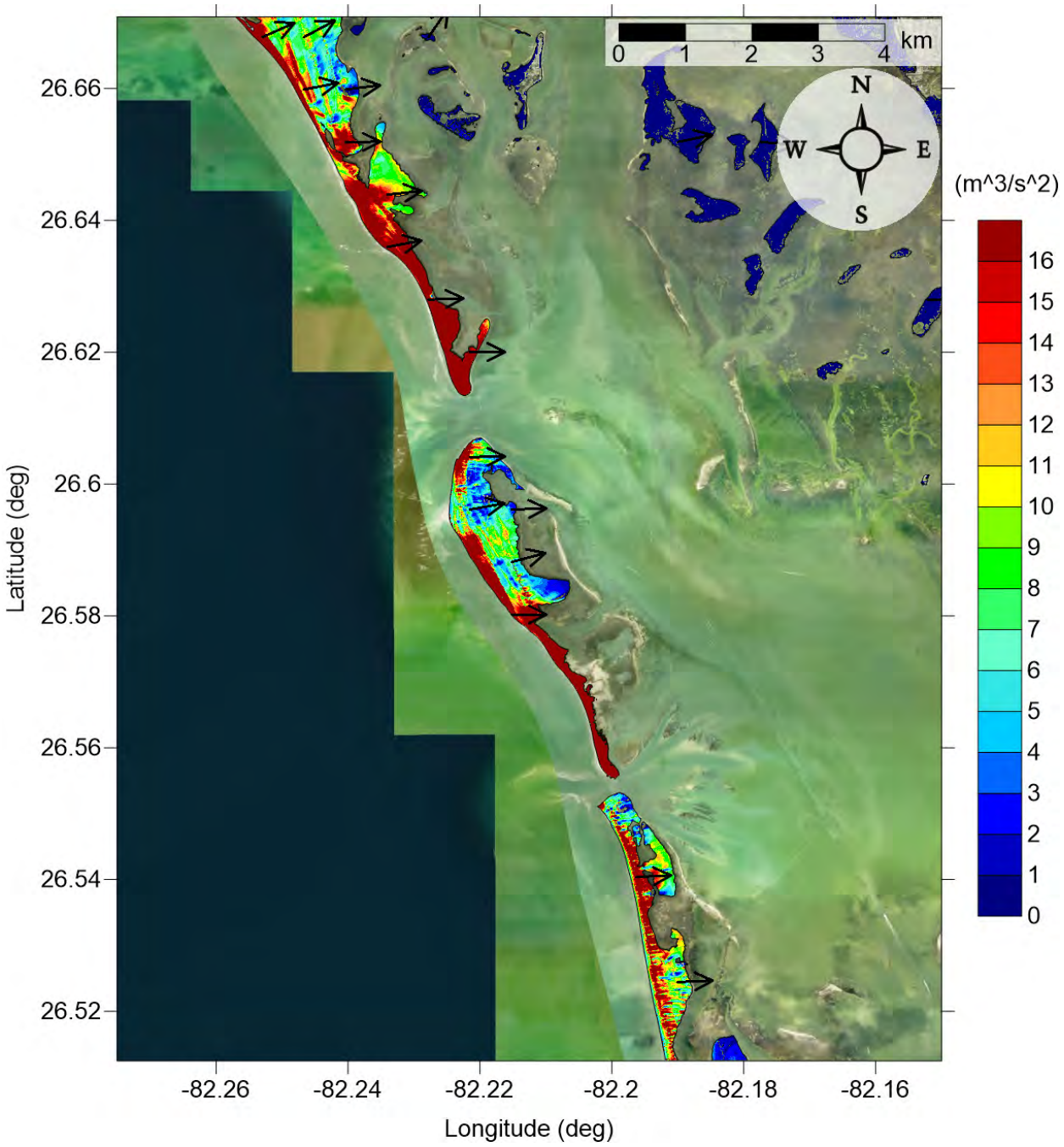

Figure 19: Maximum momentum flux (m^3/s^2) caused by the Mississippi Canyon submarine landslide in Captiva Island, FL. Arrows represent direction of maximum momentum flux. Contour drawn is the zero-meter contour for land elevation.

Don Pedro Island-Boca Grande-Captiva Island, FL
Mississippi Canyon submarine landslide
Maximum Inundation Depth

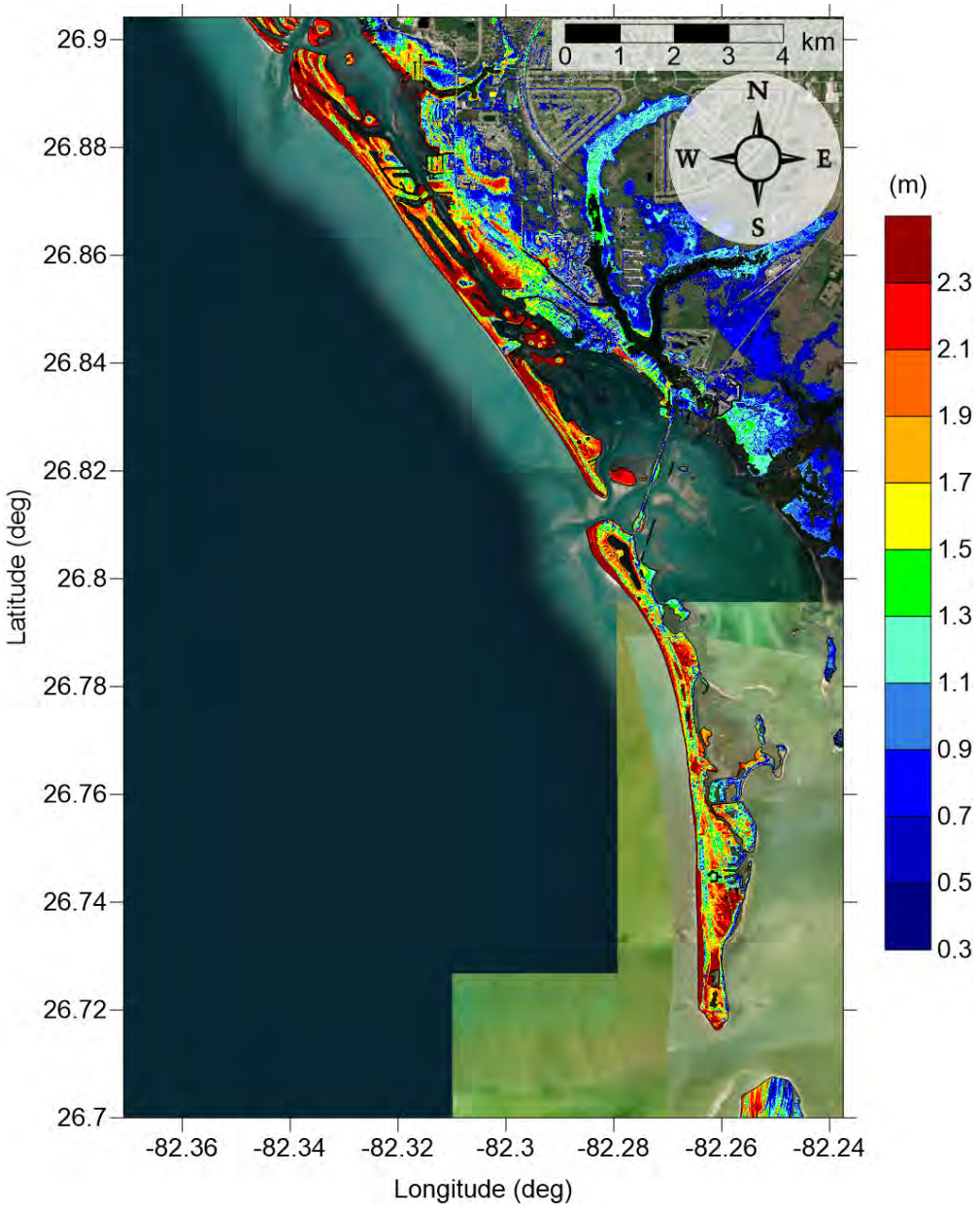

Figure 20: Maximum inundation depth (m) caused by the Mississippi Canyon submarine landslide in Don Pedro Island-Boca Grande, FL. Contour drawn is the zero-meter contour for land elevation.

Don Pedro Island-Boca Grande-Captiva Island, FL
Mississippi Canyon submarine landslide
Maximum Inundation Depth

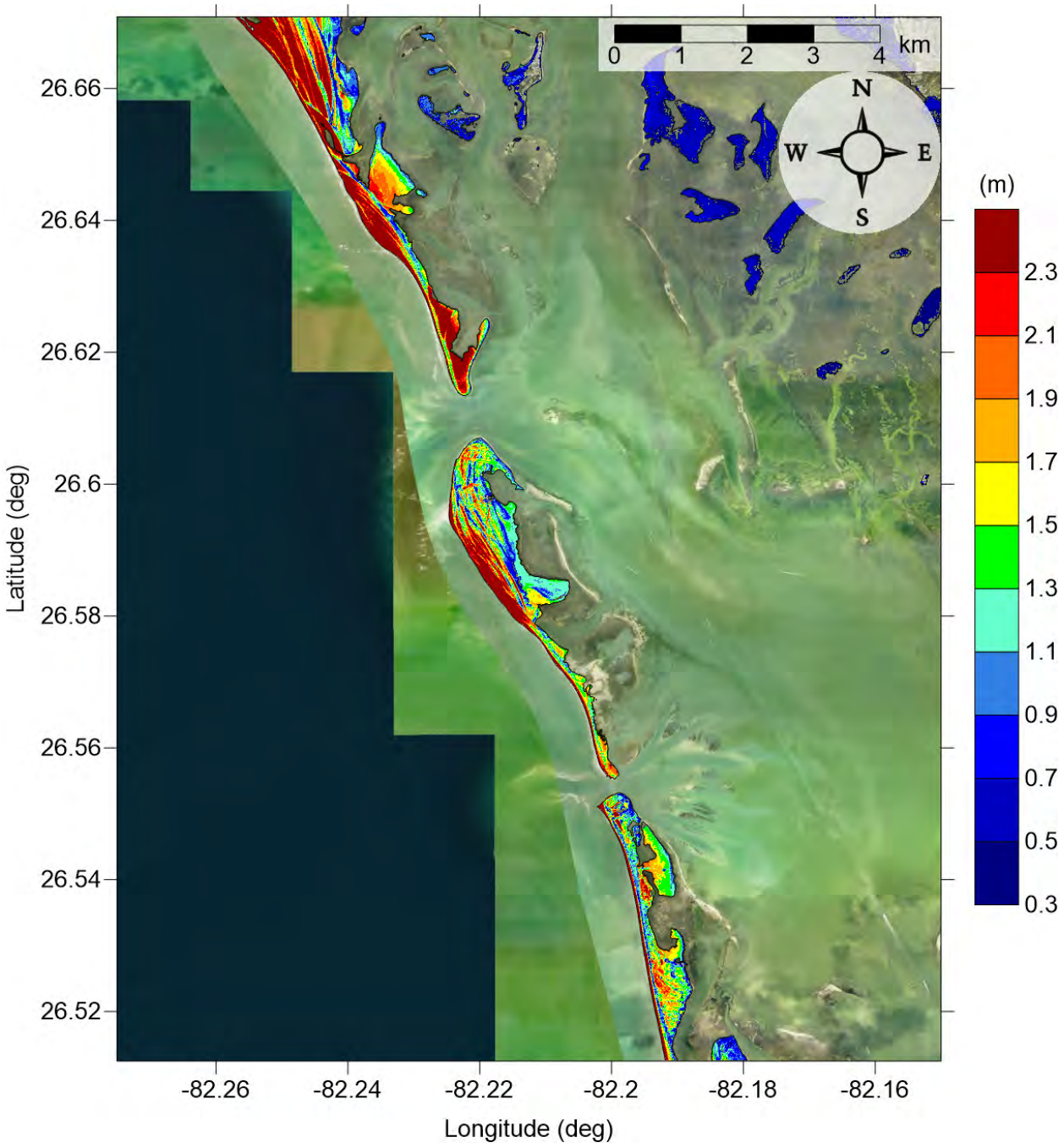

Figure 21: Maximum inundation depth (m) caused by the Mississippi Canyon submarine landslide in Captiva Island, FL. Contour drawn is the zero-meter contour for land elevation.

Don Pedro Island-Boca Grande-Captiva Island, FL
Probabilistic Submarine Landslide C
Maximum Momentum Flux

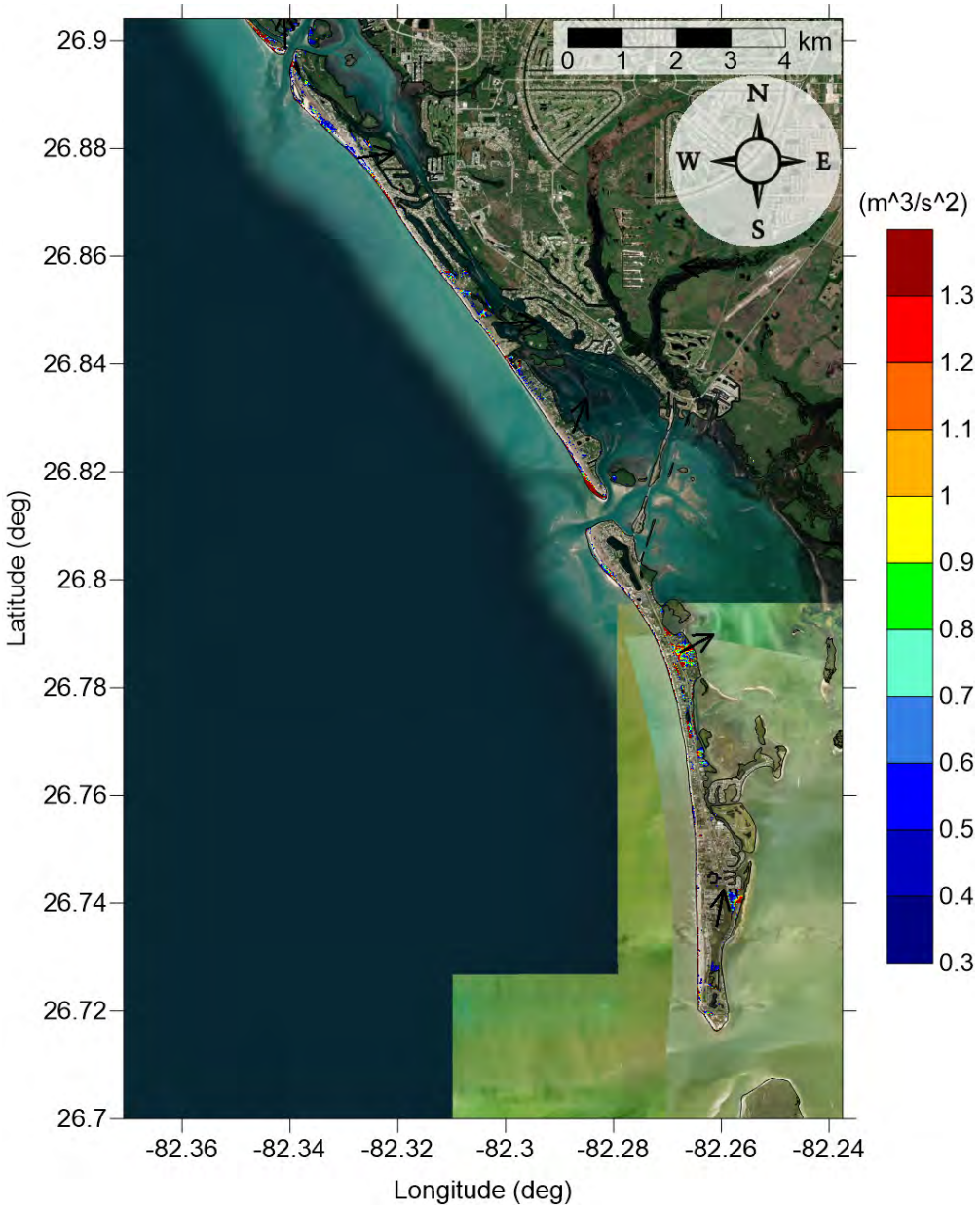

Figure 22: Maximum momentum flux (m^3/s^2) caused by the Probabilistic Submarine Landslide C in Don Pedro Island-Boca Grande, FL. Arrows represent direction of maximum momentum flux. Contour drawn is the zero-meter contour for land elevation.

Don Pedro Island-Boca Grande-Captiva Island, FL
Probabilistic Submarine Landslide C
Maximum Momentum Flux

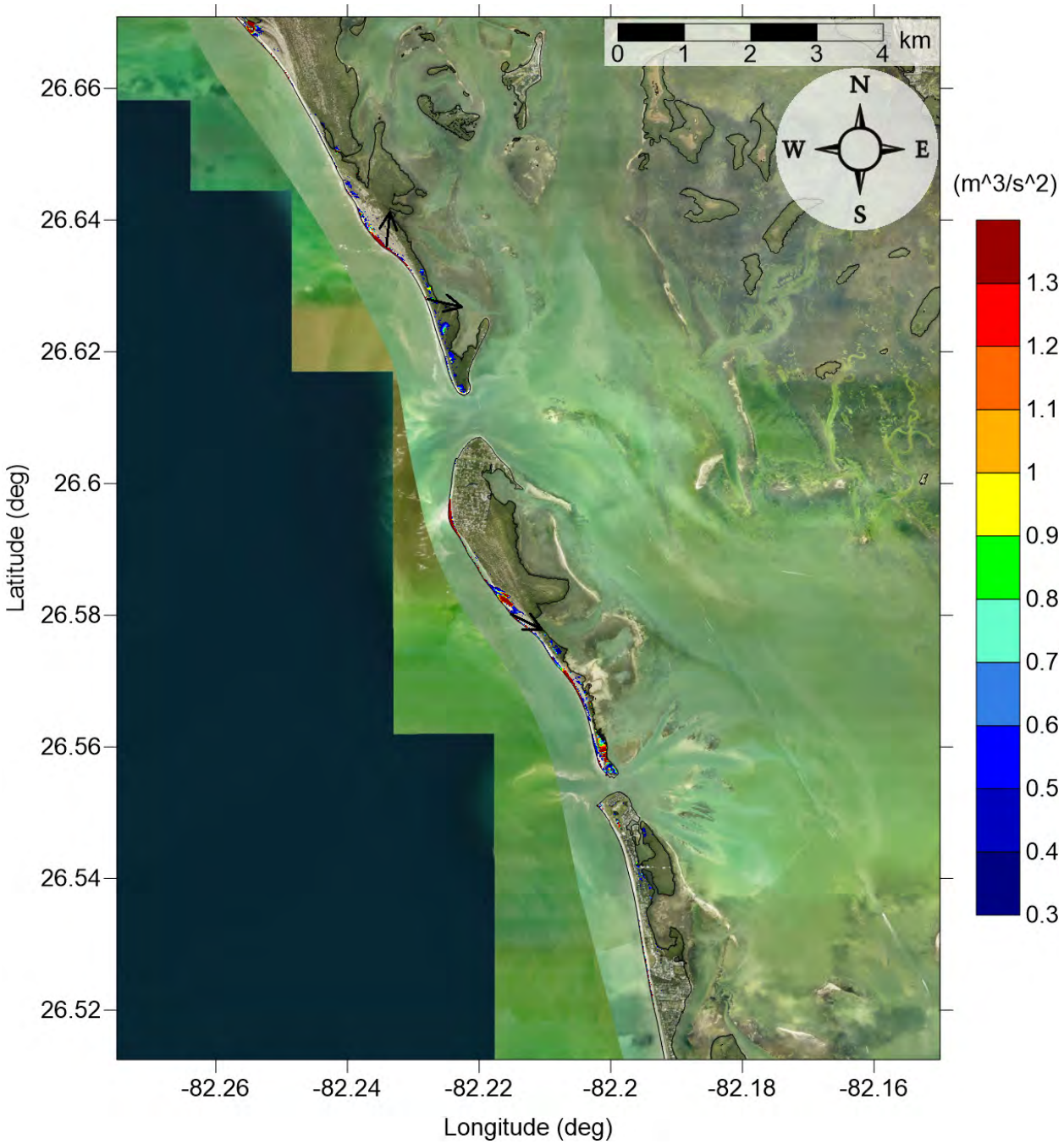

Figure 23: Maximum momentum flux (m^3/s^2) caused by the Probabilistic Submarine Landslide C in Captiva Island, FL. Arrows represent direction of maximum momentum flux. Contour drawn is the zero-meter contour for land elevation.

Don Pedro Island-Boca Grande-Captiva Island, FL
Probabilistic Submarine Landslide C
Maximum Inundation Depth

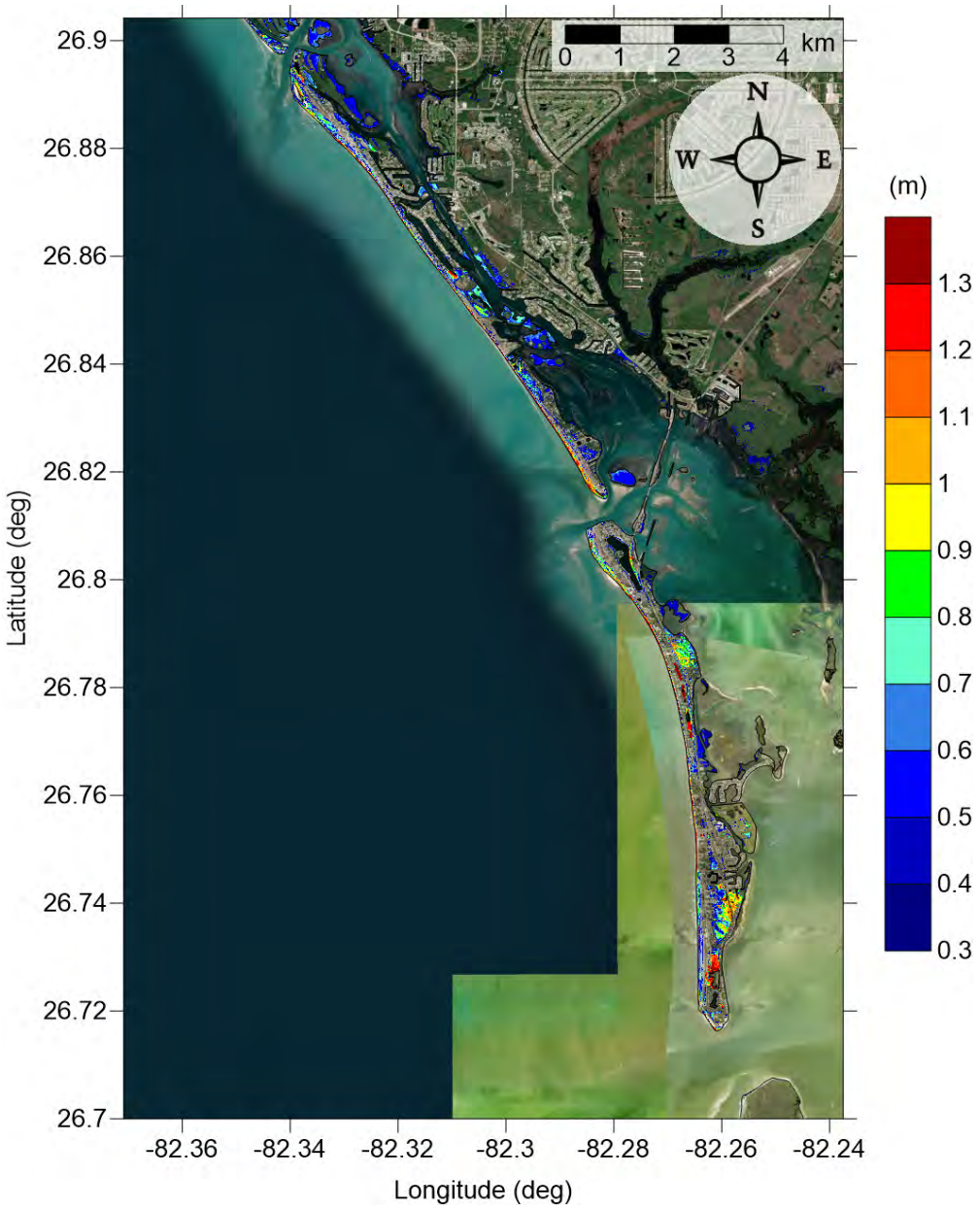

Figure 24: Maximum inundation depth (m) caused by the Probabilistic Submarine Landslide C in Don Pedro Island-Boca Grande, FL. Contour drawn is the zero-meter contour for land elevation.

Don Pedro Island-Boca Grande-Captiva Island, FL
Probabilistic Submarine Landslide C
Maximum Inundation Depth

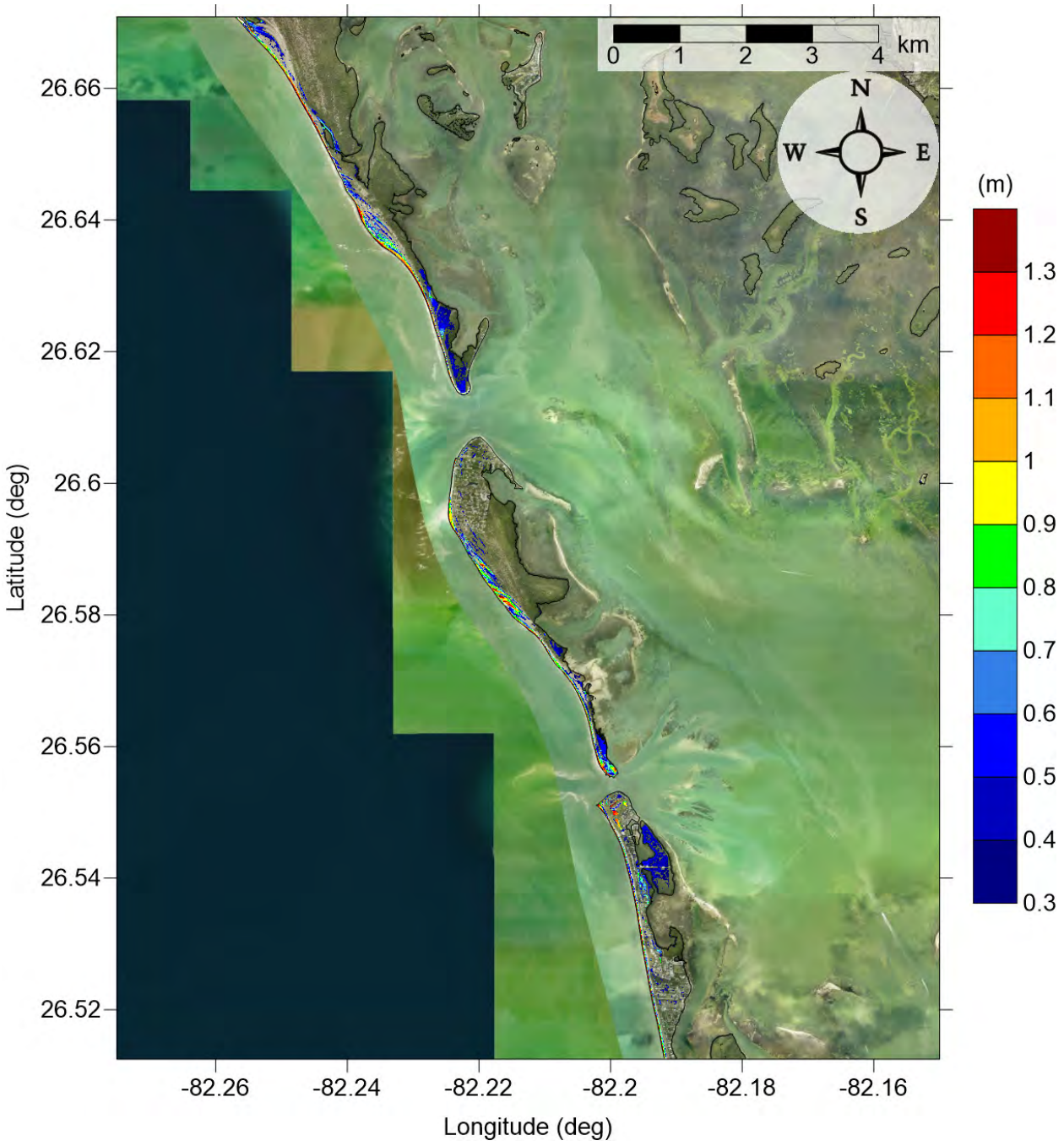

Figure 25: Maximum inundation depth (m) caused by the Probabilistic Submarine Landslide C in Captiva Island, FL. Contour drawn is the zero-meter contour for land elevation.

Don Pedro Island-Boca Grande-Captiva Island, FL
West Florida submarine landslide
Maximum Momentum Flux

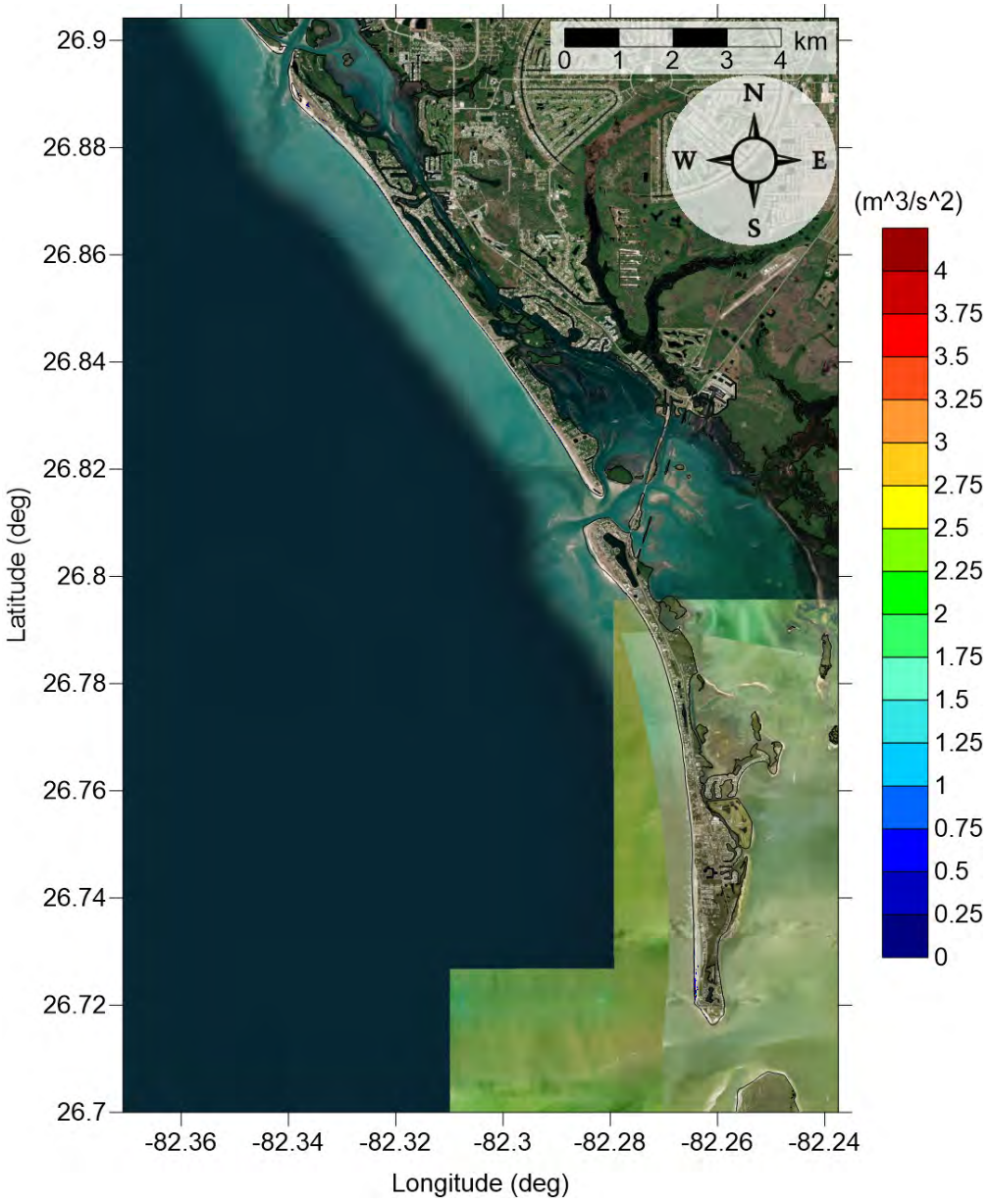

Figure 26: Maximum momentum flux (m^3/s^2) caused by the West Florida submarine landslide in Don Pedro Island-Boca Grande, FL. Arrows represent direction of maximum momentum flux. Contour drawn is the zero-meter contour for land elevation.

Don Pedro Island-Boca Grande-Captiva Island, FL
West Florida submarine landslide
Maximum Momentum Flux

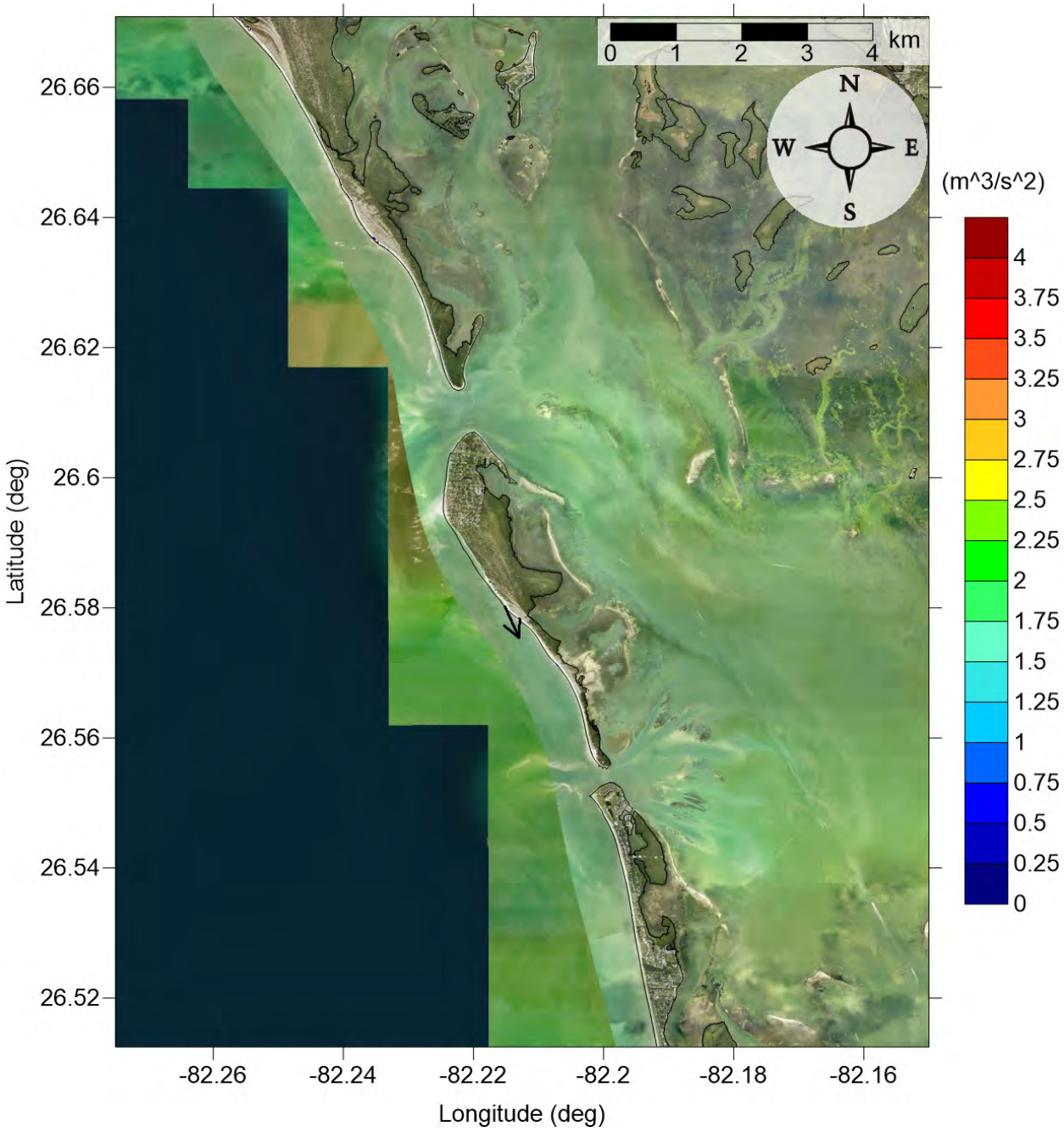

Figure 27: Maximum momentum flux (m^3/s^2) caused by the West Florida submarine landslide in Captiva Island, FL. Arrows represent direction of maximum momentum flux. Contour drawn is the zero-meter contour for land elevation.

Don Pedro Island-Boca Grande-Captiva Island, FL
West Florida submarine landslide
Maximum Inundation Depth

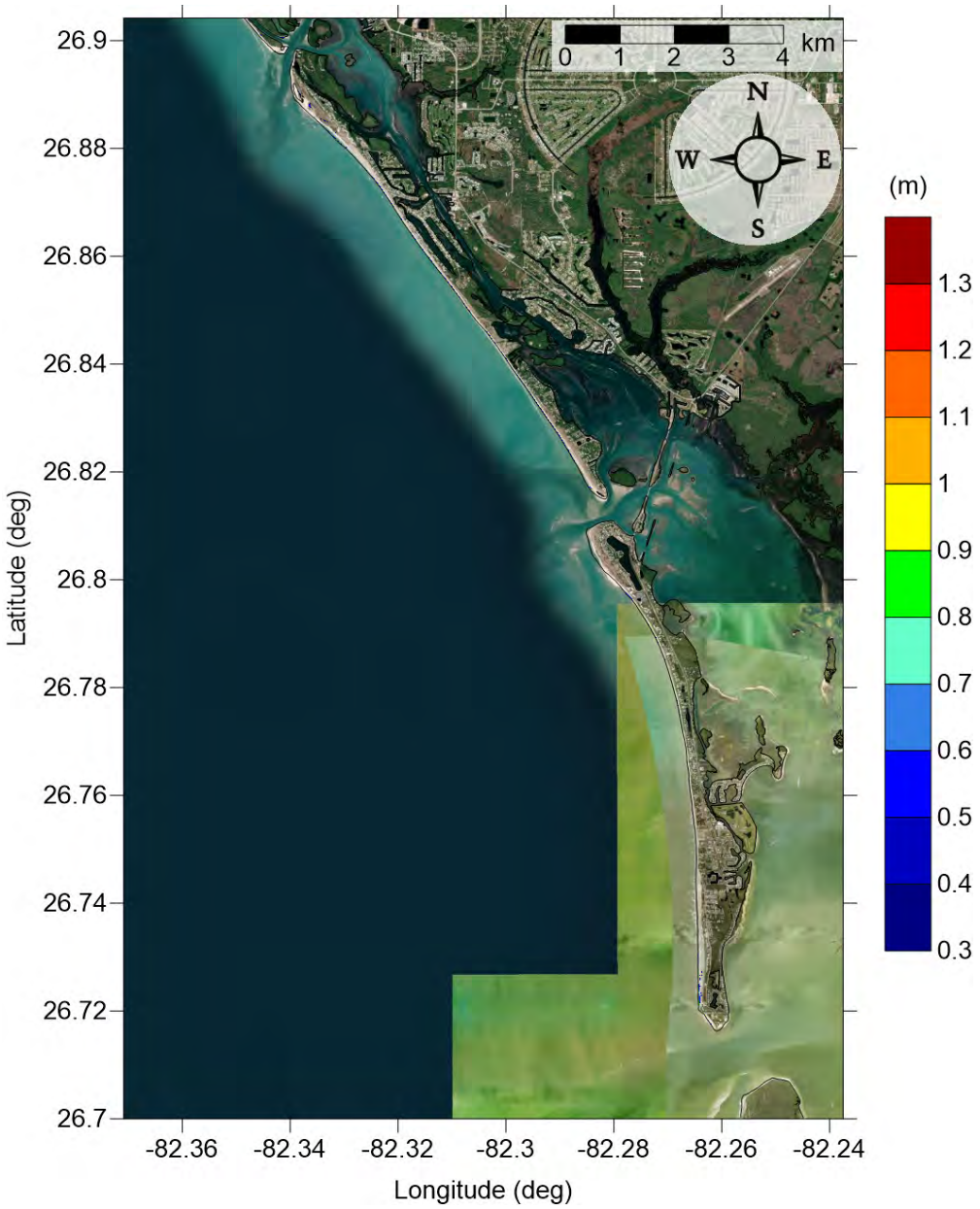

Figure 28: Maximum inundation depth (m) caused by the West Florida submarine landslide in Don Pedro Island-Boca Grande, FL. Contour drawn is the zero-meter contour for land elevation.

Don Pedro Island-Boca Grande-Captiva Island, FL
West Florida submarine landslide
Maximum Inundation Depth

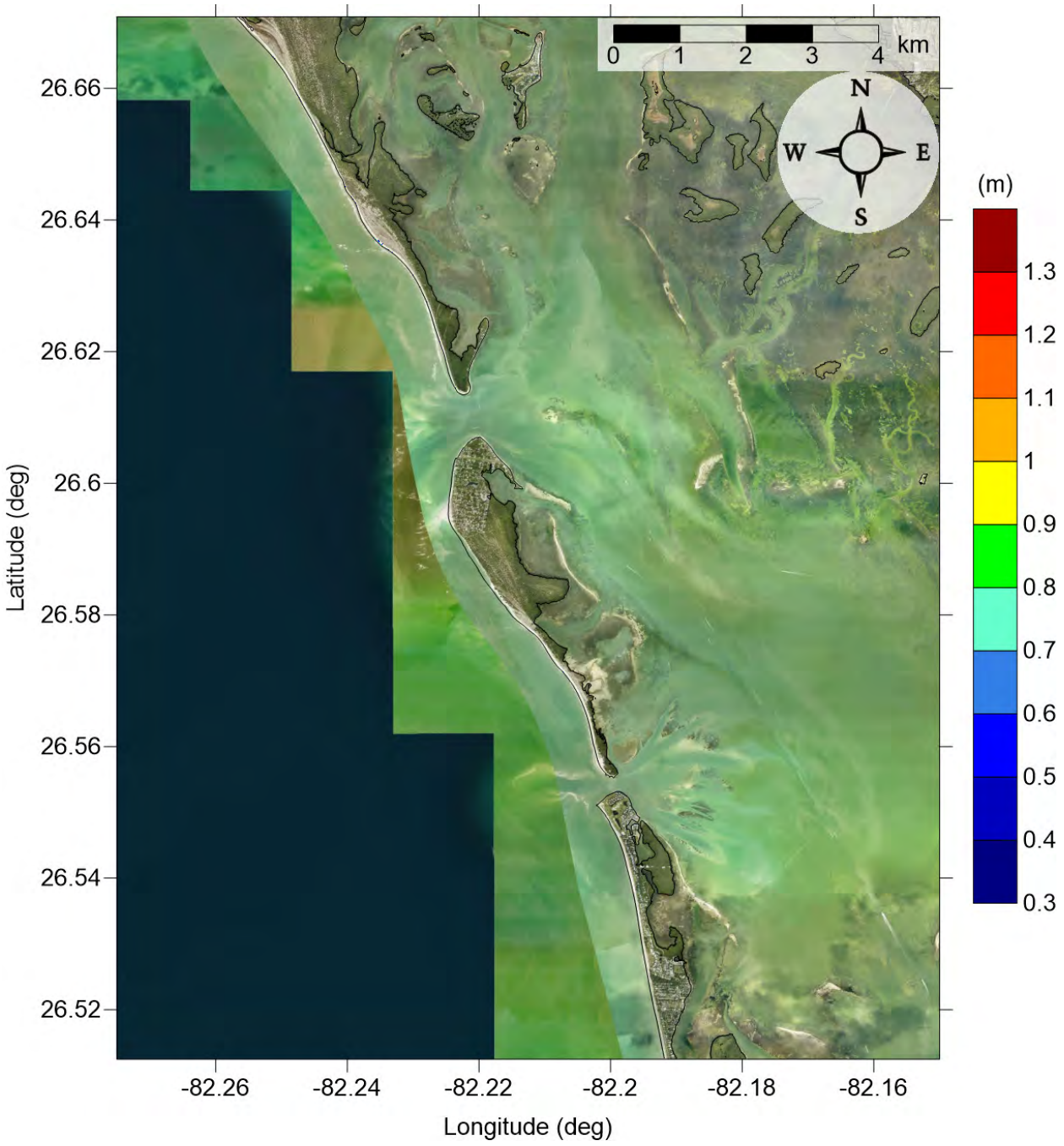

Figure 29: Maximum inundation depth (m) caused by the West Florida submarine landslide in Captiva Island, FL. Contour drawn is the zero-meter contour for land elevation.

Don Pedro Island-Boca Grande-Captiva Island, FL
Yucatán 3 submarine landslide
Maximum Momentum Flux

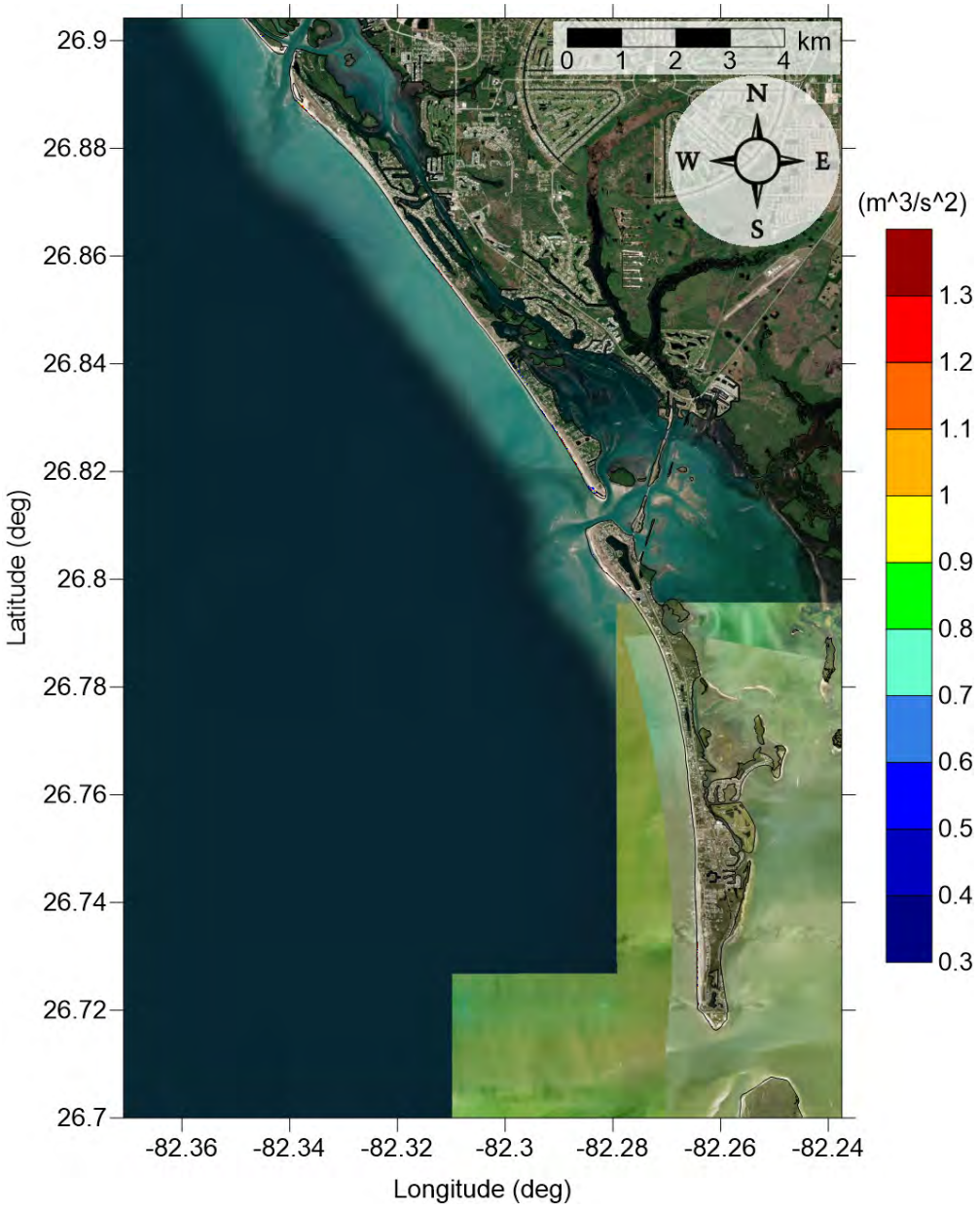

Figure 30: Maximum momentum flux (m^3/s^2) caused by the Yucatán 3 submarine landslide in Don Pedro Island-Boca Grande, FL. Arrows represent direction of maximum momentum flux. Contour drawn is the zero-meter contour for land elevation.

Don Pedro Island-Boca Grande-Captiva Island, FL
Yucatán 3 submarine landslide
Maximum Momentum Flux

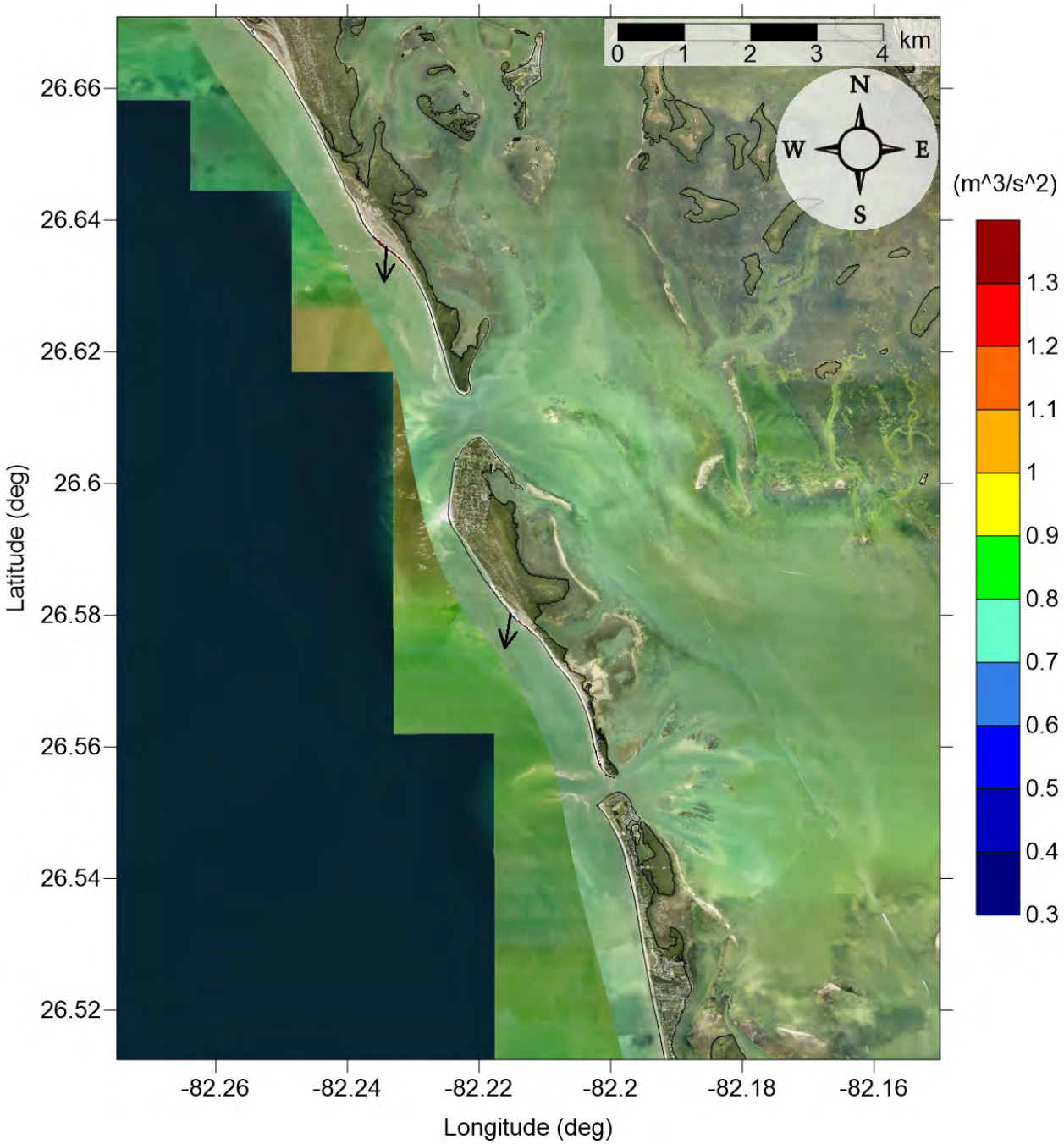

Figure 31: Maximum momentum flux (m^3/s^2) caused by the Yucatán 3 submarine landslide in Captiva Island, FL. Arrows represent direction of maximum momentum flux. Contour drawn is the zero-meter contour for land elevation.

Don Pedro Island-Boca Grande-Captiva Island, FL
Yucatán 3 submarine landslide
Maximum Inundation Depth

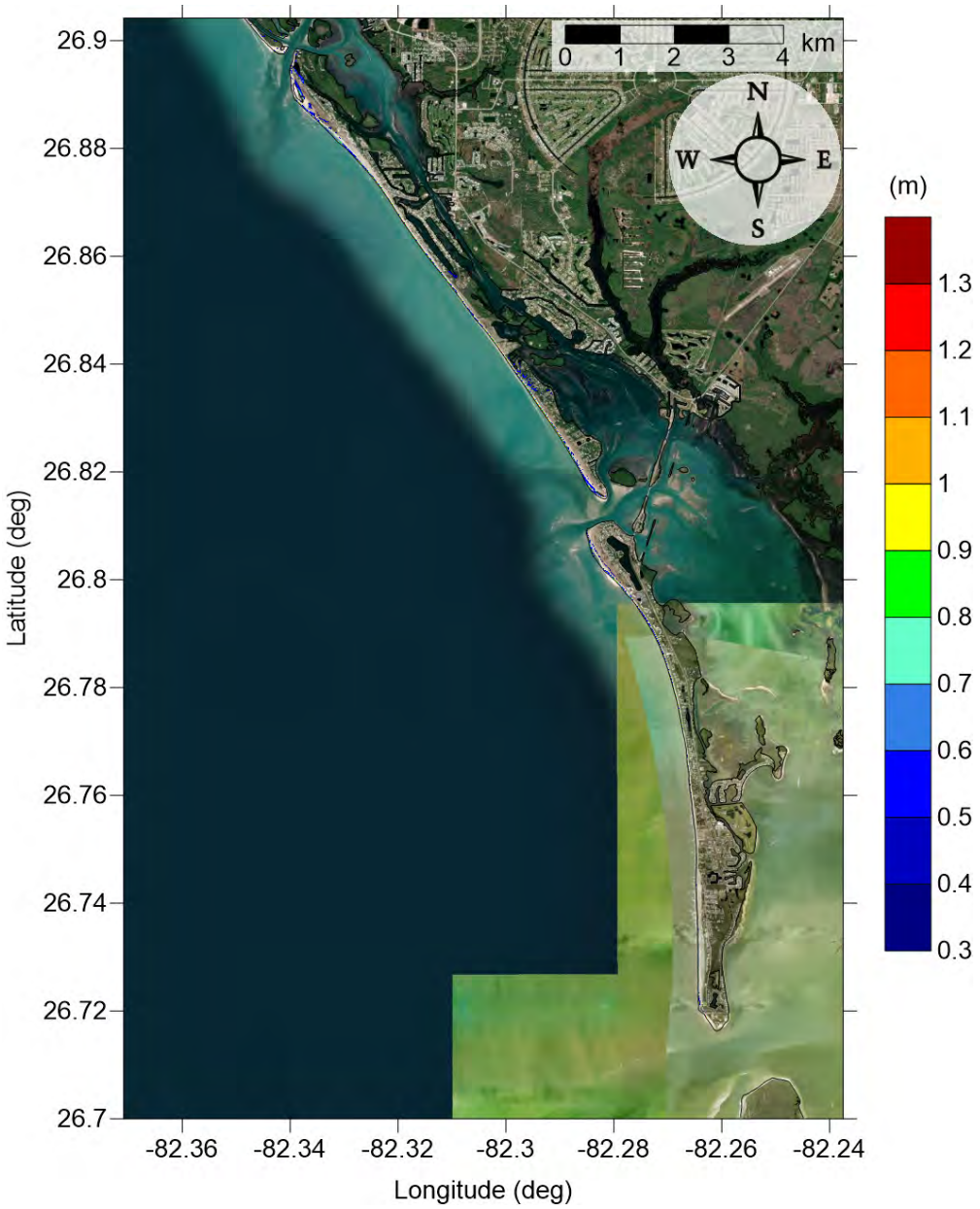

Figure 32: Maximum inundation depth (m) caused by the Yucatán 3 submarine landslide in Don Pedro Island-Boca Grande, FL. Contour drawn is the zero-meter contour for land elevation.

Don Pedro Island-Boca Grande-Captiva Island, FL
Yucatán 3 submarine landslide
Maximum Inundation Depth

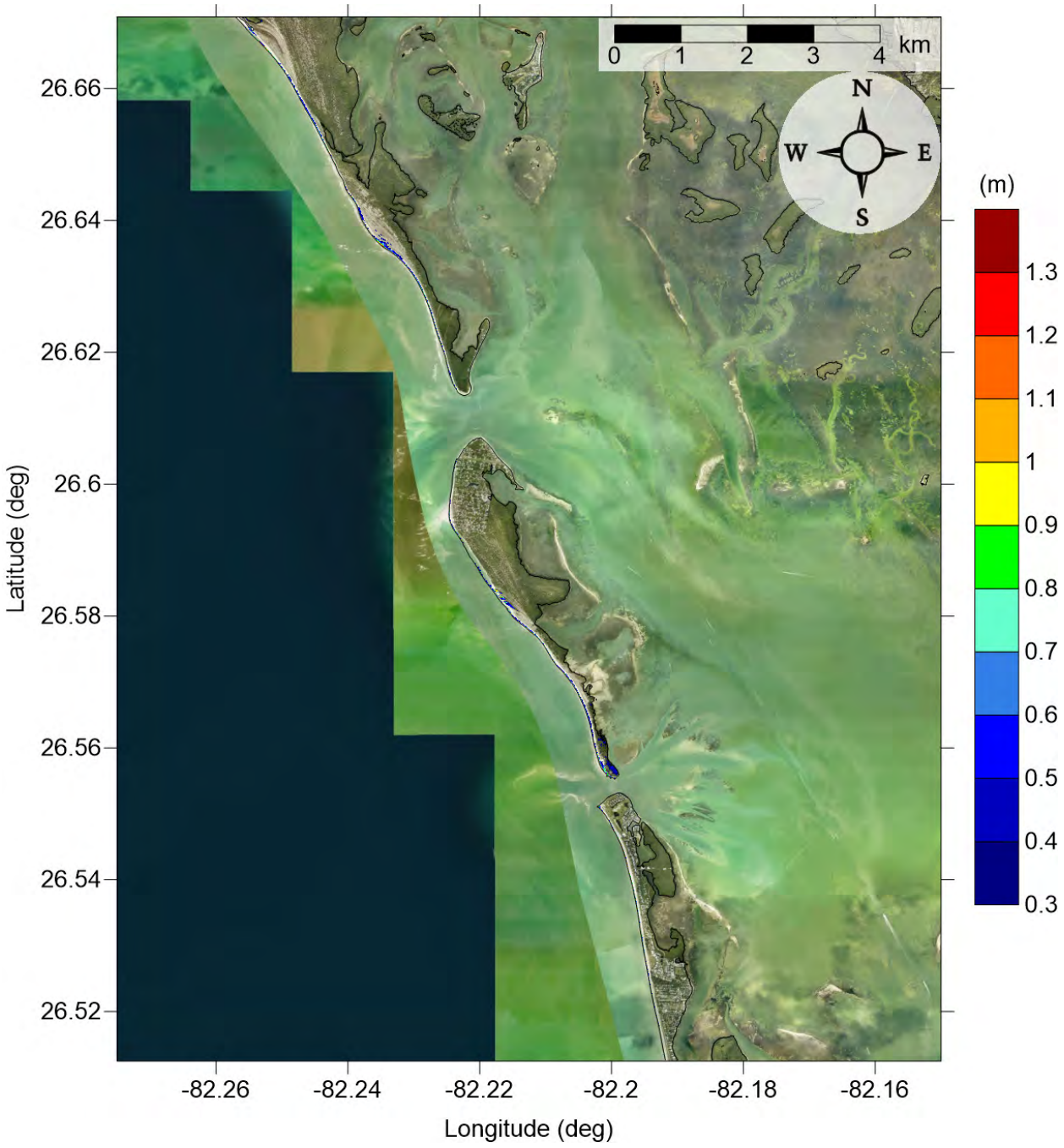

Figure 33: Maximum inundation depth (m) caused by the Yucatán 3 submarine landslide in Captiva Island, FL. Contour drawn is the zero-meter contour for land elevation.

Don Pedro Island-Boca Grande-Captiva Island, FL
Yucatán 5 submarine landslide
Maximum Momentum Flux

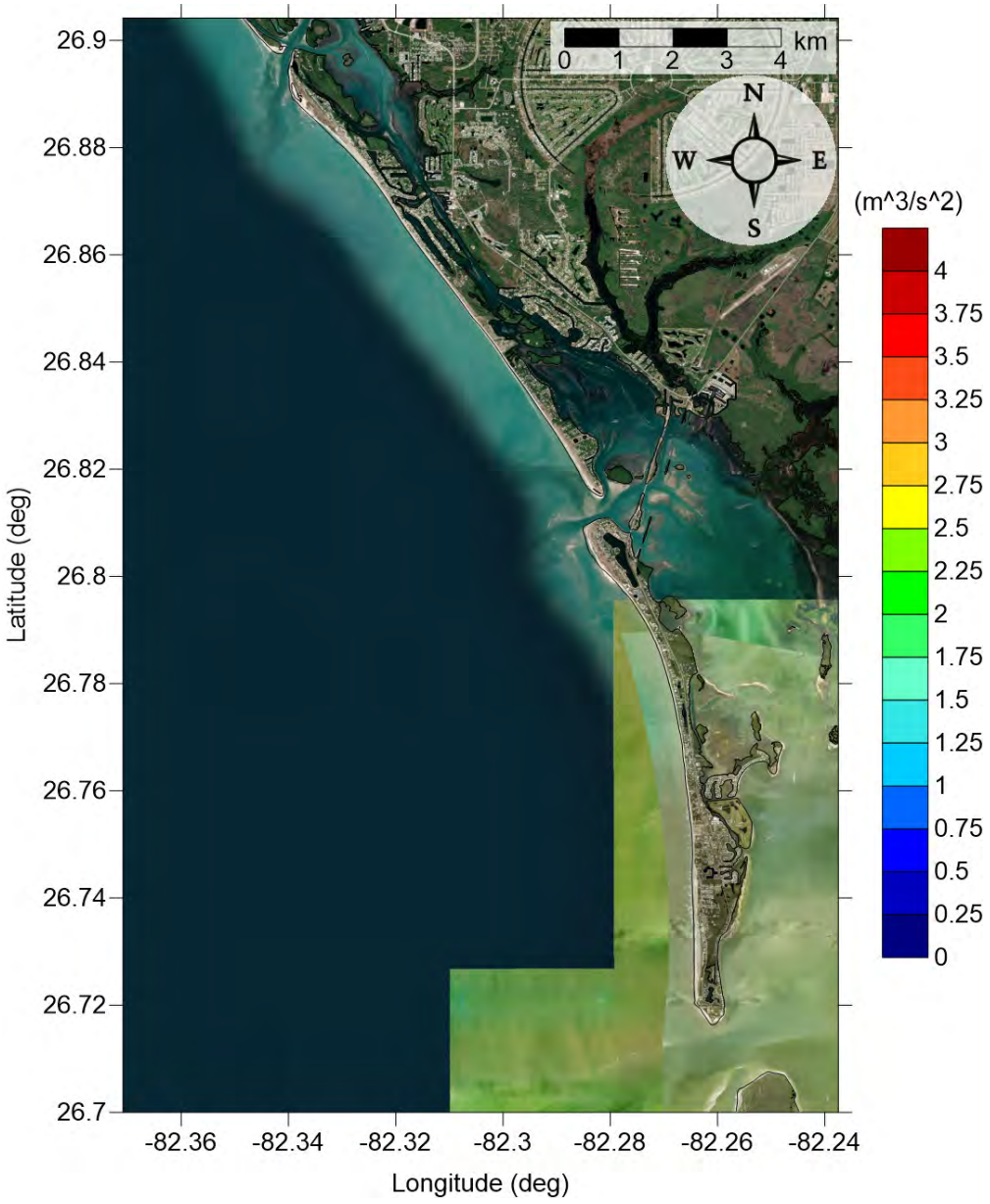

Figure 34: Maximum momentum flux (m^3/s^2) caused by the Yucatán 5 submarine landslide in Don Pedro Island-Boca Grande, FL. Arrows represent direction of maximum momentum flux. Contour drawn is the zero-meter contour for land elevation.

Don Pedro Island-Boca Grande-Captiva Island, FL
Yucatán 5 submarine landslide
Maximum Momentum Flux

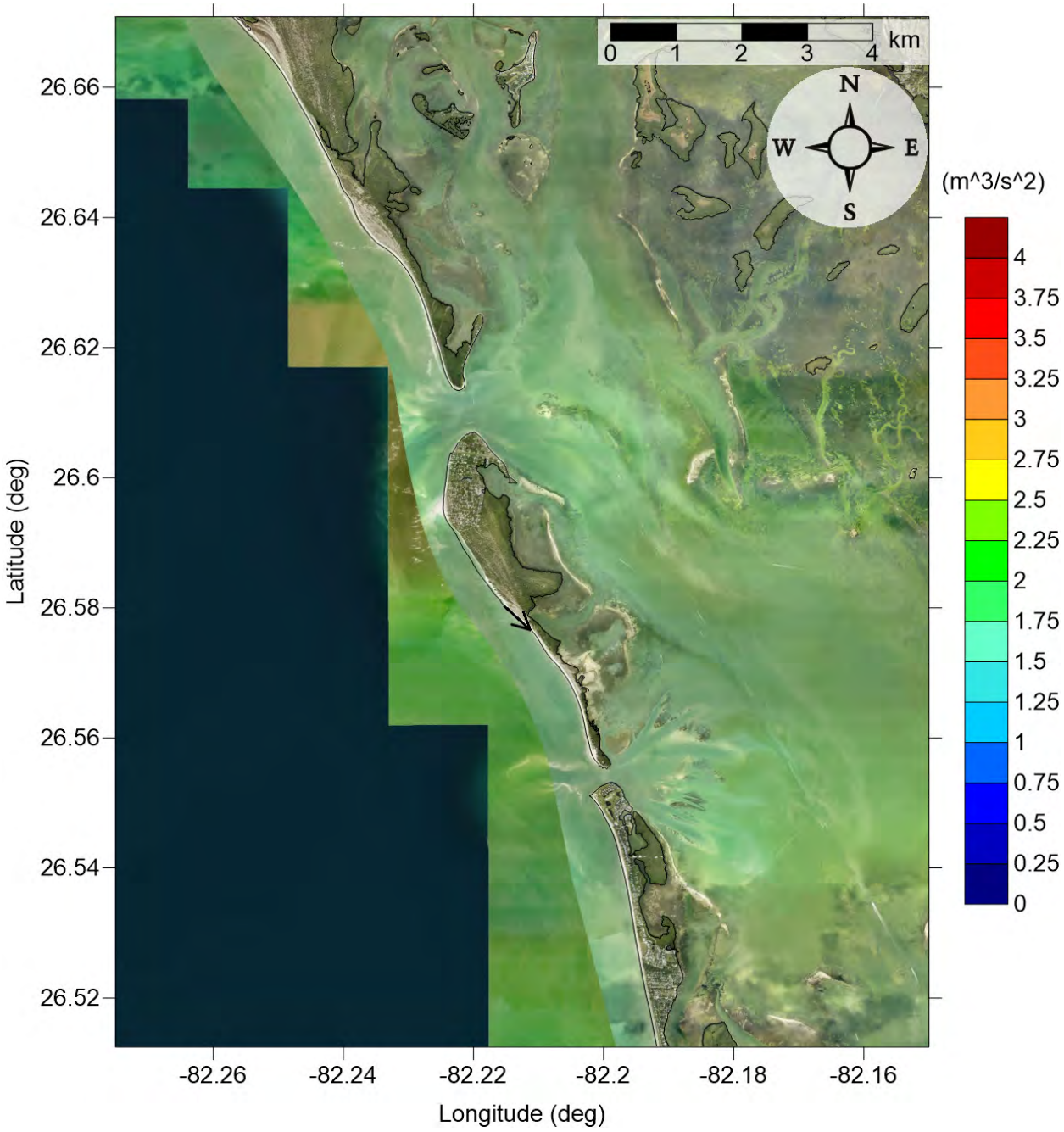

Figure 35: Maximum momentum flux (m^3/s^2) caused by the Yucatán 5 submarine landslide in Captiva Island, FL. Arrows represent direction of maximum momentum flux. Contour drawn is the zero-meter contour for land elevation.

Don Pedro Island-Boca Grande-Captiva Island, FL
Yucatán 5 submarine landslide
Maximum Inundation Depth

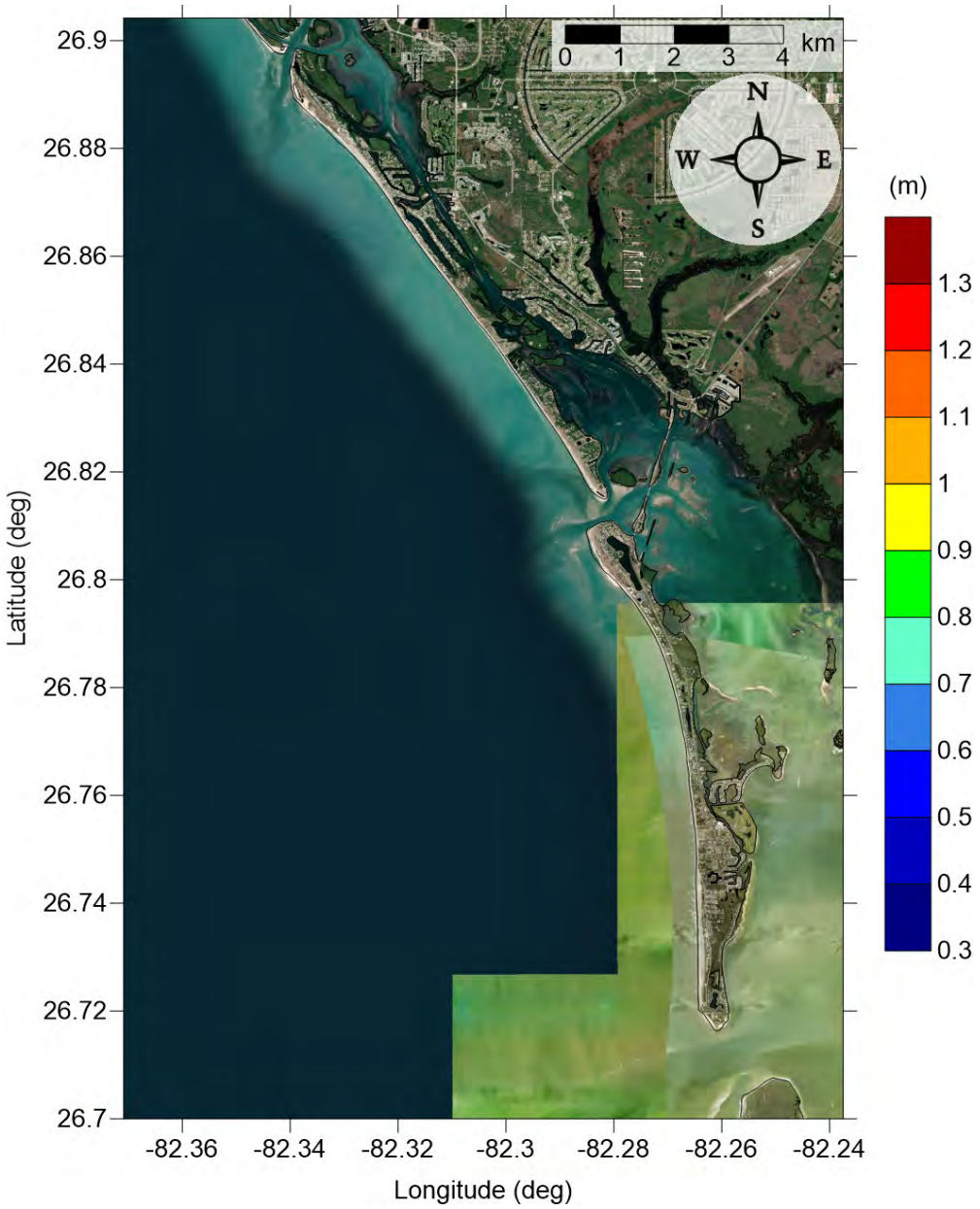

Figure 36: Maximum inundation depth (m) caused by the Yucatán 5 submarine landslide in Don Pedro Island-Boca Grande, FL. Contour drawn is the zero-meter contour for land elevation.

Don Pedro Island-Boca Grande-Captiva Island, FL
Yucatán 5 submarine landslide
Maximum Inundation Depth

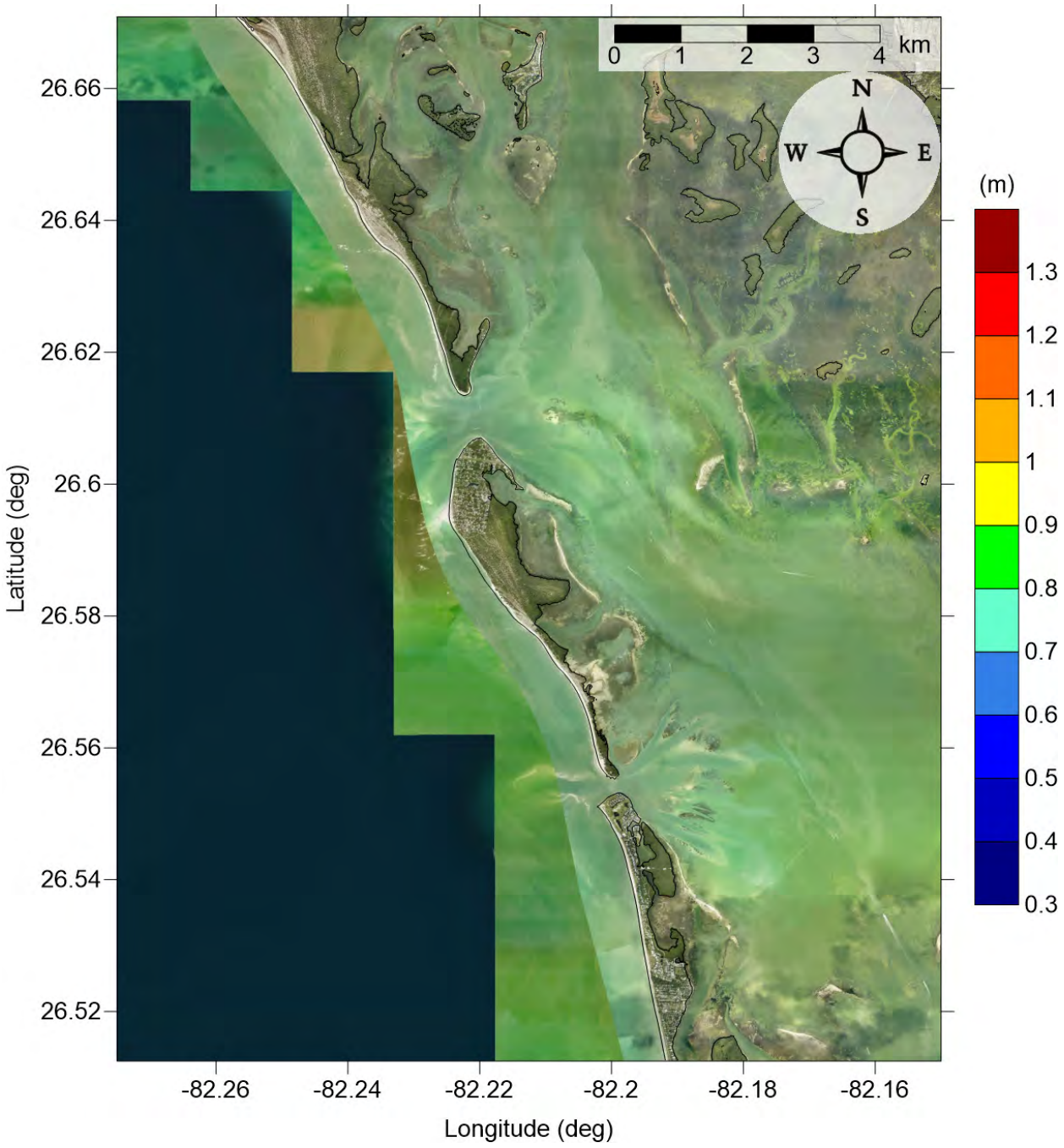

Figure 37: Maximum inundation depth (m) caused by the Yucatán 5 submarine landslide in Captiva Island, FL. Contour drawn is the zero-meter contour for land elevation.

Don Pedro Island-Boca Grande-Captiva Island, FL
All Sources
Maximum of Maximum Inundation Depth

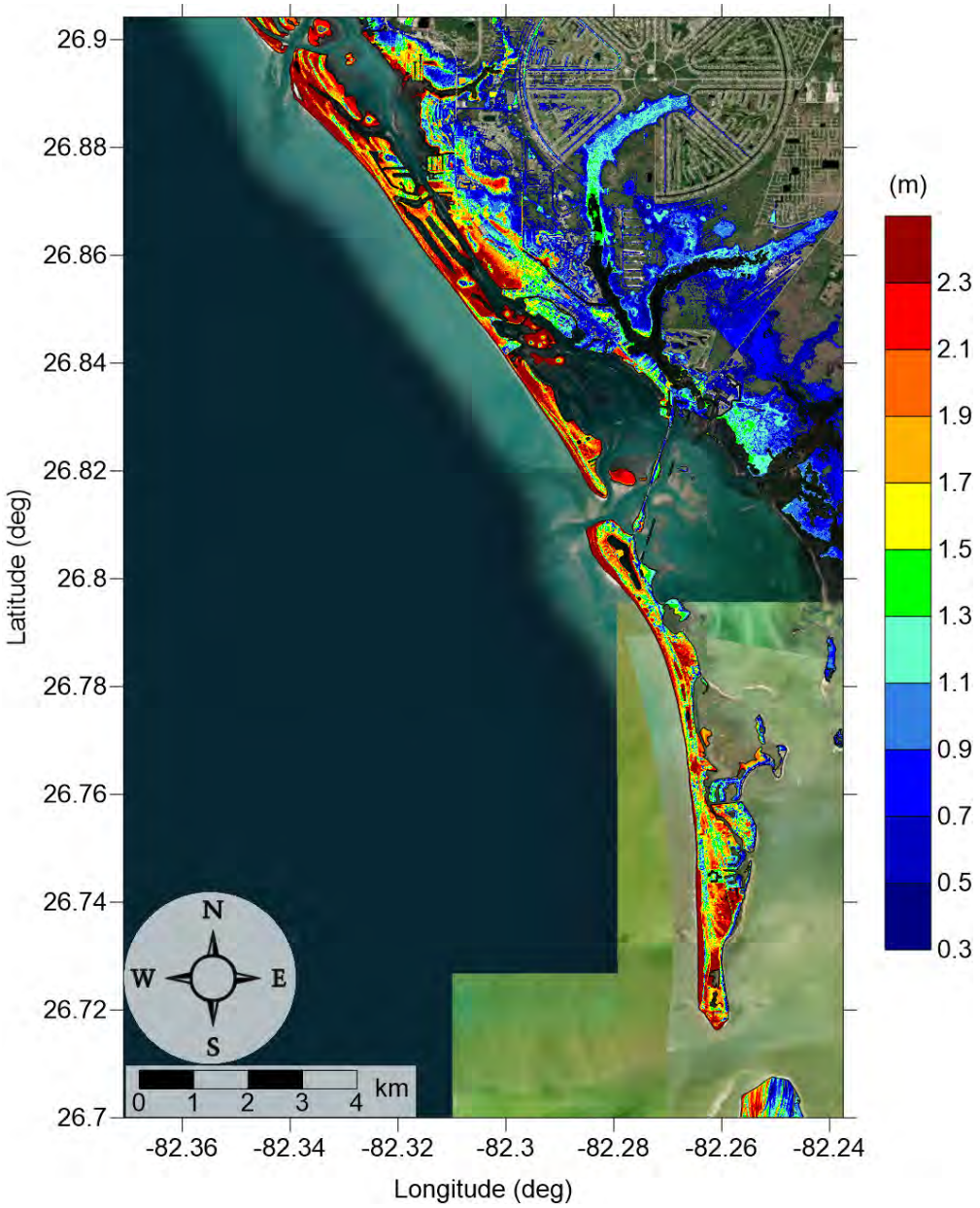

Figure 38: Maximum of maximums inundation depth (m) in Don Pedro Island-Boca Grande, FL, calculated as the maximum inundation depth in each grid cell from an ensemble of all tsunami sources considered. Contour drawn is the zero-meter contour for land elevation.

Don Pedro Island-Boca Grande-Captiva Island, FL
All Sources
Maximum of Maximum Inundation Depth

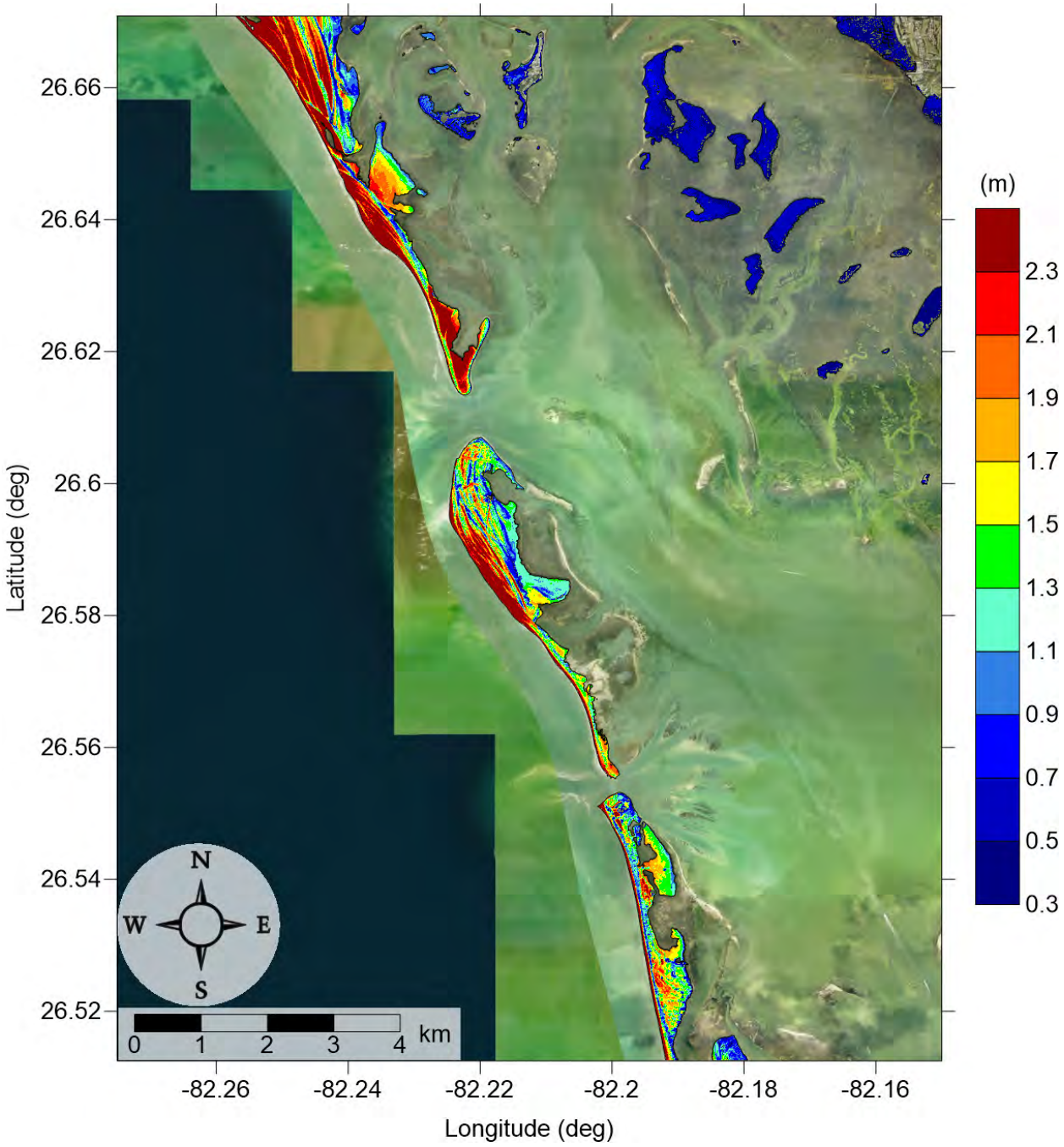

Figure 39: Maximum of maximums inundation depth (m) in Captiva Island, FL, calculated as the maximum inundation depth in each grid cell from an ensemble of all tsunami sources considered. Contour drawn is the zero-meter contour for land elevation.

Don Pedro Island-Boca Grande-Captiva Island, FL
All Sources
Maximum Inundation Depth by Source

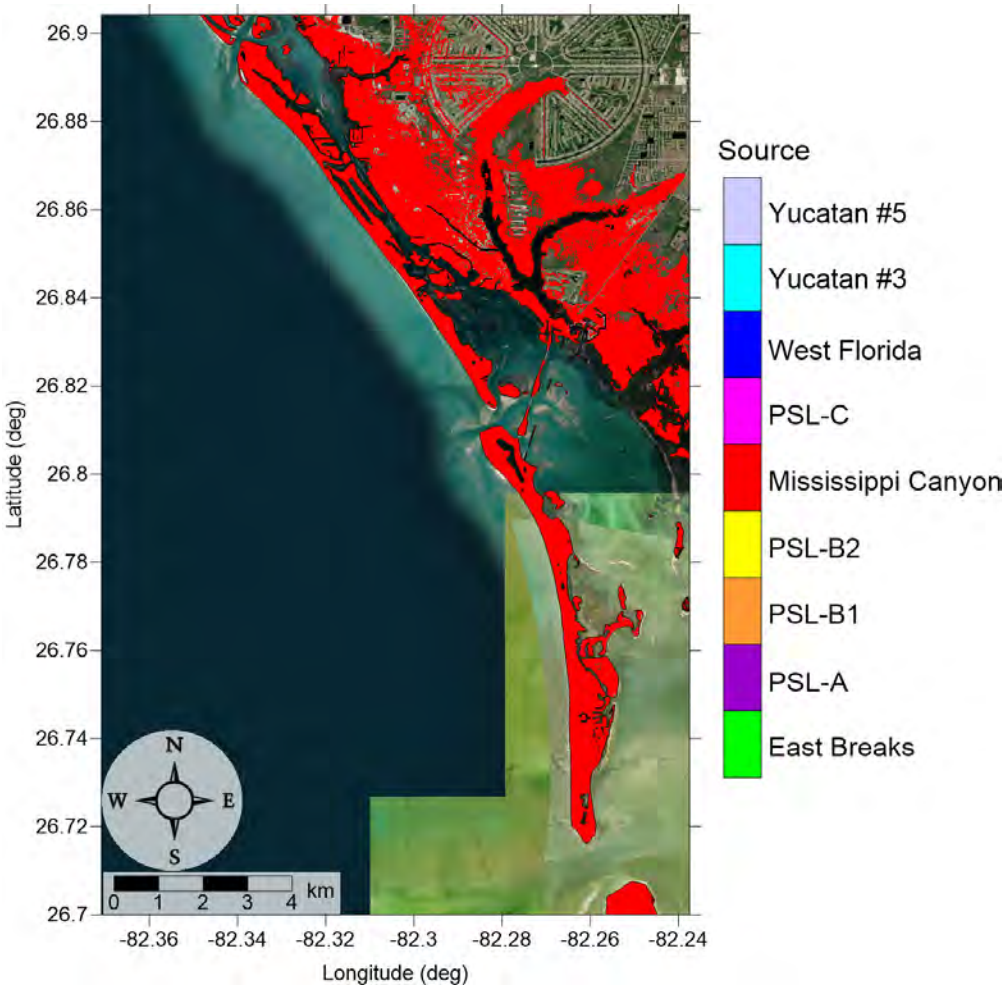

Figure 40: Indication of the tsunami source which causes the maximum of maximums inundation depth (m) in each grid cell from an ensemble of all tsunami sources in Don Pedro Island-Boca Grande, FL. Contour drawn is the zero-meter contour for land elevation.

Don Pedro Island-Boca Grande-Captiva Island, FL
All Sources
Maximum Inundation Depth by Source

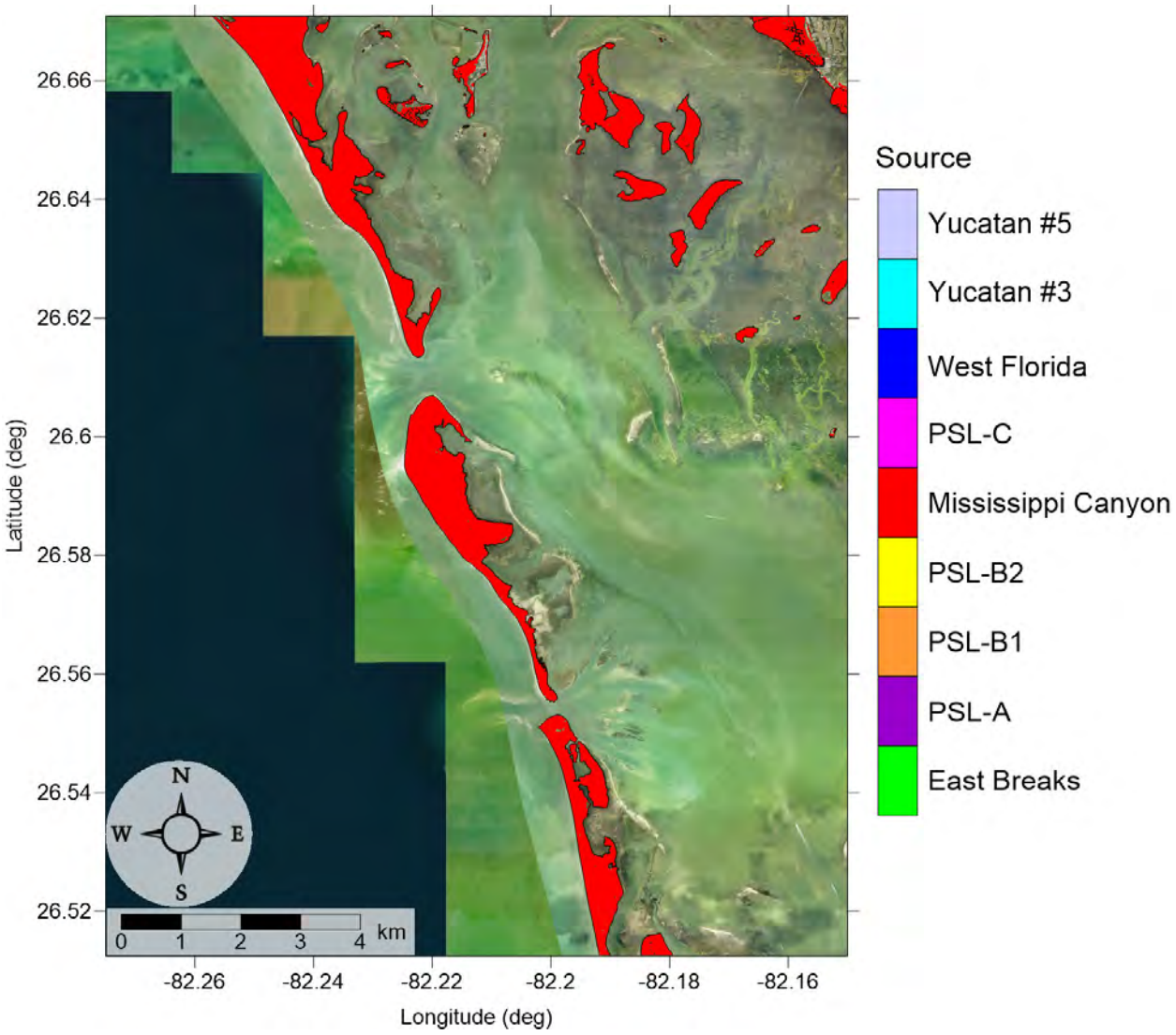

Figure 41: Indication of the tsunami source which causes the maximum of maximums inundation depth (m) in each grid cell from an ensemble of all tsunami sources in Captiva Island, FL. Contour drawn is the zero-meter contour for land elevation.

4.2 Marco Island, FL

Table 3: Maximum tsunami wave amplitude and corresponding arrival time after landslide failure at Marco Island, FL numerical wave gauge: 26°14'34.61"N, 82°25'32.45"W, approximate water depth 20 m.

Tsunami Source	Maximum Wave Amplitude (m)	Arrival Time After Landslide Failure (hr)
East Breaks	0.41	4.1
PSL-A	0.70	3.8
PSL-B1	0.78	3.1
PSL-B2	1.74	3.2
Mississippi Canyon	4.40	2.8
PSL-C	1.53	2.8
West Florida	0.85	2.3
Yucatán #3	0.62	3.2
Yucatán #5	0.30	3.2

Marco Island, FL
East Breaks submarine landslide
Maximum Momentum Flux

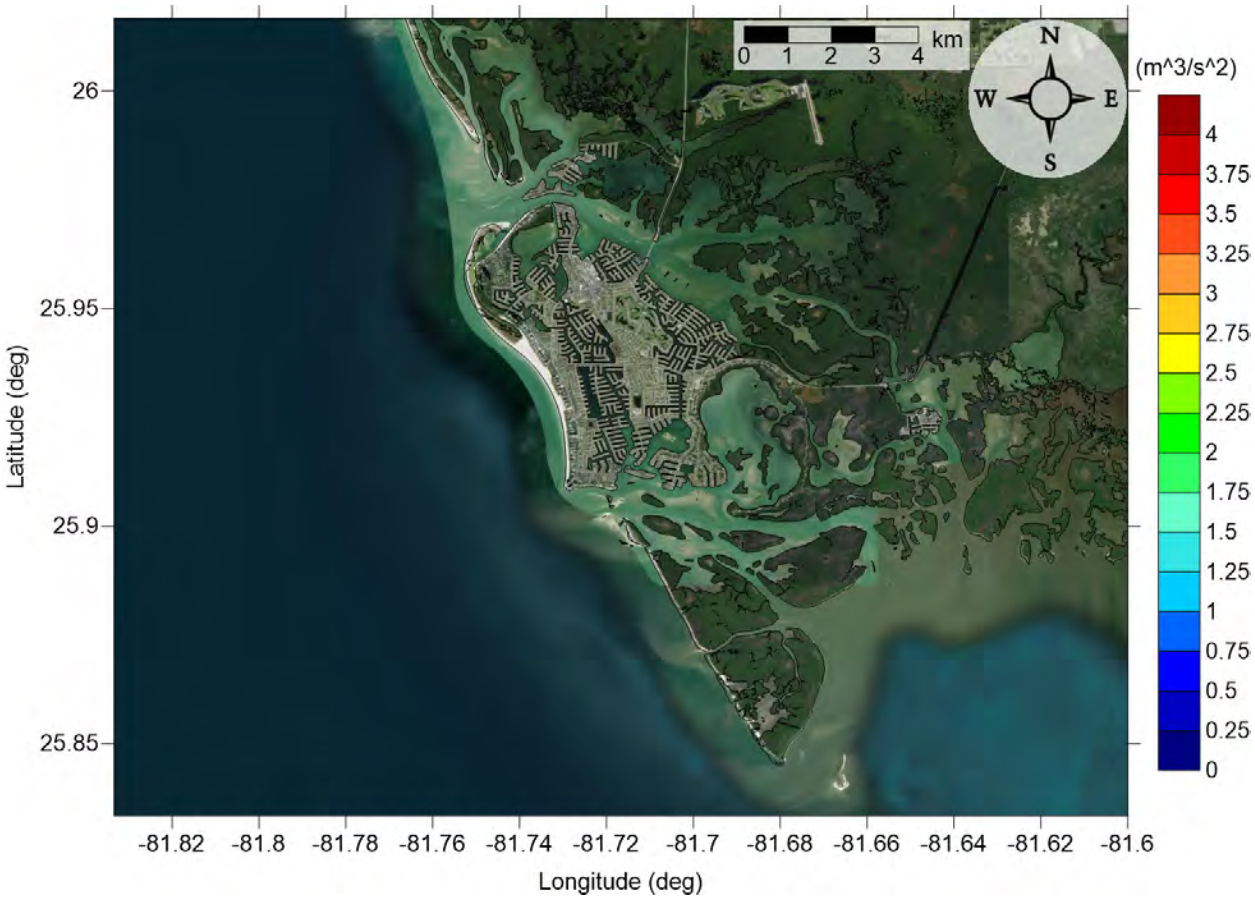

Figure 42: Maximum momentum flux (m^3/s^2) caused by the East Breaks submarine landslide in Marco Island, FL. Arrows represent direction of maximum momentum flux. Contour drawn is the zero-meter contour for land elevation.

Marco Island, FL
East Breaks submarine landslide
Maximum Inundation Depth

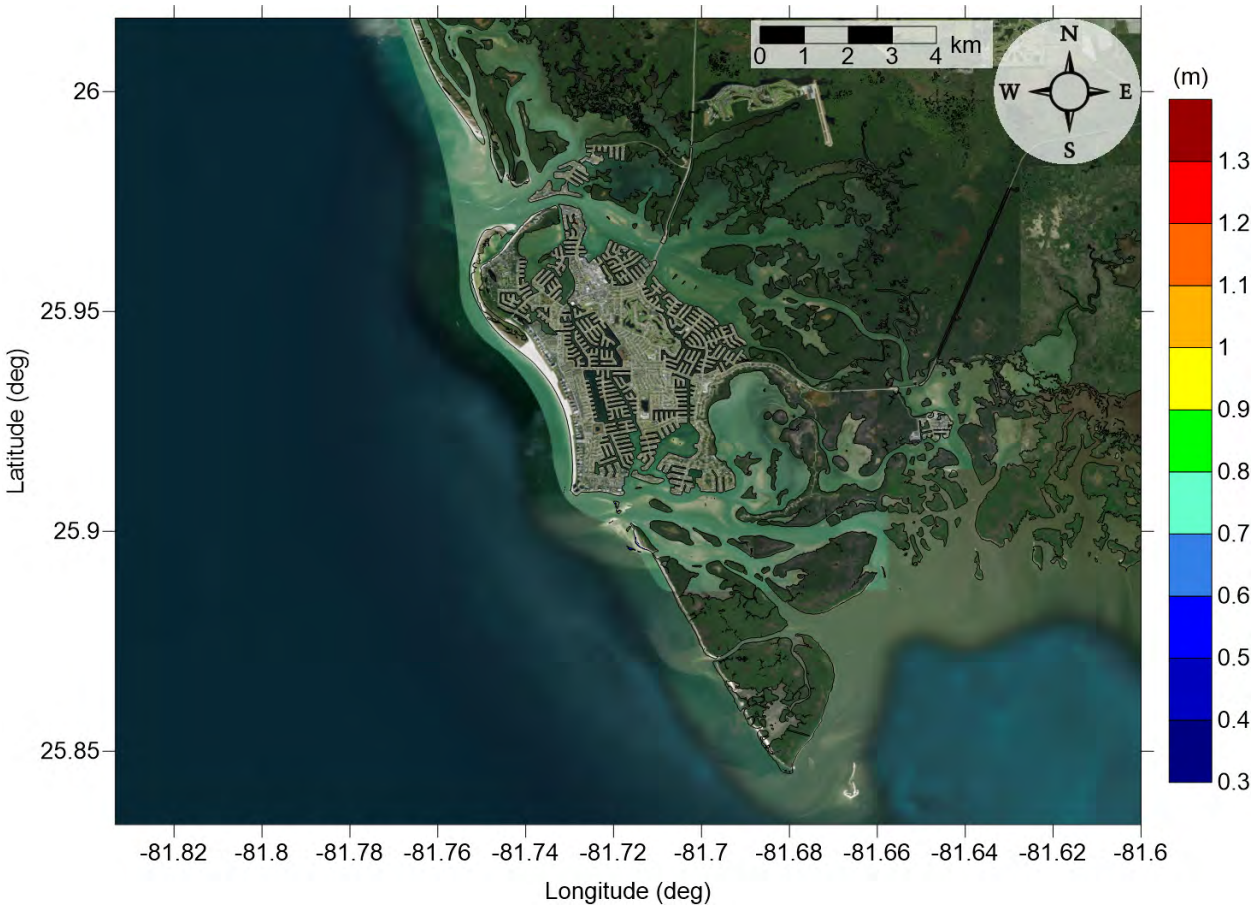

Figure 43: Maximum inundation depth (m) caused by the East Breaks submarine landslide in Marco Island, FL. Contour drawn is the zero-meter contour for land elevation.

Marco Island, FL
Probabilistic Submarine Landslide A
Maximum Momentum Flux

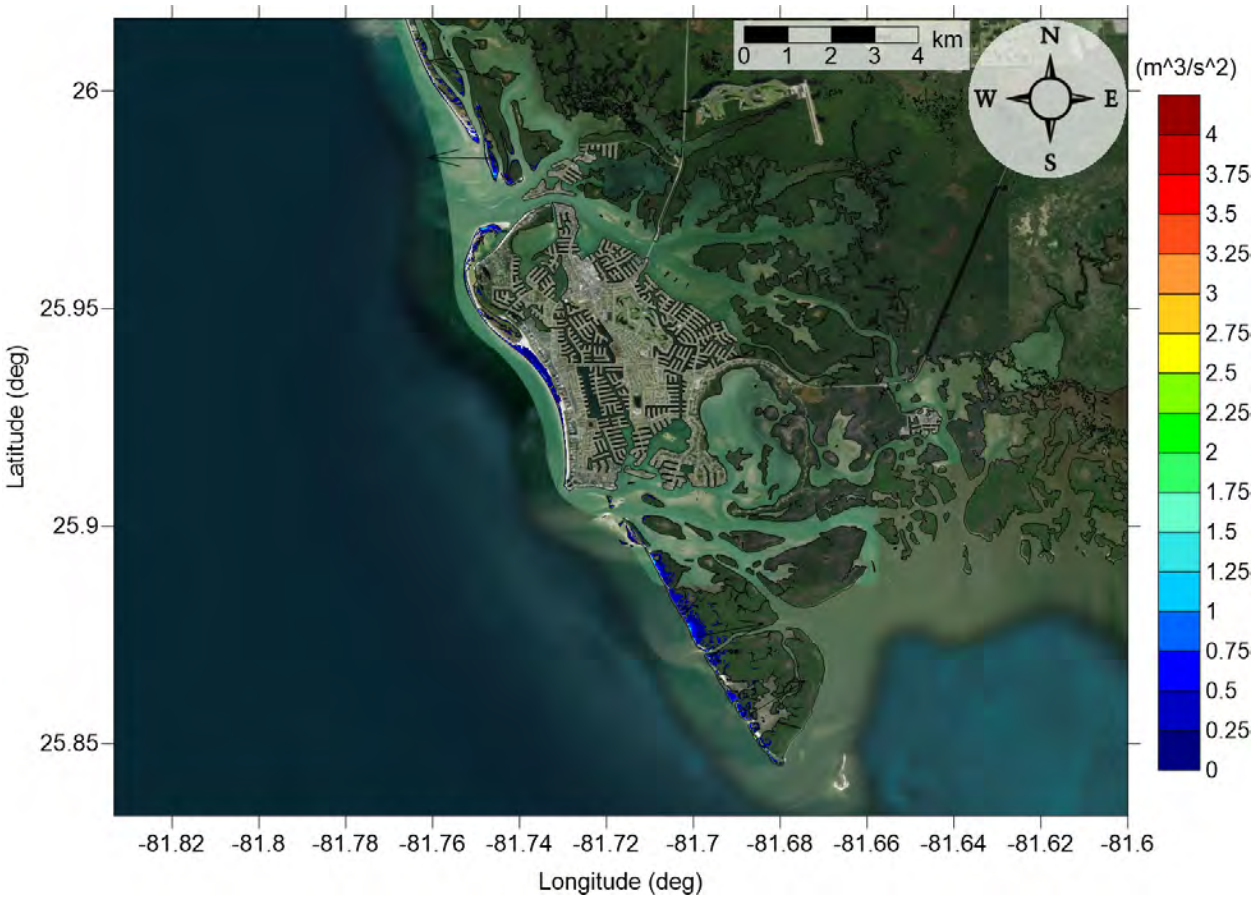

Figure 44: Maximum momentum flux (m^3/s^2) caused by the Probabilistic Submarine Landslide A in Marco Island, FL. Arrows represent direction of maximum momentum flux. Contour drawn is the zero-meter contour for land elevation.

Marco Island, FL
Probabilistic Submarine Landslide A
Maximum Inundation Depth

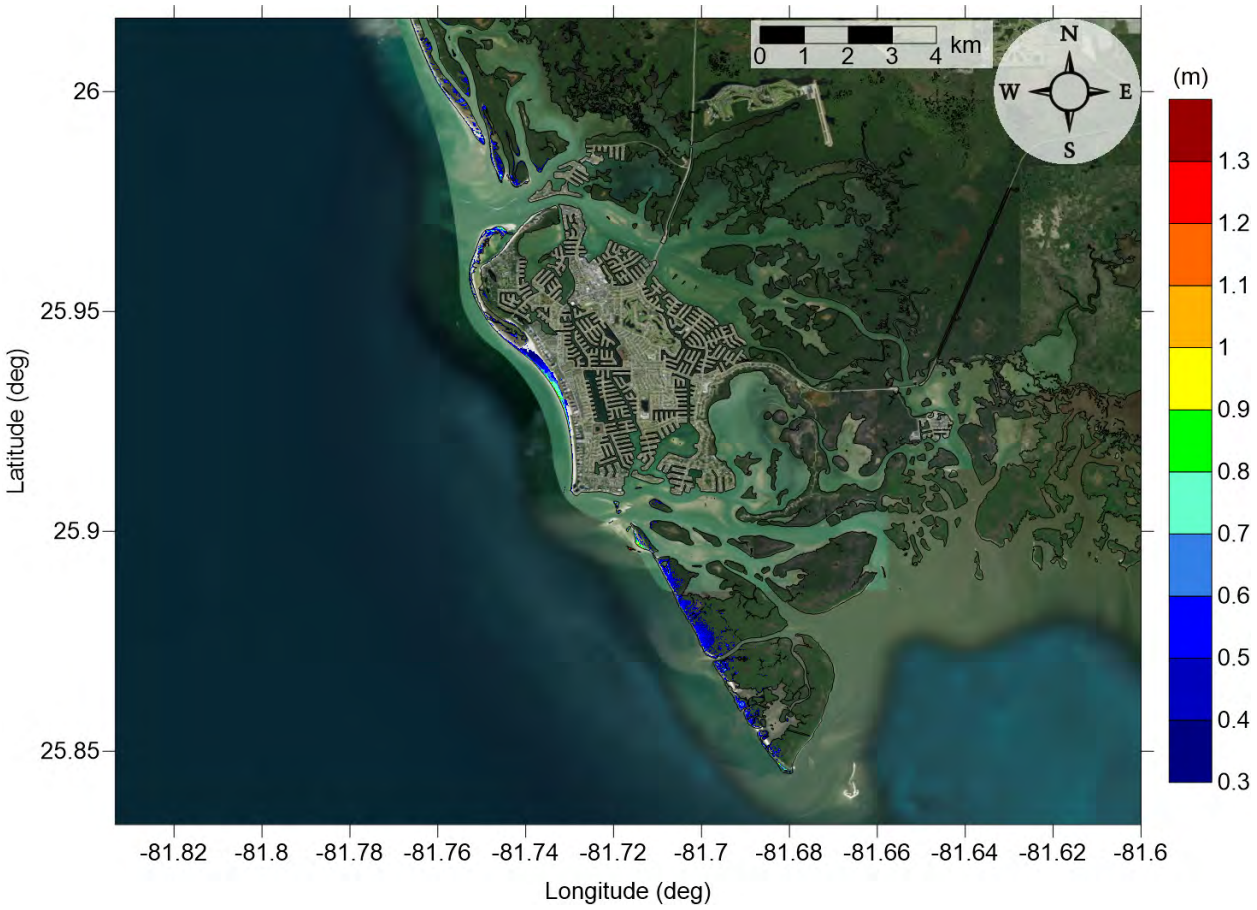

Figure 45: Maximum inundation depth (m) caused by the Probabilistic Submarine Landslide A in Marco Island, FL. Contour drawn is the zero-meter contour for land elevation.

Marco Island, FL
Probabilistic Submarine Landslide B1
Maximum Momentum Flux

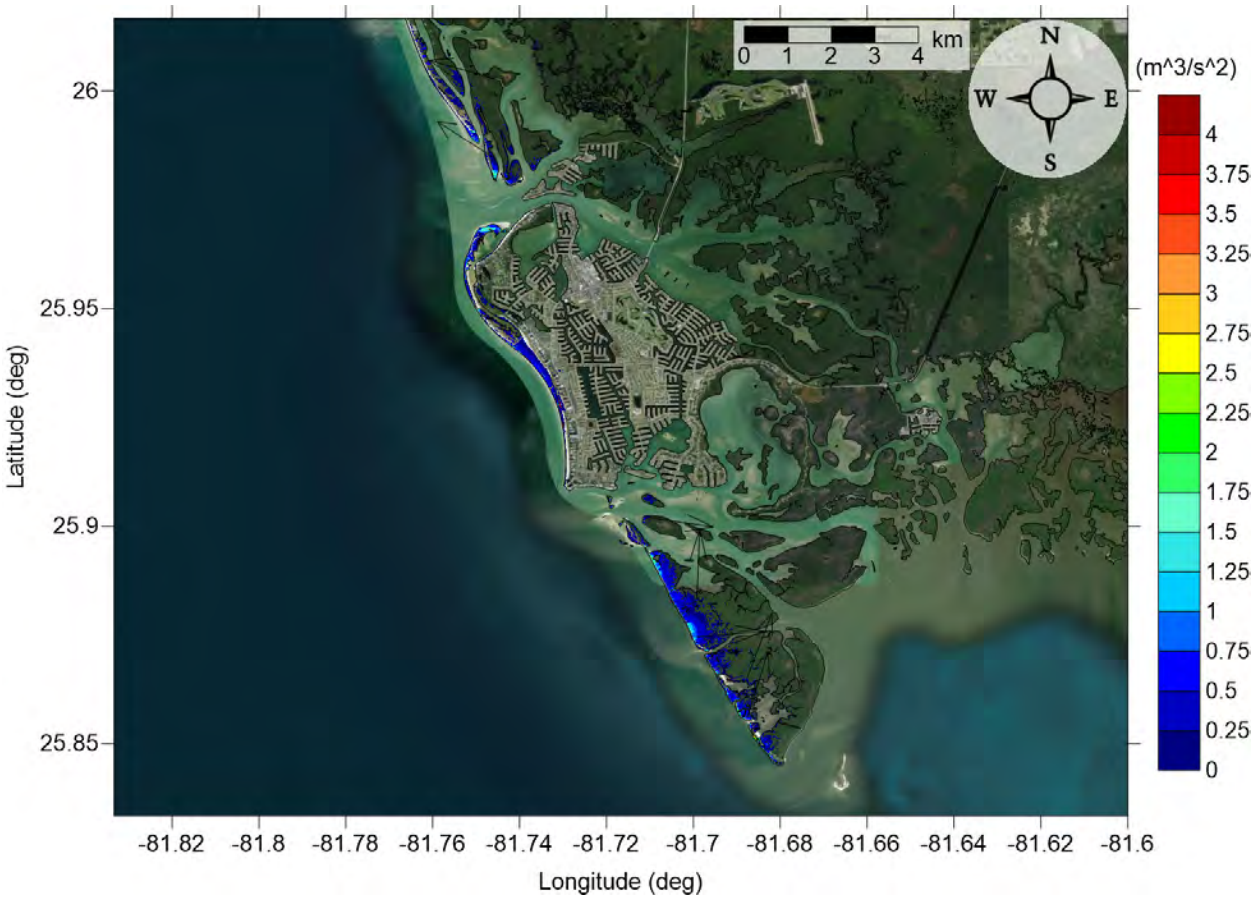

Figure 46: Maximum momentum flux (m^3/s^2) caused by the Probabilistic Submarine Landslide B1 in Marco Island, FL. Arrows represent direction of maximum momentum flux. Contour drawn is the zero-meter contour for land elevation.

Marco Island, FL
Probabilistic Submarine Landslide B1
Maximum Inundation Depth

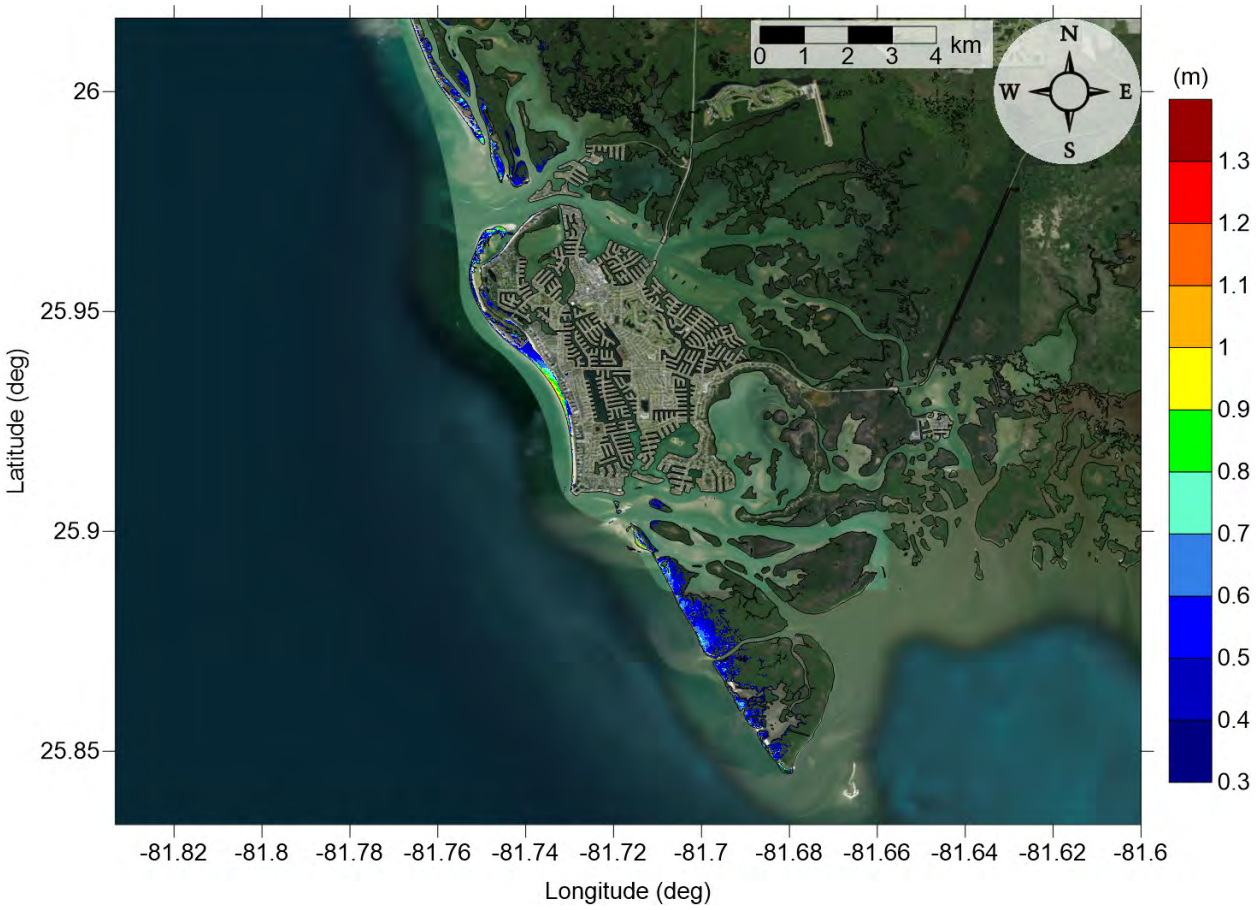

Figure 47: Maximum inundation depth (m) caused by the Probabilistic Submarine Landslide B1 in Marco Island, FL. Contour drawn is the zero-meter contour for land elevation.

Marco Island, FL
Probabilistic Submarine Landslide B2
Maximum Momentum Flux

Figure 48: Maximum momentum flux (m^3/s^2) caused by the Probabilistic Submarine Landslide B2 in Marco Island, FL. Arrows represent direction of maximum momentum flux. Contour drawn is the zero-meter contour for land elevation.

Marco Island, FL
Probabilistic Submarine Landslide B2
Maximum Inundation Depth

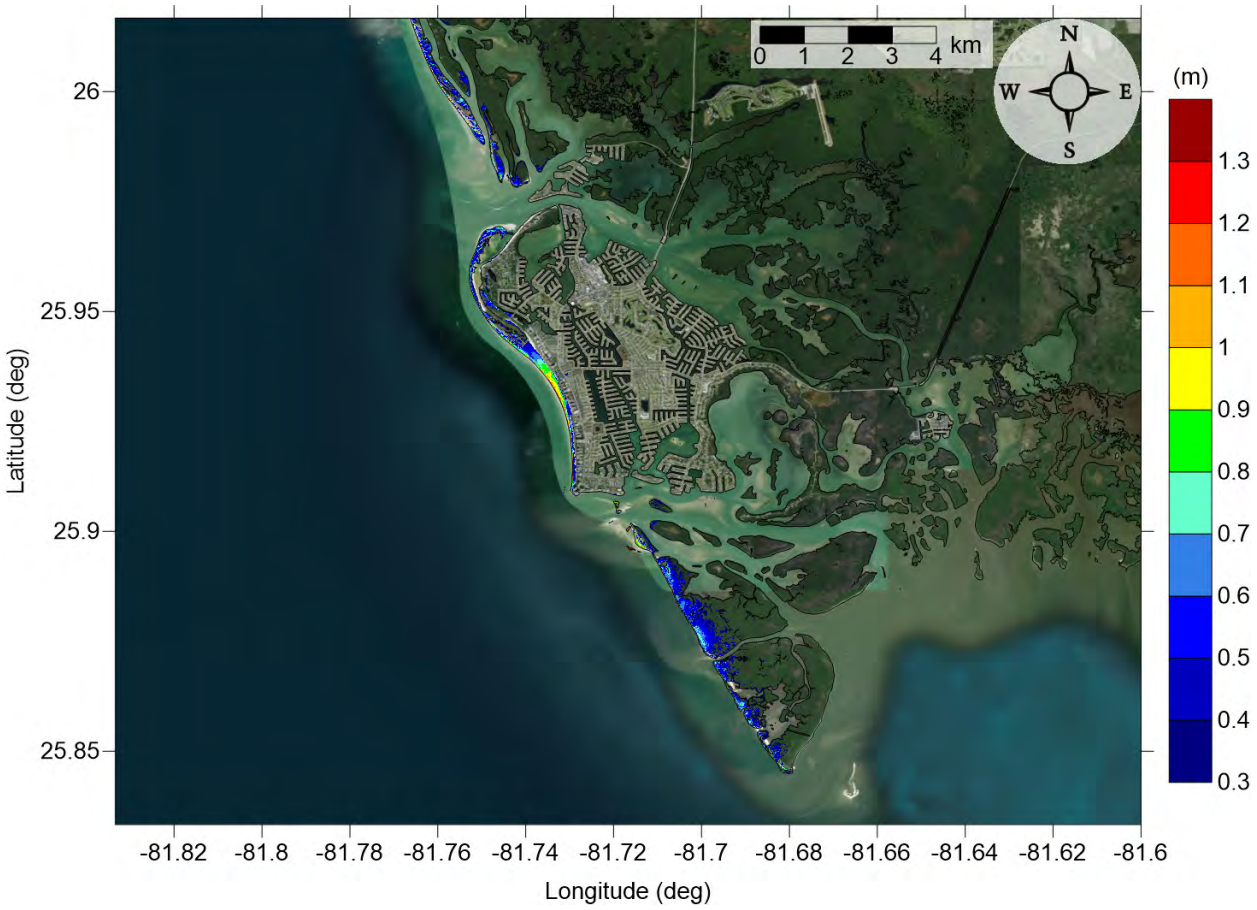

Figure 49: Maximum inundation depth (m) caused by the Probabilistic Submarine Landslide B2 in Marco Island, FL. Contour drawn is the zero-meter contour for land elevation.

Marco Island, FL
Mississippi Canyon submarine landslide
Maximum Momentum Flux

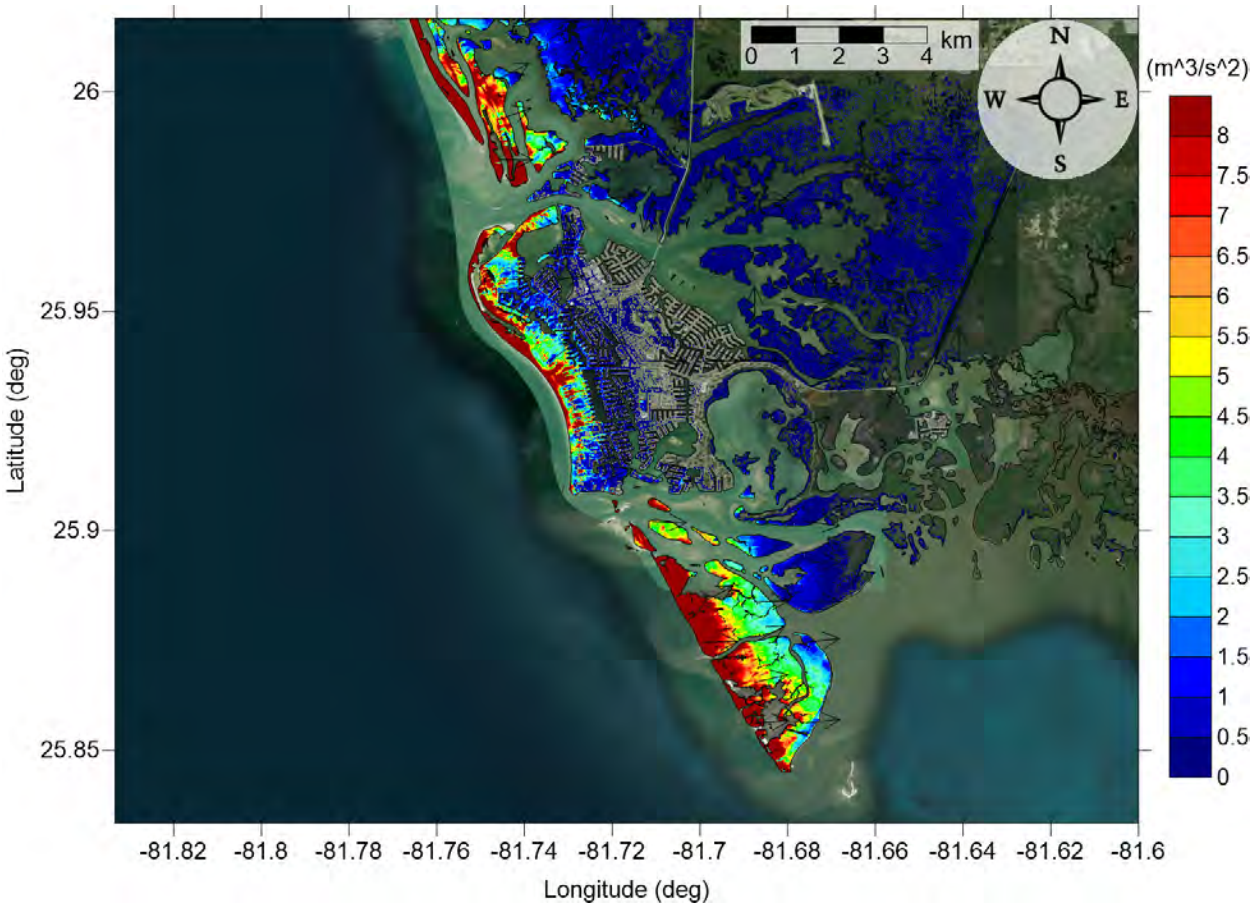

Figure 50: Maximum momentum flux (m^3/s^2) caused by the Mississippi Canyon submarine landslide in Marco Island, FL. Arrows represent direction of maximum momentum flux. Contour drawn is the zero-meter contour for land elevation.

Marco Island, FL
Mississippi Canyon submarine landslide
Maximum Inundation Depth

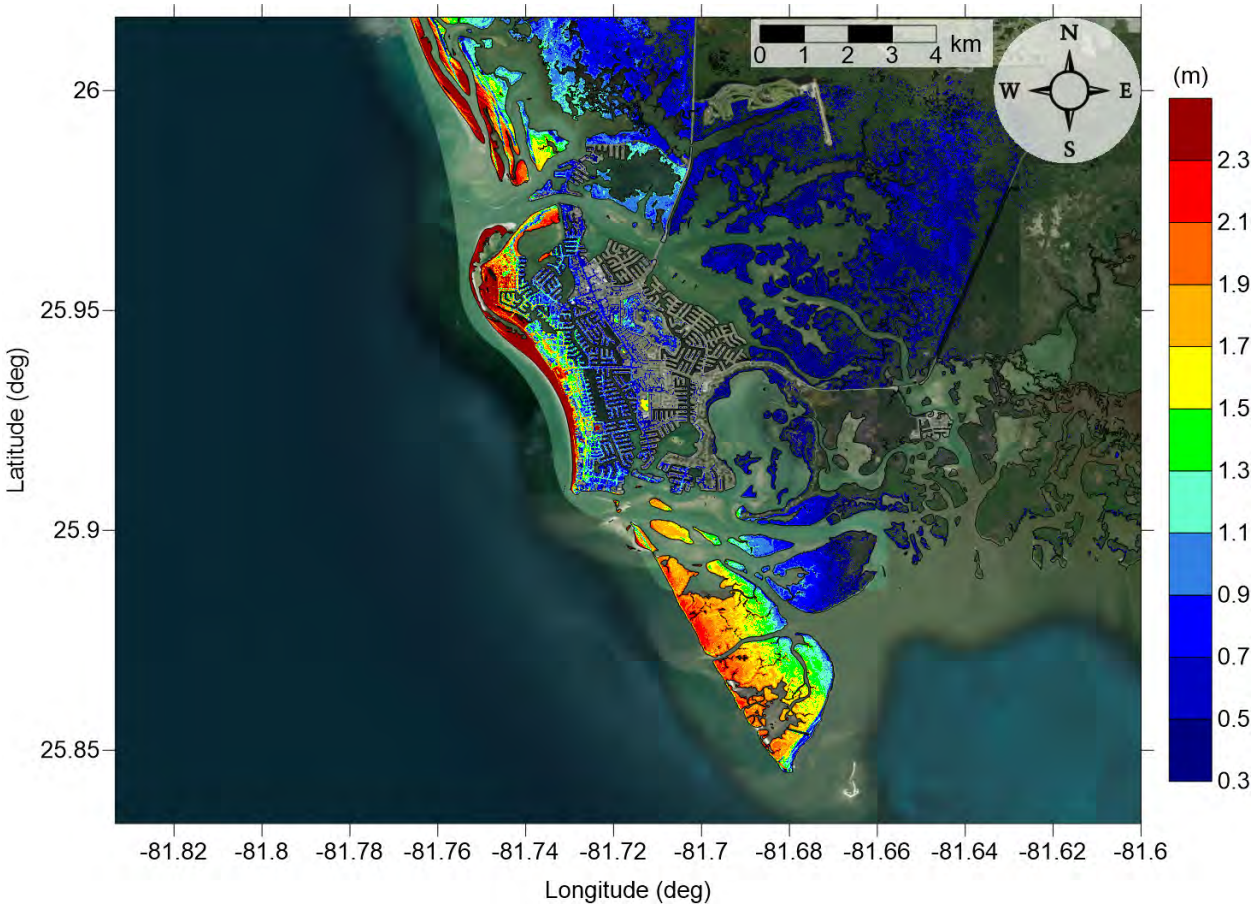

Figure 51: Maximum inundation depth (m) caused by the Mississippi Canyon submarine landslide in Marco Island, FL. Contour drawn is the zero-meter contour for land elevation.

Marco Island, FL
Probabilistic Submarine Landslide C
Maximum Momentum Flux

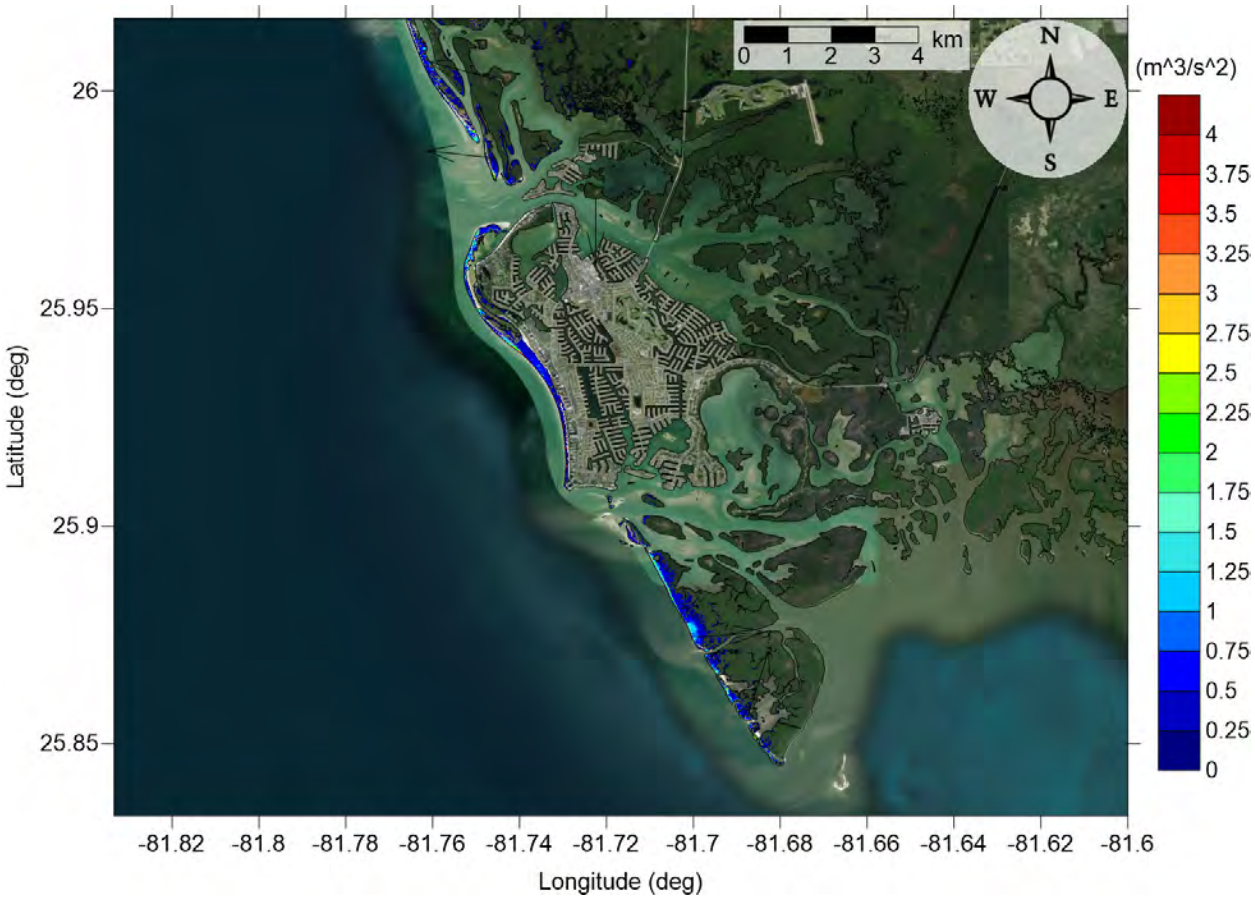

Figure 52: Maximum momentum flux (m^3/s^2) caused by the Probabilistic Submarine Landslide C in Marco Island, FL. Arrows represent direction of maximum momentum flux. Contour drawn is the zero-meter contour for land elevation.

Marco Island, FL
Probabilistic Submarine Landslide C
Maximum Inundation Depth

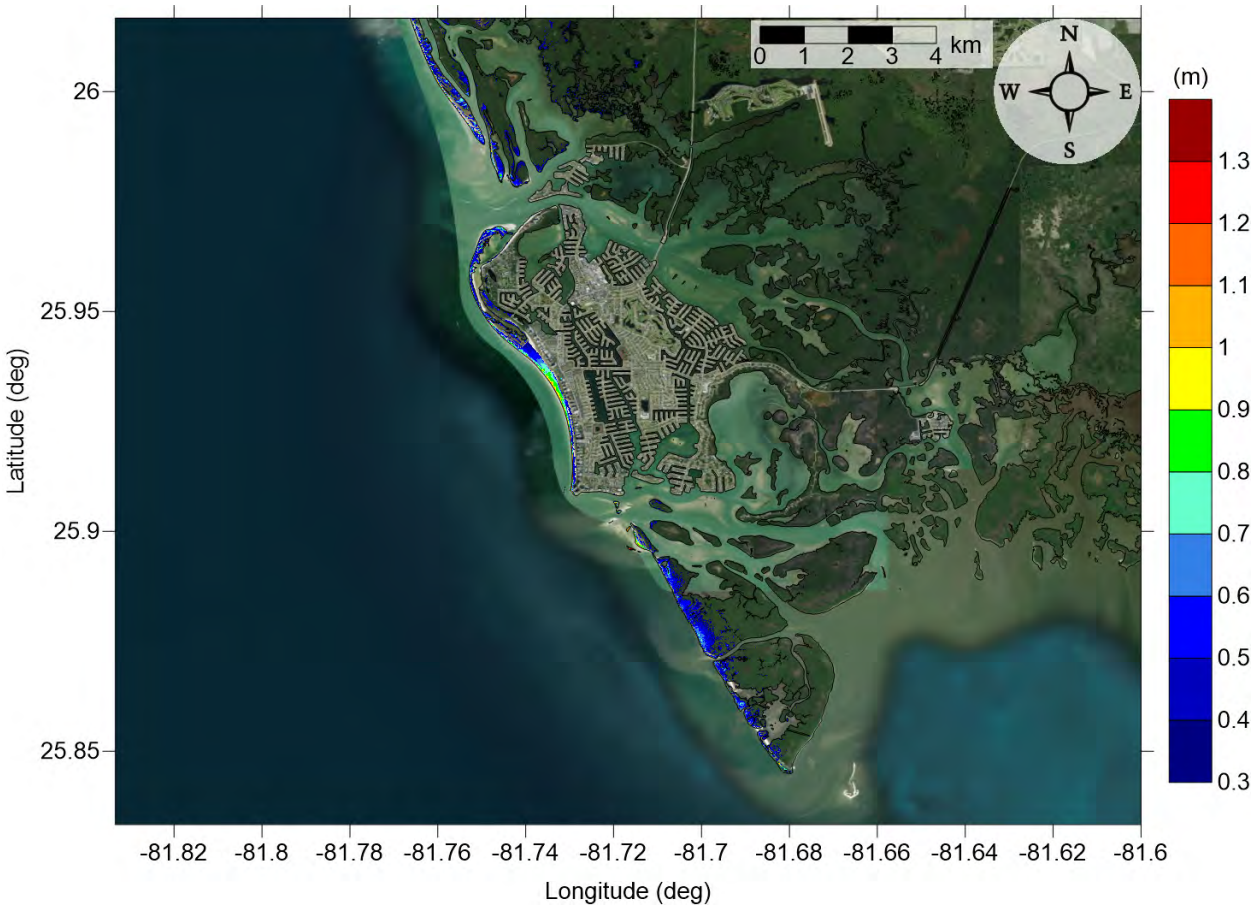

Figure 53: Maximum inundation depth (m) caused by the Probabilistic Submarine Landslide C in Marco Island, FL. Contour drawn is the zero-meter contour for land elevation.

Marco Island, FL
West Florida submarine landslide
Maximum Momentum Flux

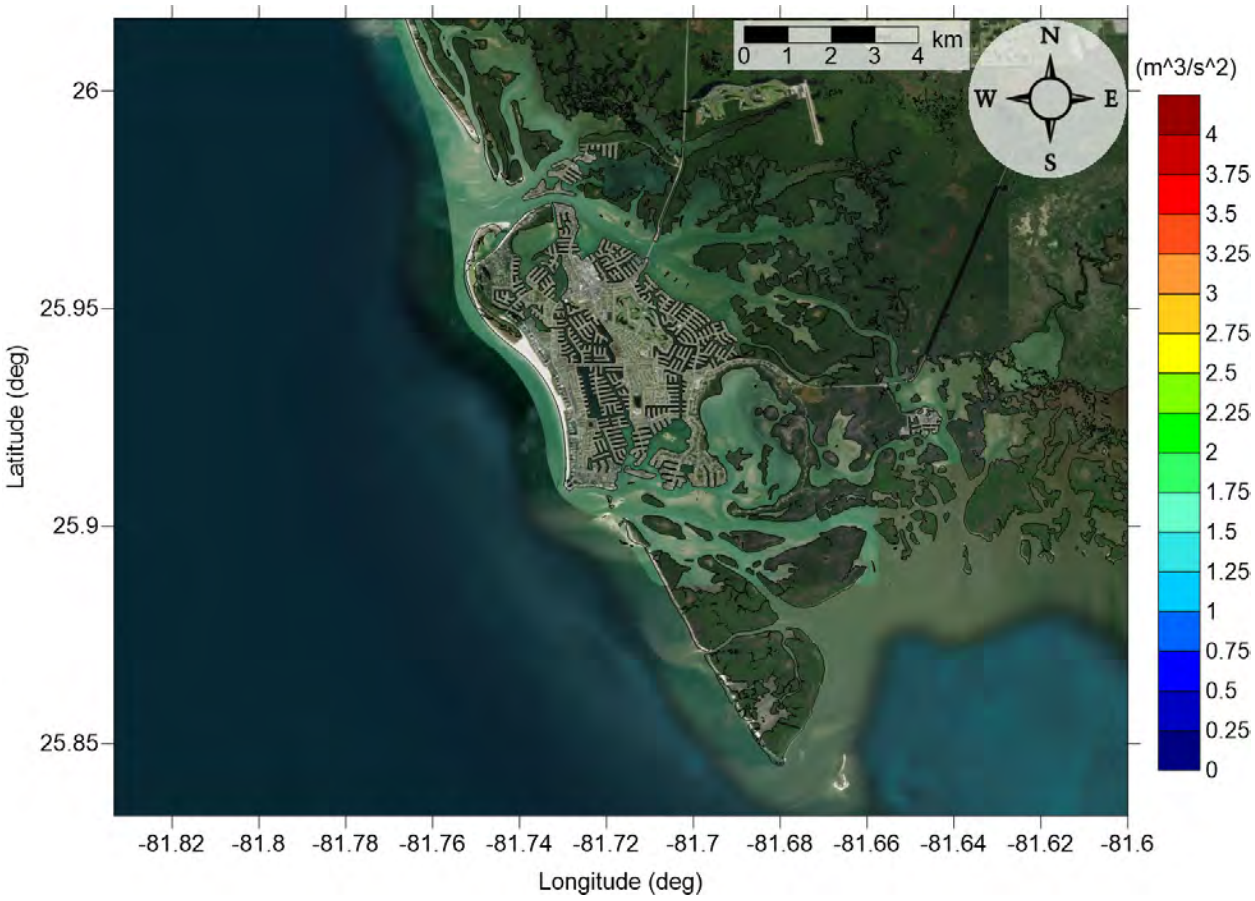

Figure 54: Maximum momentum flux (m^3/s^2) caused by the West Florida submarine landslide in Marco Island, FL. Arrows represent direction of maximum momentum flux. Contour drawn is the zero-meter contour for land elevation.

Marco Island, FL
West Florida submarine landslide
Maximum Inundation Depth

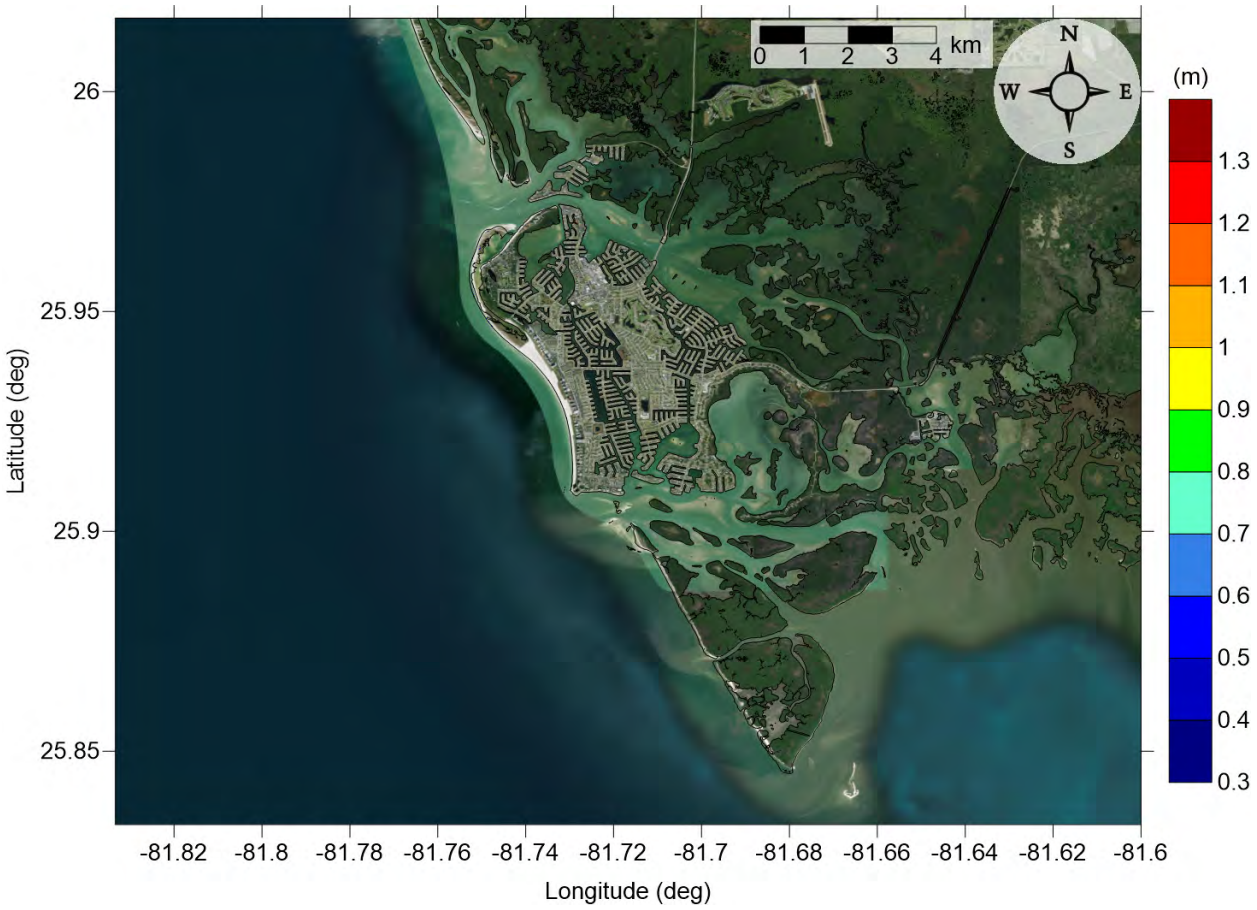

Figure 55: Maximum inundation depth (m) caused by the West Florida submarine landslide in Marco Island, FL. Contour drawn is the zero-meter contour for land elevation.

Marco Island, FL
Yucatán 3 submarine landslide
Maximum Momentum Flux

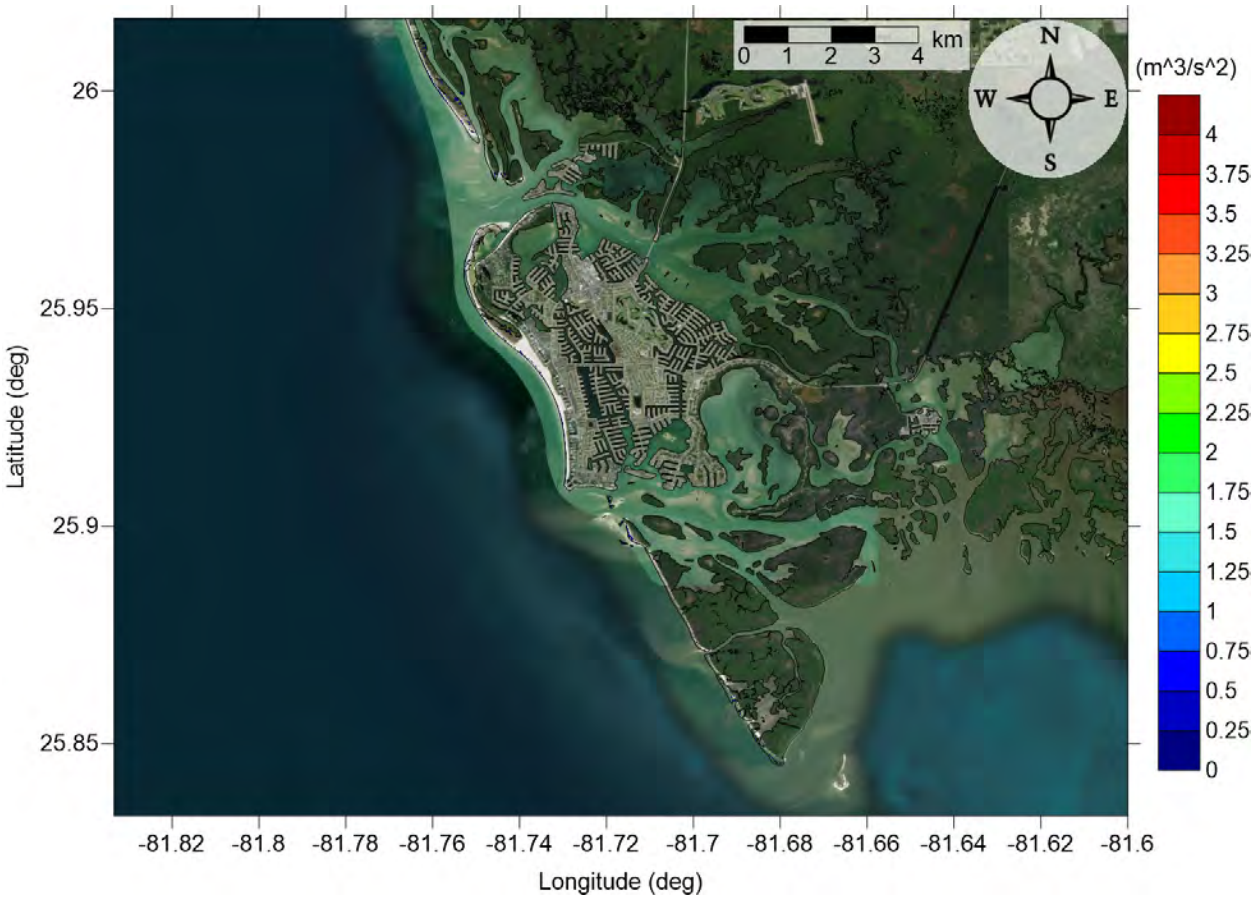

Figure 56: Maximum momentum flux (m^3/s^2) caused by the Yucatán 3 submarine landslide in Marco Island, FL. Arrows represent direction of maximum momentum flux. Contour drawn is the zero-meter contour for land elevation.

Marco Island, FL
Yucatán 3 submarine landslide
Maximum Inundation Depth

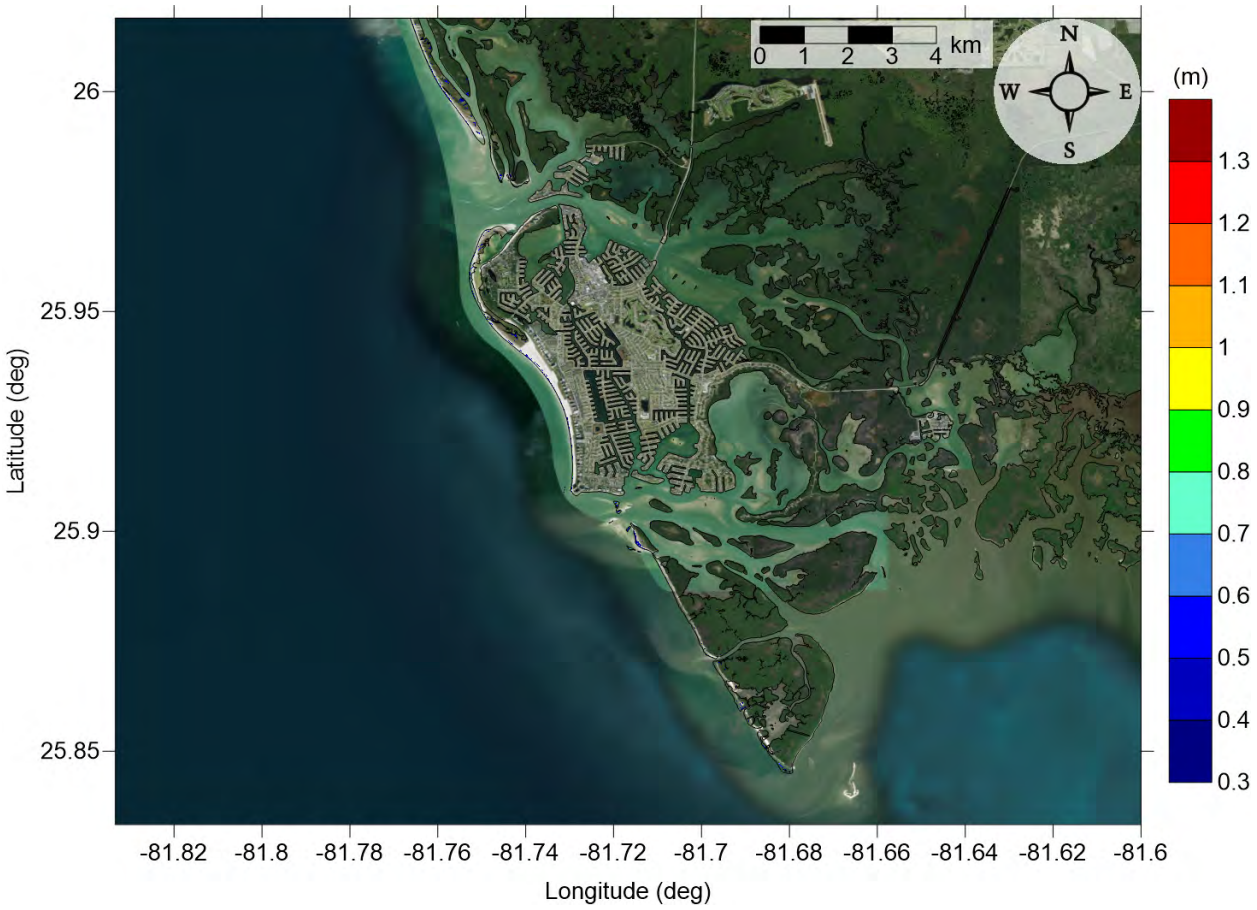

Figure 57: Maximum inundation depth (m) caused by the Yucatán 3 submarine landslide in Marco Island, FL. Contour drawn is the zero-meter contour for land elevation.

Marco Island, FL
Yucatán 5 submarine landslide
Maximum Momentum Flux

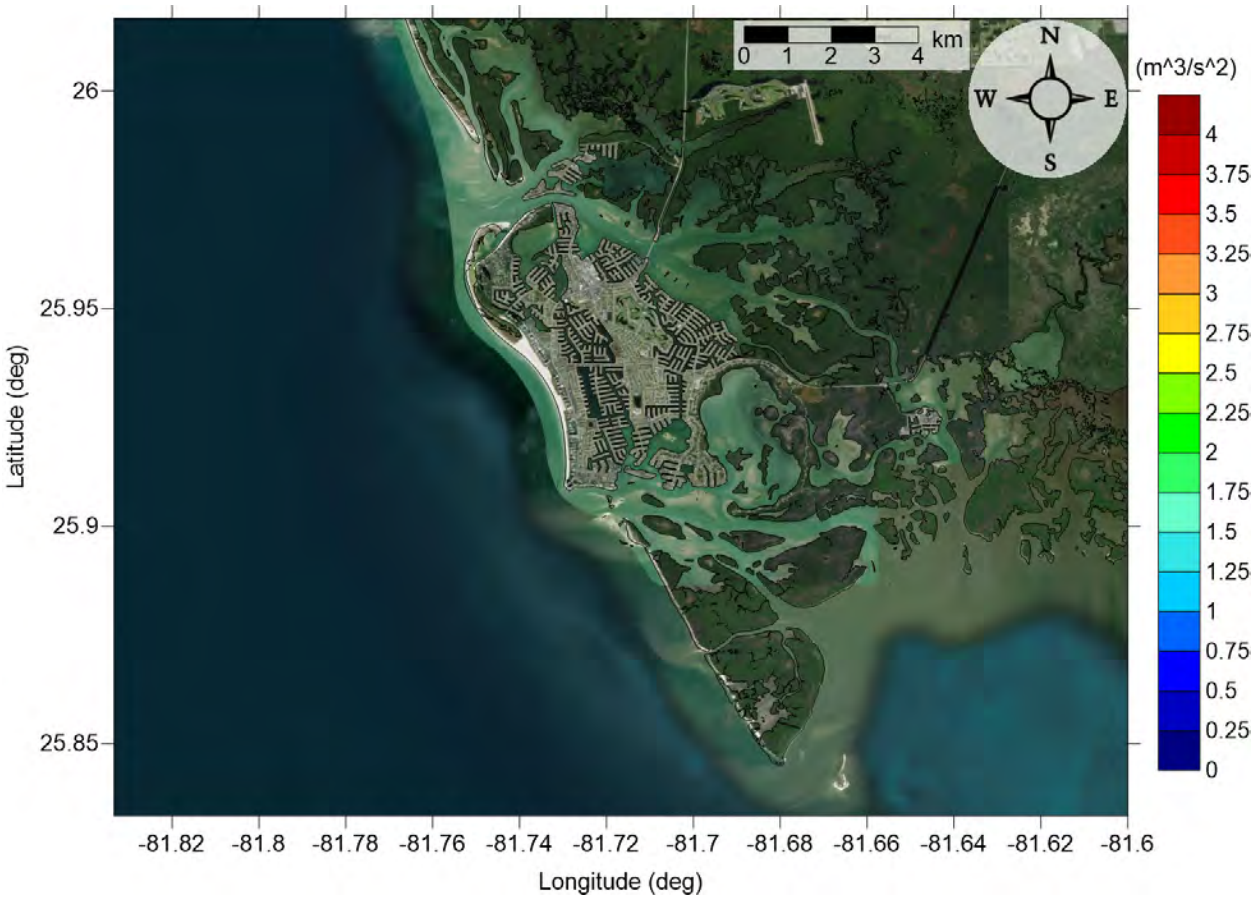

Figure 58: Maximum momentum flux (m^3/s^2) caused by the Yucatán 5 submarine landslide in Marco Island, FL. Arrows represent direction of maximum momentum flux. Contour drawn is the zero-meter contour for land elevation.

Marco Island, FL
Yucatán 5 submarine landslide
Maximum Inundation Depth

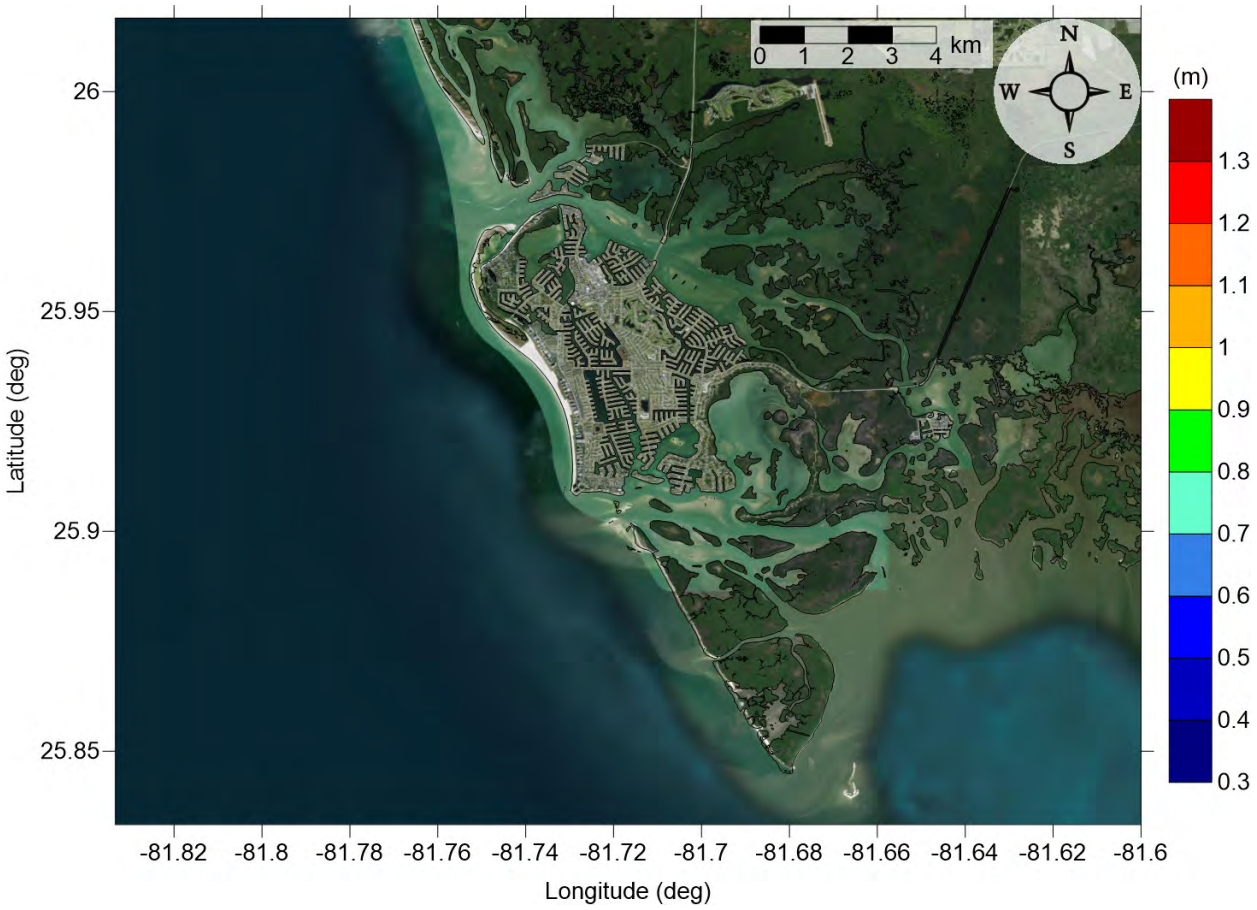

Figure 59: Maximum inundation depth (m) caused by the Yucatán 5 submarine landslide in Marco Island, FL. Contour drawn is the zero-meter contour for land elevation.

Marco Island, FL
All Sources
Maximum of Maximum Inundation Depth

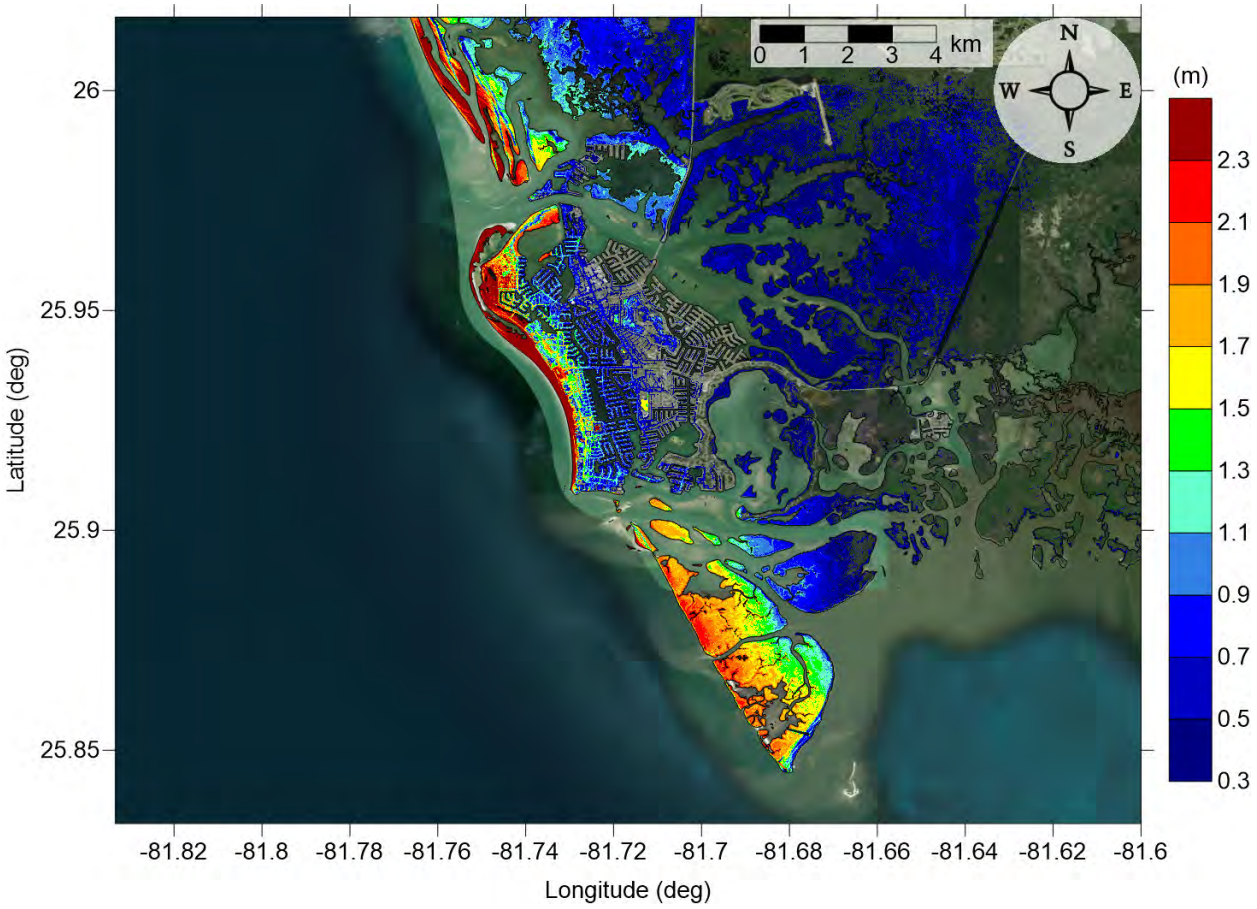

Figure 60: Maximum of maximums inundation depth (m) in Marco Island, FL, calculated as the maximum inundation depth in each grid cell from an ensemble of all tsunami sources considered. Contour drawn is the zero-meter contour for land elevation.

Marco Island, FL
All Sources
Maximum Inundation Depth by Source

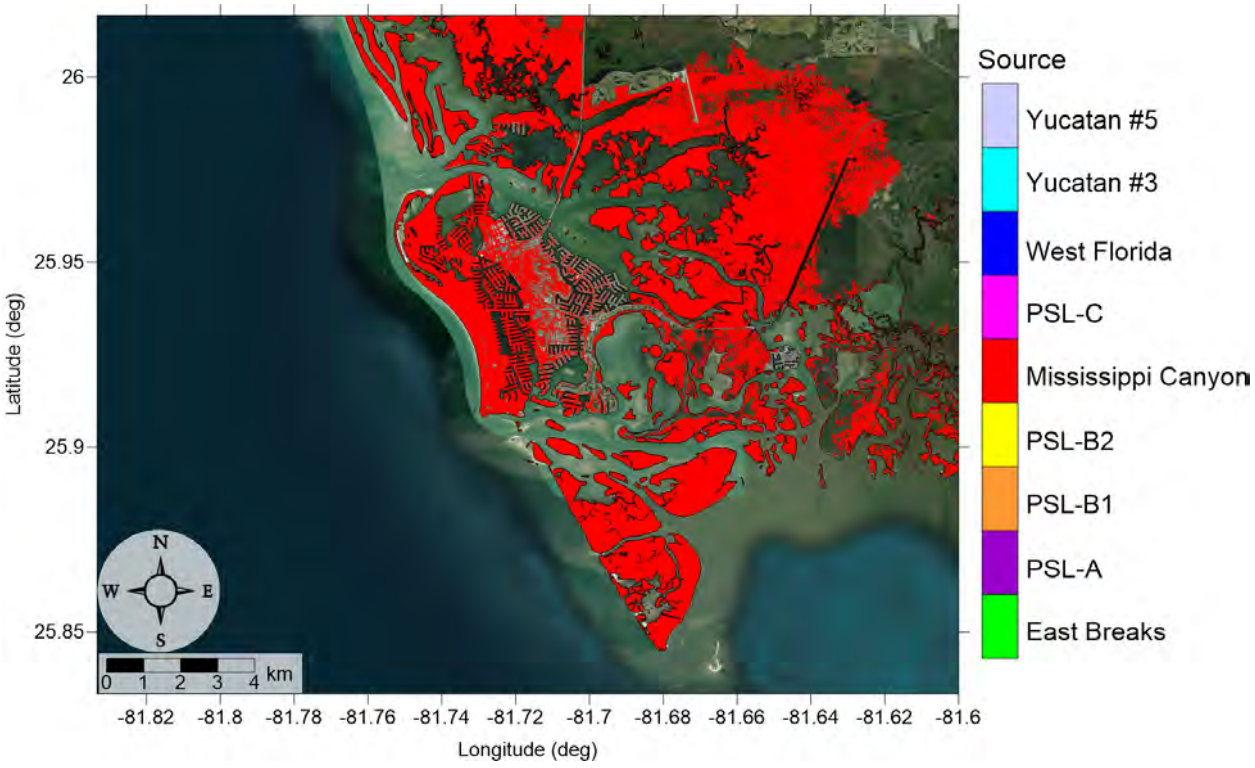

Figure 61: Indication of the tsunami source which causes the maximum of maximums inundation depth (m) in each grid cell from an ensemble of all tsunami sources in Marco Island, FL. Contour drawn is the zero-meter contour for land elevation.

5 Tsunami and Hurricane Storm Surge Inundation

Due to the limitations on availability of high-resolution (1/3 arcsecond) DEMs, detailed inundation maps for all communities along the Gulf Coast are not yet possible. In an effort to develop a first-order estimate of potential tsunami inundation for those locations where detailed inundation maps have not yet been developed, we compare tsunami inundation modeled for the communities mentioned above to hurricane storm surge modeled data. The motivation for and implications of this approach are twofold. It provides a way to assess tsunami inundation in unmapped communities based on existing storm surge flood data and also relates the level of tsunami hazard to that of another hazard that is better defined in this region. Tsunamis are not well-understood as a threat along the Gulf Coast, making tsunami hazard mitigation efforts somewhat difficult. However, hurricane is a relatively well-understood threat in this region, and hurricane preparedness approaches are well-developed. As a result, comparisons of tsunami and hurricane storm surge inundation levels provide a more understandable and accessible idea of the level of hazard presented by potential tsunami events and can serve as a basis for tsunami preparedness efforts.

The hurricane storm surge data used here is available from the Sea, Lake, and Overland Surges from Hurricanes (SLOSH) model (http://www.nhc.noaa.gov/surge/slosh.php). The SLOSH model was developed by the National Weather Service (NWS) to provide estimates of storm surge heights caused by historical, predicted, or hypothetical hurricanes based on different values for atmospheric pressure, hurricane size, forward speed, and track. It uses a polar, elliptical, or hyperbolic grid for computations, leading to higher resolutions near coastal areas of interest. Some limitations of the SLOSH model should be acknowledged. Resolution of the model varies from tens of meters to a kilometer or more. Near the coastal communities of interest here, resolution is on the order of 1 km. Sub-grid scale water and topographic features such as channels, rivers, levees, and roads, are parameterized instead of being explicitly modeled. Despite these limitations, the hurricane storm surge data from the SLOSH model is currently the best data publicly available for our purposes, and efforts have been made to ensure the validity of the SLOSH data in performing comparisons with tsunami inundation.

The SLOSH MOM results provide the worst-case storm surge for a given hurricane category and initial tide level based on a set of model runs with various combinations of parameters such as forward speed, trajectory, and landfall location. To perform the storm surge and tsunami comparisons, SLOSH storm surge elevation data was first converted to meters and adjusted from the NAVD88 to the MHW vertical datum using NOAA's VDatum tool (http://vdatum.noaa.gov/). Due to the relatively low resolution of the SLOSH data as compared to the DEMs used for tsunami modeling, the SLOSH data was interpolated to 1/3 arcsecond (10 m) resolution using a kriging method. Inundation was then determined by subtracting land elevation from the storm surge elevation.

Here, an initial high tide level is used for the SLOSH MOM results in order to compare the worst-case tsunami inundation with a worst-case storm surge scenario. The high tide SLOSH MOM data includes effects of the highest predicted tide level at each location. In comparison, water elevations in the tsunami modeling are based on the MHW datum, which averages the high water levels over the National Tidal Datum Epoch (NTDE). Within the

GOM, tidal ranges are relatively small, with diurnal ranges on the order of 1.5 ft (0.5 m) for most of the communities studied here, and slightly higher at around 2.5 ft (0.8 m) for the west coast of Florida. Thus, differences between highest tide levels and the mean of the highest tide levels are expected to be relatively small, though local bathymetric effects combined with tidal effects can still be significant.

It should be noted that the updated Saffir-Simpson Hurricane Wind Scale which delineates hurricane categories 1-5 does not include storm surge as a component of the measure of hurricane intensity and that other methods may capture the physics of hurricane severity and damage in a more appropriate manner (e.g. Kantha [2006], Basco and Klentzman [2006], Irish and Resio [2010]). However, the SLOSH MOM results take into account thousands of scenarios for a given hurricane category, resulting in a composite worst-case storm surge scenario for each Saffir-Simpson hurricane category. Thus, since hurricane preparedness, storm surge evacuation zones, and hazard mitigation efforts are based on hurricane category assignment, we aim to determine the hurricane category which produces MOM storm surge inundation ζ_h that is a best match to the tsunami MOM inundation ζ_t. That is, we determine the hurricane category which satisfies

$$min_c(|\zeta_{h_c} - \zeta_t|), \qquad c = \text{Cat1,..,Cat5} \tag{1}$$

for each grid cell. The inundation level for the best-match category is denoted $\zeta_{h_{min}}$. The actual difference between hurricane and tsunami inundation levels $\Delta\zeta = \zeta_{h_{min}} - \zeta_t$ then indicates how close of a match the best-match category actually is. Thus, positive values of $\Delta\zeta$ indicate where hurricane storm surge inundation is higher than tsunami inundation, and negative values indicate where tsunami inundation is higher. A common local practice in tsunami modeling is to only consider inundation above a threshold of 0.3 m (1 ft) [Horrillo et al., 2011, 2015]. This is due to the extensive flat and low-lying elevation found along the Gulf Coast. All depths are calculated for tsunami inundation modeling, but inundation less than 0.3 m (1 ft) is considered negligible here for inundation mapping purposes. Thus, comparisons are only made where either the tsunami or hurricane MOM inundation is at least 0.3 m (1 ft). Results for the two selected Gulf Coast communities are given in the following subsections. It is possible that tsunami inundation zone has no hurricane flooding, therefore matching with hurricane category cannot be made.

5.1 Don Pedro Island-Boca Grande-Captiva Island, FL

Don Pedro Island-Boca Grande

On a regional scale, the wide Florida GOM continental shelf provides significant damping of tsunami waves so that the majority of Florida west coast shows less tsunami inundation, based on previous findings [e.g. Horrillo et al., 2015, 2018]. Fig. 38 shows the MOM tsunami inundation affecting Don Pedro Island-Boca Grande, FL. Under the worst case scenario, tsunami waves would inundate all of the barrier islands and the mainland areas facing the GOM and around inlets. Overall water depth exhibits decreasing trend from oceanfront toward the bay, with maximum over 2 m. The MOM tsunami inundation at Don Pedro Island and Boca Grande ranges from 1 to over 2 m, but mostly over 1.5 m. Across the bay,

relatively high tsunami inundation (> 1.5 m) only occurs west of Placida Rd where it is close to Don Pedro Island, while the rest of the inundated mainland areas only sees inundation less than 1.5 m. The Mississippi Canyon landslide is responsible for the MOM inundation (see Fig. 40).

The hurricane category which best matches the tsunami inundation in Don Pedro Island-Boca Grande-Captiva Island, FL is shown in Fig. 62, and Fig. 63 shows $\Delta\zeta$ for the best-matching hurricane category satisfying Eq. 1. The hurricane category that best matches tsunami inundation closely follows the MOM tsunami inundation trend, where Category 3 appears near the beach, Category 2 runs parallel and takes up the middle section of the island, and the rest is occupied by Category 1. The difference between hurricane flooding and tsunami inundation is mostly within ± 1 m.

Captiva Island, FL

Fig. 39 shows the MOM tsunami inundation affecting Captiva Island, FL. Under the worst case scenario, tsunami would inundate all of the barrier islands. Overall water depth exhibits decreasing trend from oceanfront toward the bay, with maximum over 2 m. The MOM tsunami inundation at Cayo Costa Island is mostly over 2 m, though there are no residents on this island. On North Captiva Island, tsunami inundation over 2 m mainly occurs in its middle west section where there are no residents. The northern residential area generally have water lower than ~ 1.5 m. Similarly on Captiva Island, high water (> 2 m) only occurs along the beach, while the sea wall protected residential areas have water lower than 1.5 m. The Mississippi Canyon landslide is responsible for the MOM inundation (see Fig. 41).

The hurricane category which best matches the tsunami inundation in Captiva Island, FL is shown in Fig. 64, and Fig. 65 shows $\Delta\zeta$ for the best-matching hurricane category satisfying Eq. 1. The hurricane category that best matches tsunami inundation closely follows the MOM tsunami inundation trend, where Category 3 appears near the beach, Category 2 takes up the middle section of the island, and the rest is occupied by Category 1. The difference between hurricane flooding and tsunami inundation is mostly within ± 1 m.

Don Pedro Island-Boca Grande-Captiva Island, FL
All Sources
SLOSH Storm Surge and MOM Tsunami Inundation Comparison

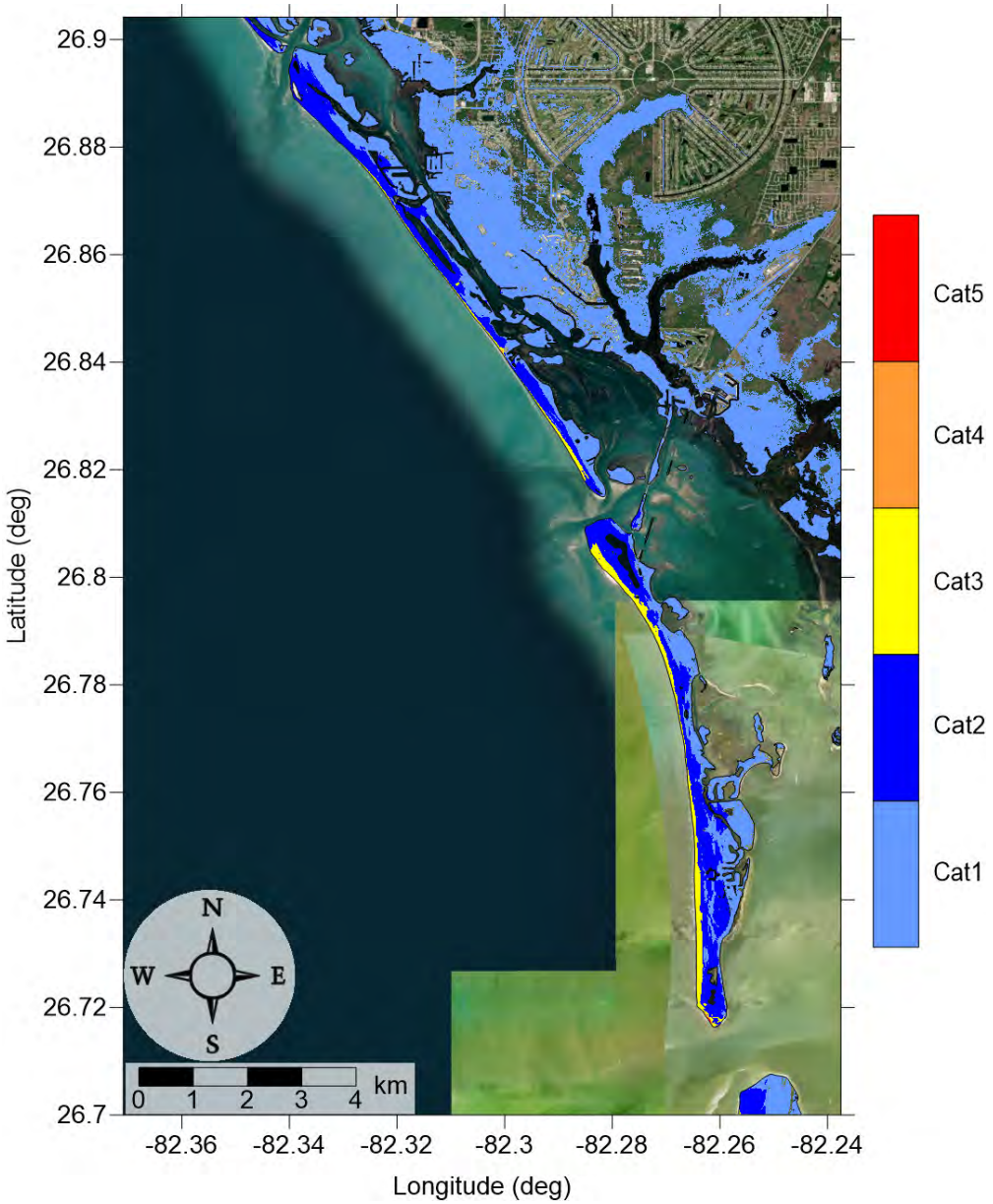

Figure 62: Hurricane category which produces inundation at high tide that best matches the MOM tsunami inundation shown in Figure 63 for Don Pedro Island-Boca Grande, FL. The contours drawn and labeled are at -5 m, -10 m, and -15 m levels.

Don Pedro Island-Boca Grande-Captiva Island, FL
All Sources
SLOSH Storm Surge and MOM Tsunami Inundation Comparison

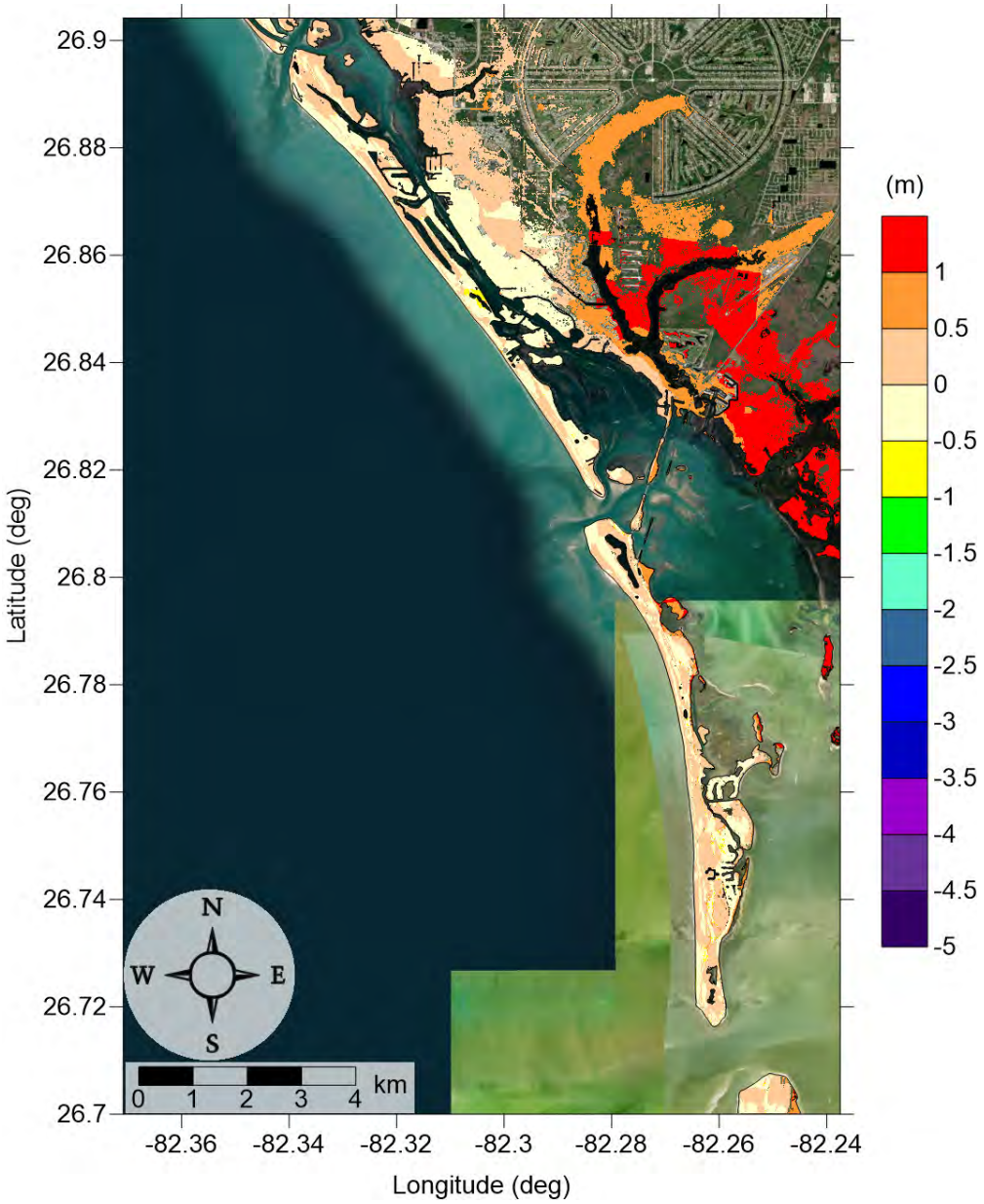

Figure 63: Actual difference $\Delta\zeta$ (in meters) between SLOSH MOM storm surge inundation and MOM tsunami inundation for the best-match hurricane category shown in Figure 62 for Don Pedro Island-Boca Grande, FL. Note that negative values indicate where tsunami inundation is higher than hurricane inundation, and pale colors indicate relatively good agreement between tsunami and storm surge inundation, i.e. $|\Delta\zeta| \leq 0.5$ m. The contours drawn and labeled are at -5 m, -10 m, and -15 m levels.

Don Pedro Island-Boca Grande-Captiva Island, FL
All Sources
SLOSH Storm Surge and MOM Tsunami Inundation Comparison

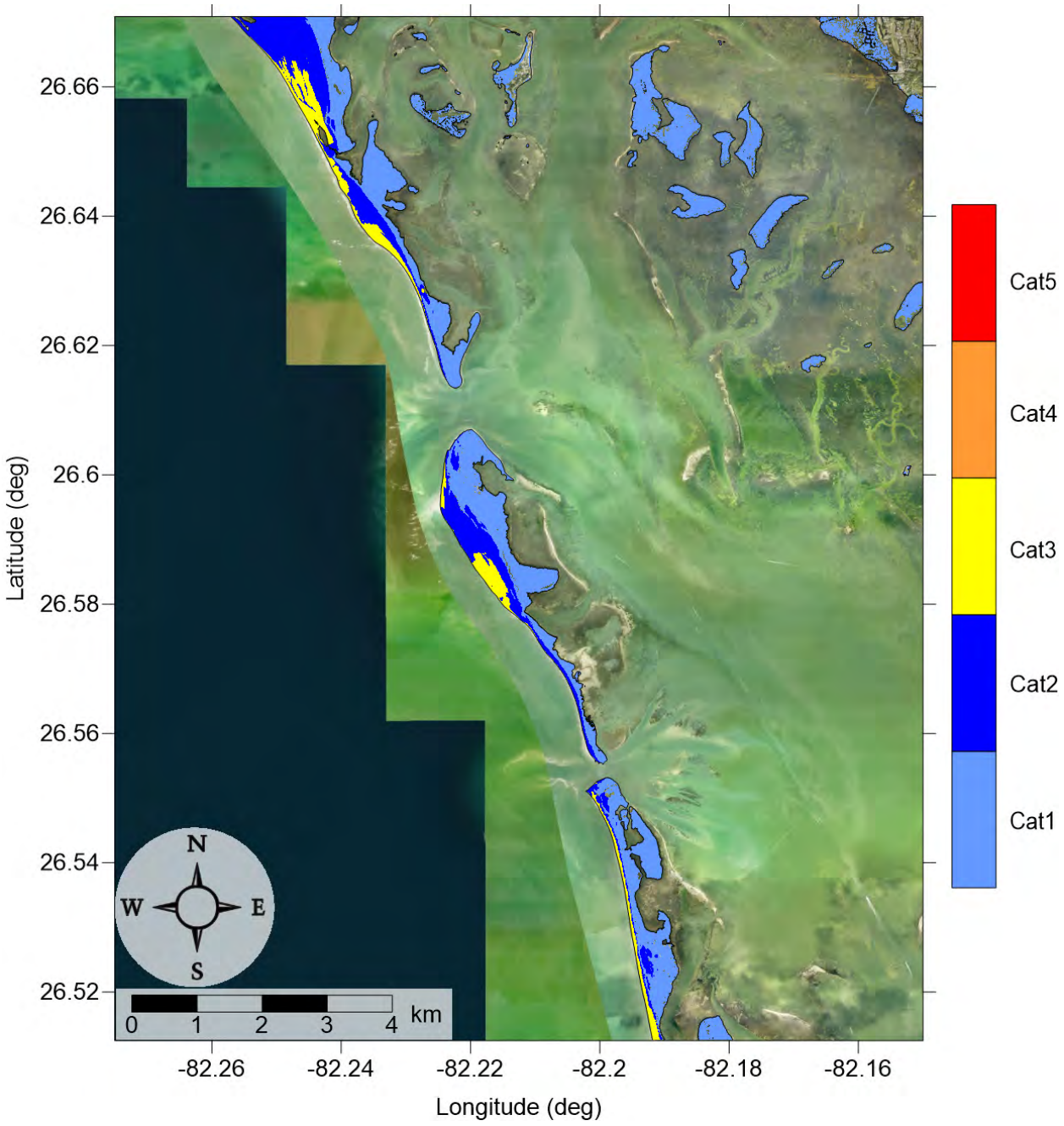

Figure 64: Hurricane category which produces inundation at high tide that best matches the MOM tsunami inundation shown in Figure 65 for Captiva Island, FL. The contours drawn and labeled are at -5 m, -10 m, and -15 m levels.

Don Pedro Island-Boca Grande-Captiva Island, FL
All Sources
SLOSH Storm Surge and MOM Tsunami Inundation Comparison

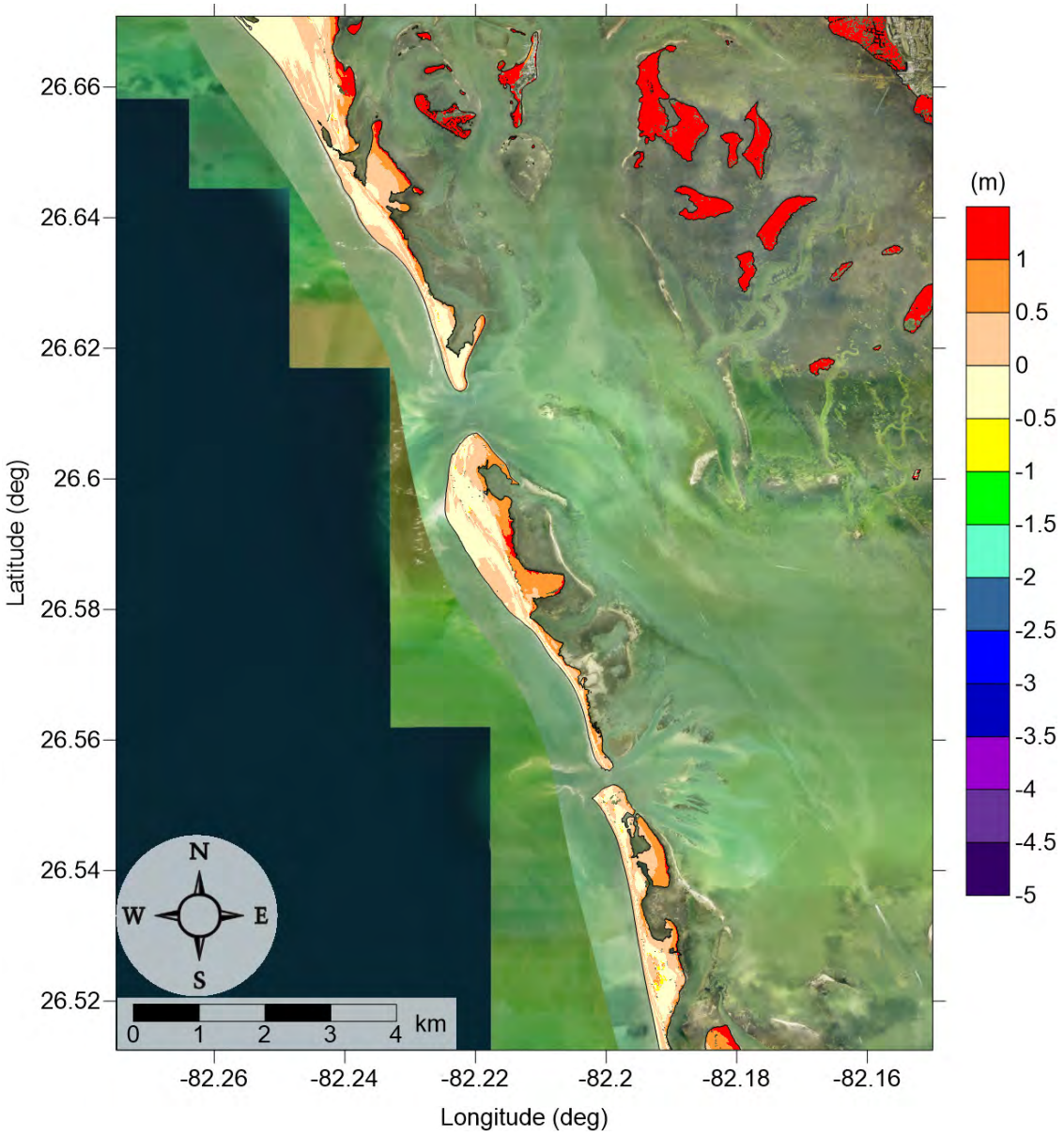

Figure 65: Actual difference $\Delta\zeta$ (in meters) between SLOSH MOM storm surge inundation and MOM tsunami inundation for the best-match hurricane category shown in Figure 64 for Captiva Island, FL. Note that negative values indicate where tsunami inundation is higher than hurricane inundation, and pale colors indicate relatively good agreement between tsunami and storm surge inundation, i.e. $|\Delta\zeta| \leq 0.5$ m. The contours drawn and labeled are at -5 m, -10 m, and -15 m levels.

5.2 Marco Island, FL

Fig. 60 shows the MOM tsunami inundation affecting Marco Island mapping area. Overall the barrier island provides ample protection for the mainland against tsunami inundation. While inundation depth at the barrier island ranges from 1 to over 3 m from the lee side to the GOM, the wetlands behind the island is mostly less than 1.3 m. Specifically, worst case scenario (MOM) inundation depth higher than 3 m mostly occurs on the beach. Larger than 2 m inundation can be expected in those communities adjacent to the beach (approximately within 1 km inland of the beach). The Mississippi Canyon landslide is responsible for the MOM inundation (see Fig. 61).

The hurricane category which best matches the tsunami inundation in this area is shown in Fig. 66. $\Delta\zeta$ for the best-match hurricane category satisfying Eq. 1 is shown in Fig. 67. The matching hurricane category distribution closely reflects that of tsunami inundation. Category 3 is only seen on a few scattered spots on the barrier island beach, and the majority of the barrier islands are between Category 2 and 1. The difference between hurricane flooding and tsunami inundation $\Delta\zeta$ is generally within $\pm$ 0.5 m for the barrier islands, however, on the wetlands between Marco Island and the mainland the difference reaches larger than 1 m, which means storm surge inundation depth is higher since tsunami waves generally cannot reach as far into the bays.

Marco Island, FL
All Sources
SLOSH Storm Surge and MOM Tsunami Inundation Comparison

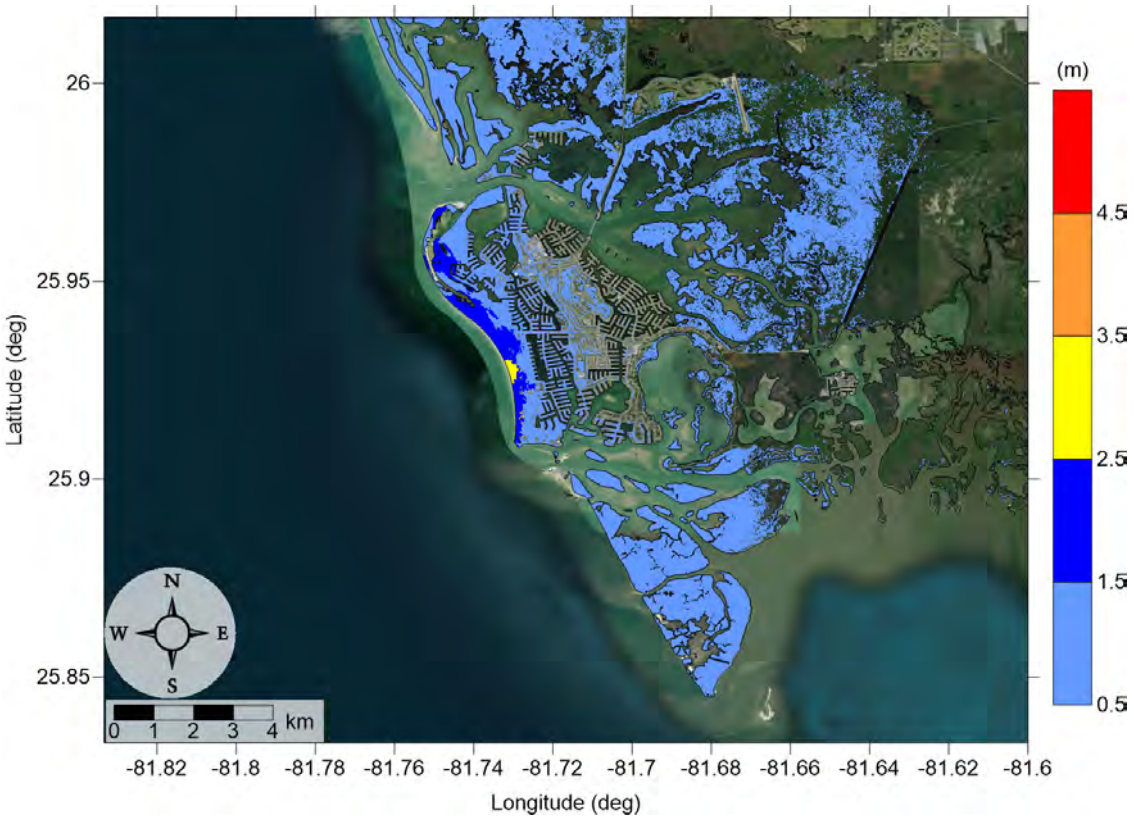

Figure 66: Hurricane category which produces inundation at high tide that best matches the MOM tsunami inundation shown in Figure 67 for Marco Island, FL. The contours drawn and labeled are at -5 m, -10 m, and -15 m levels.

Marco Island, FL
All Sources
SLOSH Storm Surge and MOM Tsunami Inundation Comparison

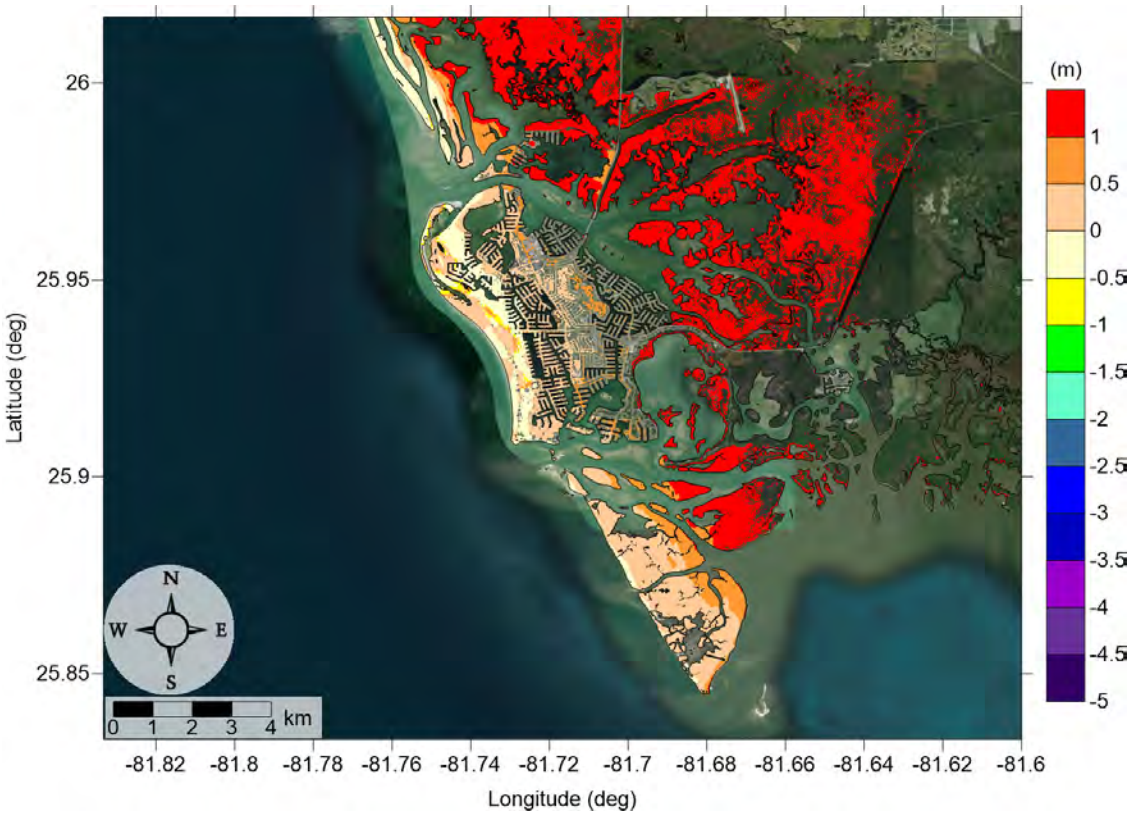

Figure 67: Actual difference $\Delta\zeta$ (in meters) between SLOSH MOM storm surge inundation and MOM tsunami inundation for the best-match hurricane category shown in Figure 66 for Marco Island, FL. Note that negative values indicate where tsunami inundation is higher than hurricane inundation, and pale colors indicate relatively good agreement between tsunami and storm surge inundation, i.e. $|\Delta\zeta| \leq 0.5$ m. The contours drawn and labeled are at -5 m, -10 m, and -15 m levels.

6 Tsunami Maritime Products

Accurate estimates of tsunami wave amplitude do not necessarily equate to the prediction of localized damaging currents in a basin or harbor [Lynett et al., 2012]. Furthermore, damage potential in ports is strongly related to the current speed. Therefore, tsunami hazard mitigation products need to be advanced to predict damage potential in basins or harbors. Past tsunamis have shown that the maritime community requires additional information and guidance about tsunami hazards and post-tsunami recovery [Wilson et al., 2012, 2013]. To accomplish mapping and modeling activities to meet NTHMP's planning/response purposes for the maritime community and port emergency management and other customer requirements, it is necessary to continue the process to include maritime products in our current inundation map development. These maritime products will help identify impact specifically on ship channels, bay inlets, harbors, marinas, and oil infrastructures (e.g., designated lightering and oil tanker waiting zones).

In this study, Don Pedro Island-Boca Grande-Captiva Island, FL and Marco Island, FL are added to the maritime portfolio, where tsunami hazard maritime products such as tsunami current magnitude, vorticity, safe/hazard zones are generated.

Lynett et al. [2014] complied a general relationship between tsunami current speed and harbor damage based on observational data, in which the current speed is divided into four ranges of damaging potential, 0 - 3 knots means unharmful currents, 3 - 6 knots corresponds to minor-to-moderate damage, 6 - 9 knots moderate-to-major damage, and over 9 knots extreme damage. Since the extent of damage is very location-dependent, to make the text concise, we associate 0 - 3 knots to unharmful currents, 3 - 6 knots to minor damage, 6 - 9 knots to moderate damage, and finally over 9 knots to major damage. The four levels are denoted with white, blue, yellow and red colors, respectively, for all the velocity contour plots within our velocity maritime products.

Using this damage-to-speed relationship, we have plotted the maximum of maximum depth-averaged velocity for each computational subdomain of the two new communities. Fig. 68 shows the minimum offshore safe depth (approximately 200 m or 100 fathoms), and the maximum of maximum velocity magnitude contour plot across the entire Gulf of Mexico (15 arcsecond resolution) for all landslide scenarios (Eastbreaks, PSL-A, PSL-B1, PSL-B2, Mississippi Canyon, PSL-C, West Florida, Yucatán #3 and Yucatán #5). Potential damaging currents ($>$ 3 knots, blue, yellow and red areas) tend to be present in most of the area shallower than the minimum offshore safe depth. However, damaging currents could reach areas deeper than 200 m close to most of the landslide generation regions. Major damaging currents ($>$ 9 knots, red) can be expected in most of the landslide generation regions, in the continental shelf adjacent to Mississippi Canyon, offshore northwest Florida, and Yucatán shelf. Moderate ($>$ 6 knots and $<$ 9 knots, yellow) damaging current areas are scattered over the continental shelf, but mostly close to areas with major damage currents.

All locations
All Sources
Maximum of Maximum Velocity Magnitude

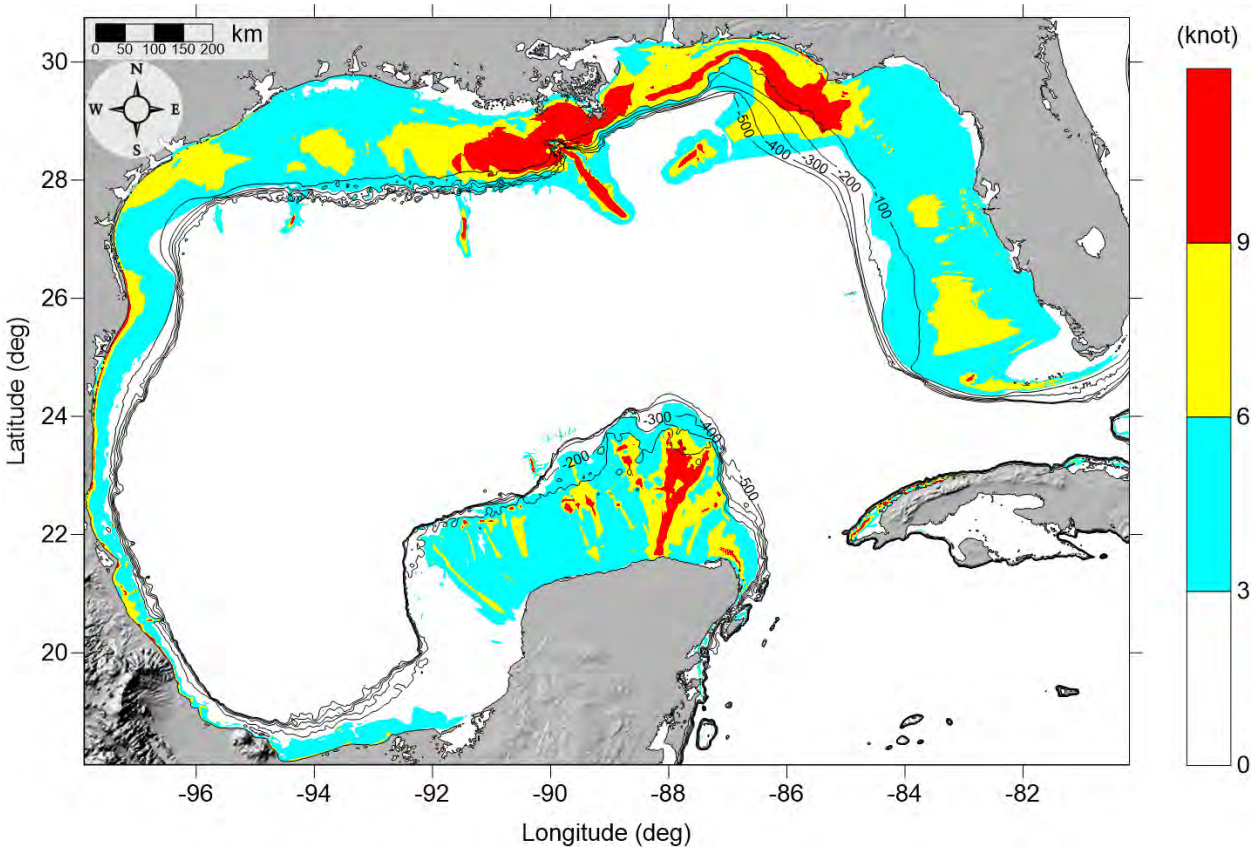

Figure 68: Maximum of maximum velocity magnitude contour in GOM for all landslide scenarios and all locations.

The MOM velocity magnitude (damaging potential) contour maps and the MOM vorticity magnitude contour maps for the finer computational subdomains of Don Pedro Island-Boca Grande-Captiva Island, FL and Marco Island, FL are presented from Fig. 69 to Fig. 80.

General trends can be observed from the different grid levels of the MOM velocity. Most of offshore region is expected to have minor damaging currents, with moderate damaging currents occurring along the coastline and jetties. Fig. 71 and Fig. 72 shows the MOM velocity magnitude contour plot result for the Don Pedro Island-Boca Grande-Captiva Island area. There is no moderate damaging currents behind the barrier islands, however, it can reach over 9 knots (major damaging current) near the bay entrances both north and south of Boca Grande and the Redfish Pass.

In Marco Island, FL, the situation is different from Don Pedro Island-Boca Grande-Captiva Island, FL. In general, tsunami currents are less severe; there are very few major damaging current locations and moderate damaging current area is much smaller.

Vorticity distribution, on the other hand, displays similar patterns between the two locations, where high vorticity appears around the barrier island, and are more intense near the bay entrances.

6.1 Don Pedro Island-Boca Grande-Captiva Island, FL

Don Pedro Island-Boca Grande-Captiva Island, FL
All Sources
Maximum of Maximum Velocity Magnitude

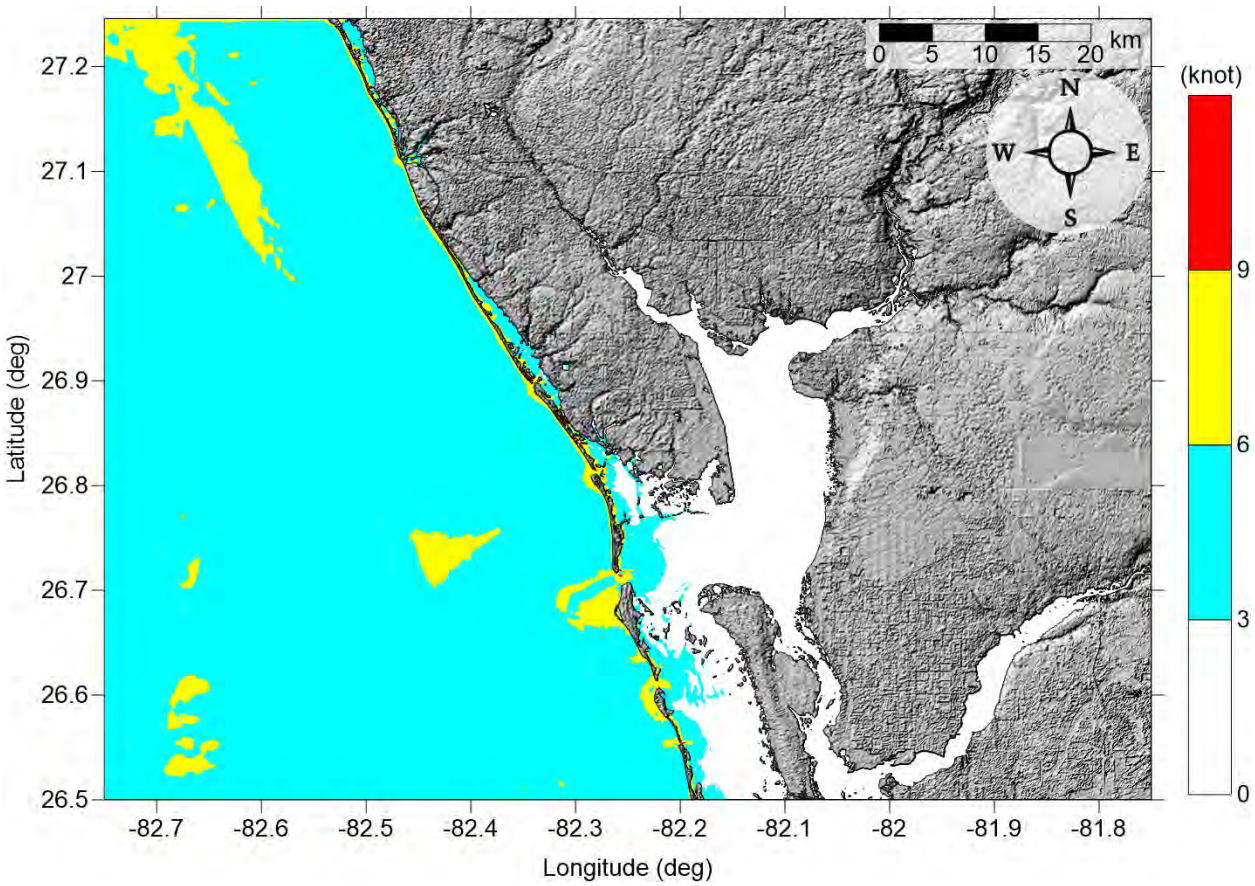

Figure 69: Maximum of maximum velocity magnitude contour in Don Pedro Island-Boca Grande-Captiva Island, FL (Grid 2 - 3 arcsecond) for all landslide scenarios.

Don Pedro Island-Boca Grande-Captiva Island, FL
All Sources
Maximum of Maximum Velocity Magnitude

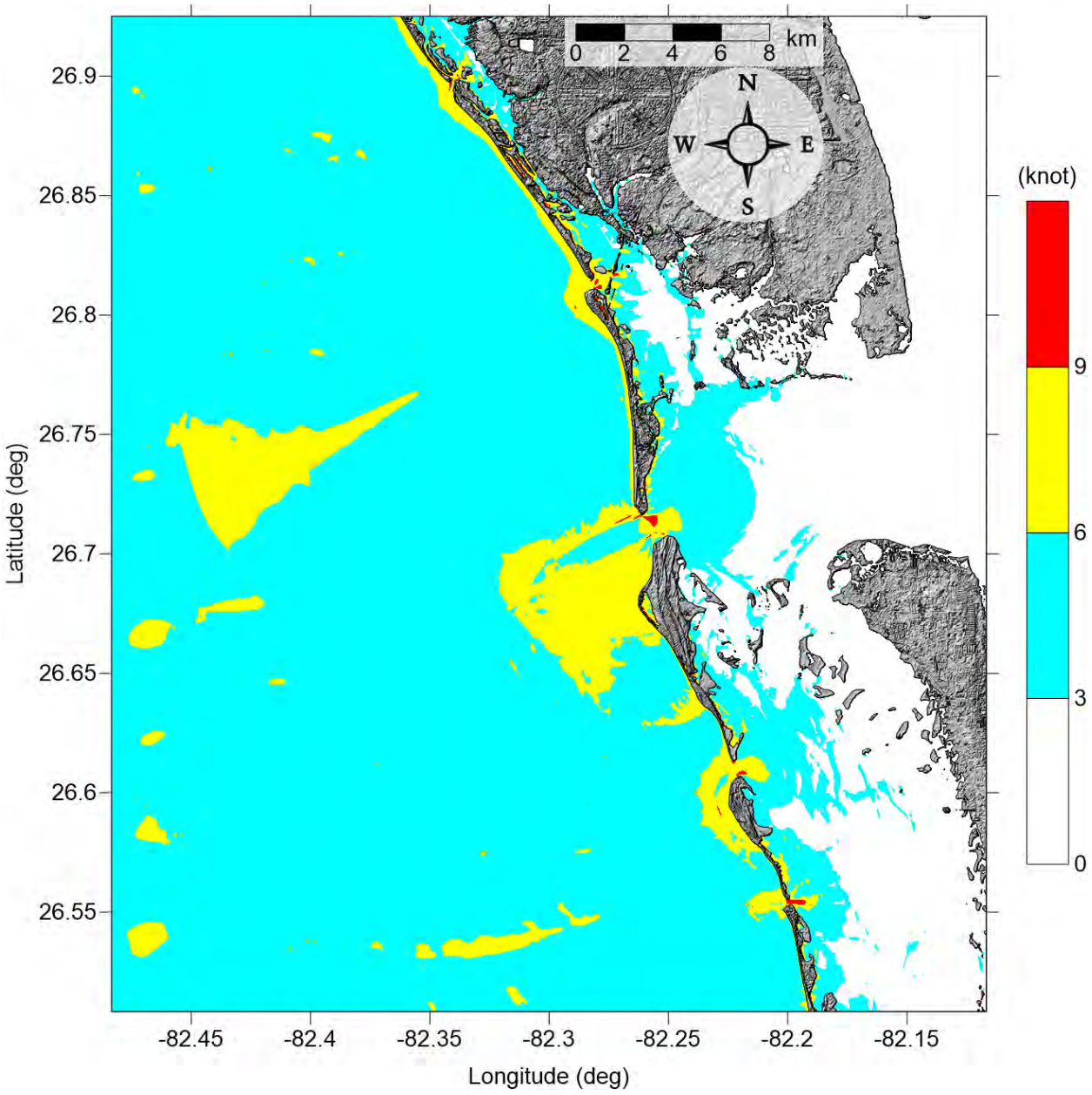

Figure 70: Maximum of maximum velocity magnitude contour in Don Pedro Island-Boca Grande-Captiva Island, FL (Grid 3 - 1 arcsecond) for all landslide scenarios.

Don Pedro Island-Boca Grande-Captiva Island, FL
All Sources
Maximum of Maximum Velocity Magnitude

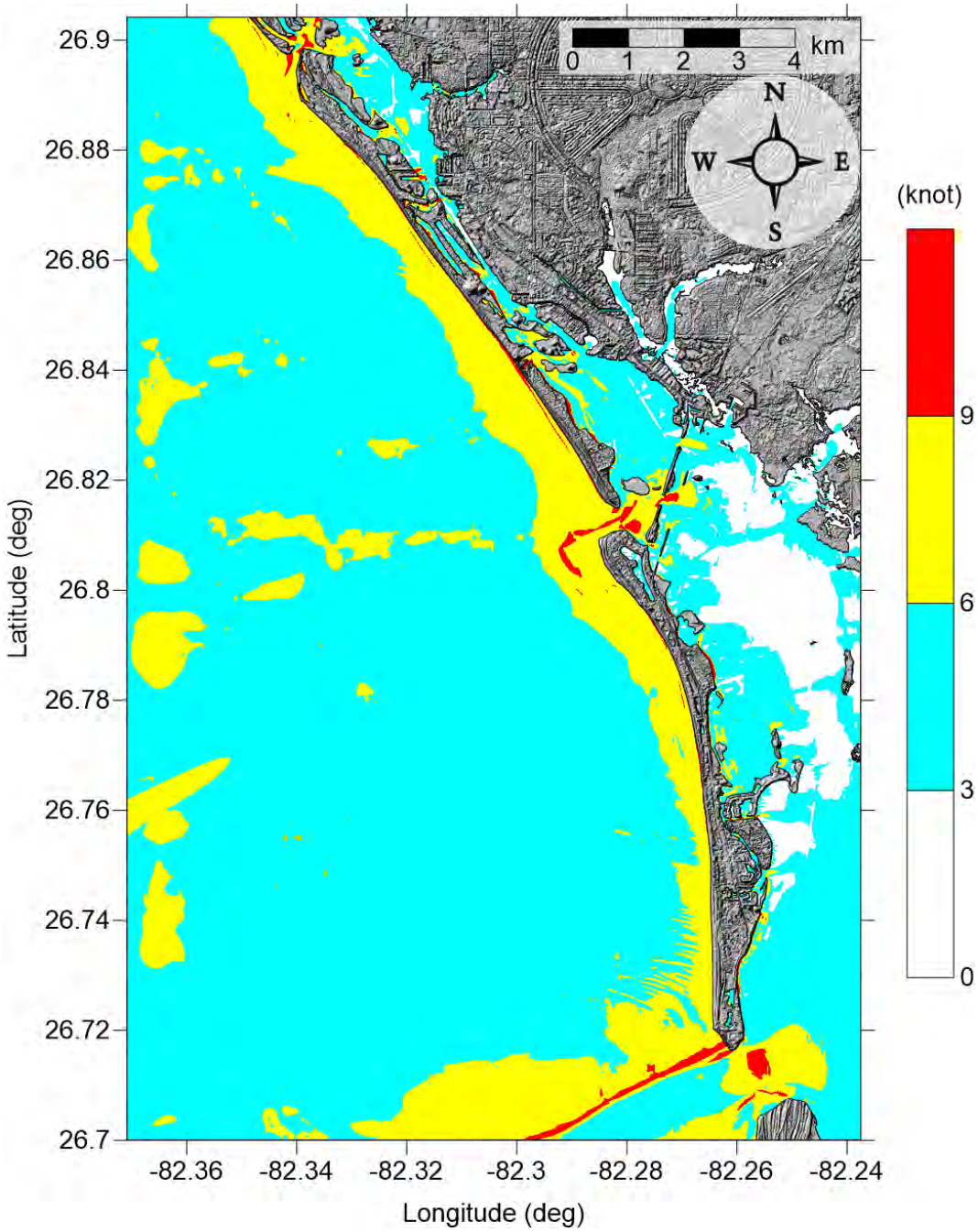

Figure 71: Maximum of maximum velocity magnitude contour in Don Pedro Island-Boca Grande, FL (Grid 4 - 1/3 arcsecond) for all landslide scenarios.

Don Pedro Island-Boca Grande-Captiva Island, FL
All Sources
Maximum of Maximum Velocity Magnitude

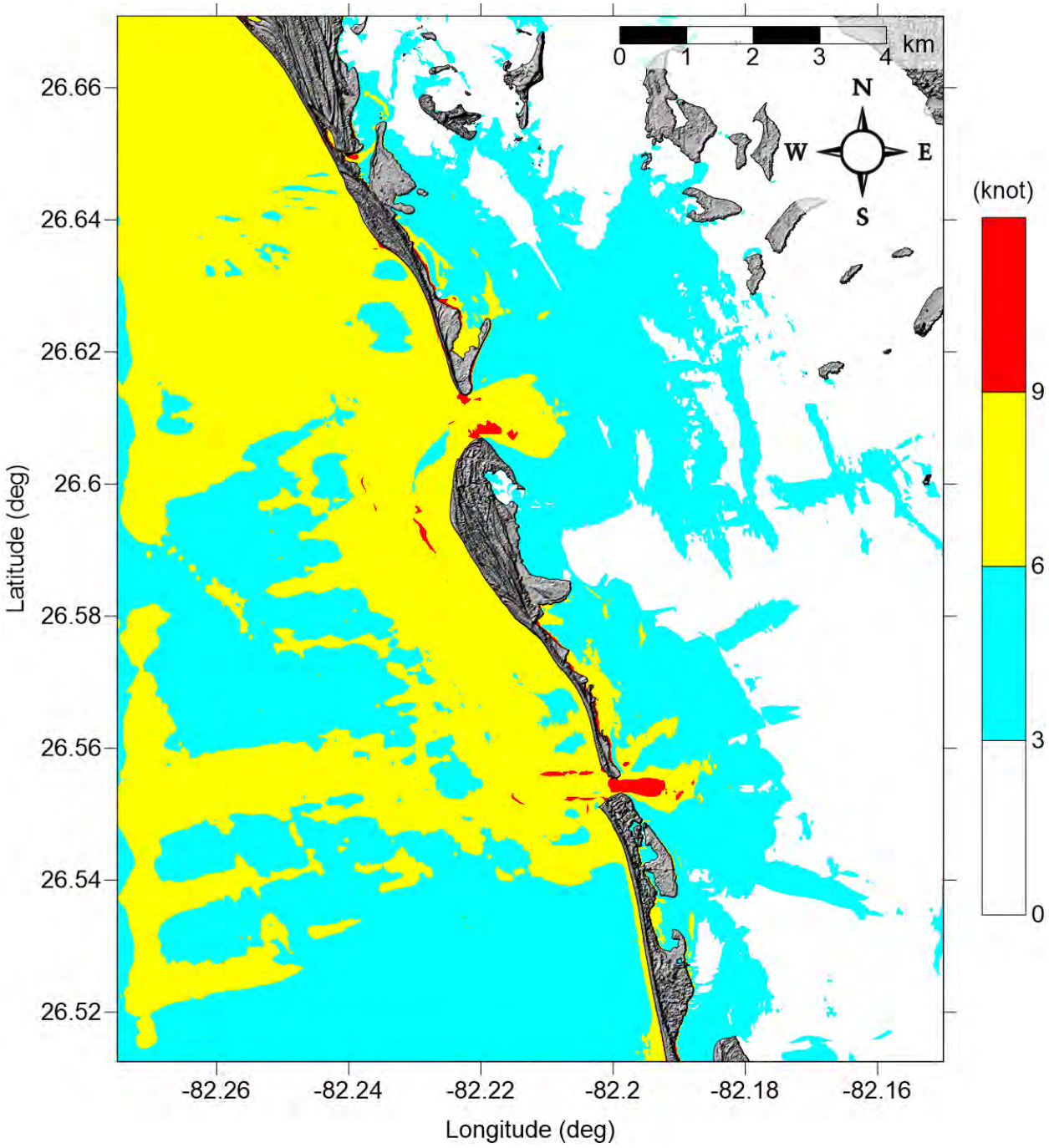

Figure 72: Maximum of maximum velocity magnitude contour in Captiva Island, FL (Grid 5 - 1/3 arcsecond) for all landslide scenarios.

Don Pedro Island-Boca Grande-Captiva Island, FL
All Sources
Maximum of Maximum Vorticity Magnitude

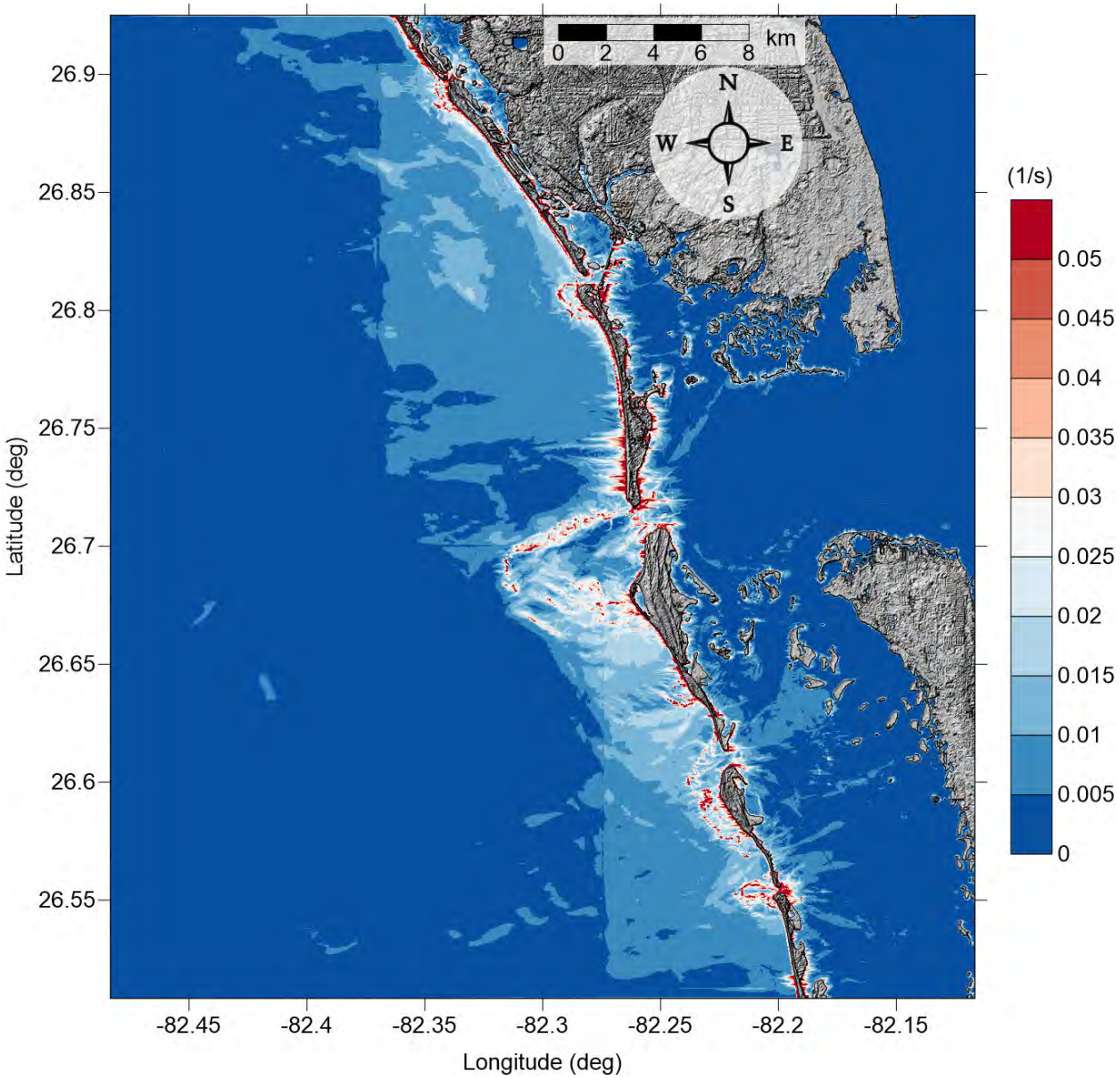

Figure 73: Maximum of maximum vorticity magnitude contour in Don Pedro Island-Boca Grande-Captiva Island, FL Grid 3 (1 arcsecond) for all landslide scenarios.

Don Pedro Island-Boca Grande-Captiva Island, FL
All Sources
Maximum of Maximum Vorticity Magnitude

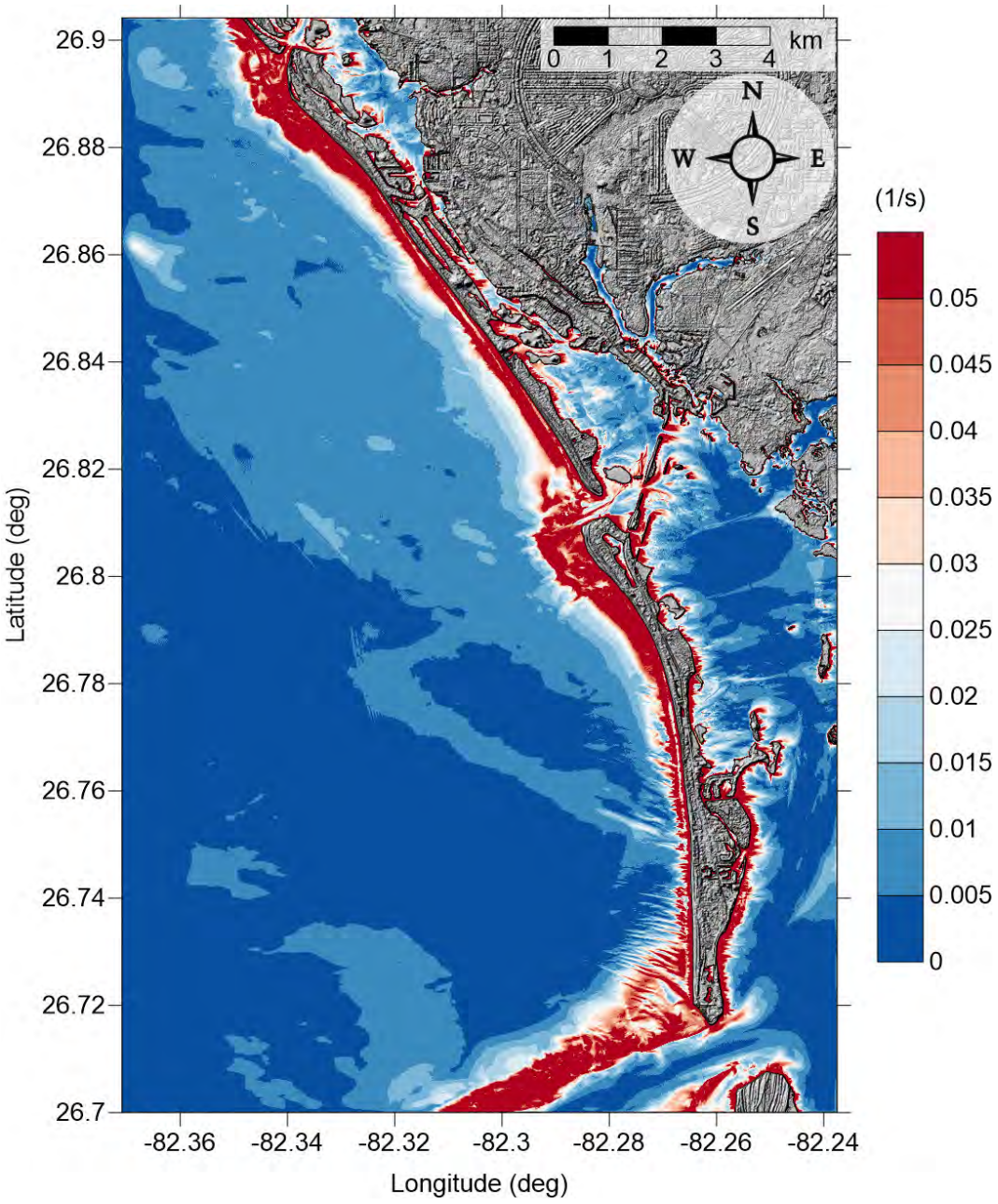

Figure 74: Maximum of maximum vorticity magnitude contour in Don Pedro Island-Boca Grande, FL Grid 4 (1/3 arcsecond) for all landslide scenarios.

Don Pedro Island-Boca Grande-Captiva Island, FL
All Sources
Maximum of Maximum Vorticity Magnitude

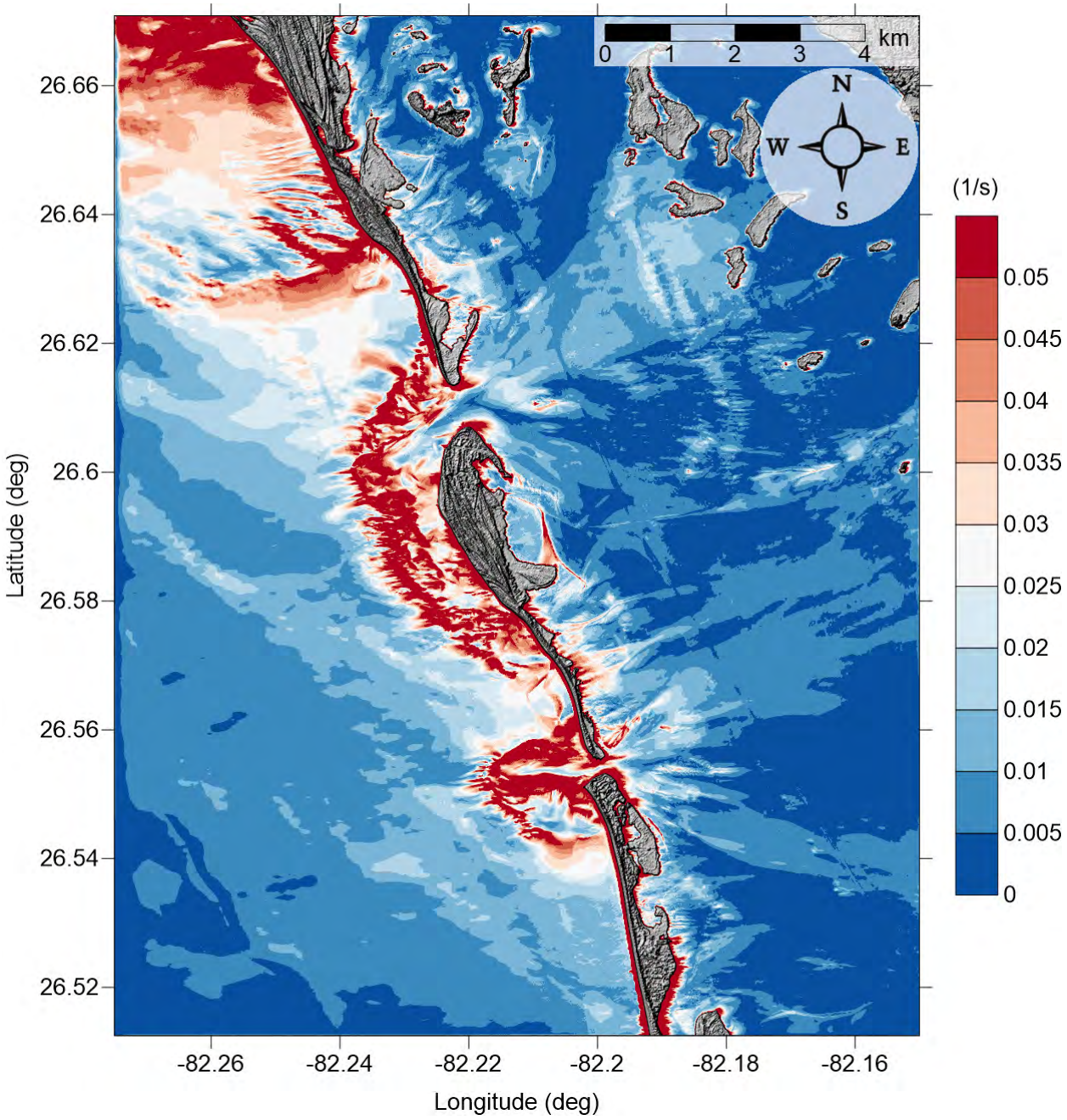

Figure 75: Maximum of maximum vorticity magnitude contour in Captiva Island, FL Grid 5 (1/3 arcsecond) for all landslide scenarios.

6.2 Marco Island, FL

Marco Island, FL
All Sources
Maximum of Maximum Velocity Magnitude

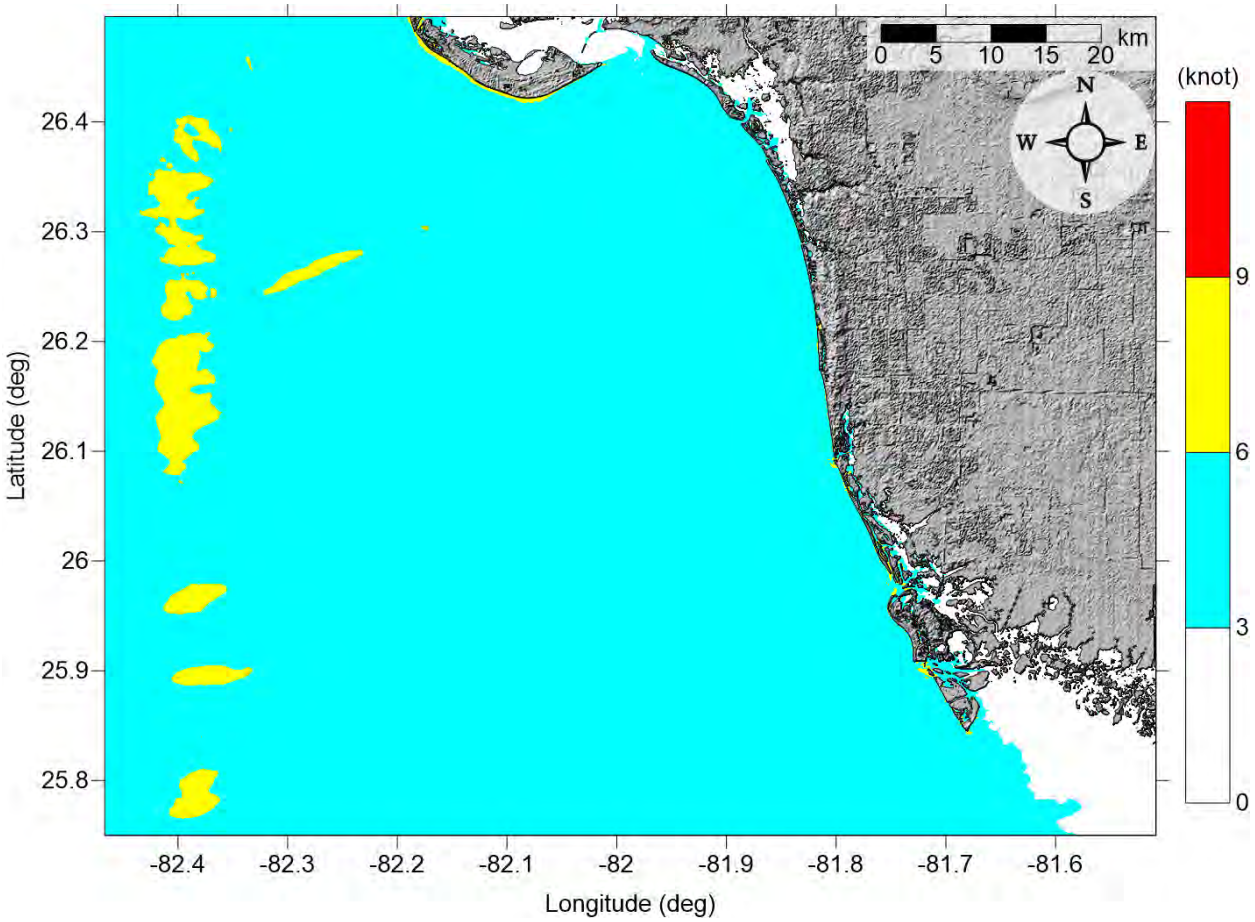

Figure 76: Maximum of maximum velocity magnitude contour in Marco Island, FL (Grid 2 - 3 arcsecond) for all landslide scenarios.

Marco Island, FL
All Sources
Maximum of Maximum Velocity Magnitude

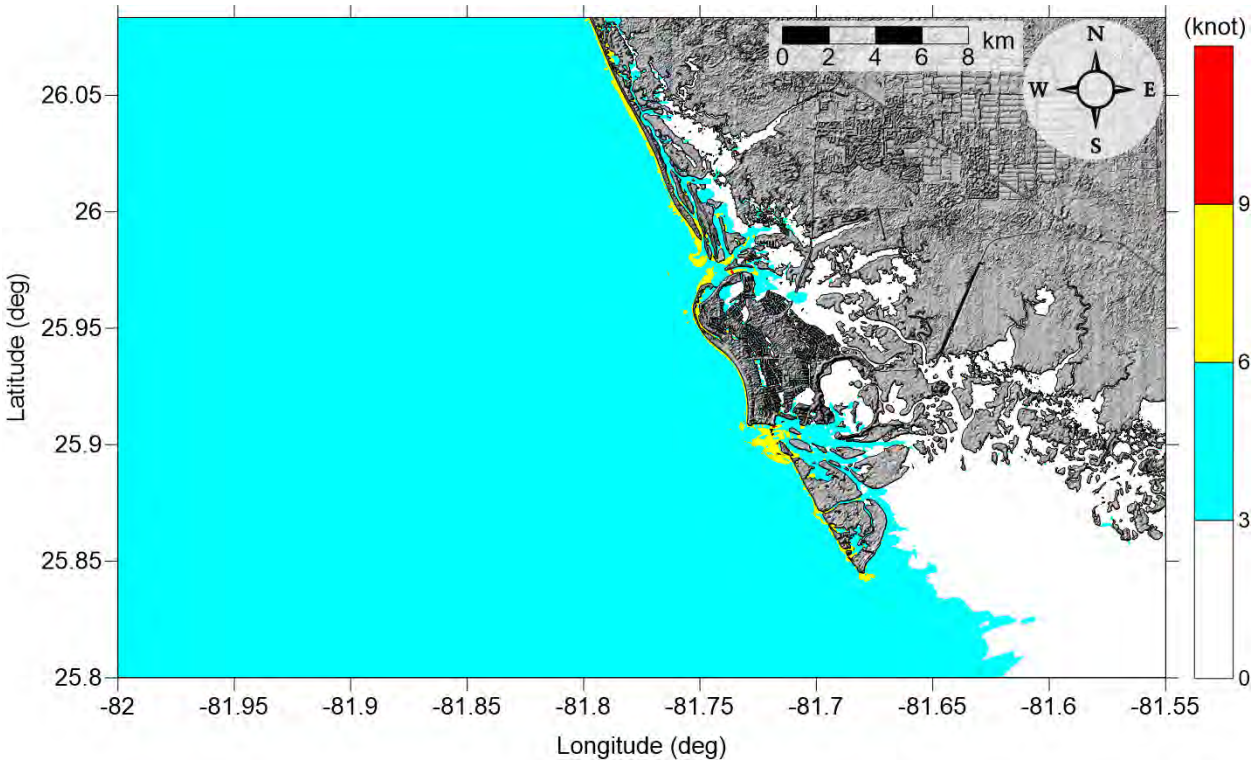

Figure 77: Maximum of maximum velocity magnitude contour in Marco Island, FL (Grid 3 - 1 arcsecond) for all landslide scenarios.

Marco Island, FL
All Sources
Maximum of Maximum Velocity Magnitude

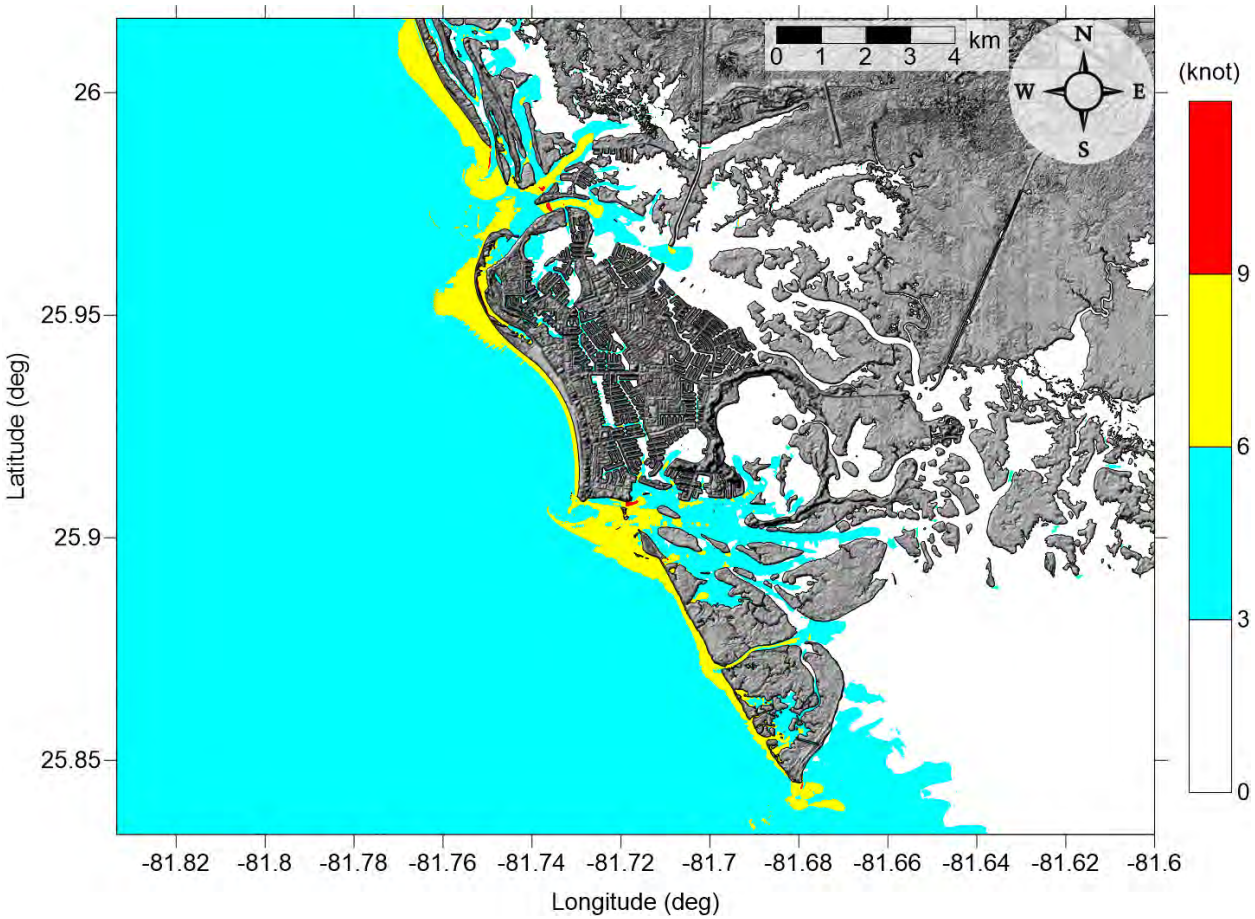

Figure 78: Maximum of maximum velocity magnitude contour in Marco Island, FL (Grid 4 - 1/3 arcsecond) for all landslide scenarios.

Marco Island, FL
All Sources
Maximum of Maximum Vorticity Magnitude

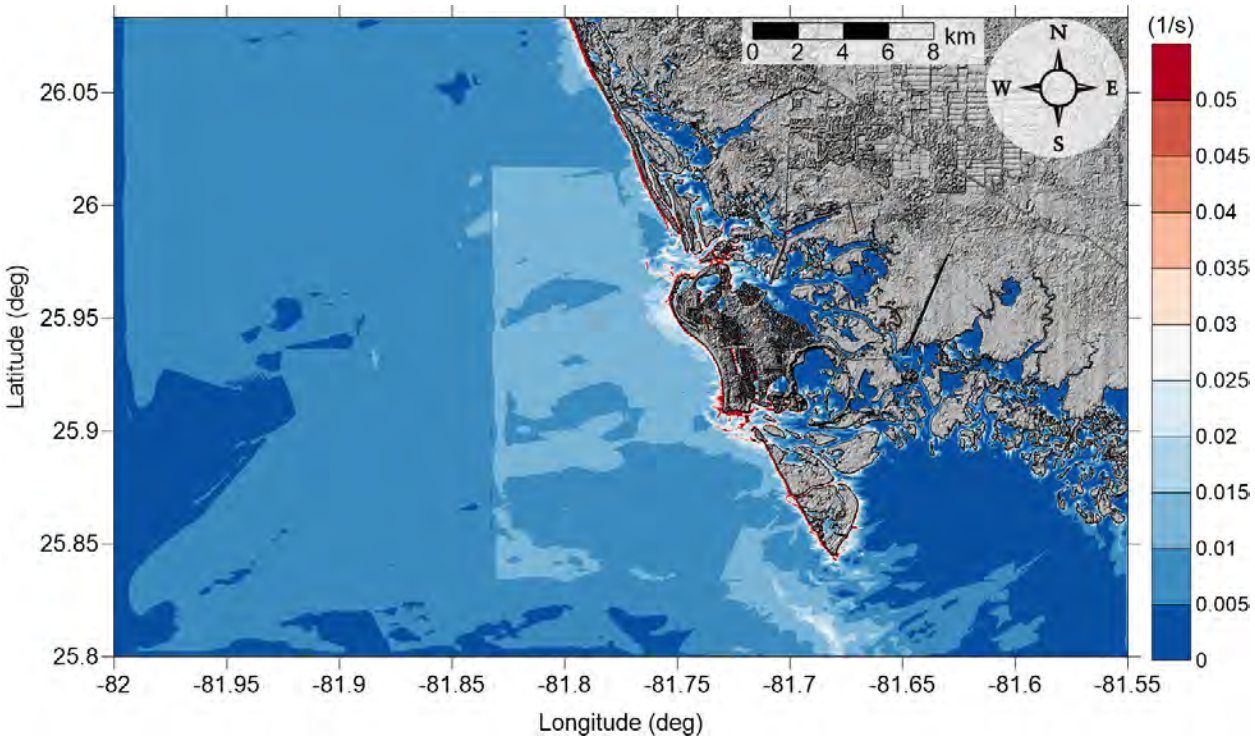

Figure 79: Maximum of maximum vorticity magnitude contour in Marco Island, FL Grid 3 (1 arcsecond) for all landslide scenarios.

Marco Island, FL
All Sources
Maximum of Maximum Vorticity Magnitude

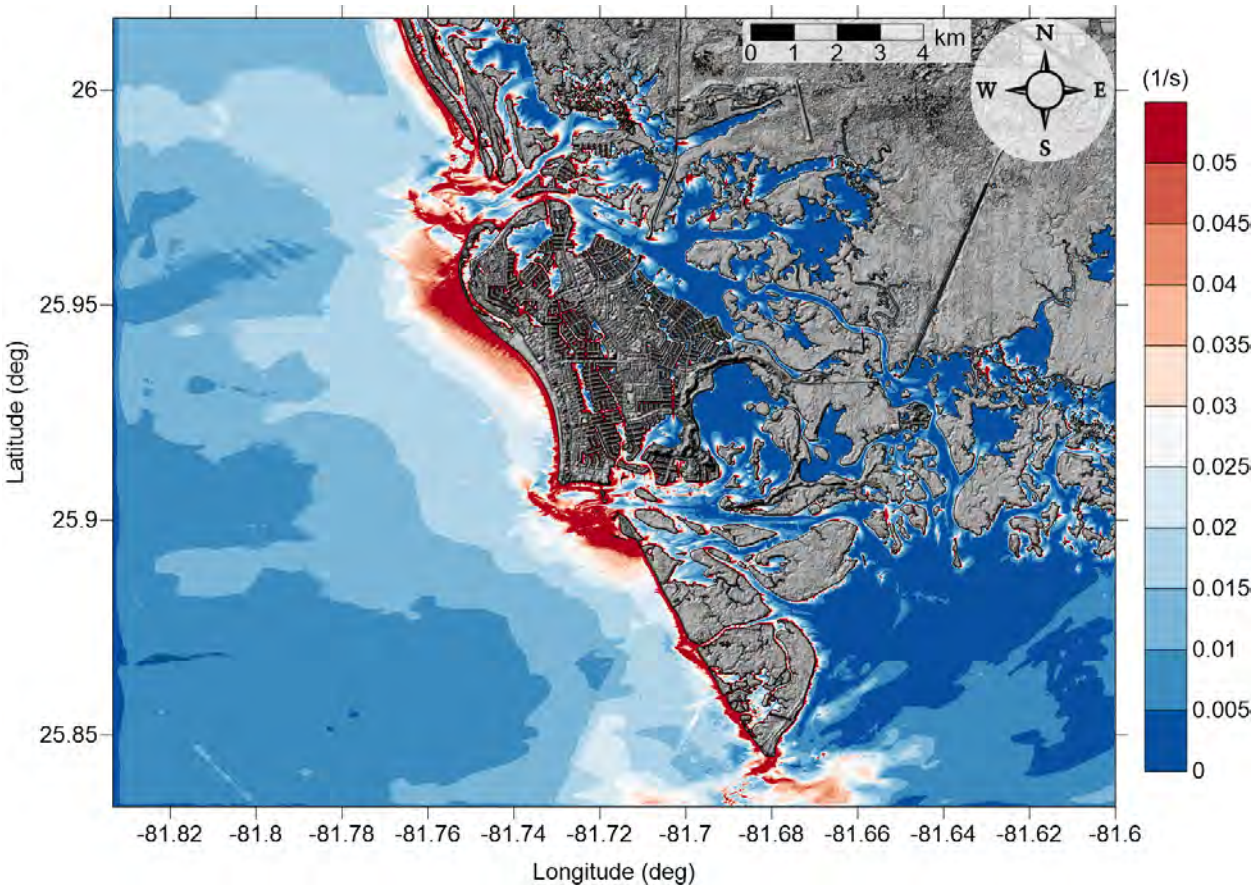

Figure 80: Maximum of maximum vorticity magnitude contour in Marco Island, FL Grid 4 (1/3 arcsecond) for all landslide scenarios.

7 Meteosunami Risk Analysis in Northwestern GOM

Although relatively rare, meteotsunamis are capable of causing coastal infrastructure damage and casualties. Analyses of water level and meteorological data in the U.S. show that meteotsunamis occur more frequently than expected, and therefore, it is important to include meteotsunami assessment in coastal hazard mitigation efforts. In this study, we conducted numerical experiments to investigate the generation and propagation of meteotsunami waves and assessed hazards on a broad scale in the northwestern Gulf of Mexico (GOM), as a continuation from northeastern GOM studies [Cheng et al., 2021, Horrillo et al., 2020]. The numerical experiments used a simple 2D depth-averaged hydrostatic shallow water model forced by an idealized atmospheric pressure disturbance on a set of trajectories and directions (1260 runs) covering the whole northwestern GOM shelf. The disturbance parameters are based on a 2010 event that generated strong meteotsunami along the Florida GOM coast. Results show that Louisiana coasts are less likely to be hit with a high meteotsunami wave than Texas, and that the convex sections of Texas coastline are more susceptible to meteotsunami waves coming from various directions. Statistical analysis indicates that pressure disturbances coming from south – east direction result in higher water level in this region. The forward speed distribution shows that 20 m/s – 25 m/s have the most potential. These results can help identify vulnerable coastal regions and pressure disturbance scenarios that most likely generate higher meteotsunami waves.

7.1 Introduction

Meteotsunamis are long waves having meteorological origins such as atmospheric gravity waves, frontal passages, squalls, and storms, which typically exhibit large pressure and/or wind-stress gradient [Monserrat et al., 2006]. Similar to ordinary tsunamis, i.e. those generated by earthquakes or landslides, meteotsunamis have periods from a few minutes to 2-3 hours. Meteotsunamis cannot be distinguished from ordinary tsunamis in terms of coastal transformation and amplification within bays and harbors [Rabinovich and Monserrat, 1996], however, they differ in that meteotsunami wave generation requires resonant coupling between the atmospheric disturbance and the shelf, otherwise sea level fluctuations would be on the order of a few centimeters solely due to the inverse barometric effects. The resonance mechanisms have been thoroughly studied, including the Proudman resonance [Proudman, 1929], Greenspan resonance [Greenspan, 1956], and shelf resonance [Monserrat et al., 2006]. Proudman resonance occurs when the pressure disturbance forward speed matches the local shallow water wave celerity, ideally traveling over a long distance, which is analogous to tsunamis generated by landslides [Monserrat et al., 2006]. In addition to the resonant coupling between the air disturbance and shelf, the generated meteotsunami could be further enhanced by shoaling effects and local harbor resonance.

Meteotsunami events have been reported to occur in oceans around the globe. The most prominent places include Mediterranean Sea, for example the Adriatic Sea and Balearic Sea; Nagasaki Bay, Japan and Longkou, China; in North America, the Great Lakes and the Atlantic coasts [Monserrat et al., 2006, Vilibić et al., 2014b, Pattiaratchi and Wijeratne, 2015]. Although meteotsunamis cannot reach the level of destruction of seismic tsunamis [Pat-

tiaratchi and Wijeratne, 2015], their damaging potential should not be ignored. Regarding the GOM, there have been several documented meteotsunami events in recent decades with wave height close to or over 1 m [Rabinovich, 2020]. On March 25, 1995, eye witnesses at Tampa Bay, Florida reported a solitary wave up to 3 m high moving southeastward followed by a line of clouds 15 min later that was generated by a large-amplitude atmospheric gravity wave [Paxton and Sobien, 1998]. On March 28, 2014, Panama City saw a sea level rise of 1.3 m. The meteotsunami wave was reported across the northwestern GOM from New Canal, Louisiana to Naples, Florida, which was caused by a squall-line initially traveling eastward along the coastline and thus moving in-phase with the wave [Olabarrieta et al., 2017]. A sharp drop in barometric pressure accompanying a south-moving frontal system over the Naples shelf resulted in a maximum wave height of 0.92 m on January 11, 2012, the largest meteotsunami on the southwestern coast of Florida between 2007 and 2015 [Paxton, 2016]. A 1.5 m high meteotsunami damaged coastal infrastructure near Naples, Captiva and Sanibel Islands in southwestern Florida on December 20, 2018, which was associated with a cold front bringing sudden temperature and pressure changes [Rabinovich, 2020].

In addition to these notable events, meteotsunamis occur much more frequently than expected. Olabarrieta et al. [2017] analyzed water level, atmospheric pressure, wind speed/direction and radar reflectivity data of three open water NOAA gauges from 1996 to 2016, and discovered that there are around 20 meteotsunami events on average in the above three locations. This result should not come as a surprise as the GOM is a region where tropical cyclones and winter storms occur frequently. However, only $1-3$ of the 20 events at each location exceeds 0.5 m. In addition, Shi et al. [2020] showed that meteotsunamis are frequently triggered by Tropical Cyclone Rainbands via a study of Atlantic hurricanes landfalling in the GOM over a 20 year span. Similar studies on the Great Lake show that there is an annual water level of 0.83 m and 10-year return water level of 1.3 m, which demonstrates that meteotsunamis as severe as the 1954 Chicago event occur more frequently than is normally thought [Bechle et al., 2016]. Along the U.S. east coast, a total of 548 meteotsunamis were recorded from 1996 to 2017 with wave height of 30 cases exceeding 0.6 m [Dusek et al., 2019].

Since these studies of past events in the U.S. all utilize NOAA tide gauges which are mostly not positioned in open oceans, they may not always capture a meteotsunami event. Moreover, these gauges may not have recorded the maximum wave [Dusek et al., 2019] because of their sparsity. Numerical modeling is often employed to bridge the gap when there is not enough data, in order to gain a better understanding of the generation, propagation, and inundation processes during meteotsunami events, which can help recreate historical events, predict potential vulnerable locations, and ultimately contribute to hazard mitigation.

There has been a plethora of numerical meteotsunami studies near the Mediterranean Sea, for example: In order to mitigate meteotsunami hazards, Šepić and Vilibić [2011] created a meteotsunami warning system by constructing a warning matrix based on previous events, theoretical estimations and numerical modelling. To investigate the generation, amplification and propagation properties of meteotsunamis in the Balearic Sea, Ličer et al. [2017] applied nested ocean modelling system (ROMS) forced by synthetic atmospheric gravity waves, and quantified the contribution of Mallorca shelves and Menorca Channel to meteotsunami intensity, and analyzed subcritical and supercritical propagation conditions. Kim and Omira [2021] identified meteotsunami hazard hot spots along the coast of Portugal using a series of

idealized numerical simulations with comparison to observed data.

In the U.S., there has been more modeling development in the Great Lakes since this region has relatively high meteotsunami occurrence. Anderson et al. [2015] showed the importance of wave reflection, focusing, and edge wave formation in enclosed basin via numerical reconstruction of the May 27, 2012 Lake Erie event. Later, Linares et al. [2016] conducted numerical experiments with different disturbance speeds and directions on northern Lake Michigan using a 3D Reynolds-averaged Navier-Stokes model, and found out that wind and pressure have similar contribution to meteotsunami hazard. For the U.S east coast, the destructive 2008 Boothbay event sparked interests from the research community [Vilibić et al., 2014b]. Whitmore and Knight [2014] and Vilibić et al. [2014a] both simulated the Boothbay meteotsunami for the purpose of the development of a meteotsunami warning system. Similar effort on numerical development was carried out in the GOM. Shi et al. [2019] employed the Coupled Ocean-Atmosphere-Waves-Sediment Transport (COAWST) modeling system and showed that tropical cyclone induced meteotsunami waves are more influenced by wind stress, and in contrast, during winter storms atmospheric pressure fluctuations dominate wave generation, especially at depth deeper than 40 m.

In Horrillo et al. [2020] and Cheng et al. [2021], we studied the generation and propagation/amplification patterns of meteotsunami waves in northeastern GOM and identify coastal communities vulnerable to meteotsunami inundation through a suite of idealized numerical experiments using parameters based on a real event. To continue with the meteotsunami effort in the GOM, this project performs similar investigations on the northwestern GOM (Texas and Louisiana coasts). Section 7.2 introduces our meteotsunami numerical scheme, grid and gauge setup. Section 7.3 derives air pressure disturbance parameters from a historical meteotsunami event in the GOM using an idealized exponential decay function, and examines the generation and propagation of the resultant waves. Section 7.5 further extends the parameter space by changing incident direction (from 0° to 330°, at 30° intervals) of the disturbance, for a total number of 1260 ($12 \times 15 \times 7$) runs. This suite of maximum water level results depicts the meteotsunami hazard distribution in the northwestern GOM by incorporating favorable directions for each community. Statistical analysis is performed to show the directions and speeds that cause large meteotsunami impacts.

7.2 Numerical model description

The numerical model utilized in this study is a 2D hydrostatic model in spherical coordinates built on the nonlinear shallow water equations. The governing equations, staggered grid setup, and numerical solution scheme are based on Kowalik et al. [2005]. In order to simulate meteotsunamis driven by atmospheric pressure disturbances, the momentum equations are modified to include spatially-dependent surface air pressure in addition to the hydrostatic pressure. Wind stress and astronomical tide contributions are not included in the equations.

The governing equations are derived from the incompressible Navier-Stokes equation and the incompressibility condition of the continuity equation in a spherical coordinates system in which λ is the longitude, ϕ is the latitude, and z denotes the normal distance from the still water level (SWL). The momentum equations along λ and ϕ directions are:

$$\frac{\partial U}{\partial t} + \frac{U}{R\cos\phi}\frac{\partial U}{\partial \lambda} + \frac{V}{R}\frac{\partial U}{\partial \phi} - \left(2\Omega + \frac{U}{R\cos\phi}\right) V\sin\phi = -\frac{g}{R\cos\phi}\frac{\partial \zeta}{\partial \lambda} - \frac{1}{\rho R\cos\phi}\frac{\partial p}{\partial \lambda} - n^2\frac{g}{D^{1/3}}\frac{U\sqrt{U^2+V^2}}{D} \tag{2}$$

$$\frac{\partial V}{\partial t} + \frac{U}{R\cos\phi}\frac{\partial V}{\partial \lambda} + \frac{V}{R}\frac{\partial V}{\partial \phi} + \left(2\Omega + \frac{U}{R\cos\phi}\right) U\sin\phi = -\frac{g}{R}\frac{\partial \zeta}{\partial \phi} - \frac{1}{\rho R}\frac{\partial p}{\partial \phi} - n^2\frac{g}{D^{1/3}}\frac{V\sqrt{U^2+V^2}}{D}, \tag{3}$$

and the continuity equation is:

$$\frac{\partial \zeta}{\partial t} + \frac{1}{R\cos\phi}\frac{\partial (UD)}{\partial \lambda} + \frac{1}{R\cos\phi}\frac{\partial (VD\cos\phi)}{\partial \phi} = 0, \tag{4}$$

where U and V are depth-averaged velocity components in the λ and ϕ directions respectively. The variable t is the time, ζ is the free surface elevation from the SWL, R is the earth's radius, Ω is the earth's angular velocity, ρ is the water density, g is the gravitational acceleration and n is the Manning's coefficient for the sea-bottom friction (0.025 $\mathrm{sm}^{1/3}$). The total depth is defined as $D = \zeta + h_b$, where h_b is the water depth. p is the atmospheric disturbance pressure.

To investigate meteotsunami effects on a global scale, and identify local as well as distant meteotsunami source areas affecting the northwestern area of the GOM, a model domain that encompasses the entire GOM (18.1 to 30.75 N, 97.9 to 80.2 W) is used. The bathymetry data were created with the NOAA Etopo1 dataset [Amante and Eakins, 2009] and referenced to the mean high water. Longitudinal and latitudinal grid spacing are both one arc-minute which achieves reasonable simulation time and resolves the meteotsunami wavelength well. A coastal wall is set at a water depth of 0.3 m to avoid runup on the wide cells on land. Outflow conditions are applied to all the boundaries of the model domain. Through numerous model runs, we found that meteotsunamis affecting mostly the northwestern GOM originate from the same region, therefore, we decided to focus this study on the northwestern GOM to investigate regional meteotsunamis only. 34 wave gauges (interpolation from the nearest four grid points) are set up at approximately 5 m deep open water locations along the coastline of northwestern GOM for hazard assessment, which record water level and air pressure every 20 seconds.

7.3 Air pressure definition

In Feburary 2010, one of the most intense meteotsunami was recorded in Clearwater Beach, Florida. The $\sim$ 1 m wave height long wave was triggered by a dry season storm, which is common during winter in GOM where low pressure systems usually move eastward and squall lines develop ahead of cold fronts [Olabarrieta et al., 2017]. This squall line came off

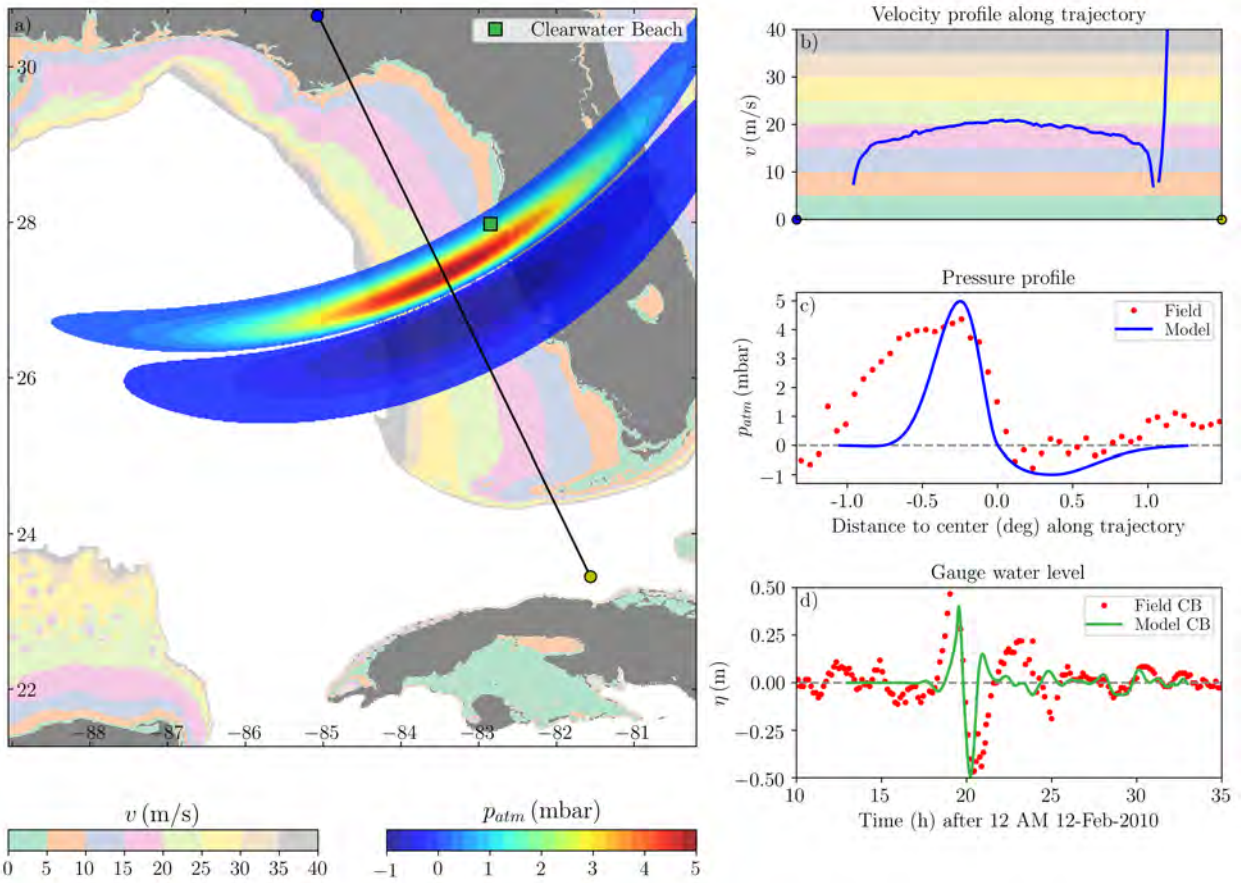

Figure 81: Model setup and Clearwater Beach gauge water level comparison for the Feb 12 2010 northern GOM meteotsunami. a) Meteotsunami atmospheric pressure contour plot and trajectory. Black solid straight line shows the trajectory on which pressure disturbance moves from the blue dot toward the yellow. Pressure contour is plotted with a lower cut-off at 0.05 mbar for both crest and trough, underneath which lies the contour of the continental shelf bathymetry expressed in terms of shallow water wave celerity $C = \sqrt{gh}$ from 0 – 40 m/s, where h is depth of ocean floor. b) Speed (shallow water wave celerity) profile along the trajectory. In this case, it follows the 20 m/s contour line. c) Air pressure profile along the trajectory, where the leading trough amplitude is 1 mbar and the crest amplitude 5 mbar. Pressure anomaly (de-tided) measurement data is from NOAA Clearwater Beach, FL station (ID: 8726724). d) De-tided water level records at NOAA Clearwater Beach (CB) gauge (dots) and model results starting at 10 am Feb 12 2010 UTC.

the Florida coast near Panama City and moved toward southeast along the isobath of the southwestern Florida shelf. A numerical representation of this event is shown in Figure 81a.

Based on radar reflectivity data from NOAA (see Figure 11 in reference Olabarrieta et al. [2017]), we constructed an idealized surface air pressure function where the amplitude of the crest A_c and trough A_t decay exponentially along both the length and width of the squall,

see Figure 81a and Equation 5,

$$P(x,y) = \begin{cases} A_c \cdot x \cdot exp\left(-(y)^2 - \left(\frac{x}{L_c}\right)^2\right), & x < 0 \\ A_t \cdot x \cdot exp\left(-(y)^2 - \left(\frac{x}{L_t}\right)^2\right), & x > 0 \end{cases}, \tag{5}$$

where (x, y) are the longitude and latitude excursions along length L, and L_c and L_t are the wavelength of the pressure crest and trough, respectively. The translation of the pressure disturbance is here simplified to a linear trajectory (single direction). Additionally, the pressure function is bent backwards (opposite of moving direction) to more realistically represent the geometry seen in the event, and is smoothed where crest and trough meet with quadratic stretching.

A customized ramping function (Equation 6) is applied to the beginning and ending of the atmospheric pressure forcing to avoid an abrupt entry or exit of the pressure disturbance. We found that 8 minutes (480 seconds) of ramping time was enough for a smooth transition. The inverse tangent function in Equation 6 is employed because of its asymptotic nature toward $x \to \pm\infty$.

$$\begin{aligned} f_{ramp} &= \frac{1}{2}\left(1 + \frac{tan^{-1}(12\frac{t'}{480} - 6)}{tan^{-1}(6)}\right) \\ t' &= \begin{cases} t, & 0 < t < 480 \\ t_{end} - t, & t_{end} - 480 < t < t_{end} \end{cases}, \end{aligned} \tag{6}$$

where t is in seconds, and t_{end} is the end time for air pressure presence.

7.4 Model benchmark results for the Feb 2010 Clearwater Beach meteotsunami

For this test case, the Etopo1 bathymetry is interpolated to a grid resolution of 15 arc-seconds to better resolve the generated waves. Figure 81 presents the model setup and result of the attempt to simulate the Feb 12, 2010 storm-induced meteotsunami.

The pressure disturbance profile parameters are estimated from NOAA Clearwater Beach, FL station (ID: 8726724) from 12 am Feb 12 to 12 am Feb 14 2010 with low frequency (period>6 h) pressure components filtered out (Figure 81c). We set crest amplitude A_c to be 5 mbar and trough amplitude A_t 1 mbar, and determined the lengths of crest L_c (0.7 deg) and trough L_t (1.05 deg) through trial-and-error until the simulated wave height reached close to 1 m. Our modeling pressure wave lengths are smaller than the field measurements, however, the Clearwater Beach pressure is likely very different in amplitudes and/or lengths than near Panama City where Proudman resonance started. Other parameters are estimated from NEXRAD reflectivity data (Figure 81a): Arc length R is 5 deg with 8 deg radius, and start and end coordinates of the pressure disturbance trajectory are (blue dot: 30.747 N, -85.107 W) and (yellow dot: 23.448 N, -81.562 W). Pressure disturbance forward speed is estimated to be 20 m/s and it takes $\sim$ 13.5 hours to complete the trajectory (cf. on methodology Sheremet et al. [2016]). Total run time is set to 20 hours to ensure that water

level fluctuations at all locations have settled down. The continental shelf bathymetry are also plotted, which is expressed in terms of shallow water wave celerity $C = \sqrt{gh}$ from 0 m/s to 40 m/s, at 5 m/s intervals. The trajectory is placed along the 15 m/s - 25 m/s band and the speed profile and the pressure profile along the trajectory are presented in Figure 81b and 81c, respectively.

The wave gauge recordings at Clearwater Beach is denoted with green line in Figure 81d alongside with NOAA de-tided water level data (dots), starting at 10 am Feb 12, 2010. Our simulation resulted in a long wave with $\sim$ 0.9 m wave height at Clearwater Beach, similar to the actual event. However, the period does not match well. The mismatch in wave period can be attributed to several factors. First, the pressure wave lengths and amplitudes are based on data collected at the station, instead of at the "source". The concept of a source is different from ordinary tsunamis in that meteotsunami waves are constantly receiving energy from air pressure disturbance throughout resonant regions, as explained thoroughly by Monserrat et al. [2006]. Second, radar reflectivity mosaic demonstrates great variability in squall line shape for the few hours leading up to the first wave. It is possible that the pressure wave length was much greater than the records at Clearwater Beach, and it can be seen changing directions. The lack of enough atmospheric measurement stations (globally) means that numerical representations of past events usually utilize idealized pressure shape [Rabinovich et al., 2021], which makes it impossible to accurately recreate the wave signal. Lastly, this simulation is designed to show that the model is capable of producing meteotsunami waves from the simplified pressure disturbance, and it was not intended to recreate the exact water level response. For a better recreation of this event, it requires a comprehensive model system that couples atmospheric, ocean, wave models, with high resolution bathymetry data.

The formation and propagation of meteotsunami waves are demonstrated in Sec. 4 (Fig. 2) from Cheng et al. [2021], and the influence of trajectory location and forward speed on wave elevation at the coastline are demonstrated in Sec. 5 (Fig. 3) from Cheng et al. [2021].

7.5 Northwestern GOM meteotsunami risk assessment

In order to study the influence of different incident directions and assess meteotsunami hazard under all possible scenarios, the parameter space covers the entire northwestern GOM with 12 incident directions that are illustrated in Figure 82a. The 12 directions are 0°, 30°, 60°, ..., and 330°, where 0° means the pressure originates from south and 90° means from west, etc., in a clockwise order. Under each incident direction scenario the same 15 trajectories and 7 speeds as Sec. 5 from Cheng et al. [2021] are used, thus there are a total of 1260 ($12 \times 15 \times 7$) cases.

Starting at gauge #2, data of all 1260 cases at every 3rd gauge are compiled into a rose diagram, which plots the maximum water level of the 105 (15×7) cases under each incident direction. Besides, maximum water level recorded from all events at each gauge are also shown at their sites with circles in corresponding size and color. Take gauge #14 for instance, there is less than $\sim$0.2 m wave resulting from pressure disturbance coming from north and west, whereas it can reach over 0.4 m from the east (including northeast and southeast) and the rest lie in the middle at around 0.3 m. Similarly for gauge #29, the only high waves are brought by meteotsunamis traveling from the northwest, because

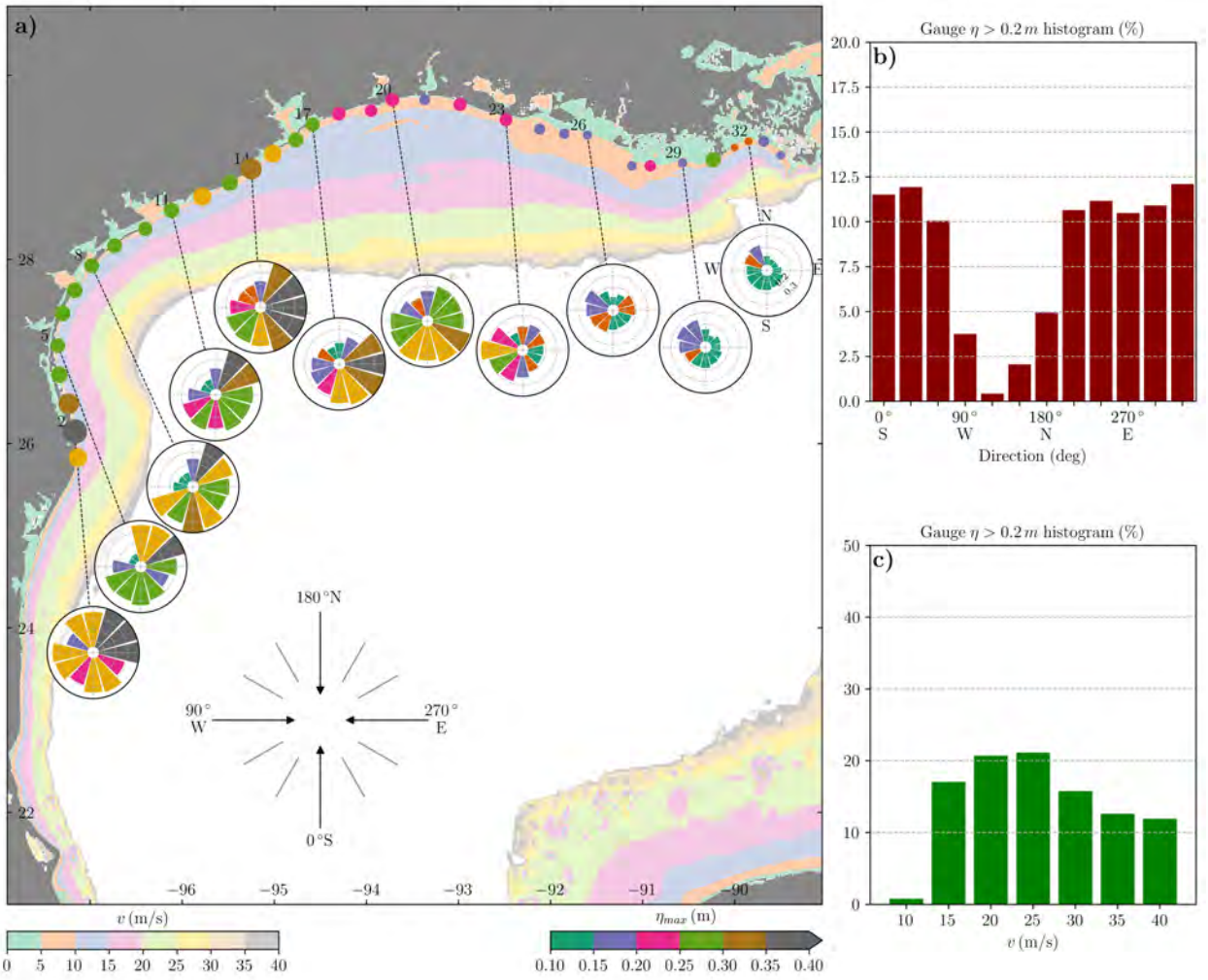

Figure 82: a) Rose diagram of select western GOM gauges each showing the maximum water level (η_{max}) recorded for each direction from a parameter study of 1260 cases (12 incident directions, each with 15 trajectories and 7 pressure disturbance forward speeds). Rose diagram radial scale (η_{max} from 0.1 m to 0.4 m) and directions (NWSE) are marked in gauge #62, which are the same for all the gauges. Maximum water level recorded from all events at each gauge are shown with circles in corresponding size and color (same color scale as the rose diagram). Contour plot of the continental shelf bathymetry is expressed in terms of shallow water wave celerity $C = \sqrt{gh}$ from 0 – 40 m/s, where h is depth of ocean floor. Incident direction is illustrated with arrows where 0° means the pressure disturbance originates from south and 90° means from west, etc., in a clockwise order. b) Incident direction distribution of cases whose recorded water level exceeds 0.2 m (each gauge counts separately). c) Pressure disturbance forward speed distribution of cases whose recorded water level exceeds 0.2 m (each gauge counts separately).

of the continental shelf tapering toward Louisiana. Under the assumptions made in this study, that is, all meteotsunamis travel in a straight line and there are equal chances of

different incident directions, overall the Texas coasts would expect higher meteotsunami water elevation than Louisiana. Within the Texas coastline, the convex sections generally face high meteotsunami waves from more directions than the concave sections. For example, Cameron County (near gauge #1–2) and Matagorda and Brazoria counties (near gauge #12–14) have convex coastlines and those in between are more protected, which is consistent to the findings in Florida GOM coast.

The maximum water level data from all cases (each gauge counts separately) is further compiled into histograms in search for directions and speeds with higher meteotsunami risk in the northeastern GOM. Figure 82b shows the distribution in incident direction where water level exceeds 0.2 m and it indicates that the most favorable direction for higher water level are 0° – 60° (south – southwest, third quadrant), and also around 210° – 330° (northeast – southeast), with each direction accounting for more than 10%. Similarly, Figure 82c shows the distribution in forward speed where water level exceeds 0.2 m. The result shows that 20 m/s – 25 m/s are the forward speeds with the most potential, together accounting for more than 50% of the cases. 15 m/s is more than 15%, the third most common speed for higher water level. The most common speed is similar to Florida GOM coast because the 15 – 30 m/s bathymetry wave celerity bands account for a large portion of the continental shelf.

8 Meteotsunamis Characterization at Clearwater FL

8.1 Introduction

In this study, the focus is kept on the perspective of harbor officials and emergency managers, who would need to get an idea of the potential threat to their community from MT. Ideally, when the characteristics of moving atmospheric disturbance (e.g., storm, squall, frontal passage, or atmospheric gravity wave) is known, it should be possible to predict the expected scenario. But that expertise may not be readily available. In this study we attempt to do a MT characterization for Clearwater,FL along the west coast of Florida to get maximum MT wave amplitude (η_{max_MT}) expected for a given environmental condition. Such a characterization would prove handy to emergency preparedness.

Some key parameters were chosen that determine most properties of a moving AD (atmospheric disturbance). This was done in relation to a particular place of interest, which is henceforth referred to as field site. The main product of this study is a set of visualization aids which can help in determining the expected impact of a given pressure front or squall movement on a particular field site. This is referring to a pilot study done for a specific point nearby to Clearwater, FL in field site 82.85 W,27.98 N (Water depth = 5 m with respect to Mean High Water). An Emergency Response Playbook (ERP) is created which consists of sets of plots which are innovatively customized for our requirements, specifying to obtain η_{max_MT}. These plots are supplemented by tables for better usability. The main parameters we use for visualization are path of AD relative to field site and its forward speed (V_{f_AD}). The path itself is characterized by its direction of motion and its distance from our field site (82.85 W,27.98 N). In the subsequent sections this idea is explained in more detail. Note that the typical moving AD used in this study is a 6 mbar squall of length 1.75 deg, arc length 5 deg and arc radius 8 deg. The possibility of being adjusted for other disturbance amplitudes is also discussed on the ERP.

As this approach is fairly new, it would require initial training of emergency planners and interested parties who are intended to use it. But it is the authors belief, that once trained the plots are fairly intuitive. This method can be used to generate ERPs for various places that can be used by emergency planners and interested parties to add the MT component to the storm surge. These ERPs are generated by running simulations using currently widely accepted MT models.

Amplitude of Trough (A_t)	1.00 mbar
Length of Trough (L_t)	1.05 deg
Amplitude of Crest (A_c)	5.00 mbar
Length of Crest (L_c)	0.70 deg
Pressure Height (p_{AD}) = $A_t + A_c$	6.00 mbar
Length of Arc (L_y)	5.00 deg
Radius of Arc (R)	8.00 deg
Angle deviation from the path vector (Yaw)	0° clock-wise

Table 4: Constant parameters of AD used in MT study for western Florida coast

Angles	0°	30°	60°	90°	120°	150°	180°	210°
	240°	270°	300°	330°				
Distances (deg)	0.0	0.5	1.0	1.5	2.0	2.5	3.0	3.5
	4.0	5.5	6.0	6.5	7.0	7.5	8.0	
V_{f_AD} (m/s)	10	15	20	25	30	35	40	

Table 5: Variable parameters of AD used in MT study for western Florida coast

8.2 Input data generation and processing for characterization

This study is based on the numerical results generated from Section 7.6 in Horrillo et al. [2020] with pressure disturbance parameters shown in Table 4, where a total of 1260 (12 directions x 15 trajectories x 7 velocities) cases were simulated using MT model. For the characterization of Clearwater, we assume that the η_{max_MT} occurs immediately after or along with the AD. Therefore we center all possible cases around Clearwater and we observed that η_{max_MT} are obtained when MT paths are closer and within the immediate continental shelf.

Maximum wave amplitudes were then post-processed for the purpose of characterization using the MT Rose frame of reference. The set of parameters that are used to characterize the effect of various AD parameters on Clearwater are shown in Table 6. Post-processing involved performing distance interpolation of η_{max_MT} observed for the various AD paths, to obtain maximum wave amplitudes for MT Rose plot. Paths for two of these cases are shown in Fig. 83.

Angles	0° 30° 60° 90° 120° 150° 180° 210° 240° 270° 300° 330°					
Distances (deg)	clockwise	0.0	0.5	1.0	1.5	2.0
	counter clockwise	0.0	-0.5	-1.0	-1.5	-2.0
V_{f_AD} (m/s)	10 15	20	25	30	35	40

Table 6: Parameters of the AD used in MT characterization for Clearwater, Florida

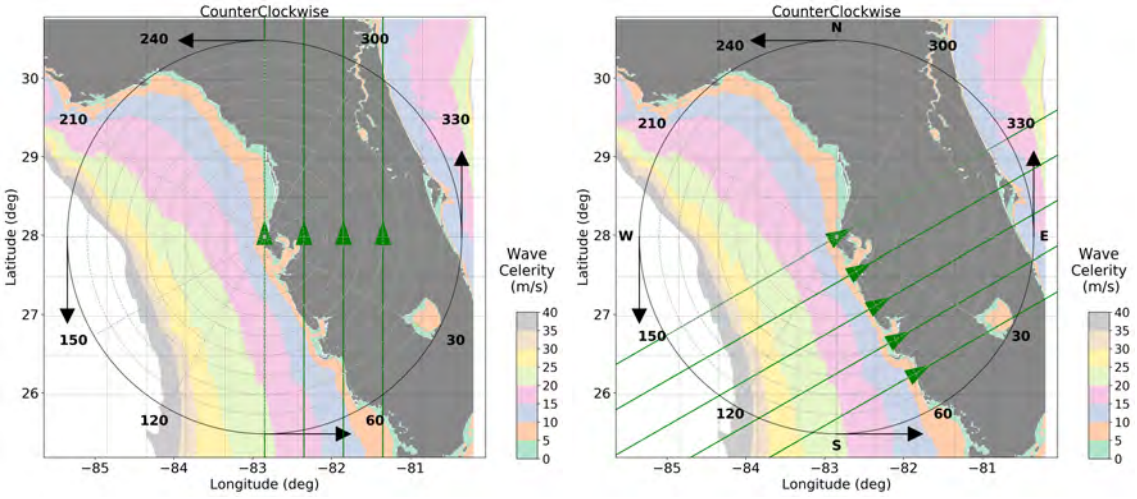

Figure 83: Various paths of AD (indicated by green lines) used in MT characterization for western Florida coast 0° (left) and 60° (right)

8.3 Meteotsunami Characterization

Characterization of η_{max_MT}s using MT rose plots is demonstrated in Fig. 84. Here, η_{max_MT} for the field site (Clearwater FL) is represented as a function of d_{AD} and ϕ_{AD} using circular barplots. d_{AD} is the distance of nearest approach of AD path from our field site. ϕ_{AD} is the angle of AD path , measured clockwise with respect to an AD traveling north. The forward speed of AD (V_{f_AD}) is indicated in the title of plot. The direction of AD relative to field site is also indicated on the title, as clockwise or counter-clockwise. In this study, a total of 7 V_{f_AD} were used. Thus 7 pairs of plots are used to characterize η_{max_MT} in a given location (Clearwater FL in this case).

The usage of MT rose plot is explained with the help of Fig. 85. Suppose an AD is approaching Clearwater with $V_{f\_AD} = 20$ m/s from NNW ($\phi_{AD} = 150°$) at $d_{AD} = 1.5$ deg. The direction of AD is counterclockwise with respect to Clearwater. Based on this information, we pick the MT rose plot shown in Fig. 85 from the 7 pairs of MT rose plots available for Clearwater. From this we select the bar that represents our d_{AD} and ϕ_{AD} as

indicated in figure. Now the expected η_{max_MT} for this case is depicted by the color of bar and its height. This gives $\eta_{max\_MT} = 0.38$ m.

A salient feature of MT rose plot is the underlying map (with equal scale latitude/ longitude) that shows the bathymetry of the region in terms of wave celerity. Proudman resonance is one of the main causes of MT. It occurs when the V_{f_AD} matches the wave celerity along its path, resulting in high η_{max_MT}. This map then aids in rationalizing the observed model estimates for η_{max_MT}.

Oftentimes ADs do not pass exactly with d_{AD}s, ϕ_{AD}s and V_{f_AD}s that were used to generate the MT rose plots. In such cases an interpolation may be done to get a reasonably good estimate for η_{max_MT}. For example, let us take the case presented in Fig. 86. Here, p_{AD} = 5 mbar, $d_{AD} = 0.6$ deg, $\phi_{AD} = 140°$ and $V_{f\_AD} = 22$ m/s. We may use the 8 adjoining cases in the plots to interpolate (using $d_{AD} = 0.5$ & 1.0 deg, $\phi_{AD} = 120°$ & 150° and $V_{f\_AD} = 20$ m/s & 25 m/s). A trilinear interpolation would give $\eta_{max\_MT} = 0.29$ m. Since $p_{AD} = 6$ mbar was applied to generate the plots, a linear scaling needs to be applied to obtain the result for $p_{AD} = 5$ mbar. This gives $\eta_{max\_MT} = 0.24$ m. This approximation can however be off by as high as 20%. Accurate predictions require simulation of the specific scenario, which takes relatively more time and resources. Even if an interpolation were not performed, a quick look at the amplitudes for adjoining cases should give a reasonable idea of the worst case scenario. In the case shown in Fig 86, an AD moving at $V_{f\_AD} = 20$ m/s counterclockwise with respect to Clearwater at $d_{AD} = 1.0$ deg and $\phi_{AD} = 150°$ causes the highest η_{max_MT}.

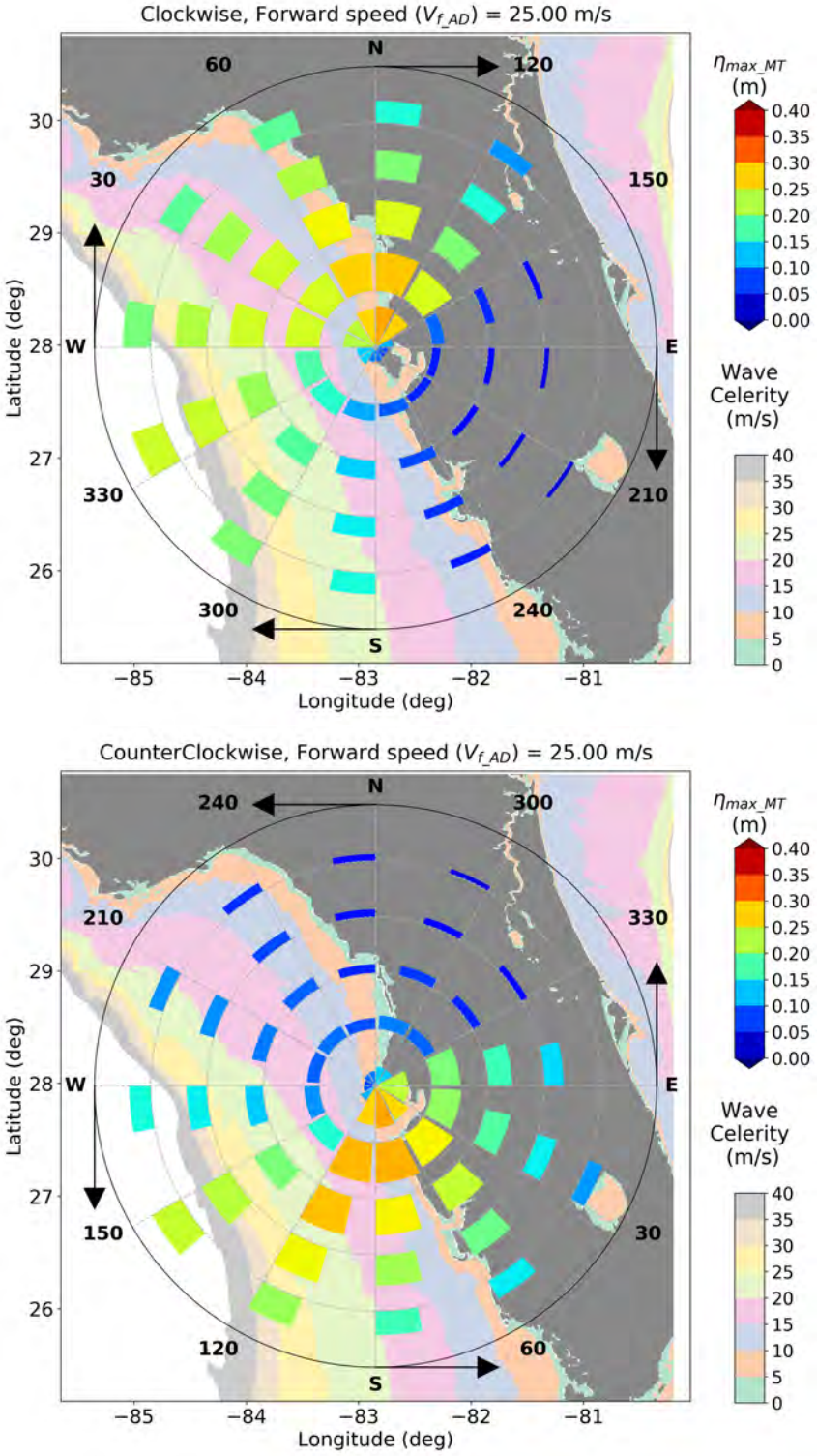

Figure 84: η_{max_MT}(m) at field site near Clearwater Beach (82.85 W 27.98 N) Water depth = 5.0 m from MHW, represented by height of bars for an AD (p_{AD} = 6 mbar) with V_{f_AD} = 25 m/s Clockwise (Top) and Counter-Clockwise (bottom) relative to field site for different directions ϕ_{AD} and d_{AD}

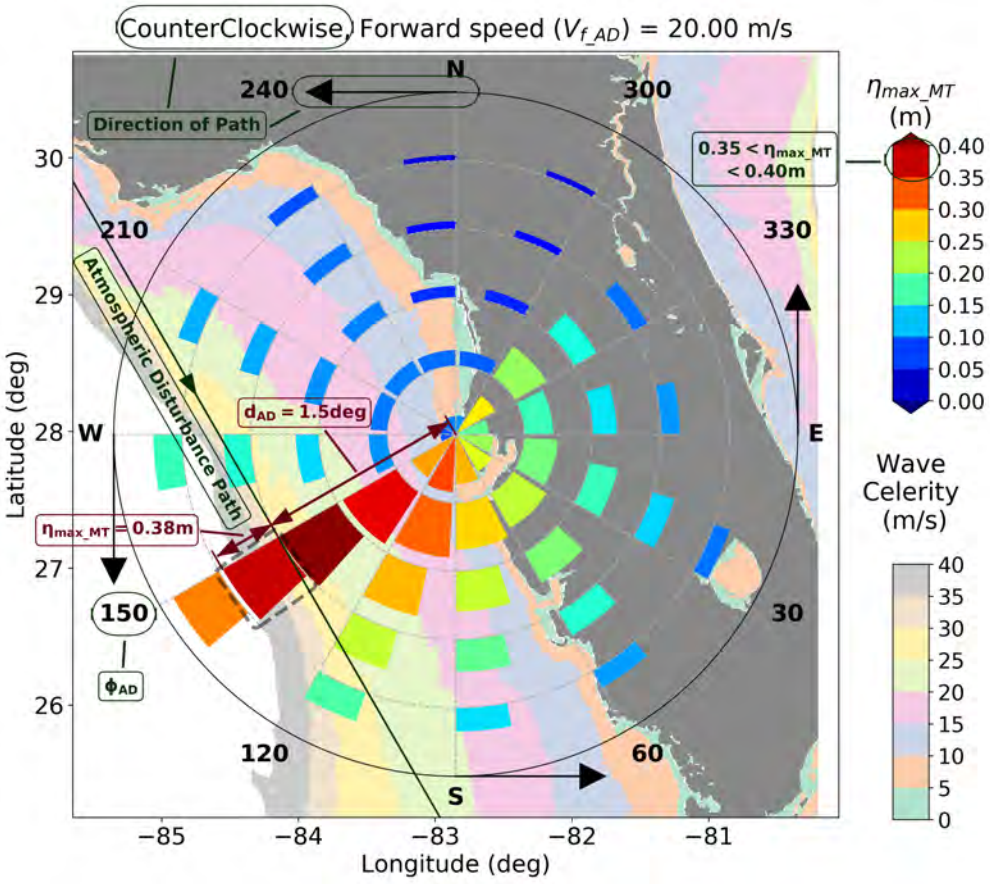

Figure 85: MT Rose plot explained for η_{max_MT} at field site near Clearwater Beach (82.85 W 27.98 N), Water depth = 5.0 m from MHW represented by height of bars for an AD(p_{AD} = 6 mbar) from direction $\phi_{AD} = 150°$ moving CounterClockwise relative to field site, with $d_{AD} = 1.5$ deg and $V_{f\_AD} = 20$ m/s

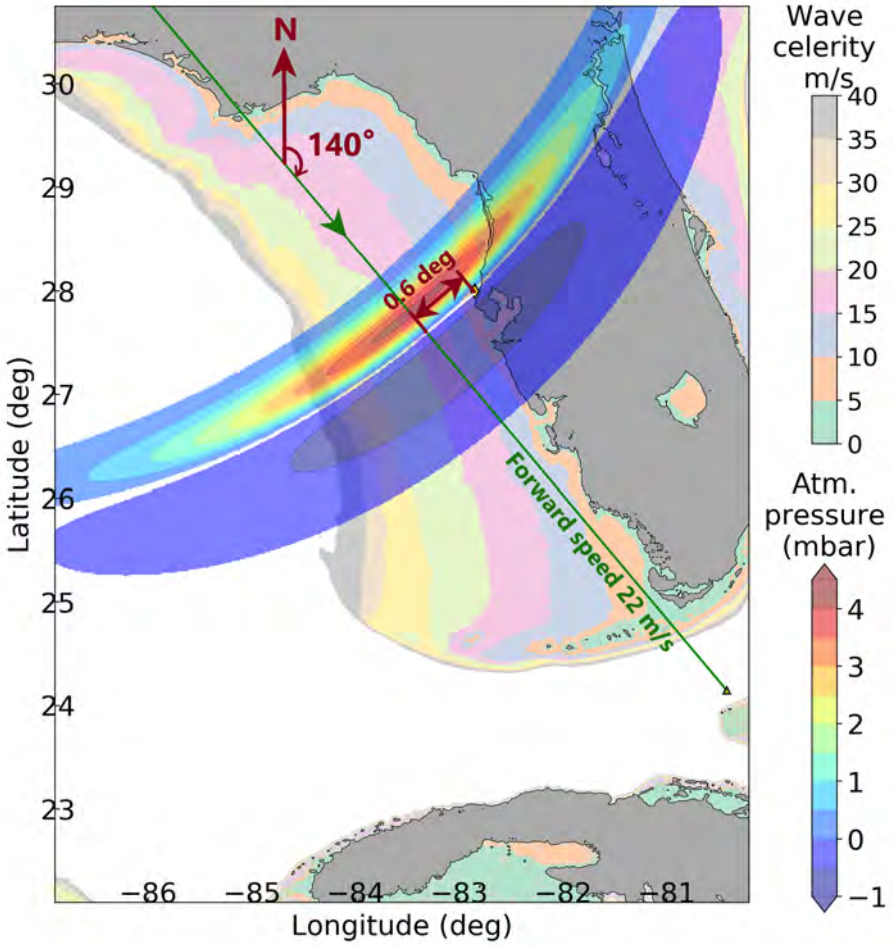

Figure 86: An AD (p_{AD} = 5 mbar) at ϕ_{AD} = 140°, d_{AD} = 0.6 deg from field site near Clearwater Beach (82.85 W 27.98 N), Water depth = 5.0 m from MHW with V_{f_AD} = 22 m/s counter-clockwise relative to field site (Clearwater,FL)

8.4 Sensitivity Study

In Section 7.2, it was mentioned that many parameters were assumed constant in generating MT Rose plots. In this section, the effect of some of these parameters is studied. Shown in Fig. 87 and 88 are 2 cases that are being analyzed here. Fig. 87 represents a predominantly offshore traveling disturbance, i.e. The peak of pressure amplitude of AD is located over the water during its nearest approach to Clearwater Fl. The path it takes aids MT generation. Fig. 88 on the other hand represents a disturbance with peak inland. This effectively reduces the η_{max_MT} generated by it. These 2 cases were specifically chosen to qualitatively study the influence of geographical features on the parameters being used.

Pressure height (p_{AD}), length of Pressure crest (L_c), Length of arc (L_y) and Radius of arc (R) are the parameters that are being studied here. Shown in Fig. 89 - Fig. 92 are the results of sensitivity studies for these parameters.

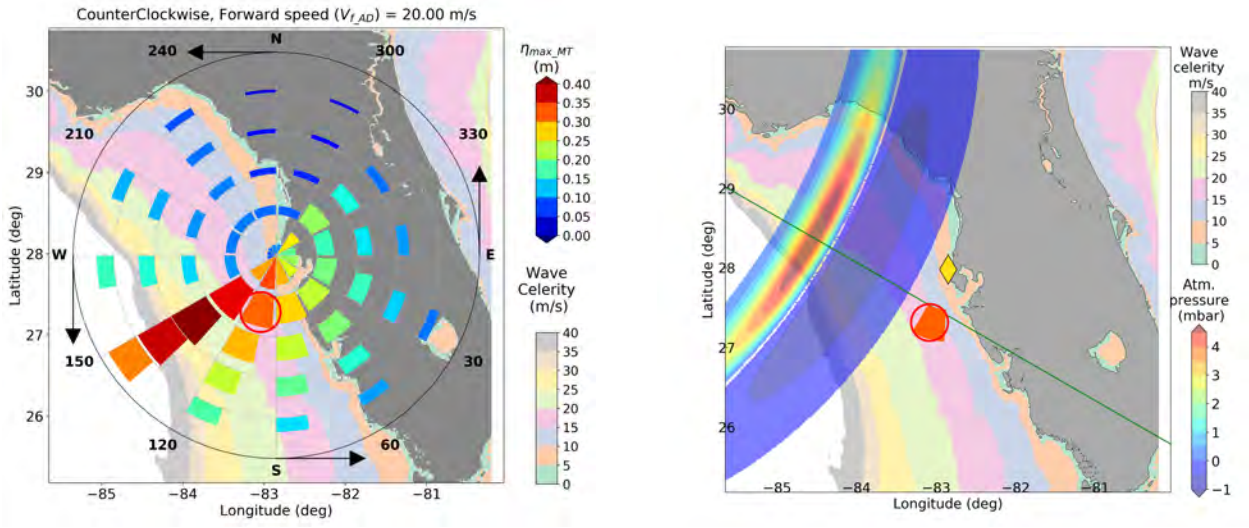

Figure 87: sensitivity study for case 1 - Field site near Clearwater FL AD offshore

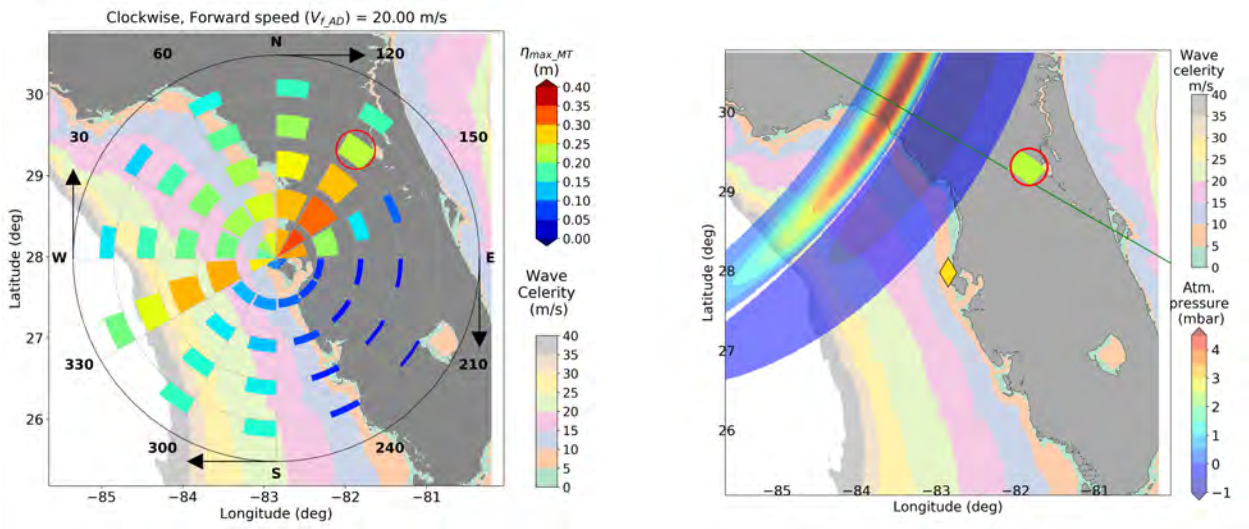

Figure 88: sensitivity study for case 2 - Field site near Clearwater FL AD partially on land

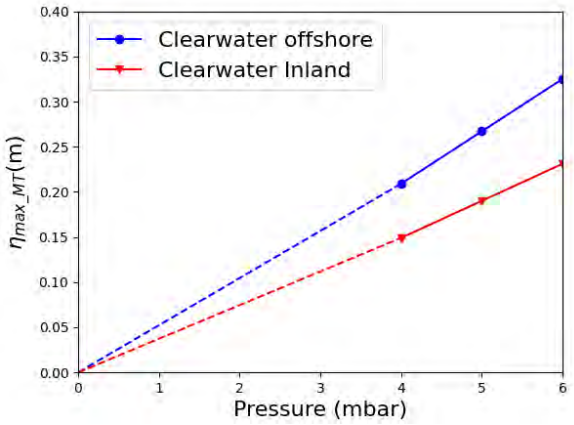

Figure 89: sensitivity study for parameter p_{AD} (Pressure Height)

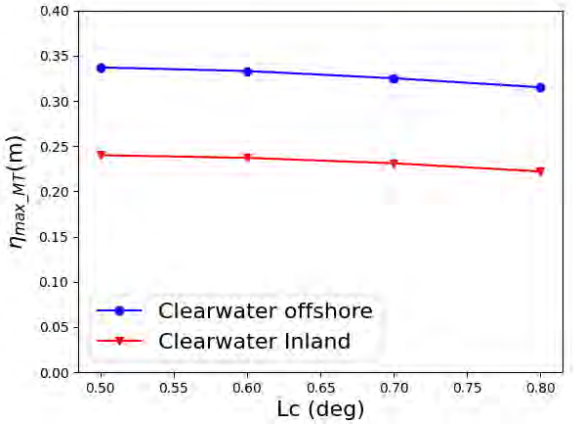

Figure 90: sensitivity study for parameter L_c (Length of Crest)

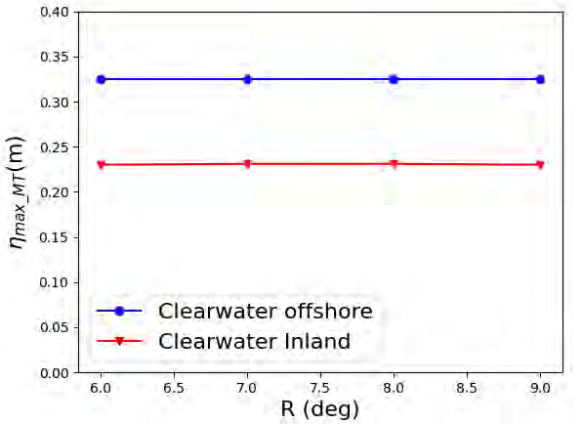

Figure 91: sensitivity study for parameter R (Radius of Arc)

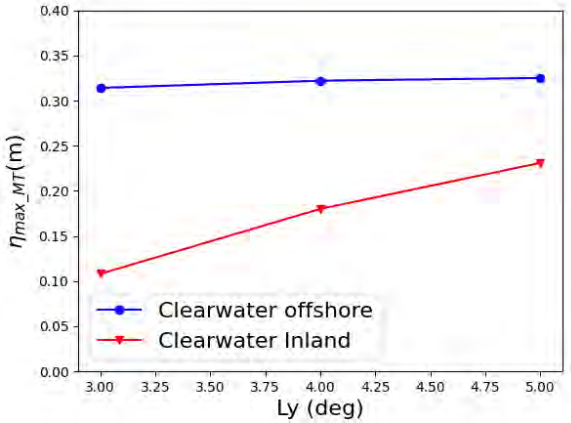

Figure 92: sensitivity study for parameter L_y (Length of Arc)

The sensitivity study in Fig. 89 shows a clear linear relationship between pressure and η_{max_MT} observed. This allows us to use a linear factor to account for the difference from the amplitude used to generate the plots. The Crest Length(L_c) and Radius of Arc(R) in Fig. 90 and 91 did not show significant change in the generated MT amplitudes. Length of Arc (L_y) indicated in Fig. 92 did not affect the η_{max_MT} for offshore case (Case 1). In the inland case (Case 2), there is a decrease in η_{max_MT} with decrease in Arc length of AD. This is because there is a significant decrease in the portion of the AD above the water.

This sensitivity study shows that there are unique location specific factors that need to be addressed while trying to come up with general formulations. One such factor is the transfer of energy from the AD to nearby body of water of the field site. Difference in pressure can be linearly factored in and while other parameters used in the study can be assumed constant. Note that this is a preliminary study. Further study needs to be done to gain a broader understanding of the same.

8.5 Clearwater FL Case Study Results

Based on our study the highest η_{max_MT}s are observed for an AD moving with V_{f_AD} = 20 m/s at ϕ_{AD} of 120-150 ° (from NW) as indicated in Fig. 93. The cases shown have η_{max_MT} between 0.3 and 0.45 m. Among these, AD with $\phi_{AD} = 150°$, $d_{AD} = 1$ deg and moving counter-clockwise with respect to Clearwater gives the highest η_{max_MT}. There is a possibility of higher MT amplitudes not being captured due to the limited number of cases being represented in this plot. For example, one of the cases shown in Olabarrieta et al. [2017] has a MT amplitude of 0.5 m which is 20% higher than that observed in this analysis. This possibility has been noted earlier in the discussion on interpolation.

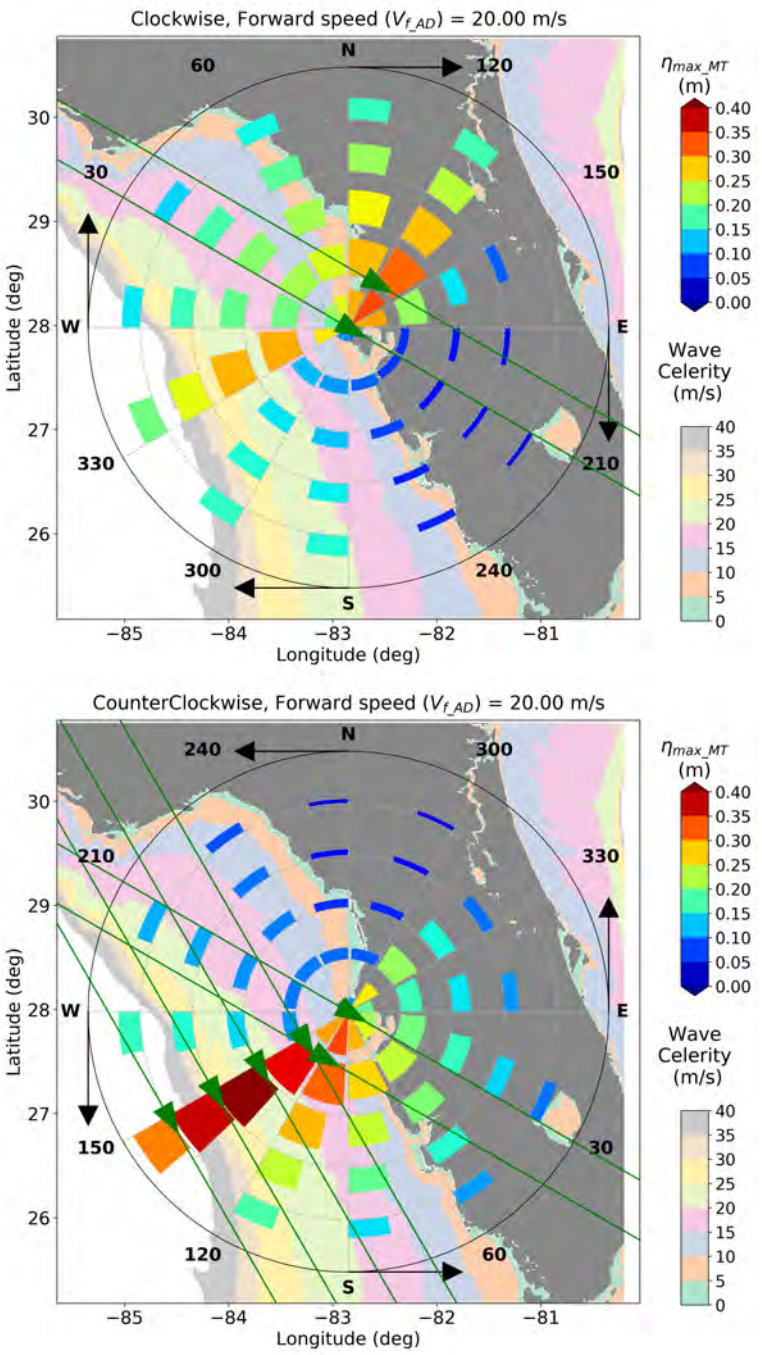

Figure 93: AD cases for field site near Clearwater Beach, FL (82.85 W,27.98 N) for which highest η_{max_MT} are observed

8.6 Summary

A new method of numerical MT data characterization has been proposed using MT Rose Plots. The idea of MT Rose Plots has been described in great detail. This takes us one

step closer to be able to characterize most of the scenarios that can potentially cause MTs in our places of interest. A study was done to analyze the sensitivity of some of the constant parameters used in MT Rose plot generation. A case study was done for Clearwater, FL to identify possible scenarios that could lead to high η_{max_MT} events.

9 Application of ANN in Meteotsunami Water Level Prediction

9.1 Introduction

To provide a broader and faster way to predict the hazards on a broad scale in the northeastern Gulf of Mexico, an optimal artificial neural network (ANN) was trained using the large combination of pressure propagating speed and path generated from the numerical simulations. Regression analysis of the output of ANN was performed, and the results are consistent with numerical simulation with a correlation coefficient greater than 98%. The formula of the ANN was then presented, providing a reliable predicting method for water level caused by meteotsunamis.

Rapid and accurate hazard forecasting is important for prompt evacuations and reducing casualties during natural disasters. Recently, other more simplistic methods based on published data such as analytical data, experimental data, and numerical data can be used to predict the behavior of the physical model or natural phenomenon. For example, there are already several studies in the Ocean Engineering field where Artificial Intelligence tools Neural Networks can be applied to tackle the behavior of the physical model or natural phenomenon reasonably. A rapid and accurate tsunami inundation forecasting approach using convolutional neural networks (CNNs) was developed by Makinoshima et al. [2021] for early warning. Numerical tsunami forecasting experiments for Tohoku demonstrated excellent performance with average maximum tsunami amplitude and tsunami arrival time forecasting errors of 0.4m and 48 s, respectively, for 1,000 unknown synthetic tsunami scenarios.

This study is based on the numerical results generated from Section 7.6 in Horrillo et al. [2020] with pressure disturbance parameters shown in Table 4, where a total of 1260 (12 directions x 15 trajectories x 7 velocities) cases were simulated using MT model. An additional 4320 (18 directions x 15 trajectories x 16 velocities) cases within the same input parameter ranges were also included, therefore there are a total of 5580 cases. A database of MT effects is generated to train an ANN in order to provide a broader and faster way to predict the hazards in the northeastern GOM. Additionally, regression analysis of ANN output is performed, and the results are compared with the numerical simulation. Furthermore, the formula of the ANN is presented, providing a reliable and fast method of predicting hazard caused by meteotsunamis.

9.2 Artificial Neural Network (ANN) Structures

ANN technology has been applied extensively in engineering. This is due to the ability of ANNs to solve discontinuous and non-linear problems, and to predict results of a complex system based on various selected input parameters with robustness, adaptability, and high accuracy [Jiang et al., 2010]. One of the most common type of ANN used for data analysis is the multi-layer perceptron (MLP) networks based on the Back-Propagation (BP) learning algorithm [Atkinson and Tatnall, 1997] which is used in this study.

The 5-30-20-1 BP neural network architecture (Figure 94) is used in this study. The five input layer neurons perform the function of distributing, scaling (if it is necessary), and

transfer the five inputs to the processing elements of the next layer. The second and third layers are the processing or hidden layer, and the neurons process the inputs and send their results to the next layer. Finally, the output-layer neuron represent the maximum water level in the northeastern GOM. The Marquardt–Levenberg algorithm (MLA) was used to optimize the ANN, and the stochastic gradient descend method was used for learning procedure.

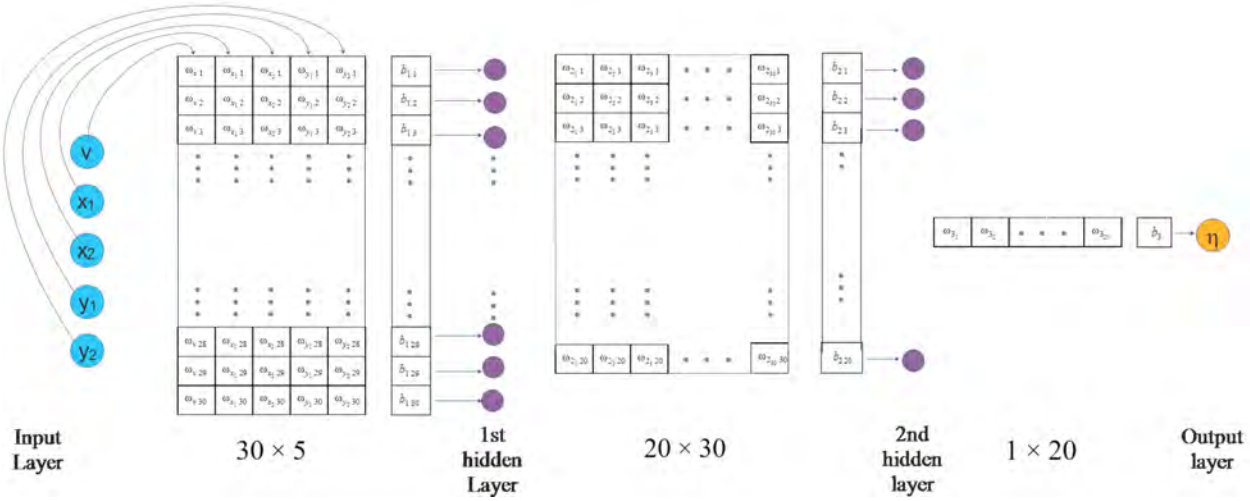

Figure 94: Neural network architecture.

The linear transfer function is used between hidden layer and output layer as shown in Equation (7), where ω_{3i} and b_3 are the interconnection weights and bias between the second hidden layer and output layer, respectively. Index i represents the ith nodes in the second hidden layer and each Z_{2i} can be calculated using Equation (8).

$$H = \sum_{i=1}^{20} \omega_{3i} \cdot Z_{2i} + b_3, 1 < i < 20 \tag{7}$$

$$\begin{aligned} &Z_{2i} = tansig(\textstyle\sum_{j=1}^{30} \omega_{2ij} \cdot Z_{1ij} + b_{2i}), \\ &1 < i < 20,\ 1 < j < 30 \end{aligned} \tag{8}$$

Where j represents the jth nodes in the first hidden layer, the $tansig$ function is defined in Equation (9). Each Z_{1ij} can be calculated using Equation (10). Where all the five inputs and the output are normalized inputs within a range of [-1,1], and the range of the original 5 inputs are $10 < v < 40, -92° < x_1$ & $x_2 < -77°, 20° < y_1$ & $y_2 < 35°$.

$$tansig(A) = \frac{2}{1 + e^{-2A}} - 1 \tag{9}$$

$$\begin{aligned} &Z_{1j} = tansig(\omega_{vj} \cdot v + \omega_{x_1 j} \cdot x_1 + \omega_{x_2 j} \cdot x_2 \\ &+\omega_{y_1 j} \cdot y_1 + \omega_{y_2 j} \cdot y_2 + b_{1j}), 1 < j < 30 \end{aligned} \tag{10}$$

Weight(ω) and bias(b) in Eq. (7) – (10) in hidden and output layers of ANN are achieved from the trained Artificial Neural Networks.

Mean squared errors (MSE) and correlation coefficient R are two factors selected to evaluate the quality of the predicted results of the ANN as shown in Equations (11) and (12). N is the number of evidence data and T_i is the reference data (target values). In addition, O_i represents the predicted values using the trained Neural Networks. $\bar{O}$ and $\bar{T}$ are the average values of the reference data and outputs of the Neural Network, respectively. Notably, smaller MSE and a proximity of R to 1 implies a more accurate prediction, referring to a better quality of the Neural Networks.

$$\text{MSE} = \frac{\sum_{i=1}^{N} (O_i - y_{\text{desired}})^2}{N} \tag{11}$$

$$R = 1 - \frac{\sum_{i=1}^{N} (O_i - y_{\text{desired}})}{\sum_{i=1}^{N} (O_i - \bar{y}_{\text{desired}})} \tag{12}$$

In the present study, 4000 out of the 5580 CFD simulation results are randomly selected and used as the data base to train the ANN, the other 1580 are later used to test the trained ANN. Limited values of input-output variables are tabulated in Table 7. Moreover, to avoid over-fitting, early stopping approach presented by Prechelt [1998] is applied by classifying the inputs-outputs of our numerical simulated data in three random groups. 70% of the numerical simulated data are used to train the ANN, 15% are used to validate the trained ANN to avoid over-fitting, and the other 15% are used to test the quality of the ANN.

Table 7: Input and output ranges for ANNs

	Variables	**Range**	**Units**
Input	longitude of the start point (x1)	-77 to -92	Degree
	longitude of the end point (x2)	-77 to -92	Degree
	latitude of the start point (y1)	20 to 35	Degree
	latitude of the end point (y2)	20 to 35	Degree
	Wind speed (V)	10 to 40	m/s
Output	Maximum MT water level(H)	0 to 0.35	m

The predicted data are validated with the test data using a linear regression model. In addition, the linear regression analysis are performed for the training sample set, validation sample set, test sample set, and all sample set, respectively, the results are shown in Figure 95.

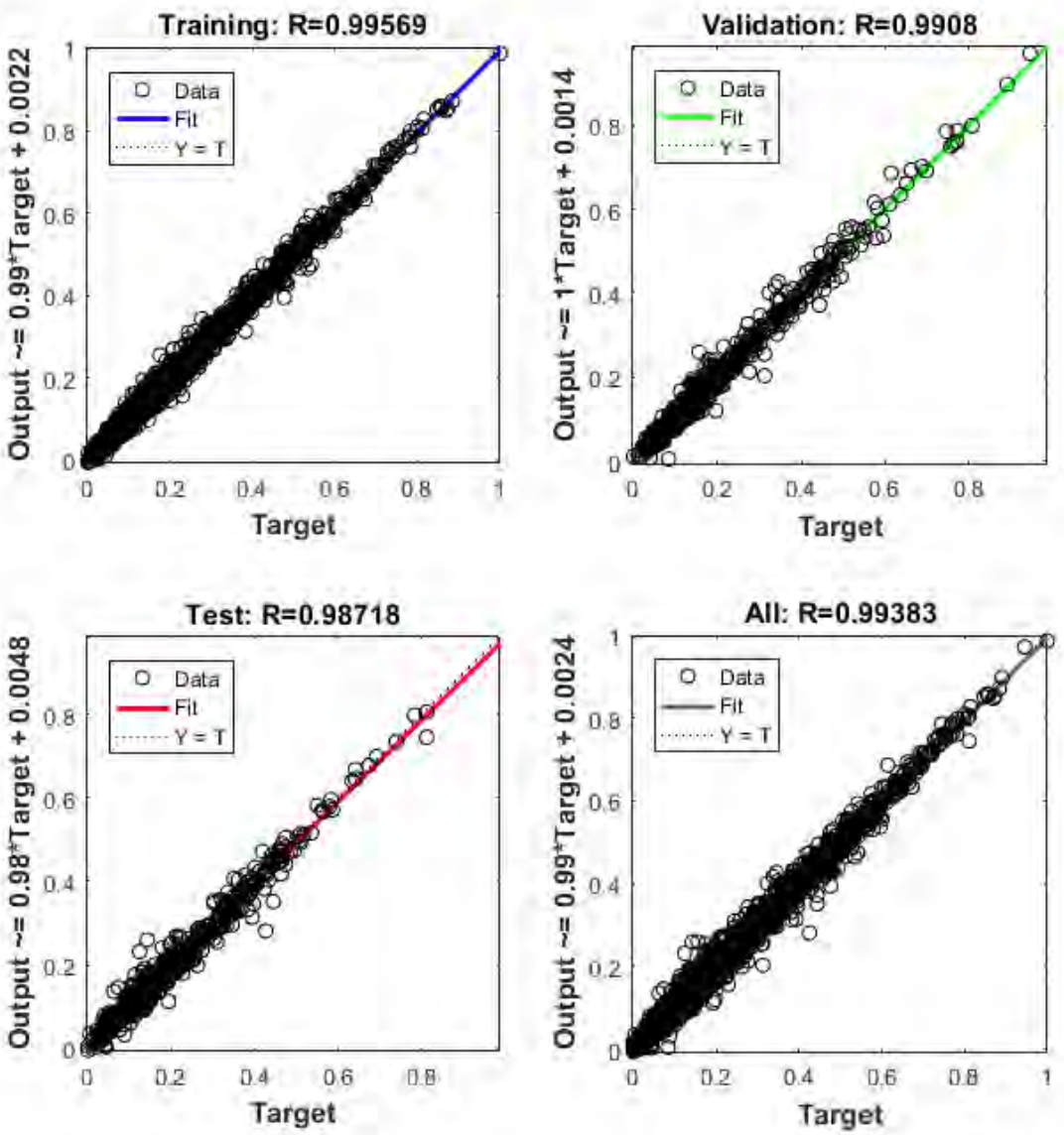

Figure 95: Regression Analysis of the Neural network's output using (**a**) training sample set (**b**) validating sample set (**c**) testing sample set (**d**) all sample set.

As shown in Figure 95, the output data from the neural network matches quite well with the targeted data with correlation coefficients $R > 98\%$ for all the four sample sets. In addition, the other 1580 numerical simulated data are used to test the trained ANN. The correlation analysis was performed using the same method, with a $R = 99.88\%$. Thus, it can be concluded that the selected ANN is able to accurately predict the maximum water level under different trajectories and velocity conditions.

Furthermore, all the 5580 simulation data are combined as a whole sample set. The Neural Network's prediction for all the 5580 cases were compared with the original simulation

data. The results of the simulation and error of the predictions of the ANN are listed in the Figure 96.

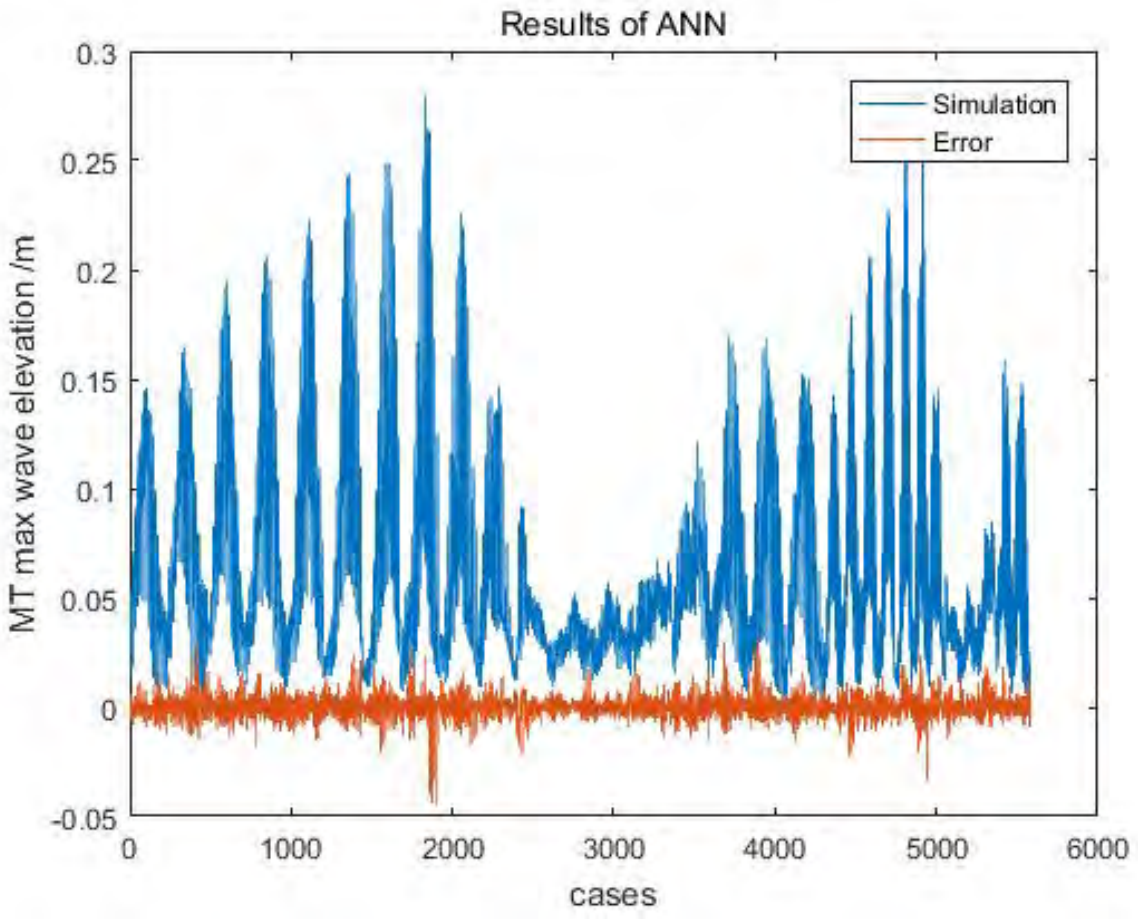

Figure 96: Comparison between the prediction from trained ANN and the simulation results.

As can be concluded by looking at Figure 96, the differences for all 5880 cases are relatively small compared to the actual simulation results. So, we can conclude that the ANN can be used to substitute the traditional simulation method if the forecast time is limited and still providing a reasonably good prediction.

9.3 Conclusions and future work

To provide a broader and faster way to predict the hazards on a broad scale, an optimal artificial neural network (ANN) was trained using data from a large number of MT simulations in the northeastern GOM. By varying incident direction, prescribed trajectory location and forward speed of the pressure disturbance, 5580 runs were performed in order to generate a database of meteotsunami effects to train an ANN. The inputs and output of the sample set were first normalized to the range of [-1, 1] respectively. An optimal artificial neural network (ANN) is then obtained using the 2800 training sample sets generated from the numerical

simulation and the 600 validating sample set and another 600 sample set are used to prevent over fitting and improve and test the structure of the Neural Network in order to optimize the performance of the neural network. Additionally, regression analysis of the output of ANN is performed using the training, validating, testing and the whole 4000 sample set, resulting a correlation (R) bigger than 99%. Whats more, the other 1580 simulation data are used to test the performance of the trained Artificial Neural Network, and the results are compared with the numerical simulation, showing a correlation (R) bigger than 97%, which is better than expected. Furthermore, the formula of the ANN is presented, providing a reliable yet timely predicting method comparing to the traditional CFD method which could take longer to forecast the maximum wave elevation caused by the MT.

In the current study, the length of trajectory is fixed, so the trained Neural Network can only be used to forecast the maximum wave elevation generated by the MT within that specific zone. In the future, more data need to be generated within different area in the Gulf of Mexico in order to get a more comprehensive predicting tool for us to forecast and mitigate the hazard caused by MTs. In addition, current study only took the pressure disturbance trajectory and speed into account, and other aspects of the pressure still need to be considered.

10 Conclusions

This project focused on the implementation of recent developments in the tsunami science recommended by the National Tsunami Hazard Mitigation Program - Modeling Mapping Subcommittee - Strategic Plan (NTHMP-MMS-SP) into our current Gulf of Mexico (GOM) tsunami mitigation products. Three main developments for tsunami mitigation have been created under this project for two new communities in the GOM (Don Pedro Island-Boca Grande-Captiva Island, FL and Marco Island, FL) that will provide guidance to state emergency managers for tsunami hazard mitigation and warning purposes. The first task is the development of tsunami inundation maps for the two selected communities with nine landslide sources. The second is the comparison between existing SLOSH hurricane flooding data and our tsunami inundation result for the two new communities in order to facilitate temporal-low-order estimate for tsunami hazard areas (community) where inundation studies have not yet been assigned/executed or where little bathymetric and elevation data exists. The third is to produce maritime products (maximum of maximum (MOM) velocity and velocity magnitude maritime maps) for both communities to help identify impact specifically on ship channels, bay inlets, harbors, marinas, and other infrastructures. An additional task is a study where we conducted numerical experiments to investigate the generation and propagation of meteotsunami waves and assessed hazards on a broad scale in the northwestern Gulf of Mexico (GOM), as a continuation from northeastern GOM studies [Cheng et al., 2021, Horrillo et al., 2020]. Also in this study we attempt an MT characterization for Clearwater,FL along the west coast of Florida to get maximum MT wave amplitude (η_{max_MT}) expected for a given pressure disturbance condition using MT Rose Plots. This characterization can be used to generate Emergency Response Playbooks (ERP) for various places that can be used by emergency planners and interested parties to add the MT component to the storm surge. Last, to provide a broader and faster way to predict the hazards on a broad scale in the northeastern Gulf of Mexico, an optimal artificial neural network (ANN) was trained using the large combination of pressure propagating speed and path generated from the numerical simulations.

Tsunami wave propagation and inundation in Don Pedro Island-Boca Grande-Captiva Island, FL and Marco Island, FL was also modeled to obtain maximum inundation and extent, momentum flux, current velocity and vorticity maps considering the entire suite of nine landslide sources. On a regional scale, the wide Florida GOM continental shelf provides significant damping of tsunami waves so that the majority of Florida west coast shows less tsunami inundation. For Don Pedro Island-Boca Grande, FL, under the worst case scenario, tsunami waves would inundate all of the barrier islands and the mainland areas facing the GOM and around inlets. Overall water depth exhibits decreasing trend from oceanfront toward the bay, with maximum over 2 m. The MOM tsunami inundation at Don Pedro Island and Boca Grande ranges from 1 to over 2 m, but mostly over 1.5 m. Across the bay, relatively high tsunami inundation (> 1.5 m) only occurs west of Placida Rd where it is close to Don Pedro Island, while the rest of the inundated mainland areas only sees inundation less than 1.5 m. The MOM tsunami inundation at Cayo Costa Island is mostly over 2 m, though there are no residents on this island. On North Captiva Island, tsunami inundation over 2 m mainly occurs in its middle west section where there are no residents. The northern

residential area generally have water lower than $\sim$ 1.5 m. Similarly on Captiva Island, high water ($>$ 2 m) only occurs along the beach, while the sea wall protected residential areas have water lower than 1.5 m. For Marco Island, FL, overall the barrier island provides ample protection for the mainland against tsunami inundation. While inundation depth at the barrier island ranges from 1 to over 3 m from the lee side to the GOM, the wetlands behind the island is mostly less than 1.3 m. Specifically, worst case scenario (MOM) inundation depth higher than 3 m mostly occurs on the beach. Larger than 2 m inundation can be expected in those communities adjacent to the beach (approximately within 1 km inland of the beach). For both communities, MOM tsunami inundation is produced solely by the Mississippi Canyon failure. This geological failure is the largest in both, area and volume of material removed, and therefore produces the highest amplitude wave of all simulated sources.

While high-resolution tsunami inundation studies have been completed for these 18 communities and are planned for additional locations, vulnerability assessments are still essential for coastal locations where inundation studies have not yet been performed or planned, or where there is a lack of high-resolution bathymetric and/or elevation data. Therefore, we aim to extend the results of the completed mapping studies in order to provide estimates of tsunami inundation zones for hazard mitigation efforts in unmapped locations. We anticipate that communities which lack detailed tsunami inundation maps, but which have modeled hurricane storm surge information, would be able to use the results presented here to estimate their potential tsunami hazard level based on their regional topographical/bathymetric features. We stress, however, that such results should be used only in a broad, regional sense given the differences seen among and within communities based on local details of bathymetry, topography, and geographical location within the GOM basin. There is no guarantee that comparison results will be identical in areas with similar topography, and comparisons should only be made after understanding the limitations and simplifications of the methodology presented here. Comparisons of MOM tsunami inundation results with the SLOSH MOM high tide storm surge inundation indicate that while the details of referencing tsunami inundation to hurricane storm surge is dependent on local topographic effects, general regional trends can be identified. For Don Pedro Island-Boca Grande-Captiva Island, FL, the hurricane category that best matches tsunami inundation closely follows the MOM tsunami inundation trend, where Category 3 appears near the beach, Category 2 runs parallel and takes up the middle section of the island, and the rest is Category 1. The difference between hurricane flooding and tsunami inundation is mostly within $\pm$1 m. Similarly for Captiva Island, FL, the hurricane category that best matches tsunami inundation closely follows the MOM tsunami inundation trend, where Category 3 appears near the beach, Category 2 takes up the middle section of the island, and the rest is Category 1. The difference between hurricane flooding and tsunami inundation is mostly within $\pm$1 m. For Marco Island, FL, Category 3 is only seen on a few scattered spots on the barrier island beach, and the majority of the barrier islands are between Category 2 and 1. The difference between hurricane flooding and tsunami inundation $\Delta\zeta$ is generally within $\pm$0.5 m for the barrier islands, however, on the wetlands between Marco Island and the mainland the difference reaches larger than 1 m, which means storm surge inundation depth is higher since tsunami waves generally cannot reach as far into the bays.

We produced the MOM velocity and vorticity magnitude maps for all the landslide scenarios, for Don Pedro Island-Boca Grande-Captiva Island, FL and Marco Island, FL, based on a simplified current velocity damage scale where we associate 0 - 3 knots to unharmful currents, 3 - 6 knots to minor damage, 6 - 9 knots to moderate damage, and over 9 knots to major damage. The four damage levels are denoted with white, blue, yellow and red colors, respectively.

From the MOM velocity magnitude results in the entire Gulf of Mexico, it can be observed that, potential damaging currents ($>$ 3 knots, blue, yellow and red areas) tend to be present in most of the area shallower than the minimum offshore safe depth (approximately 200 m or 100 fathoms). However, damaging currents could reach areas deeper than 200 m close to most of the landslide generation regions. Major damaging currents ($>$ 9 knots, red) can be expected in most of the landslide generation regions, in the continental shelf adjacent to Mississippi Canyon, offshore northwest Florida, and Yucatán shelf. Moderate ($>$ 6 knots and $<$ 9 knots, yellow) damaging current areas are scattered over the continental shelf, but mostly close to areas with major damage currents. For Don Pedro Island-Boca Grande-Captiva Island, FL, general trends can be observed from the different grid levels of the MOM velocity. Most of offshore region is expected to have minor damaging currents, with moderate damaging currents occurring along the coastline and jetties. There is no moderate damaging currents behind the barrier islands, however, it can reach over 9 knots (major damaging current) near the bay entrances both north and south of Boca Grande and the Redfish Pass. In Marco Island, FL, the situation is different from Don Pedro Island-Boca Grande-Captiva Island, FL. In general, tsunami currents are less severe; there are very few major damaging current locations and moderate damaging current area is much smaller. Vorticity distribution, on the other hand, displays similar patterns between the two locations, where high vorticity appears around the barrier island, and are more intense near the bay entrances.

Tsunami hazard maritime products such as tsunami current magnitude, vorticity, safe/hazard zones would be central for future developments of maritime hazard maps, maritime emergency response and as well as infrastructure planning.

Although relatively rare, meteotsunamis are capable of causing coastal infrastructure damage and casualties. Analyses of water level and meteorological data in the U.S. show that meteotsunamis occur more frequently than expected, and therefore, it is important to include meteotsunami assessment in coastal hazard mitigation efforts. In this study, we conducted numerical experiments to investigate the generation and propagation of meteotsunami waves and assessed hazards on a broad scale in the northwestern Gulf of Mexico (GOM), as a continuation from northeastern GOM studies [Cheng et al., 2021, Horrillo et al., 2020]. The numerical experiments used a simple 2D depth-averaged hydrostatic shallow water model forced by an idealized atmospheric pressure disturbance on a set of trajectories and directions (1260 runs) covering the whole northwestern GOM shelf. Results show that Louisiana coasts are less likely to be hit with a high meteotsunami wave than Texas, and that the convex sections of Texas coastline are more susceptible to meteotsunami waves coming from various directions. Statistical analysis indicates that pressure disturbances coming from south – east direction result in higher water level in this region. The forward speed distribution shows that 20 m/s – 25 m/s have the most potential. These results can help identify vulnerable coastal regions and pressure disturbance scenarios that most likely generate higher meteotsunami

waves.

Also in this study we attempt an MT characterization for Clearwater, FL along the west coast of Florida to get maximum MT wave amplitude (η_{max_MT}) expected for a given pressure disturbance condition using MT Rose Plots. This characterization can be used to generate Emergency Response Playbooks (ERP) for various places that can be used by emergency planners and interested parties to add the MT component to the storm surge. Last, to provide a broader and faster way to predict the hazards on a broad scale, an optimal artificial neural network (ANN) was trained using data from a large number of MT simulations in the northeastern GOM. Regression analysis of the output of ANN was performed, and the results are consistent with numerical simulation with a correlation coefficient greater than 98%.

Although the recurrence of destructive tsunami events have been verified to be quite low in the GOM, our work has confirmed that submarine landslide events with similar characteristics to those used here, have indeed the potential to cause severe damage to GOM coastal communities. GOM is a region where tropical cyclones and winter storms occur frequently. From 1996 to 2016, there are around 20 meteotsunami events on average in Florida. Our results indicate meteotsunami water level could reach as high as 0.5 m in some locations and has the potential to cause damage. Therefore, this work is intended to provide guidance to local emergency managers to help managing urban growth, evacuation planning, and public education with the final objective to mitigate potential landslide tsunami and meteotsunami hazards in the GOM.

Acknowledgments

This work was supported by the National Oceanic and Atmospheric Administration (NOAA) under awards NA20NWS4670066, "Development of two tsunami inundation maps and continuation of the meteotsunami characterization for the GOM". The authors wish to thank all NTHMP modeling and Mapping Subcommittee members and GOM's emergency manager representatives for their helpful insights. Special thanks go to Brad Baker for their helpful insight and support. Also thank Kelly Carignan and Kelly Stroker for providing the DEMs. High resolution inundation maps are available from `http://www.tamug.edu/tsunami/NTHMP/NTHMP.html` or by contacting corresponding author upon request.

References

C. Amante and B. Eakins. ETOPO1 1 arc-minute global relief model: Procedures, data sources and analysis. *NOAA Technical Memorandum NESDIS NGDC-24. National Geophysical Data Center, NOAA*, 2009. doi: 10.7289/V5C8276M. [accessed 01-March-2019].

E. J. Anderson, A. J. Bechle, C. H. Wu, D. J. Schwab, G. E. Mann, and K. A. Lombardy. Reconstruction of a meteotsunami in Lake Erie on 27 may 2012: Roles of atmospheric conditions on hydrodynamic response in enclosed basins. *Journal of Geophysical Research: Oceans*, 120(12):8020–8038, 2015.

P. M. Atkinson and A. R. Tatnall. Introduction neural networks in remote sensing. *International Journal of remote sensing*, 18(4):699–709, 1997.

D. Basco and C. Klentzman. On the classification of coastal storms using principles of momentum conservation. In *Proc. 31st Int. Conf. on Coastal Eng.* ASCE, 2006.

A. J. Bechle, C. H. Wu, D. A. Kristovich, E. J. Anderson, D. J. Schwab, and A. B. Rabinovich. Meteotsunamis in the Laurentian Great Lakes. *Scientific reports*, 6:37832, 2016.

J. D. Chaytor, E. L. Geist, C. K. Paull, D. W. Caress, R. Gwiazda, J. U. Fucugauchi, and M. R. Vieyra. Source characterization and tsunami modeling of submarine landslides along the yucatán shelf/campeche escarpment, southern gulf of mexico. *Pure and Applied Geophysics*, 173(12):4101–4116, Dec 2016. ISSN 1420-9136. doi: 10.1007/s00024-016-1363-3. URL `https://doi.org/10.1007/s00024-016-1363-3`.

H. Chen, L. He, W. Qian, and S. Wang. Multiple aerodynamic coefficient prediction of airfoils using a convolutional neural network. *Symmetry*, 12(4):544, 2020.

W. Cheng, J. Horrillo, and R. Sunny. Numerical analysis of meteotsunamis in the northeastern gulf of mexico. *Natural Hazards*, Sep 2021. ISSN 1573-0840. doi: 10.1007/s11069-021-05009-9.

B. Dugan and J. Stigall. Origin of overpressure and slope failure in the Ursa region, northern Gulf of Mexico. In D. C. Mosher, R. C. Shipp, L. Moscardelli, J. D. Chaytor, C. D. P. Baxter, H. J. Lee, and R. Urgeles, editors, *Submarine Mass Movements and Their Consequences*, pages 167–178. Springer Netherlands, 2010.

P. K. Dunbar and C. S. Weaver. *U.S. States and Territories National Tsunami Hazard Assessment: Historical Record and Sources for Waves*. U.S. Department of Commerce, National Oceanic and Atmospheric Administration, National Geophysical Data Center Tech. Rep.No. 3, 2008.

G. Dusek, C. DiVeglio, L. Licate, L. Heilman, K. Kirk, C. Paternostro, and A. Miller. A meteotsunami climatology along the US East Coast. *Bulletin of the American Meteorological Society*, 100(7):1329–1345, 2019.

E. L. Geist, J. D. Chaytor, T. Parsons, and U. ten Brink. Estimation of submarine mass failure probability from a sequence of deposits with age dates. *Geosphere*, 9(2):287–298, 2013.

H. P. Greenspan. The generation of edge waves by moving pressure distributions. *Journal of Fluid Mechanics*, 1(6):574–592, 1956.

S. T. Grilli, O.-D. S. Taylor, C. D. P. Baxter, and S. Maretzki. A probabilistic approach for determining submarine landslide tsunami hazard along the upper east coast of the United States. *Mar. Geol.*, 264:74–97, 2009.

C. B. Harbitz, F. Løvholt, and H. Bungum. Submarine landslide tsunamis: How extreme and how likely? *Nat. Hazards*, 72(3):1341–1374, 2014.

C. W. Hirt and B. D. Nichols. Volume of fluid method for the dynamics of free boundaries. *J. Comput. Phys.*, 39:201–225, 1981.

J. Horrillo. *Numerical Method for Tsunami calculations using Full Navier-Stokes equations and the Volume of Fluid method*. PhD thesis, University of Alaska Fairbanks, 2006.

J. Horrillo, A. Wood, C. Williams, A. Parambath, and G. Kim. Construction of tsunami inundation maps in the Gulf of Mexico. Technical report, Award Number: NA09NWS4670006 to the National Tsunami Hazard Mitigation Program (NTHMP), National Weather Service Program Office, NOAA, 2011. avail. from http://www.tamug.edu/tsunami/NTHMP.html.

J. Horrillo, A. Wood, G.-B. Kim, and A. Parambath. A simplified 3-D Navier-Stokes numerical model for landslide-tsunami: Application to the Gulf of Mexico. *J. Geophys. Res.-Oceans*, 118:6934–6950, 2013. doi:10.1002/2012JC008689.

J. Horrillo, A. Pampell-Manis, C. Sparagowski, L. Parambath, and Y. Shigihara. Construction of five tsunami inundation maps for the Gulf of Mexico. Technical report, Award Number: NA12NWS4670014 and NA13NWS4670018 to the National Tsunami Hazard Mitigation Program (NTHMP), National Weather Service Program Office, NOAA, 2015. avail. from http://www.tamug.edu/tsunami/NTHMP.html.

J. Horrillo, W. Cheng, A. Pampell-Manis, and J. Figlus. Implementing nthmp-mms strategic plan in tsunami hazard mitigation products for the Gulf of Mexico. Technical report,

Award Number: NA14NWS4670049 to the National Tsunami Hazard Mitigation Program (NTHMP), National Weather Service Program Office, NOAA, 2016. avail. from http://www.tamug.edu/tsunami/NTHMP.html.

J. Horrillo, W. Cheng, and J. Figlus. Development of four additional tsunami inundation maps with revision of Port Aransas, TX and updating existing ones with maritime products. Technical report, Award Number: NA15NWS4670031 and NA16NWS4670039 to the National Tsunami Hazard Mitigation Program (NTHMP), National Weather Service Program Office, NOAA, 2017. avail. from http://www.tamug.edu/tsunami/NTHMP.html.

J. Horrillo, W. Cheng, and J. Figlus. Development of two tsunami inundation maps in the GOM and inclusion of the USGS' Yucatan landslide tsunami sources. Technical report, Award Number: NA17NWS4670015 to the National Tsunami Hazard Mitigation Program (NTHMP), National Weather Service Program Office, NOAA, 2018. avail. from http://www.tamug.edu/tsunami/NTHMP.html.

J. Horrillo, W. Cheng, J. Figlus, and K. W. Development of two tsunami inundation maps in the GOM and inclusion of the Meteotsunami characterization for Panama City, FL. Technical report, Award Number: NA18NWS4670078 to the National Tsunami Hazard Mitigation Program (NTHMP), National Weather Service Program Office, NOAA, 2019. avail. from http://www.tamug.edu/tsunami/NTHMP.html.

J. J. Horrillo, W. Cheng, R. Sunny, and A. J. Y. Shang. Development of two tsunami inundation maps and continuation of the meteotsunami characterization for the gom. Technical report, Award Number: NA19NWS4670015 to the National Tsunami Hazard Mitigation Program (NTHMP), National Weather Service Program Office, NOAA, 2020. avail. from http://www.tamug.edu/tsunami/NTHMP.html.

J. L. Irish and D. T. Resio. A hydrodynamics-based surge scale for hurricanes. *Ocean Eng.*, 37:69–81, 2010.

J. Jiang, J. Zhang, G. Yang, D. Zhang, and L. Zhang. Application of back propagation neural network in the classification of high resolution remote sensing image: take remote sensing image of beijing for instance. In *2010 18th International Conference on Geoinformatics*, pages 1–6. IEEE, 2010.

D. Kamari, M. Tadjfar, and A. Madadi. Optimization of sd7003 airfoil performance using tbl and cbl at low reynolds numbers. *Aerospace Science and Technology*, 79:199–211, 2018.

L. Kantha. Time to replace the Saffir-Simpson hurricane scale? *Eos, Transactions American Geophysical Union*, 87(1):3–6, 2006.

A. Kharal and A. Saleem. Neural networks based airfoil generation for a given cp using bezier–parsec parameterization. *Aerospace Science and Technology*, 23(1):330–344, 2012.

J. Kim and R. Omira. The 6–7 july 2010 meteotsunami along the coast of portugal: insights from data analysis and numerical modelling. *Natural Hazards*, 106(2):1397–1419, Mar 2021. ISSN 1573-0840. doi: 10.1007/s11069-020-04335-8.

W. Knight. Model predictions of Gulf and Southern Atlantic Coast tsunami impacts from a distribution of sources. *Sci. of Tsunami Hazards*, 24:304–312, 2006.

K. Kosowski, K. Tucki, and A. Kosowski. Application of artificial neural networks in investigations of steam turbine cascades. *Journal of Turbomachinery*, 132(1), 2010.

Z. Kowalik, W. Knight, T. Logan, and P. Whitmore. Numerical modeling of the global tsunami: Indonesian tsunami of 26 December 2004. *Science of Tsunami Hazards*, 23(1): 40–56, 2005.

Á. Linares, A. J. Bechle, and C. H. Wu. Characterization and assessment of the meteotsunami hazard in northern Lake Michigan. *Journal of Geophysical Research: Oceans*, 121(9):7141–7158, 2016.

M. Ličer, B. Mourre, C. Troupin, A. Krietemeyer, A. Jansá, and J. Tintoré. Numerical study of Balearic meteotsunami generation and propagation under synthetic gravity wave forcing. *Ocean Modelling*, 111:38 – 45, 2017. ISSN 1463-5003. doi: https://doi.org/10.1016/j.ocemod.2017.02.001.

A. M. López-Venegas, J. Horrillo, A. Pampell-Manis, V. Huérfano, and A. Mercado. Advanced tsunami numerical simulations and energy considerations by use of 3D - 2D coupled models: The October 11, 1918, Mona Passage tsunami. *Pure Appl. Geophys.*, 172(6):1679–1698, 2015.

P. J. Lynett, J. C. Borrero, R. Weiss, S. Son, D. Greer, and W. Renteria. Observations and modeling of tsunami-induced currents in ports and harbors. *Earth and Planetary Science Letters*, 327:68–74, 2012.

P. J. Lynett, J. Borrero, S. Son, R. Wilson, and K. Miller. Assessment of the tsunami-induced current hazard. *Geophysical Research Letters*, 41(6):2048–2055, 2014.

F. Makinoshima, Y. Oishi, T. Yamazaki, T. Furumura, and F. Imamura. Early forecasting of tsunami inundation from tsunami and geodetic observation data with convolutional neural networks. *Nature communications*, 12(1):1–10, 2021.

S. Maretzki, S. Grilli, and C. D. P. Baxter. Probabilistic SMF tsunami hazard assessment for the upper east coast of the United States. In V. Lykousis, D. Sakellariou, and J. Locat, editors, *Submarine Mass Movements and Their Consequences*, pages 377–385. Springer Netherlands, 2007.

D. Masson, C. Habitz, R. Wynn, G. Pederson, and F. Lovholt. Submarine landslides: Processes, triggers and hazard protection. *Philos. Trans. R. Soc. A*, 364:2009–2039, 2006.

S. Monserrat, I. Vilibić, and A. B. Rabinovich. Meteotsunamis: atmospherically induced destructive ocean waves in the tsunami frequency band. *Natural Hazards and Earth System Science*, 6(6):1035–1051, Dec. 2006.

M. Olabarrieta, A. Valle-Levinson, C. J. Martinez, C. Pattiaratchi, and L. Shi. Meteotsunamis in the northeastern Gulf of Mexico and their possible link to El Niño Southern Oscillation. *Natural hazards*, 88(3):1325–1346, 2017.

A. Pampell-Manis, J. Horrillo, Y. Shigihara, and L. Parambath. Probabilistic assessment of landslide tsunami hazard for the northern Gulf of Mexico. *J. Geophys. Res.-Oceans*, 2016. doi:10.1002/2015JC011261.

C. B. Pattiaratchi and E. Wijeratne. Are meteotsunamis an underrated hazard? *Philosophical Transactions of the Royal Society A: Mathematical, Physical and Engineering Sciences*, 373(2053):20140377, 2015.

C. K. Paull, D. W. Caress, R. Gwiazda, J. Urrutia-Fucugauchi, M. Rebolledo-Vieyra, E. Lundsten, K. Anderson, and E. J. Sumner. Cretaceous–paleogene boundary exposed: Campeche escarpment, gulf of mexico. *Marine Geology*, 357:392–400, 2014.

C. H. Paxton and D. A. Sobien. Resonant interaction between an atmospheric gravity wave and shallow water wave along Florida's west coast. *Bulletin of the American Meteorological Society*, 79(12):2727–2732, 1998.

L. D. Paxton. Development of a forecast process for meteotsunami events in the Gulf of Mexico. Master's thesis, University of South Florida, 2016.

L. Prechelt. Automatic early stopping using cross validation: quantifying the criteria. *Neural Networks*, 11(4):761–767, 1998.

J. Proudman. The effects on the sea of changes in atmospheric pressure. *Geophysical Supplements to the Monthly Notices of the Royal Astronomical Society*, 2(4):197–209, 1929.

A. Rabinovich and S. Monserrat. Meteorological tsunamis near the Balearic and Kuril Islands: Descriptive and statistical analysis. *Natural Hazards*, 13(1):55–90, 1996.

A. B. Rabinovich. Twenty-seven years of progress in the science of meteorological tsunamis following the 1992 daytona beach event. *Pure and Applied Geophysics*, 177(3):1193–1230, 2020.

A. B. Rabinovich, J. Šepić, and R. E. Thomson. The meteorological tsunami of 1 November 2010 in the southern Strait of Georgia: a case study. *Natural Hazards*, 106(2):1503–1544, Mar 2021. ISSN 1573-0840. doi: 10.1007/s11069-020-04203-5.

J. Šepić and I. Vilibić. The development and implementation of a real-time meteotsunami warning network for the Adriatic Sea. *Natural Hazards and Earth System Sciences*, 11(1): 83–91, 2011.

A. Sheremet, U. Gravois, and V. Shrira. Observations of meteotsunami on the Louisiana shelf: a lone soliton with a soliton pack. *Natural Hazards*, 84(2):471–492, Nov 2016. ISSN 1573-0840. doi: 10.1007/s11069-016-2446-2.

L. Shi, M. Olabarrieta, A. Valle-Levinson, and J. C. Warner. Relevance of wind stress and wave-dependent ocean surface roughness on the generation of winter meteotsunamis in the Northern Gulf of Mexico. *Ocean Modelling*, 140:101408, 2019.

L. Shi, M. Olabarrieta, D. S. Nolan, and J. C. Warner. Tropical cyclone rainbands can trigger meteotsunamis. *Nature communications*, 11(1):1–14, 2020.

U. S. ten Brink, H. J. Lee, E. L. Geist, and D. Twichell. Assessment of tsunami hazard to the U.S. East Coast using relationships between submarine landslides and earthquakes. *Mar. Geol.*, 264:65–73, 2009a.

U. S. ten Brink, D. Twichell, P. Lynett, E. Geist, J. Chaytor, H. Lee, B. Buczkowski, and C. Flores. Regional assessment of tsunami potential in the Gulf of Mexico. *U. S. Geol. Surv. Admin. Rep.*, 2009b.

I. Vilibić, K. Horvath, N. Strelec Mahović, S. Monserrat, M. Marcos, Á. Amores, and I. Fine. Atmospheric processes responsible for generation of the 2008 Boothbay meteotsunami. *Natural Hazards*, 74(1):25–53, Oct 2014a. ISSN 1573-0840. doi: 10.1007/s11069-013-0811-y.

I. Vilibić, S. Monserrat, and A. B. Rabinovich. Meteorological tsunamis on the US East Coast and in other regions of the World Ocean. *Natural Hazards*, 74(1):1–9, Oct 2014b. ISSN 1573-0840. doi: 10.1007/s11069-014-1350-x.

S. Wang, G. Sun, W. Chen, and Y. Zhong. Database self-expansion based on artificial neural network: An approach in aircraft design. *Aerospace Science and Technology*, 72: 77–83, 2018.

P. Whitmore and B. Knight. Meteotsunami forecasting: sensitivities demonstrated by the 2008 Boothbay, Maine, event. *Natural Hazards*, 74(1):11–23, Oct 2014. ISSN 1573-0840. doi: 10.1007/s11069-014-1056-0.

R. Wilson, C. Davenport, and B. Jaffe. Sediment scour and deposition within harbors in california (usa), caused by the march 11, 2011 tohoku-oki tsunami. *Sedimentary Geology*, 282:228–240, 2012.

R. I. Wilson, A. R. Admire, J. C. Borrero, L. A. Dengler, M. R. Legg, P. Lynett, T. P. McCrink, K. M. Miller, A. Ritchie, K. Sterling, et al. Observations and impacts from the 2010 chilean and 2011 japanese tsunamis in california (usa). *Pure and Applied Geophysics*, 170(6-8):1127–1147, 2013.

H. Wu, X. Liu, W. An, S. Chen, and H. Lyu. A deep learning approach for efficiently and accurately evaluating the flow field of supercritical airfoils. *Computers & Fluids*, 198: 104393, 2020.

Y. Yamazaki, Z. Kowalik, and K. F. Cheung. Depth-integrated, non-hydrostatic model for wave breaking and run-up. *Int. J. Numer. Meth. Fl.*, 61:473–497, 2008.